diamond

Diamond Light Source Ltd

2021/22

Contents

DIAMOND LIGHT SOURCE ANNUAL REVIEW 2021/22

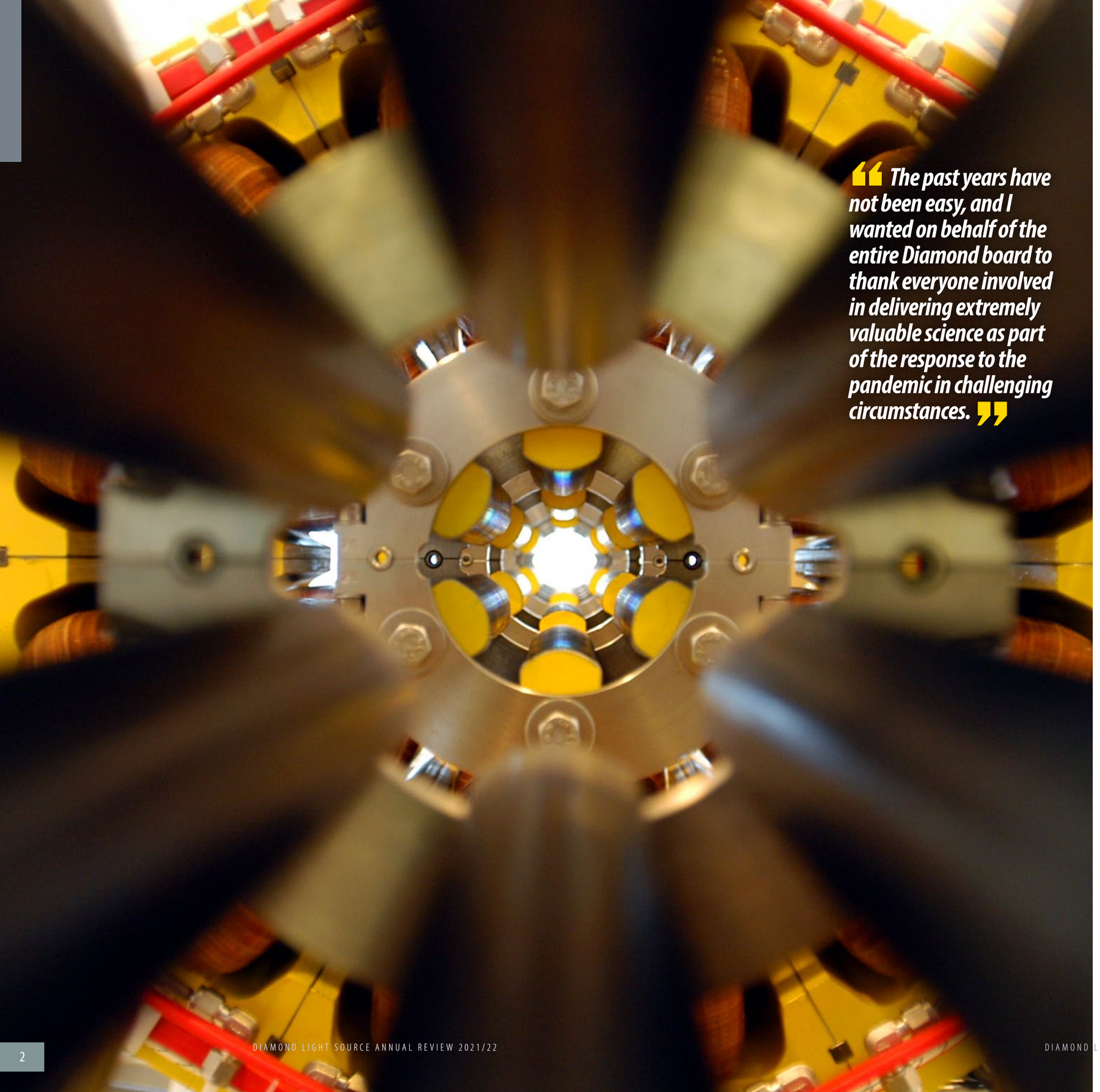

Foreword

2022 celebrates a double anniversary for Diamond - 20 years since the company was set-up to design, build and operate the UK's national synchrotron and 15 years of delivering science and innovation to the science community. Diamond has made some considerable growth and leaps in this timeframe that have made a major contribution to science in general and the UK's global leadership in this field. Indeed, the socio-economic study published in the past year highlighted a cumulative monetised impact of at least £1.8 billion from the impressive contribution of Diamond to UK science and the economy through our many strands of output including research, patents, software and applications, training, and our extensive programme of external engagement.

The next exciting chapter for Diamond rests with the large upgrade Diamond-II programme. Budget pressures are felt everywhere but I believe that this investment in science is essential for the UK to move forward and cement its leadership position on the global stage. The board is committed to making the case to the Government on this basis and to fight for appropriate funding that secures our bright future for the next 20 years.

Finally, the past years have not been easy, and I wanted on behalf of the entire Diamond board to thank everyone involved in delivering extremely valuable science as part of the response to the pandemic in challenging circumstances. Diamond has kept its doors open to researchers exploring a wide range of scientific endeavours. Diamond's ongoing success is down to the outstanding people in all areas of the organisation.

Professor Sir Adrian Smith
Chairman of the Board of Directors

CEO Welcome

As the financial year is ending, the pandemic has become an endemic disease that we are all trying to manage as best as possible whilst returning to our day-to-day activity of running the facility. A sense of caution matched with a desire for normality is hard to balance but at Diamond we have done our best to keep going, managing risks as we could under the new circumstances. Added to this challenge, the war in Ukraine has unsettled many staff and members of our user community. As always, we have been resourceful in the face of such challenges and deployed a range of measures supporting staff and users in relocating their affected families to safety. In 2022 we do however have much to celebrate with a special double anniversary for Diamond, marking 20 years since the company was first created through the Joint Venture Agreement between the UK Government through the Central Council of the Laboratory of the Research Councils and the Wellcome Trust at the time, as well as 15 years since we first opened our doors to our research community. We will be marking this important milestone with multiple activities across the year including a large-scale photographic exhibition.

Our first socioeconomic impact report carried out together with Technopolis, along with support from our funding agencies, was launched in May last year. The report received over 2,000 views and some 1,500 downloads and has become an influential piece of work within the research infrastructure community with many learning from its methodology and approach. With 14,000 researchers interested in using our instruments, our position remains very strong given that Diamond has for the period 2007-2020 achieved a cumulative monetised impact of at least £1.8 billion whilst costing each UK taxpayer only £2.45 per year for this amazing impact. These tremendous benefits are a credit to our dedicated staff, contractors and agency workers who enable innovation, push the boundaries of what can be measured and offer excellent support and service to the science delivered internally as well as externally.

Our peer review publications have reached 11,500 as we close the year. We are heartened that 50% of the catalogue is now published straight away with open access and the quality remains very strong with over 42% in journals with impact factors of five and above. COVID-19 made it impossible to allow users back on site for experiments for much of the past two years, so it was difficult to continue to support more specialised experiments despite the heroic work of many at Diamond to compensate for the loss of hands-on user engagement. We anticipate therefore a temporary drop in the annual number of publications, noting that it takes two to three years from measurement to publication.

Ensuring our science is widely disseminated has always been a priority and one of the highlights of the past year was welcoming Sir David Attenborough to the facility where he hosted a major BBC documentary on the last days of the Dinosaurs. Other successful campaigns included the COVID Moonshot, which is driving five drug compounds into the first stages of clinical trials required. We have also seen an amazing cataloguing of high-resolution images of beetles for the Natural History Museum, enabled by the transfer of robotics technology for sample changing from MX beamlines to the imaging beamline 13.

For the period 2021-2022, we received 1,116 proposals for experiments on our instruments via peer reviewed access routes, requesting a total of 12,635 shifts. After peer review, 719 proposals were awarded beamtime. This resulted in 6,983 experimental shifts being awarded across 33 beamlines and eight electron microscopes. We welcomed 2,460 on-site user visits from academia across all instruments, with an additional 4,253 remote user visits. The machine continues to perform to a high standard with 97.4 % uptime and 110 hours mean time between failures (MTBF). Diamond also provides services critical to industry in the UK, with over 200 companies making use of the facility since operations began, normally paying £3 million per annum for proprietary access.

The Diamond-II upgrade programme, an integrated upgrade of the synchrotron, beamlines and computational facilities, critical to maintaining our world-leading status, further progressed with preliminary funding allocated by Science and Technology Facilities Council (STFC) and Wellcome in early summer 2021. A major milestone in securing full funding from the UK Government was achieved with approval of the Outline Business Case (OBC) by the Department for Business, Energy and Industrial Strategy (BEIS) and Her Majesty's Treasury (HMT). This approval also builds on an early commitment of support from Wellcome for their funding share. Together with the Technical Design Report (TDR) for the machine completed and approved by the Diamond Machine Advisory Committee, alongside Conceptual Design Reports (CDRs) for three flagship beamlines, Diamond is in a very strong position to complete the Full Business Case later in 2022, which is the last stage of approval required for release of full funding for the Programme.

Success to date in planning and securing funding for Diamond-II owes a tremendous amount to Dr Laurent Chapon, who took a lead in developing the science case, introduced the idea of increasing the energy of the storage ring to optimise performance of beamlines for the key needs of our research community, and was the first Diamond-II Programme Director. Laurent has now taken up the position of Associate Laboratory Director for Photon Sciences and Director of the Advanced Photon Source at Argonne National Laboratory, USA – chapeau !

This year it has been very pleasing to witness the rise of the DIAD beamline. This is the first in the world able to switch between imaging and diffraction in a matter of seconds and its presence is already drawing an international community positioning Diamond as world-leading once again. Scientific success abounds elsewhere in Diamond too, illustrated throughout this Review. For example, this year on I04, an international team investigated the potential of new molecules with antibiotic properties, examining how these interact at a molecular level, with the aim to develop a new family of antibiotics. Our integrated facilities also achieved great science with a collaborative team from University of Queensland, University of Leeds, University of Cambridge and University of Paris-Saclay who studied next-generation composite glass at the electron Physical Sciences Imaging Centre (ePSIC) that can be used for smartphones or solar panels by determining the structure of this new material.

Throughout 2021, Diamond undertook an assessment process run by the National Co-ordinating Centre for Public Engagement (NCCPE), and in October we were delighted to be presented with the Bronze Engage Watermark award. This recognises the commitment of Diamond to Public Engagement with over 80,000 visitors reached so far through a programme of engagement at the heart of the facility supporting the UK Skills' agenda in science, technology, engineering and mathematics (STEM). Our work with undergraduates and postgraduates is also strengthening with a total cohort this year reaching 136 in total - PhDs (109), Year in Industry (12) and Summer Placements (15). Using the methodologies developed to integrate virtual activities into visitor numbers, Diamond has had over 7,300 significant interactions with 'virtual' visitors. These include 2,949 for scientific and technical events, 267 undergraduate and postgraduate interactions, 3,828 school students and members of the public, and 279 VIPs and Stakeholders. Over 95% of all these were virtual while we continued to adjust to the second year of the pandemic. Amongst the few in person interactions, we worked hard to maintain within ongoing restrictions at the time, was the Diamond Academy – a work experience programme for secondary students organised by our Public Engagement team. We were delighted to welcome 36 students to work alongside Diamond volunteer supervisors on 18 different projects across the organisation.

Diamond is a flagship investment for the UK with returns far beyond the science delivered and I remain very optimistic that our future Diamond-II upgrade will enable us to remain world-leaders in the field. However, the greatest asset Diamond has in delivering transformative science and innovation is the staff in every single part of the organisation, all of whom play an essential role in our success. Every staff member deserves a special thank you!

Added to this, I have been greatly impressed over the past year with the work of the employee led inclusion groups, for example the proactive changes brought around disability awareness through the universal accessibility group, which resulted in improved processes, website, education for managers and staff as well as enhanced support for those affected. Widening participation is another important issue, and we hope that many interested in applying to Diamond, would experience a welcoming and nurturing environment. Probably the biggest challenge we face as an organisation is continuing to recruit and retain excellent people at a time when public sector pay was frozen (this is now lifted) so a priority for the future for Diamond must be to persuade policy makers that major investment in capital must be matched by appropriate investment in people.

Professor Andrew Harrison OBE
CEO Diamond Light Source

Supporting International COVID-19 Research

Diamond Light Source has continued to give international COVID-19 researchers high priority access to beamtime throughout the year, despite lockdown restrictions around the world. Over the year, 530 shifts were delivered across all instruments for COVID-19 research. The work taking place at Diamond is grouped into those projects developing understanding of the virus structure and function, new vaccine design and efficiency, drug development (including both new drugs and re-purposing existing drugs) and developing new therapies.

Understanding how the virus operates

Several studies have continued to develop detailed understanding of the SARS-CoV-2 viral mechanisms and structure. These significant and rapid fundamental research efforts have already resulted in the licensing of several vaccines which have been rolled out to many millions around the world in rapid vaccination programmes. In addition, neutralising monoclonal antibodies (mAbs) have been developed to be used prophylactically or therapeutically.

A research group led by Professor Peijun Zhang (Director of the Electron Bio-Imaging Centre (eBIC) at Diamond and Professor of Structural Biology at the University of Oxford) have continued their work on unlocking the structure of the SARS-CoV-2 virus[1]. The research team used the cryo-electron microscopy (cryo-EM) facilities at eBIC to investigate viral replication in a Vero cell line under near-native conditions. They reported critical structural events such as viral RNA transport portals and native virus spike structures. Their approach gave a holistic view of SARS-CoV-2 infection from the whole cell to individual molecules and the study results validated previous findings from studies using electron microscopy on plastic-embedded samples. The study further expands knowledge on viral assembly and egress of SARS-CoV-2 as well as its presence in other membrane compartments. It also confirms the value of cryo-EM and soft X-ray tomography as techniques to investigate whole cell morphology with the advantages of frozen-hydrated conditions and fast sample preparation.

Professor Jonathan Grimes (Diamond Fellow and Professor of Structural Biology at the University of Oxford) worked in collaboration with a number of University colleagues on two projects studying coronavirus mechanisms. The first aimed to improve understanding of the mechanism of coronavirus RNA capping which, though an important feature of the viral life cycle, is poorly understood[2]. Using numerous assay techniques, the group demonstrated the vital function of the nucleotidyltransferase (NiRAN) domain of SARS-CoV-2 non-structural protein 12 (nsp12) in viral synthesis. They also showed that this activity can be inhibited by remdesivir triphosphate which highlights the NiRAN domain as a possible target for repurposed antiviral drugs.

In the second study Professor Grimes was part of a group performing further characterisation of the virus using biochemical techniques[3].

The Titan Krios is a state-of-the-art fully automated electron microscope designed for rapid, stable, high-resolution data collection on frozen-hydrated samples.

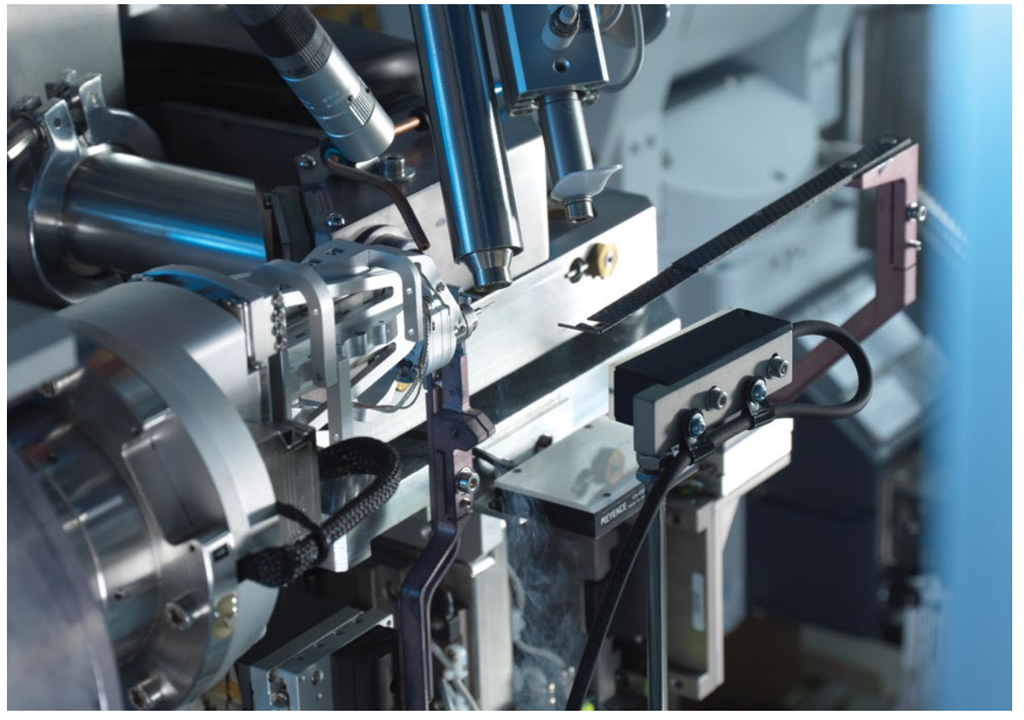

Image of Beamline I03.

Crystals of the RBD protein.

Coronaviruses have relatively large single-stranded RNA genomes and to maintain the fidelity of these genomes they rely on a complex of two non-structural proteins (nsp14 and nsp10). The study allowed a biochemical characterisation of the nsp14- nsp10 complex and developed assay systems that could screen for inhibitors. This work highlighted domains that could be possible targets for antiviral drugs and identified several drugs and molecules that could be developed or re-purposed to inhibit the nuclease activity of the nsp14-nsp10 complex. These included ebselen which has been shown to inhibit the SARS-CoV-2 major protease (M^{pro}) and the HIV integrase inhibitor raltegravir, revealing the potential for multifunctional inhibitors in COVID-19 treatment.

Efficacy of the vaccine

The rapid development of vaccines and mAbs against COVID-19 through intensive international collaboration has been one of the positive highlights of the pandemic. Although current vaccines elicit neutralising antibody responses to the virus spike derived from early isolates, new strains have emerged with multiple mutations.

Many studies are ongoing to assess the impact of these therapies against the new variants of the virus and the ability of these different variants to evade antibody responses**.** Recent studies include data collected automatically at Diamond on macromolecular crystallography beamline I03 (see MX intro section showing how previously infected or vaccinated individuals respond to the new variants and antibodies).

A large international group studied the ability of mAbs and convalescent and vaccine sera to neutralise two Delta variant viruses (B.1.617.1 and B.1.617.2) that were first reported in India but spread globally[4]. The group used beamline I03 at Diamond to determine the crystal structures of the variants.

Although neutralisation of both viruses was reduced compared with earlier strains there was no evidence of widespread antibody escape, suggesting that the current generation of vaccines will provided protection against B.1.617, although reduced titres may lead to some breakthrough infections. However, there was concern that some unvaccinated individuals infected with earlier variants may be more at risk of reinfection with B.1.617.2. These findings provide important new insights to influence immunisation policy.

The Beta variant has been particularly difficult to neutralise using serum induced by the early pandemic. To understand this, an international collaboration performed a study to understand the antigenic landscape of the Beta variant[5]. The study included an in-depth structure-function analysis of potent mAbs from volunteers infected with the Beta variant and generated 674 mAbs from beta infected individuals. The authors also performed a detailed structure-function analysis of the 27 most potent mAbs: one binding the spike N-terminal domain (NTD), the rest the receptor-binding domain (RBD).

Structural analyses took place using data gathered on beamline I03 and this will add to the increased understanding of the structure and behaviour of the different variants, which will have an important impact on the design and use of available vaccines. This ongoing research will also assist the development of future vaccination strategies.

This group performed analysis on different variants including P.1 from Brazil and Beta from South Africa (B.1.351) and Alpha from the UK (B.1.1.7)[6]. Structural analysis at Diamond showed how mAbs neutralise all three variants, and that P.1 is easier to neutralise than other similar receptor-binding domain (RBD) mutations. The study showed that the South African variant B.1.351 was of greatest concern.

In another recent paper in *Cell* an international research group studied the neutralisation of Omicron by a large panel of sera collected from early infected individuals and those vaccinated with three doses of the Oxford/Astra Zeneca or Pfizer vaccines[7].

The rapid emergence of the Omicron variant in the background of high Beta variant immunity implies that the virus may have evolved to escape neutralisation by Beta-specific serum.

The study mapped the Omicron RBD mutations and revealed Omicron to be structurally similar but the most antigenically distant variant and that the variant escaped neutralisation by most mAbs.

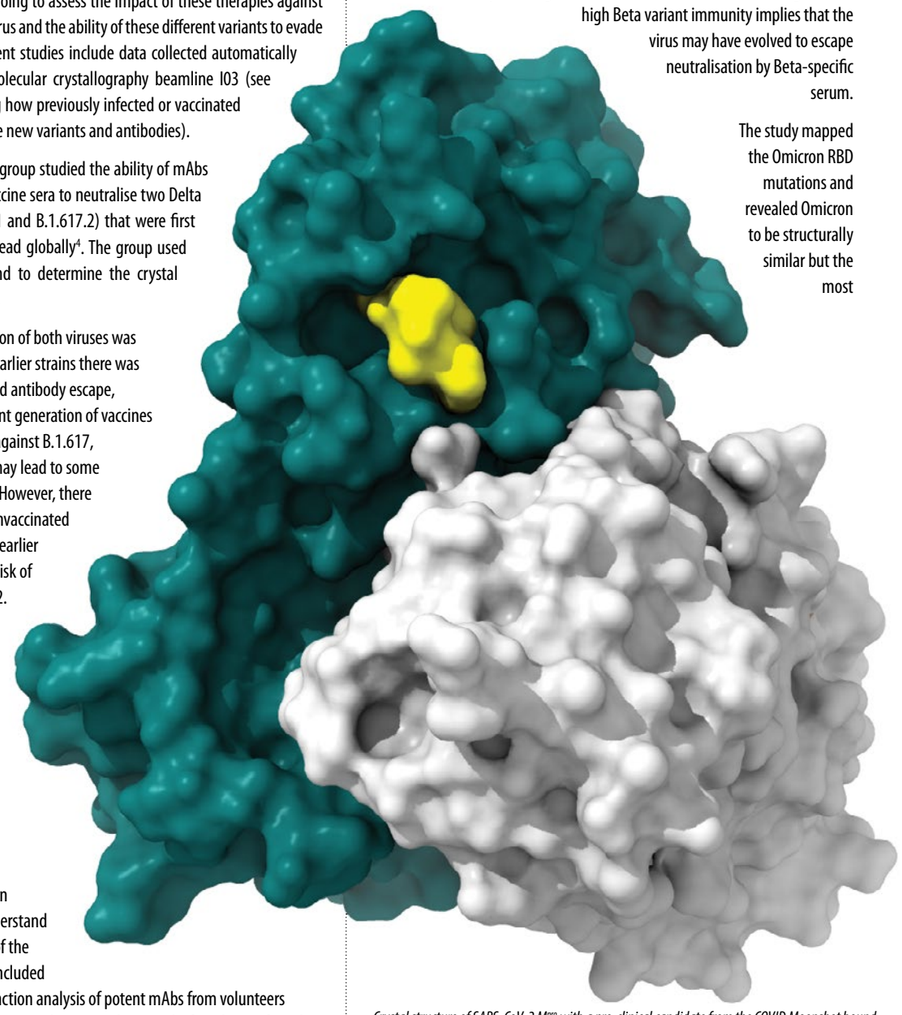

Crystal structure of SARS-CoV-2 M^{pro} with a pre-clinical candidate from the COVID Moonshot bound (shown in yellow). The COVID Moonshot, of which Diamond is a founding member, has received funding of £8 million from Wellcome, on behalf of the COVID-19 Therapeutics Accelerator to develop a globally accessible antiviral.

The researchers commented that although the large number of mutational changes seen in Omicron leads to a fall in vaccine effectiveness, it is likely that protection from severe infection will be maintained. The study demonstrated that a third vaccine dose is effective in boosting neutralisation titres against Omicron and that booster vaccination programmes should add considerable protection against Omicron infection.

Drug development (both repurposing and new drugs)

To defeat the current pandemic and manage the impact of SARS-CoV-2 in the future, a combination of new drugs, repurposed drugs and other therapies will be required. Diamond is playing a key role supporting research groups around the world to develop effective therapies. Major screening studies are taking place to identify new drug candidates, repurposed antivirals are being investigated and there is ongoing development of vaccines that can tackle new variants. The urgency of the current global pandemic demands rapid action.

Throughout the pandemic a research collaboration between Diamond, Exscientia (Oxford), Scripps Research Institute in California and Leuven University has aimed to accelerate the path to clinical trials for potential antiviral treatments, both now and in the future.

Two potential drug targets are the main protease (M^{pro}) and the papain-like protease (PL^{pro}) which are essential for the coronavirus replication cycle. The international research group conducted extensive experimental screens of the drug repurposing ReFRAME library of 12,000 therapeutic agents[8]. The library was developed at Calibr, the drug development division of the Scripps Research Institute with funding from the Bill and Melinda Gates foundation. The screens identified two potential drug candidates, the caspase-1 inhibitor SDZ 224015, which was found to be a potent irreversible inhibitor of M^{pro}, and tarloxotinib, a clinical stage epidermal growth factor receptor inhibitor was an inhibitor of PL^{pro}. This is the first reported PL^{pro} inhibitor with drug-like properties. Diffraction data were collected from crystals cryo-cooled at Diamond with X-ray diffraction data collected at beamlines I04-1 and I24. As both compounds have already undergone safety evaluation in humans, they are trial candidates for rapid clinical evaluation against COVID-19.

A collaboration between Diamond and Israeli research groups designed a computational pipeline to help identify irreversible inhibitors based on structures of targets with non-covalent binders[9]. The so-called *covalentiser* was developed to identify covalent analogues of non-covalent binders.

Covalent irreversible inhibitors have become increasingly popular over the last decade as chemical probes and drugs. These offer several advantages over non-covalent inhibitors such as prolonged residence time, improved selectivity, and an ability to compete with high affinity natural substrates, but designing new covalent inhibitors is challenging.

The group used a pre-compiled database of *covalentiser* results to look for possible candidate inhibitors for SARS-CoV-2 proteins. Using the protocol allowed discovery of several covalent kinase inhibitors and optimised a potent covalent COVID-19 protease inhibitor, with a low-cost, modular, and fast synthesis.

The protocol was prospectively validated against various kinases, as well as in a rapid drug discovery campaign against the SARS-CoV-2 main protease. Co-crystal structural data were collected at Diamond on beamline I04-1 to confirm the computational model.

These results point to many other potential targets that may be targeted by a covalent analogue of a known ligand, potentially shortening the time and effort in finding future covalent inhibitors.

Other therapies

An international collaboration continued their work on neutralising single domain antibodies (nanobodies) which have significant potential as an effective treatment against COVID-19[10]. They appear to offer considerable advantages over conventional antibodies as their small size and stability mean they can be formulated for respiratory administration which results in improved bioavailability, easier administration, and improved therapeutic compliance. They can also be manufactured using readily available microbial systems.

The research group isolated four nanobodies that bind different epitopes on the receptor binding domain (RBD) of the SARS-CoV-2 spike protein. These neutralise the virus *in vitro* with picomolar potency. X-ray crystallography diffraction data were collected and processed at beamlines I03, I04 and I24 at Diamond. Cryo-EM results were obtained at eBIC.

In a Syrian hamster model of COVID-19, the group showed that treatment either systemically (intraperitoneal route) or via the respiratory tract (intranasal route) with a single dose of the most potent nanobody prevented disease progression.

The researchers suggested that combinations of nanobodies that target different epitopes may improve resilience in combating new variants of the virus.

References

1. Mendonça, L. *et al*. Correlative multi-scale cryo-imaging unveils SARS-CoV-2 assembly and egress. *Nat Commun.* **12,** 4629 (2021). DOI: 10.1038/s41467-021-24887-y
2. Walker, A. *et al*. The SARS-CoV-2 RNA polymerase is a viral RNA capping enzyme. *Nucleic Acids Research* **49,** 13019–13030 (2021) DOI: 10.1093/nar/gkab1160
3. Baddock, H. *et al*. Characterisation of the SARS-CoV-2 ExoN (nsp14ExoN–nsp10) complex: implications for its role in viral genome stability and inhibitor identification. *Nucleic Acids Research* **50,** 1484–1500 (2022). DOI: 10.1093/nar/gkab1303
4. Liu, C. *et al*. Reduced neutralization of SARS-CoV-2 B.1.617 by vaccine and convalescent serum. *Cell* **184,** 16 P4220-4236 (2021). DOI: 10.1016/j.cell.2021.06.02
5. Liu, C. *et al*. The antibody response to SARS-CoV-2 Beta underscores the antigenic distance to other variants. *Cell Host & Microbe* **30,** P53-68 (2021). DOI: 10.1016/j.chom.2021.11.013
6. Dejnirattisai, W. *et al*. Antibody evasion by the P.1 strain of SARS-CoV-2. *Cell* **184,** P2939-2954(2021). DOI: 10.1016/j.cell.2021.03.055
7. Dejnirattisai, W. *et al.* SARS-CoV-2 Omicron-B.1.1.529 leads to widespread escape from neutralizing antibody responses. *Cell* **185,** P467-484.E15 (2022). DOI: 10.1016/j.cell.2021.12.046
8. Redhead, M. *et al*. Bispecific repurposed medicines targeting the viral and immunological arms of COVID-19. *Scientific Reports* **11,** 13208 (2021). DOI: 10.1038/s41598-021-92416-4
9. Zaidman, D. *et al*. An automatic pipeline for the design of irreversible derivatives identifies a potent SARS-CoV-2 Mpro inhibitor. *Cell Chemical Biology* **28,** P1795-1806 (2021). DOI: 10.1016/j.chembiol.2021.05.018
10. Huo, J. *et al*. A potent SARS-CoV-2 neutralizing nanobody shows therapeutic efficacy in the Syrian golden hamster model of COVID-19. *Nature Communications* **12,** 5469 (2021). DOI: 10.1038/s41467-021-25480-z

Key Facts and Figures

Facility usage

In our fifteenth year of operations (1st April 2021 to 31st March 2022), we received 1,116 proposals for experiments on our instruments via peer reviewed access routes, requesting a total of 12,635 shifts. After peer review, 719 proposals were awarded beamtime. This resulted in 6,983 experimental shifts being awarded across 33 beamlines and the six electron microscopes delivering time to academic users. Throughout April and May 2021, the weekly operating hours continued to be limited to four days due to the pandemic; there was less experimental time available and the user programme was adjusted as a result. We also experienced a reduction in the number of proposal submissions due to the pandemic. However, from June 2021 we reverted back to our usual six day operation and across the full year we welcomed 2,460 onsite user visits from academia across all instruments, with an additional 4,253 remote user visits. The machine continues to perform to the highest standard with 97.4% uptime and 107.9 hours mean time between failures (MTBF).

User shifts requested, awarded and delivered by group, beamline and electron microscope 2021/22

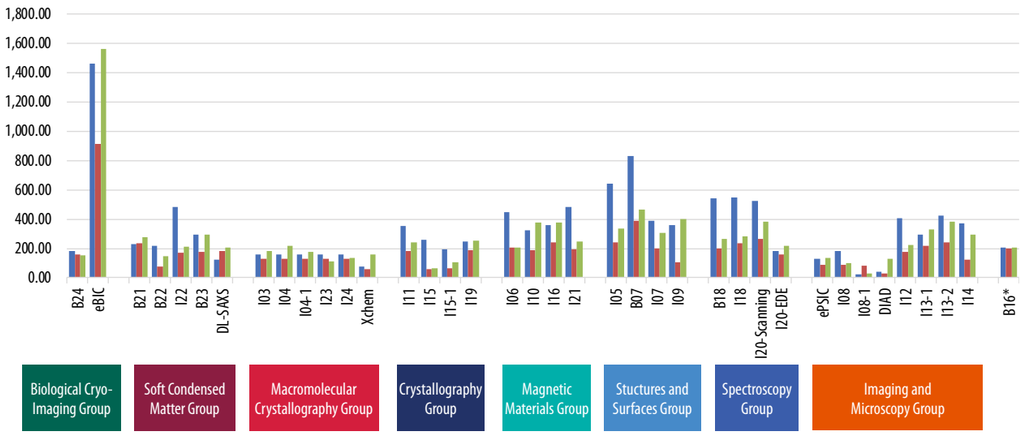

* B16 is the Test beamline, with 50% of beamtime for users. The rest is used for in-house developments for all beamlines.

Total user shifts requested, awarded and delivered

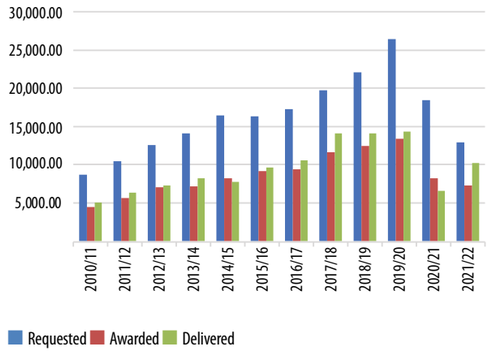

Total numbers of proposals and users per year

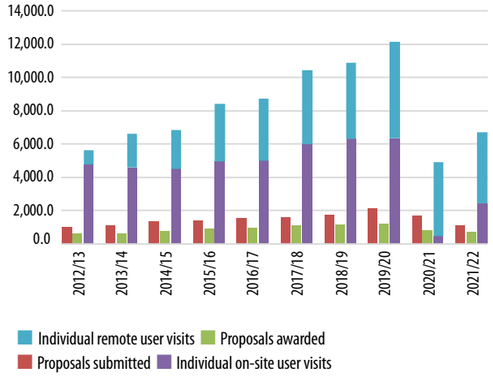

** Staff visits are now included for academic access routes, in house research is still excluded*

Proposals by discipline and research theme

Experimental shifts scheduled by Diamond by main subject area for 2021/22

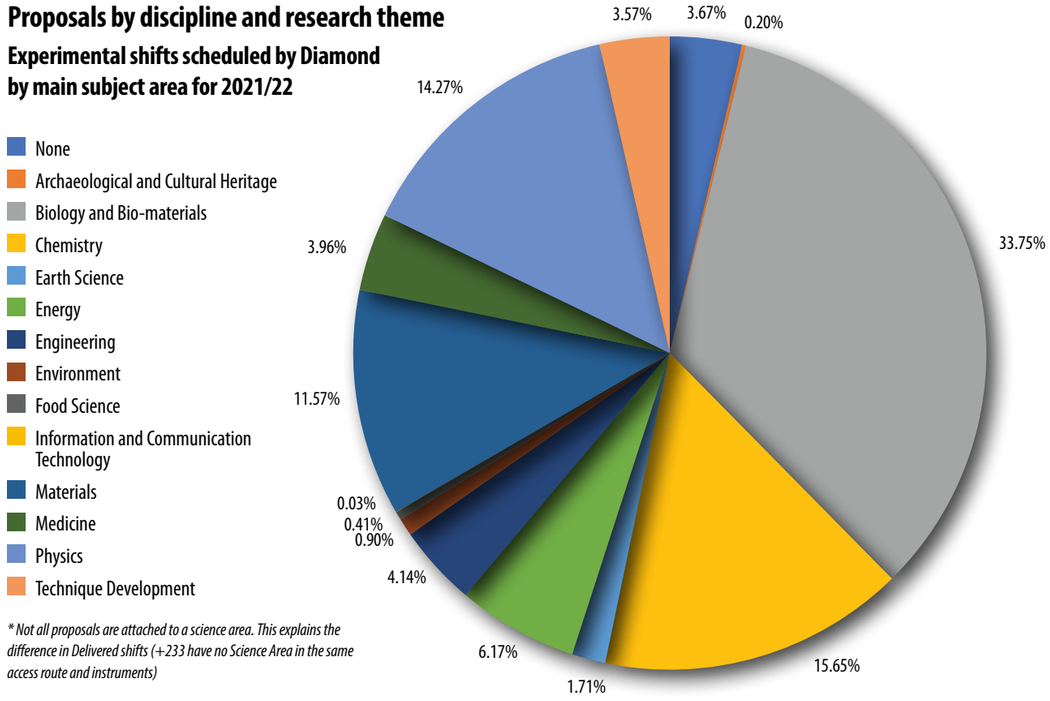

** Not all proposals are attached to a science area. This explains the difference in Delivered shifts (+233 have no Science Area in the same access route and instruments)*

Cumulative number of items in Diamond Publications Database by our scientists and users and cumulative number of protein structures solved

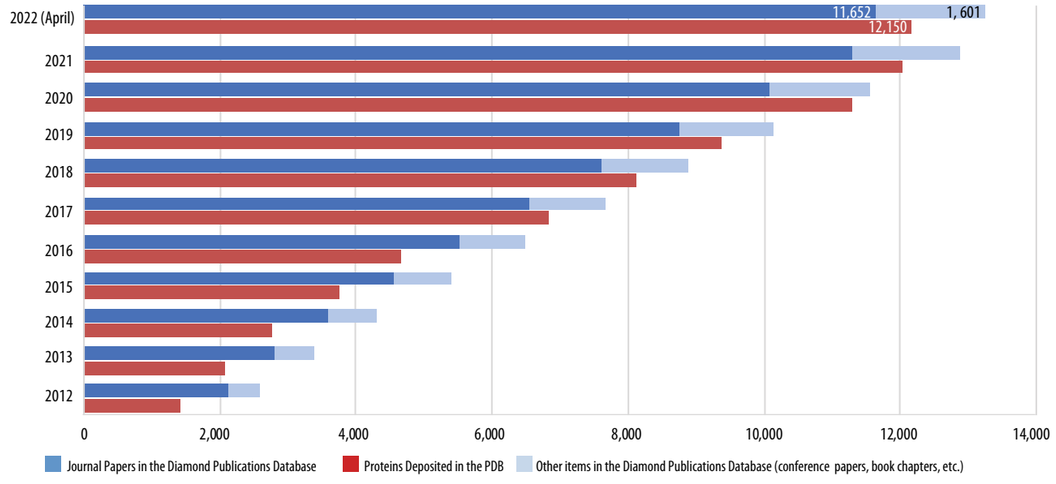

Machine performance

	2010/11	2011/12	2012/13	2013/14	2014/15	2015/16	2016/17	2017/18	2018/19	2019/20	2020/21	2021/22
Total no. operational beamlines by end FY	19	20	22	24	25	26	28	31	32	32	33	33
Scheduled hours of machine operation	5808	6000	5832	5976	5808	5928	5688	6072	5904	5913	4345*	5396*
Scheduled hours of user operation	4728	5064	4872	5088	4944	5040	4584	5160	4992	4992	3445*	4532*
Machine uptime %	97.5	97.7	98.3	98.2	97.6	97.6	98.7	98.2	98.4	98.1	96.2	97.4
Mean time between failures (hours)	28.5	55.4	52.4	60.3	38.6	119.4	103.1	79.9	90.3	104.7	132	107.9

** hours reduced due to COVID*

Beamline Development and Technical Summary

In its fifteenth year of experiments, Diamond is now operating with 33 beamlines and eight electron microscopes dedicated for experiments. A further five instruments are available for experiment support and sample preparation. Ten of the instruments specialise in life sciences and make up eBIC (electron Bio-Imaging Centre), with two provided for industry use in partnership with Thermo Fisher Scientific. Two of the electron microscopes are dedicated to advanced materials research and are supplied by Johnson Matthey and the University of Oxford. These, along with a further instrument for sample preparation, form ePSIC (electron Physical Science Imaging Centre) and are operated under strategic collaboration agreements to provide for substantial dedicated peer reviewed user access. Both eBIC and ePSIC are next to the Hard X-ray Nanoprobe beamline (I14). Along with eBIC and ePSIC, the UK X-ray Free Electron Laser (XFEL) Hub, the Membrane Protein Laboratory (MPL), the XChem fragrment screening facility and the Offline SAXS facility make up the complementary integrated facilities available at Diamond. For academic research, Diamond instruments (beamlines and microscopes) are free at the point of access through peer review. For proprietary research, access can be secured through Diamond's industry team.

The instruments and beamlines are organised into eight science groups as described below.

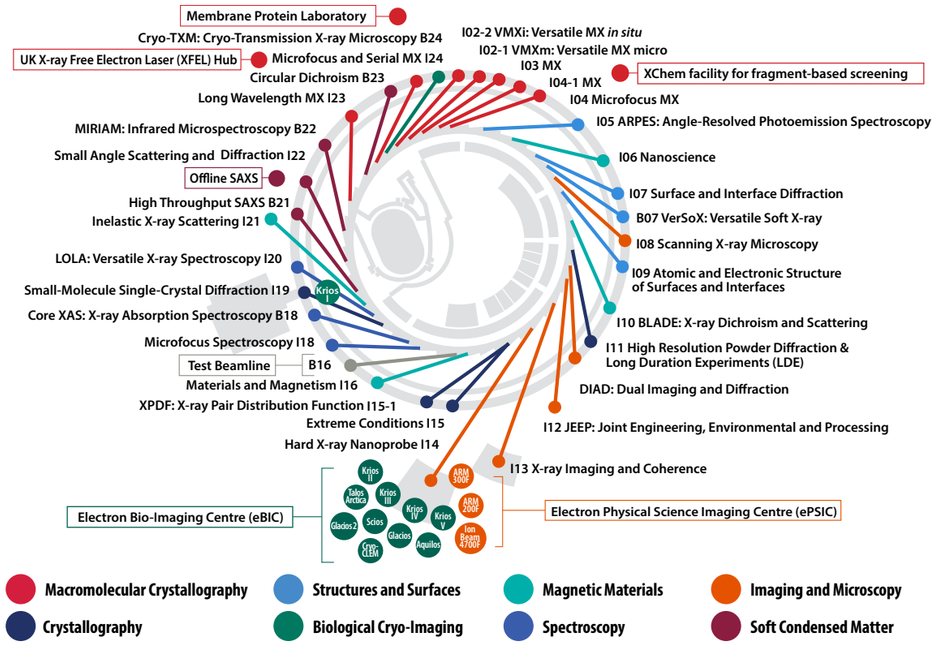

Electron Microscopes

Microscope	Main Capabilities	Accelerating Voltages	Operational Status
Titan Krios I	Cryo-EM, Cryo-ET	80, 120, 200, 300 kV	Operational
Titan Krios II	Cryo-EM, Cryo-ET	80, 120, 200, 300 kV	Operational
Titan Krios III	Cryo-EM, Cryo-ET	80, 120, 200, 300 kV	Operational
Titan Krios IV	Cryo-EM, Cryo-ET	80, 120, 200, 300 kV	Operational
Titan Krios V	Cryo-EM, Cryo-ET	80, 120, 200, 300 kV	Operational
Talos Arctica	Cryo-EM, Cryo-ET, MicroED	200 kV	Operational
Glacios	Cryo-EM, Cryo-ET	200 kV	Operational
Glacios 2	Cryo-EM, Cryo-ET, MicroED	200 kV	Operational
Scios	Cryo-SEM, Cryo-FIB	3 to 30 kV	Operational
Aquilos 2	Cryo-SEM, Cryo-FIB	3 to 30 kV	Operational
JEOL ARM200F	Atomic scale STEM imaging, EELS, EDX, electron diffraction	80, 200 kV	Operational
JEOL ARM300F	Atomic scale TEM and STEM imaging, electron diffraction, 4D-STEM, EDX	30, 60, 80, 160, 200, 300 kV	Operational
JEOL Ion Beam 4700F	SEM, FIB	1 to 30 kV	Operational

Diamond's beamlines: current operational status April 2022

Beamline Name and Number	Main Techniques	Energy / Wavelength Range	Status
I02-1 - Versatile MX micro (VMXm)	Micro- and nano-focus in vacuum cryo-macromolecular crystallography (VMXm)	7 - 28 keV	Optimisation
I02-2 - Versatile MX *in situ* (VMXi)	*In situ* microfocus macromolecular crystallography, Serial Synchrotron Crystallography	10 - 25 keV	Optimisation
I03 - MX	Macromolecular crystallography (MX), Multiwavelength Anomalous Diffraction (MAD)	5 - 25 keV	Operational
I04 - Microfocus MX	MX, MAD, variable and microfocus MX	6 - 18 keV	Operational
I04-1 - Monochromatic MX	MX, XChem fragment screening	13.53 keV (fixed wavelength)	Operational
I05 - ARPES	Angle-Resolved PhotoEmission Spectroscopy (ARPES) and nano-ARPES	18 - 240 eV; 500 eV	Operational
I06 - Nanoscience	X-ray Absorption Spectroscopy (XAS), X-ray photoemission microscopy and X-ray magnetic circular and linear dichroism	80eV - 2200eV	Operational
I07 - Surface and Interface Diffraction	Surface X-ray diffraction, Grazing Incidence X-ray Diffraction (GIXD), Grazing Incidence Small Angle X-ray Scattering (GISAXS), X-ray Reflectivity (XRR)	6 - 30 keV	Operational
B07 - VerSoX: Versatile Soft X-ray	Branch C: Ambient Pressure XPS and NEXAFS	110 - 2800 eV	Operational
	Branch B: NEXAFS and High-Throughput XPS	45 - 2200 eV	Optimisation
I08 - Scanning X-ray Microscopy	Scanning X-ray microscopy, NEXAFS/ XANES, X-ray fluorescence	I08 branch: 250 eV - 4.4 keV	Operational
		I08-1 - Soft and Tender X-ray Ptychography branch: 250 - 2000 eV	Optimisation
I09 - Atomic and Electronic Structure of Surfaces and Interfaces	XPS (including HAXPES), X-ray Standing Waves (XSW), Near Edge X-ray Absorption Fine Structure (NEXAFS), energy-scanned photoelectron diffraction	Hard X-rays: 2.1 - 18+ keV Soft X-rays: 0.1 - 2.1 keV (currently 0.1 - 1.9 keV)	Operational
I10 - BLADE: Beamline for Advanced Dichroism Experiments	Soft X-ray resonant scattering, XAS and X-ray magnetic circular and linear dichroism	Circular: 400-1600eV; Linear Horizontal: 250-1600eV; Linear Vertical: 480-1600eV	Operational
I11 - High Resolution Powder Diffraction	X-ray powder diffraction	7 - 25keV (1.7 - 0.5 - 2.1 Å)	Operational
DIAD: Dual Imaging and Diffraction	Simultaneous time-resolved X-ray imaging and X-ray powder diffraction	8 - 38 keV	Optimisation
I12 - JEEP: Joint Engineering, Environmental and Processing	Time-resolved imaging and tomography; 2D detector for time-resolved powder diffraction, single crystal diffraction and diffuse scattering; energy dispersive X-ray diffraction (EDXD); high-energy small angle X-ray scattering (limited capability)	53 keV - 150 keV monochromatic or continuous white beam	Operational
I13 - X-ray Imaging and Coherence	Phase contrast imaging, tomography, full-field microscopy (under commissioning), coherent diffraction and imaging (CXRD,CDI), ptychography and photocorrelation spectroscopy (XPCS) (under commissioning), innovative microscopy and imaging	Imaging branch: 8 - 30keV	Operational
		Coherence branch: 7 - 20keV	
I14 - Hard X-ray Nanoprobe	Nanofocus X-ray fluorescence (XRF), X-ray absorption spectroscopy (XAS), and transmission diffraction (XRD) mapping., differential phase contrast (DPC) imaging,), ptychography and tomography	5 - 23 keV	Operational
I15 - Extreme Conditions	Powder diffraction, single crystal diffraction	Monochromatic and focused 20 - 80 keV White beam	Operational
I15-1 - XPDF	X-ray Pair Distribution Function (XPDF)	40, 65, and 76 keV	Operational
I16 - Materials and Magnetism	Resonant and magnetic single crystal diffraction, fundamental X-ray physics	2.5 - 15 keV	Operational
B16 - Test beamline	Diffraction, imaging and tomography, topography, reflectometry	4 - 20 keV monochromatic focused 4 - 45 keV monochromatic unfocused White beam	Operational
I18 - Microfocus Spectroscopy	Microfocus X-ray Absorption Spectroscopy (XAS), X-ray fluorescence (XRF) and X-ray diffraction (XRD) mapping and tomography	2.05 - 20.5 keV	Operational
B18 - Core XAS	X-ray Absorption Spectroscopy (XAS)	2.05 - 35 keV	Operational
I19 - Small-Molecule Single-Crystal Diffraction	Small-molecule single-crystal diffraction	5 to 25 keV / 0.5 to 2.5 Å	Operational
I20 - LOLA: Versatile X-ray Spectroscopy	X-ray Absorption Spectroscopy (XAS), X-ray Emission Spectroscopy (XES) and Energy Dispersive EXAFS (EDE)	Dispersive branch: 6 - 26 keV	Operational
		Scanning branch: 4.5 - 20 keV	Operational
I21 - Inelastic X-ray Scattering	Resonant Inelastic X-ray Scattering (RIXS), X-ray Absorption Spectroscopy (XAS)	Currently 250 - 1500 eV (to be upgraded to 250 - 3000 eV)	Operational
B21 - High Throughput SAXS	BioSAXS, solution state small angle X-ray scattering	8 - 15 keV (set to 13.1 keV by default)	Operational
I22 - Small Angle Scattering and Diffraction	Small angle X-ray scattering and diffraction: SAXS, WAXS, USAXS, GISAXS. Micro-focus.	7 - 20 keV	Operational
B22 - MIRIAM: Multimode InfraRed Imaging And Mircrospectroscopy	FTIR microscopy & FPA imaging FTIR and THz spectroscopy NEW FTIR nanospectroscopy s-SNOM and AFM IR	microFTIR: 5,000-500cm^{-1}(2-20µm) FTIR/THz:10,000-10cm^{-1}(1-1000µm) nanoFTIR: 14000-800cm^{-1}(2.5-12.5µm)	Operational (AFM IR commissioning)
I23 - Long Wavelength MX	Long wavelength macromolecular crystallography	2.1 - 11 keV (1.1 - 5.9 Å)	Operational
B23 - Circular Dichroism	Circular Dichroism (CD)	Module A: 125-500nm for CD Imaging at 50 µm spatial resolution, and 96-cell HTCD. Module B: 180-650nm for MMP Imaging at 50 µm spatial resolution.	Operational
I24 - Microfocus and Serial MX	MX, MAD, Serial Crystallography, high energy MX	7 - 30.0 keV	Operational
B24 - Cryo Transmission X-ray Microscopy (TXM)	Full field X-ray imaging	200eV - 2600eV	Operational

Diamond-II update

Diamond Light Source has established itself as a world-class synchrotron facility enabling research by leading academic and industrial groups in physical and life sciences. Diamond has pioneered a model of highly efficient and uncompromised infrastructure offered as a user-focussed service driven by technical and engineering innovation. To continue delivering the world-changing science that Diamond leads and enables, Diamond-II is a co-ordinated programme of development that combines a new machine and new beamlines with a comprehensive series of upgrades to optics, detectors, sample environments, sample delivery capabilities and computing. The user experience will be further enhanced through access to integrated and correlative methods as well as broad application of automation in both instrumentation and analysis.

There are several steps to take toward achieving the Diamond-II vision of expanding the UK's research capabilities. In the first year of preliminary funding, a significant project milestone was passed in November 2021 in securing the Outline Business Case (OBC). Since then, Diamond's dedicated project teams of engineering and research professionals have shifted the focus to the Technical Design Report (TDR), due for completion later this year. Additionally, the priority flagship beamlines have engaged with their respective user communities and issued Conceptual Design Reports (CDRs) that outline their advanced research capabilities.

Architect's impression of the Diamond Extension Building (DEB), bottom right, to be constructed as part of the Diamond-II project, and link bridge to the synchrotron.

This comprehensive programme of scientific and technical updates will push the boundaries of UK research into new territories. Achieving this phenomenal level of change with as little impact on Diamond operations as possible will mean meticulous planning and involvement from staff across all divisions of the organisation. Some of these staff were part of the original Diamond team responsible for the construction of the initial machine more than 20 years ago. In addition to the project management team, the associated phases of the project fall under four distinct work packages:

- **Machine** – to cover every stage of machine upgrade from design, procurement and testing through to removal of old components and assembling and installation of new components.
- **Beamlines** – to include modification of existing beamlines to accommodate the new beam source and building of new flagship beamlines.
- **Data and Computation** – to manage a new IT infrastructure, including software developments to manage instrumentation, control, acquisition & detector readouts and data analysis for high rate applications.
- **Infrastructure** – to oversee requirements for the additional ~10,000 m^2 of assembly/storage space required for the upgrade (on and off site), upgrade infrastructure systems for the new machine and provide necessary general manpower effort across technical groups.

A new generation of lightsources

We are entering a new era of opportunity with the advent of fourth generation synchrotrons, the so-called Diffraction Limited Storage Rings (DLSRs). The progress in accelerator technology and the decrease of the electron horizontal emittance between one and two orders of magnitude offers the scientific community the opportunity to exploit much brighter photon beams and an increased coherence over a large energy range.

The proposed Diamond-II new machine lattice will be based on Double Triple Bend Achromats (DTBAs). This means an increased brightness and coherence of a factor of up to 70 and provides mid-section straights to retain and enhance all beamlines on bending magnets while offering additional sources for five new beamlines.

This design increases the electron beam energy from 3.0 to 3.5 GeV providing greatly increased photon flux at higher energies.

To match the extraordinary gains offered by the Diamond-II machine there will be a major renewal and upgrade of existing beamline technologies to meet the new scientific demands. Diamond-II will see enhancements in beam quality and beam stability through new X-ray optics and instrumentation, state-of-the-art sample delivery, and manipulation through the development of optimised sample environments and scientific software solutions that meet the beamline demands for the acquisition, visualisation and analysis of data.

This transformational upgrade will take several years of planning, a dark period of 18 months during which there will no light for the user community followed by a period to launch the five flagship beamlines and a comprehensive series of other upgrades, which will bring a total of 38 instruments around the synchrotron ring.

Delivery of flagship beamlines for Diamond-II

Three new beamlines will be available for day one operations 6 months after the dark period following extensive commissioning with the new machine: K04, an ultra-high throughput beamline for MX and XChem; SWIFT, the beamline for fast operando spectroscopy; and CSXID, beamline for Coherent Soft X-ray Imaging and Diffraction. Two other flagship beamlines, BERRIES, beamline for X-ray Raman Scattering and pink-beam X-ray Emission Spectroscopy (XES), and the beamline for nano-Angle-Resolved Photoemission Spectroscopy (ARPES) will be available at a later stage in the Diamond-II programme.

K04 beamline

The K04 XChem flagship builds on the success and oversubscription of the XChem fragment screening facility, developed in tandem with the evolution of beamline I04-1. The Diamond-II machine configuration necessitates removing beamline I04-1, providing the opportunity to rebuild it on the new K04 straight, delivering a beamline of vastly increased flux and brilliance, along with extreme automation. The resulting order-of-magnitude increase

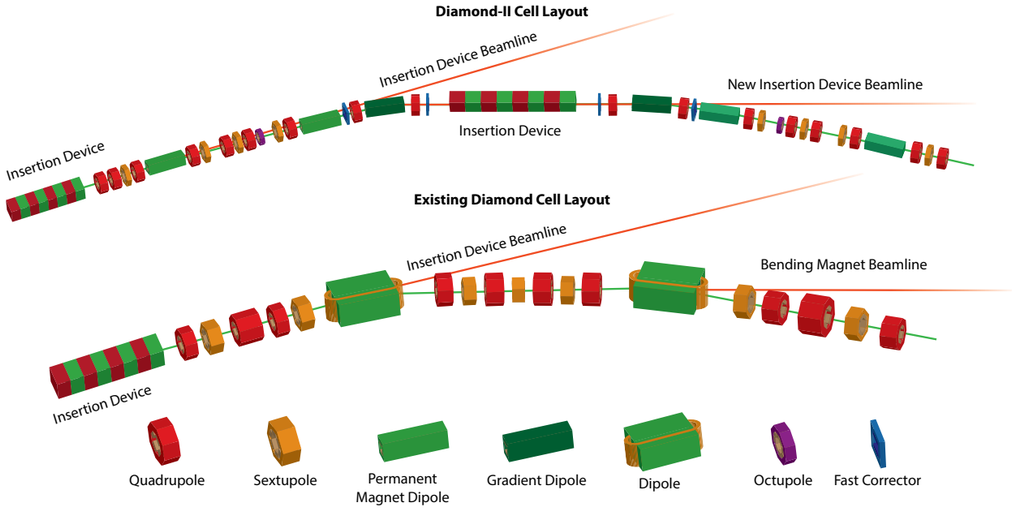

Schematic of the current Diamond DBA (Double Bend Achromat, bottom) and the proposed design for a DTBA (Double Triple Bend Achromat) for Diamond-II (top).

in throughput will fundamentally shift the scientific scope of crystallographic fragment screening. On the one hand, a far larger range of classes of drug targets will become viable, even when diffraction is weak. On the other hand, routinely large experiments will help achieve the coming revolution in rational drug discovery, by allowing all key interactions and conformations to be observed in 3D up front, providing the raw data that future algorithms will be able to exploit to design clinic-ready drug candidates from scratch.

SWIFT beamline

This new beamline, called SWIFT (Spectroscopy WithIn Fast Timescales), will be a high flux beamline optimised for the study of samples under operando conditions, and with the added potential to investigate sample heterogeneities at the 20 µm scale. The beamline will exceed the capabilities of the other X-ray Absorption Spectroscopy (XAS) beamlines at Diamond for experiments that require an element of time resolution in dilute samples, and will bridge the existing spatial resolution gap between beamlines I18 and B18. It is expected that SWIFT will serve a very broad scientific community and that it will also significantly enhance Diamond's capabilities for industrially relevant X-ray spectroscopy.

The new source, a multi-pole wiggler, will provide a significant improvement in flux over B18, and will consequently allow the investigation of faster processes in more dilute samples (fluorescence detection mode on the millisecond time regime), while keeping the efficiency of the continuous energy scans which have been proven very successful. An additional end-station providing a smaller focal spot is also proposed for the beamline, to allow SWIFT to perform spatially resolved studies of heterogeneous systems. It is anticipated that the scope of this project will also include, from day one, appropriate experimental infrastructure, to support complex environments and experimental conditions.

CSXID beamline

Today, there is global effort to further understand and control the emergent properties of quantum materials, with the promise of next-generation low-cost, energy-efficient devices. The Coherent Soft X-ray Imaging and Dynamics (CSXID) beamline will be for high-resolution, element selective 3D imaging and dynamic studies of new and novel materials. With an array of leading-edge sample environments and detectors coupled to a high-intensity polarised soft X-ray beamline specifically designed to take full advantage of the large increase in coherent flux from the Diamond-II upgrade, CSXID will revolutionise our ability to explore the static and dynamic 3D nanotexture of quantum materials. The beamline will facilitate state-of-the-art discovery research and innovation which directly relates to national grand challenges such as the Nanoscale Design of Functional Materials and New Quantum Technologies, as well as research themes in the physical sciences such as Condensed Matter: Electronics Structure, Magnetism and Magnetic Materials, Spintronics, Materials for Energy Applications and Energy Storage. These areas are addressed by enhancing nanoscale 3D imaging of the chemical and physical processes critical for the development of dial-up phenomena in complex oxides, low-energy consumption and secure data-storage materials, as well as speeding up the dynamics of topologically protected spin textures.

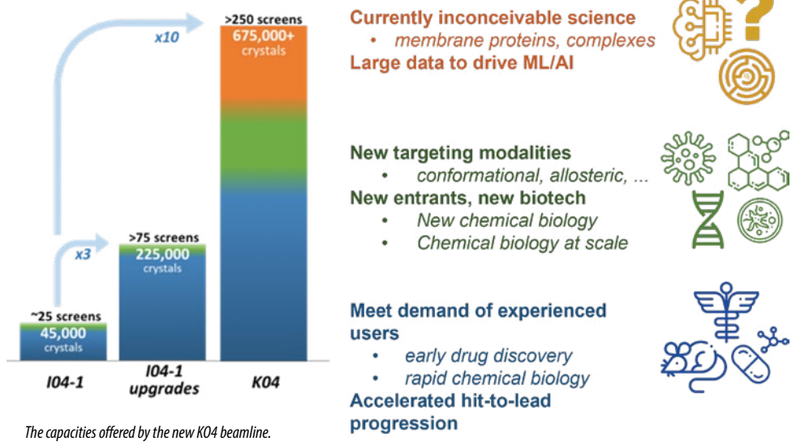

The capacities offered by the new K04 beamline.

Macromolecular Crystallography Group

Dave Hall, Science Group Leader

Macromolecular crystallography (MX) exploits the hard energy, high flux X-rays created at Diamond Light Source to enable our international academic and industrial user community to investigate the structure and function of biological macromolecules at atomistic resolution and up to millisecond timescales. This provides deep insight into the details of biological activity key to our understanding of the processes of life, exemplified by the selection of outstanding scientific highlights in this section.

Diamond provides access to a suite of seven MX beamlines[1] to a large international academic and industrial user community. The beamlines cover a very broad range of capabilities from high throughput, micro and nano-focus beams, extremely long wavelengths, room temperature *in situ* collection from crystallisation plates, (time resolved) serial synchrotron crystallography (SSX), a fragment-based screening platform (XChem) and the Membrane Protein Laboratory.

The COVID-19 pandemic continued to have impact on the research carried out on the beamlines as well as on the user programme and how we operated the suite of MX beamlines. For a significant period of this report the MX team continued to operate the beamlines whilst users were not able to come to site due to (inter)national restrictions. User access continued to be supported either via remote access, automated collection or with on-site staff support to enable experiments requiring sample handling, preparation or more complex data collections such as crystallisation for VMXi, XChem fragment screening, long wavelength experiments on I23 or serial synchrotron crystallography and room temperature collection at I24 and VMXi. As restrictions have eased over time opportunities for site-based access for users have been provided as soon as possible.

Early in 2020 a special rapid access user call opened for COVID-19 research with, to date, 69 proposals received from groups from across the world studying a range of SARS-CoV-2 targets via MX, cryo-EM, bioSAXS and SR-CD. Access was provided to the high throughput beamlines I03 and I04 for rapid turnaround of high-resolution structures, room temperature studies on I24 and VMXi, drug repurposing studies across the MX beamlines and the XChem I04-1 facility undertook large scale fragment screening where over this period the team improved the duty cycle per sample by 33%, in part following the installation of an Eiger2 XE detector capable of operating at 500 frames per second, bringing it in line with earlier installations on I03 and I04.

To date there have been nine successful fragment screening campaigns supported by the I04-1 XChem facility with data collected from more than 22,000 crystals (Figure 1). One such screen on the Main protease triggered the COVID Moonshot initiative[2] to design an antiviral drug in a fully open manner which already has lead candidates. In parallel automated unattended data collection (UDC) has been used for several SARS-CoV-2 projects including a concerted campaign coordinated through University of Oxford to study the antigenic landscape of variants with a focus on Spike domains complexing with Fab and ACE2. To date over 59 structures have been deposited in the PDB (public protein data bank repository) from this campaign. Overall, more than 25,000 data sets have been collected on Diamond MX beamlines related to COVID-19 research since February 2020 with over 20% of the SARS-CoV-2 structures in the PDB deposited as a result of work at Diamond. See the Supporting international COVID-19 research section for more details.

UDC has also undergone continuous improvements over the year to broaden the capability across beamlines I03, I04 and I04-1 and provide more options for our users with this access mode now becoming increasingly popular, in particular with industrial users. To handle the variable beam size and flux characteristics across the energy range of beamline I04, the use of radiation dose in calculations for UDC has been implemented. To date more than 60,000 data sets have been collected across these beamlines via UDC. Collecting automatically with rapid turnaround frees up significant user time and provides

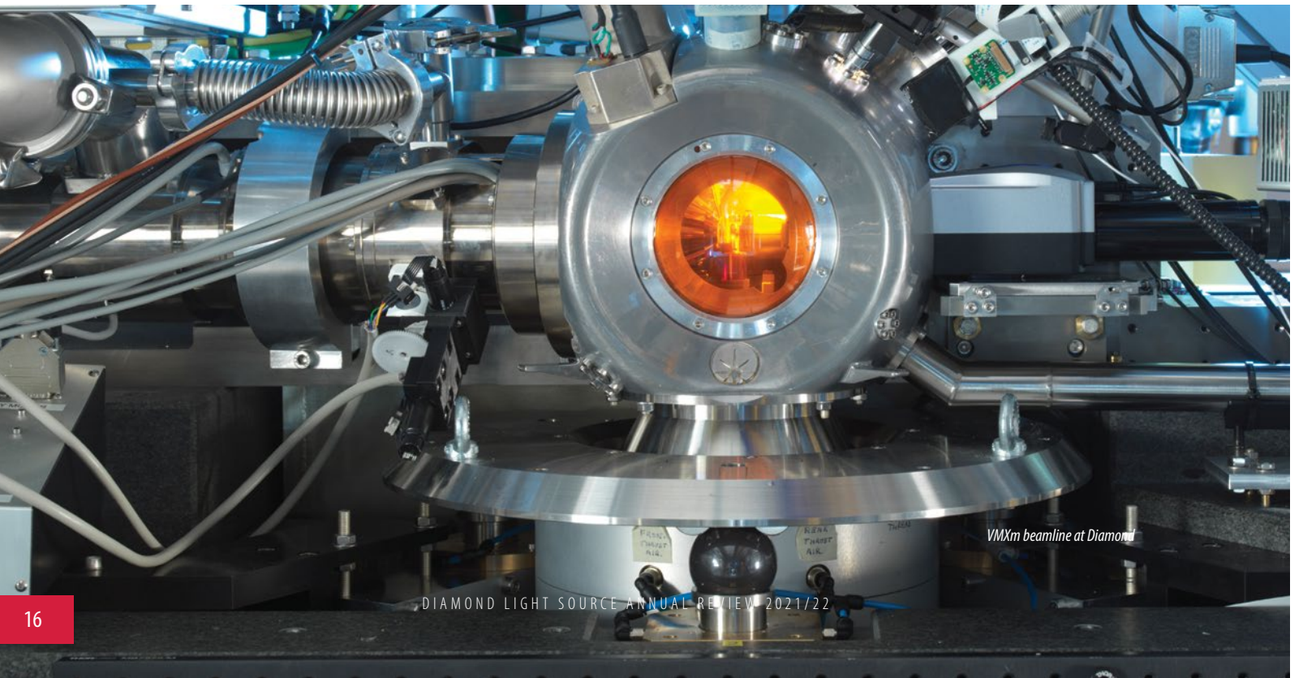

VMXm beamline at Diamond

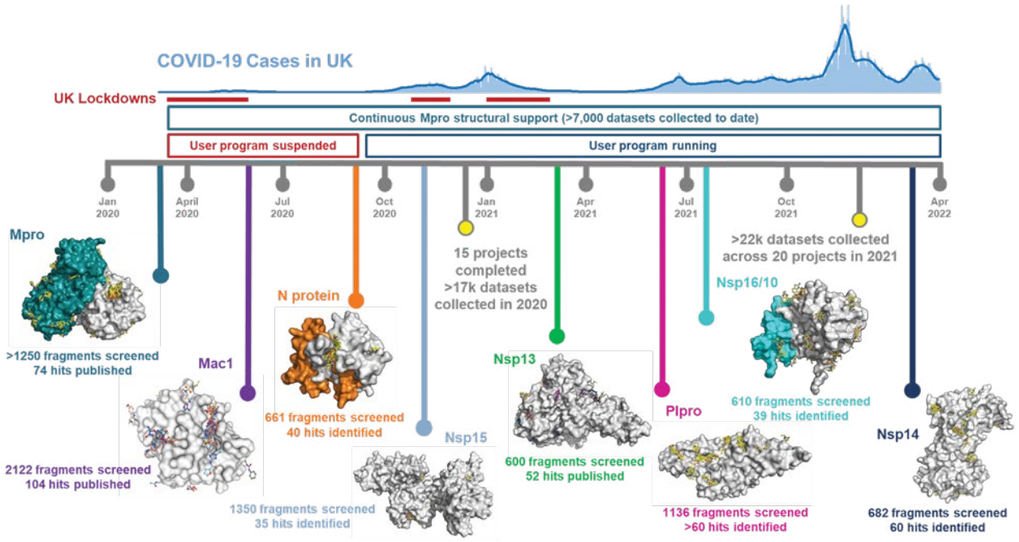

Figure 1. XChem campaigns on SARS-CoV-2 targets.

rapid, consistent feedback to their research aims.

No one cannot fail to be aware of the impressive results made in the last year of AI driven automated protein structure prediction by AlphaFold2 (DeepMind) and Robetta (Baker, University of Washington). These have had a profound impact on the field of structural biology and are being actively used to aid experimental structure determination. To this end we have implemented AlphaFold2 into our automated pipelines so that users can provide their target sequence and we generate predicted protein structures that are used in downstream automated software to aid experimental structure solution more readily than previously possible.

Despite the success of AlphaFold2 in producing models for molecular replacement for successful phasing, several projects have still required the long-wavelength beamline I23 for structure solution. An app is now available to help evaluate the potential success for phasing for native sulphur SAD phasing. In addition, an increasing number of projects are using the extended wavelength range of the beamline to determine the nature of elements bound to proteins, nucleic acids and their complexes to gain further insight into their chemistry and function.

I04 has recently introduced the option to dial a target dose instead of an exposure time. This is calculated using Raddose3D assuming a standard protein sample. Developments are ongoing to include additional sample information that can be provided by the user. This dose-based mechanism is implemented in UDC as well as the interactive GUI and is available over the entire beamline energy (6 – 18 keV) and beam size (8 x 5 to 110 x 100 μm^2 (h x v)) range. This option provides the user with a much better guide for different experimental aims without the risk of under- or overexposing samples.

I24 continues to offer tuneable microfocus MX with extremely high flux densities at all energies. The I24 monochromator was replaced this year, upgrading one of the oldest components on the beamline resulting in significantly increased beam stability at the sample position. A cadmium telluride Eiger detector is now available allowing efficient high energy (>20 keV) data collection. The use of high energies exploits the energy dependence of how X-rays interact with crystals and allows more data to be collected from each crystal, especially when they are of a limited size[3]. The ease of use and breadth of SSX available at I24 has continued to develop: both static and light/substrate driven dynamic SSX is available as well as tools such as anaerobic data collection and offline slurry characterisation. Developments will feed into the I24 KMX flagship upgrade for Diamond-II.

VMXi has achieved routine room temperature structure determination from crystals as small as 10 µm *in situ* within crystallisation plates, including of COVID-19 targets. User operation is fully remote with rapid automated feedback when crystals have been identified within plates. Typical room temperature datasets comprise data from 1-12 individual crystals and resolutions better than 1.8 Å are regularly achieved. In partnership with the XFEL Hub at Diamond, time resolved SSX is being developed for VMXi.

The micro/nanofocus MX beamline VMXm will enable data collection from crystals smaller than 1 µm. Work has continued throughout this year to further improve beam delivery across the beamline energy range, sample handling and data acquisition and analysis such that it can currently cater for crystals in the range 2-10 µm in size mounted on TEM grids and special holders. The beamline has recently announced a call to the user community for applications for use of commissioning beamtime.

Excellent progress continues to be made on the electron diffraction HeXI project with successful external scientific reviews completed and a full beamline-grade Conceptual Design Review for phase 1 recently finalised. The commissioning of offline electron microscopes, detectors, and software continues to inform conceptual design and technical decisions in collaboration with Diamond support groups. Productive external collaborations are also in place with user groups, institutes, and industry to further facilitate hardware, workflow, and processing solutions for rapid, routine electron diffraction.

Throughout the last year work has continued for the Diamond-II upgrade programme. Much work has been done to identify critical components requiring upgrading across the suite as well as look at future competitive upgrade paths, including work on the conceptual design reviews for K04 (flagship beamline to replace and transform I04-1 XChem) and KMX, a flagship project to upgrade I24 to further improve the serial synchrotron crystallography offer alongside upgrading its microfocus capabilities.

1. https://www.diamond.ac.uk/Instruments/Mx.html
2. https://postera.ai/moonshot
3. Storm, S. L. S. et al. Experimental evidence for the benefits of higher X-ray energies for macromolecular crystallography. *IUCrJ* **8**, (2021). DOI: 10.1107/S2052252521008423

High-resolution photoreceptor structures offer a blueprint for new methods and applications

Related publication: Bada Juarez, J. F., Judge, P. J., Adam, S., Axford, D., Vinals, J., Birch, J., Kwan, T. O. C., Hoi, K. K., Yen, H.-Y., Vial, A., Milhiet, P.-E., Robinson, C. V., Schapiro, I., Moraes, I., & Watts, A. Structures of the archaerhodopsin-3 transporter reveal that disordering of internal water networks underpins receptor sensitization. *Nature Communications*, **12**(1), 629. (2021). DOI: 10.1038/s41467-020-20596-0

Publication keywords: Archaerhodopsin; Optogenetics; Receptor Sensitisation; Ion transport; Lipidic cubic phase

Archaerhodopsin-3 (AR3) is a light-sensitive protein expressed by *Halorubrum sodomense*, an organism that grows in the Dead Sea. Mutants of the protein are routinely used in neuroscience experiments to selectively silence individual nerve cells and detect changes in transmembrane voltage. However, these mutants are designed without knowledge of the protein's structure.

An international team of researchers visualised the photoreceptor at unprecedented resolution using the I24 and B23 beamlines and reported the first ever structure of the ground state of AR3. In this state, the protein is configured to transport one H^+ ion across the cell membrane for each photon absorbed. The team was also able to crystallise the photoreceptor in a second conformation, a desensitised state that AR3 adopts in the prolonged absence of light.

The superb resolution achieved for these AR3 structures is among the highest for a wild-type membrane protein deposited in the Protein Data Bank.

The high-resolution crystal structures were essential for understanding the workings of the protein. Obtaining such high-quality diffraction data would not have been possible without the state-of-the-art microfocus I24 beamline at Diamond.

Circular Dichroism (CD) measurements from the B23 Beamline allowed the team to quantify the alpha-helical content of AR3 and correlate it with other biophysical information.

This *data* provides structural biologists and protein engineers with the 'blueprints' to AR3, opening the way for the development of new tools and methodologies in the fields of neuroscience, cell biology and beyond.

Archaerhodopsin-3 (AR3) is a light-sensitive protein produced by the archaebacterium *Halorubrum sodomense*, which grows in the Dead Sea. The protein converts energy from sunlight to a transmembrane electrical gradient, which is used by the organism to power growth and reproduction. In the laboratory, AR3 can also be expressed recombinantly in mammalian cells and is used extensively in neurobiology experiments. When light is shone on nerve cells containing AR3, the protein prevents them from transmitting nerve impulses. This selective silencing of nerves (a methodology known as optogenetics[1]) is used by neuroscientists to understand the roles of individual neurons in brain function. The photoreceptor is also used to measure electrical voltages across cell membranes *in vivo*[2]. Although AR3 is widely used in several types of laboratory experiment, the lack of structural data for the photoreceptor has hindered the development of new methods. The data produced in this research provide the detailed blueprints for the protein and pave the way for new applications in neurobiology and biotechnology.

Like many light-sensitive receptor proteins, AR3 is found in the membrane of the archaebacterial cell. It absorbs light using a chromophore, retinal, which is better known as one of the forms of Vitamin A. When light shines on the retinal, it changes shape, transitioning from an extended all-*trans* isomer to a bent 13-*cis* isomer. The protein can also adopt a desensitised state, in which it does not respond to light, but until now the process of inactivation has not been understood. The high-resolution structural data obtained from crystals of AR3 (Fig. 1a) on the I24 microfocus beamline at Diamond Light Source, have enabled the molecular mechanisms of AR3 desensitisation to be explained, and these insights have implications for our understanding of other receptor proteins.

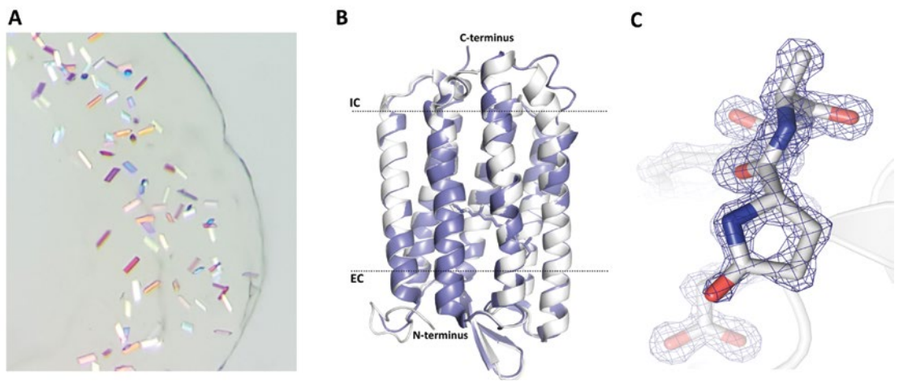

Figure 1: (a) Crystals of AR3 visualised under circularly polarised light; (b) Overlay of the structures of the resting state of AR3 (white) and the related protein, bacteriorhodopsin (purple). Secondary structure elements are shown in ribbon representation. The chromophore is shown in stick representation. The approximate positions of the intracellular (IC) and extracellular (EC) sides of the membrane are indicated with dotted lines; (c) The pyroglutamyl group at the N-terminus of AR3 is generated by the removal of the signal peptide and the modification of Gln7. The 2Fobs–Fcalc electron density map (blue mesh) is contoured at 1.2σ.

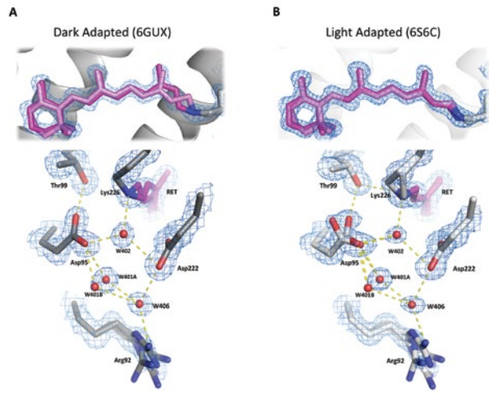

Figure 2: Comparison of the internal structures of the desensitised (PDB: 6GUX) and resting state (PDB: 6S6C) structures of AR3. (Top) In the desensitised state (left) the C13 = C14 retinal bond has been modelled with 70% cis and 30% trans isomers (dark and light pink respectively). In the LA state (right) retinal is modelled in the all-trans state only, but as two different conformers. (Bottom) Structures of the internal H-bond networks close to the retinal chromophore. Predicted H-bonds are indicated by yellow dashes. The 2Fobs–Fcalc electron density maps (blue mesh) are contoured at 1.2σ.

Wild-type AR3 was expressed in the native organism and purified, unusually, without the use of detergent. It was crystallised in lipidic cubic phase and diffraction data were acquired on the I24 beamline at cryo temperatures. One subset of the crystals was grown in the absence of light and diffraction data collected from these samples were used to generate the dark-adapted, desensitised structure, which was solved to 1.3 Å resolution. The second subset of crystals was grown under illumination and the data collected gave rise to the resting state structure. At 1.07 Å resolution, the light-adapted, resting-state structure is one of the highest resolution membrane protein structures solved to date (Fig. 1b).

The structures show that AR3 undergoes a series of previously unobserved post-translational modifications during its maturation, including the cleavage of the first six amino acids at the N-terminus, the cyclisation of Gln7 to form a pyroglutamyl group and the covalent conjugation of retinal to Lys226 via a Schiff base (Fig. 1c)[3]. There are key differences between the resting and desensitised states of the protein in the chromophore and the surrounding region of the protein. In the desensitised state (PDB: 6GUX), 13-*cis* and all-trans retinal isomers are present in a calculated occupancy ratio of 70% and 30%, respectively (Fig. 2). In the resting state (PDB:6S6C), the chromophore is resolved as two different conformations of the same all-*trans* isomer (Fig. 2), with relative occupancies of 75% and 25%. The structures also suggest that the amino acids and water molecules inside the protein are more mobile in the resting state than in the desensitised state.

The energy barriers to isomerisation of the retinal were calculated using the crystal structures as a starting point. In the desensitised form, the 13-*cis* isomer of retinal was more stable than the all-*trans* isomer, (ΔGcis-trans = −1.9 kcal/mol). The relatively small difference in energies is consistent with the presence of both isomers in the crystal structure. In contrast, the energy difference between the isomers in the resting state is larger (ΔGcis-trans = 10.9 kcal/mol) and the all-trans form is more stable (Fig. 3). The energetic profiles are determined by the environment of the retinal[5] in each state, which is in turn dependent on the order and position of the internal water molecules and the stability of the networks of non-covalent bonds surrounding the chromophore. Our structures suggest that the greater internal disorder of the resting state heavily influences the response of the protein to visible light. In contrast, the lower internal mobility in the desensitised state may prevent AR3 from being activated.

These AR3 structures are a major advance for the study of structure-function relationships of integral membrane proteins. The resolution obtained (1.07 Å), using diffraction data from the I24 microfocus beamline, is currently unmatched for this group of proteins. The structural information generated will now provide the details required to design improved protein variants for use in optogenetics experiments, and for applications in biotechnology. Calculations, using the structures as a starting point, reveal how small differences in the electronic environment of the chromophore binding site can determine the behaviour of the resting and desensitised states of the protein. Finally, the differences revealed in the order of internal water molecules and the associated networks of non-covalent bonds between the two states, may help us to unlock the more complex mechanisms of activation and desensitisation observed in mammalian receptor proteins.

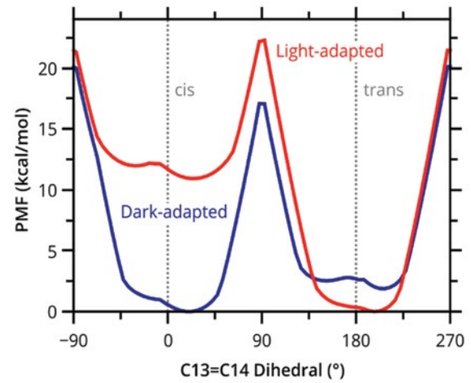

Figure 3: Calculated potentials of mean force (PMF) for the isomerisation of the C12–C13 = C14–C15 dihedral of retinal in dark-adapted (blue) and light-adapted (red) AR3. The PMF was computed by sampling the retinal isomerisation from all-trans to 13-cis and vice versa. Each point on the curve is generated from two independent 0.5 ns QM(SCC-DFTB)/MM MD trajectories, initiated from two separated equilibrated starting structures. The protein backbone was fixed in place, but all other atoms (including those in the chromophore and amino acid sidechains) were allowed to move.

References:

1. Pastrana, E. Optogenetics: controlling cell function with light. *Nature Methods*. **8**(1), 24–25 (2011). DOI: 10.1038/nmeth.f.323
2. Chow, B. Y. *et al.* High-performance genetically targetable optical neural silencing by light-driven proton pumps. *Nature*. **463**(7277), 98–102 (2010). DOI: 10.1038/nature08652
3. Hoi, K. *et al.* Detergent-free Lipodisq Nanoparticles Facilitate High-Resolution Mass Spectrometry of Folded Integral Membrane Proteins. *Nano Letters*, **21**(7), 2824–2831 (2021). DOI: 10.1021/acs.nanolett.0c04911
4. Ihara, K. *et al*. Met-145 is a key residue in the dark adaptation of bacteriorhodopsin homologs. *Biophysical Journal*. **67**(3), 1187–1191 (1994) DOI: 10.1016/S0006-3495(94)80587-9
5. Baudry, J. *et al.* Simulation Analysis of the Retinal Conformational Equilibrium in Dark-Adapted Bacteriorhodopsin. *Biophysical Journal*. **76**(4), 1909–1917 (1999). DOI: 10.1016/S0006-3495(99)77349-2

Funding acknowledgement:
This work was supported by the BBSRC (BB/N006011/1), DSTL (DSTLX-1000099768), Wellcome Trust (20289/Z/16/Z) and the DFG (SFB 1078). Additional funding is acknowledged from BEIS and the ERC.

Corresponding authors:
Dr Isabel Moraes, National Physical Laboratory, isabel.moraes@npl.co.uk
Prof. Anthony Watts, Oxford University, anthony.watts@bioch.ox.ac.uk

Protein Periscopes regulate bacterial interactions

Related publication title: Whelan F., Lafita A., Gilburt J., Dégut C., Griffiths S. C., Jenkins H. T., St John A. N., Paci E., Moir J. W. B., Plevin M. J., Baumann C. G., Bateman A., & Potts J. R. Periscope Proteins are variable-length regulators of bacterial cell surface interactions. *Proc Natl Acad Sci* **118,** (2021). DOI: 10.1073/pnas.2101349118

Publication keywords: Protein structure; SHIRT; Cell adhesion; Bacteria; Gram positive; *Streptococcus*; Immune evasion

Bacteria can adapt to changing environments by altering their cell surface. In human pathogens, this variability has been implicated in immune evasion. Researchers sought to understand one potential mechanism (length variation of proteins on the bacterial surface) through studies of repetitive bacterial proteins.

Sgo0707 is a repetitive protein found on the surface of the bacteria *Streptococcus gordonii*. The team used X-ray diffraction on Diamond Light Source's Macromolecular Crystallography (MX) beamline (I03) to study the atomic structure of repeats from Sgo0707. They also investigated the shape of longer regions of Sgo0707 in solution, approximating the structure of the protein on the surface of bacteria, using small-angle X-ray scattering methods on the High Throughput SAXS beamline (B21).

High-resolution structures of Sgo0707 repeats revealed a novel structure the researchers named 'SHIRT'. Studies suggested that SHIRT repeats adopt a rod-like conformation that would project the functional domain of Sgo0707 away from the bacterial cell surface. The researchers identified that Sgo0707 and many related proteins exhibit apparent repeat number variability and called these 'Periscope Proteins' to reflect their rod-like shape and role in projecting a functional domain away from the bacterial cell surface.

Their identification of this large class of Periscope Proteins suggests that many bacteria can use protein length variation as a way of adapting their surface to a changing environment. Such understanding is important in a range of settings, such as studies of bacterial colonisation of tissues and surfaces, including implanted medical devices.

Mechanisms of dynamic bacterial surface variation are a key component of bacterial survival and adaptation in a range of challenging and complex environments[1]. Such mechanisms include changes in capsular polysaccharide or changes in expression of protein adhesins. One mechanism, to date under-recognised, is length variation of repetitive bacterial cell surface proteins. Gram-positive bacteria, such as staphylococcal and streptococcal species, produce cell surface-anchored repetitive proteins such as SasG and Rib and previous studies suggest variation in the number of repeats[2]. In addition to sequence repeats, such proteins present an N-terminal domain, predicted to be involved in host colonisation, to the extracellular environment (Fig. 1). We previously characterised repeats from SasG[3] and Rib[4] and showed that they form stable folded domains that, when arrayed in tandem, form highly elongated structures. In this study we sought to characterise the repetitive region of a third bacterial surface protein, Sgo0707 from *Streptococcus gordonii*.

With 82-100% identity between adjacent domains, the identification of the structured boundaries of repeat domains is a difficult task, especially with limited PDB homologues for guidance; biophysical characterisation of an initially predicted folded repeat ('ΔN-Sgo_R2') indicated a well-folded domain. However, when we solved the structure at a resolution of 0.95 Å via the use of X-ray crystallography and a*b initio* molecular replacement (MR) using an idealised β-strand, this construct appeared to be N-terminally truncated (Fig. 2; PDB 7AVJ). It was clear that N-terminal extension and C-terminal truncation would complete the domain fold and we were able to solve the structure of a completed domain at a resolution of 0.82 Å (Fig. 2; PDB 7AVK). This Sgo0707 domain contained no definition in the Pfam database and formed a novel fold, and thus we named the domain 'SHIRT' (Streptococcal High Identity Repeats in Tandem; Pfam entry PF18655). The SHIRT domain contains a mixed α/β fold, comprising seven β-strands constituting two main β-sheets, with a single short intra-domain α-helix.

Using our newly-identified SHIRT domain definitions, we sought to structurally characterise a tandem SHIRT domain construct (Sgo_R3-R4); the structure revealed a short (Pro-Ala-Pro) linker between adjacent domains, as well as a very limited inter-domain interface (Fig. 2; PDB 7AVH). This arrangement was validated using thermal unfolding experiments, which showed that Sgo_R3-R4 was no more thermally stable than the single domain in isolation (Fig. 2, T_m = 76-77 °C).

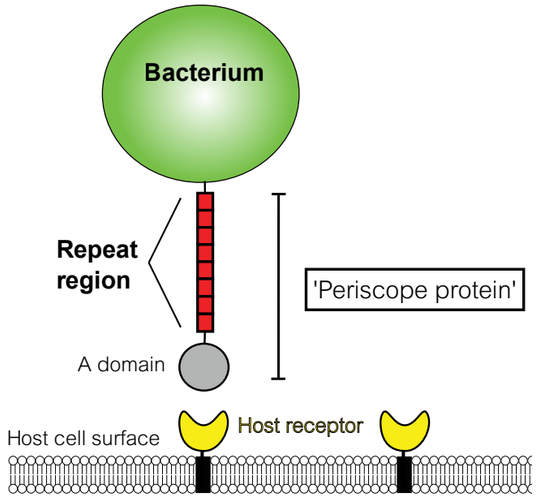

Figure 1: Periscope Proteins are often C-terminally attached to the bacterial cell wall, have an N-terminal folded (A) domain involved in host colonisation and have a highly repetitive region.

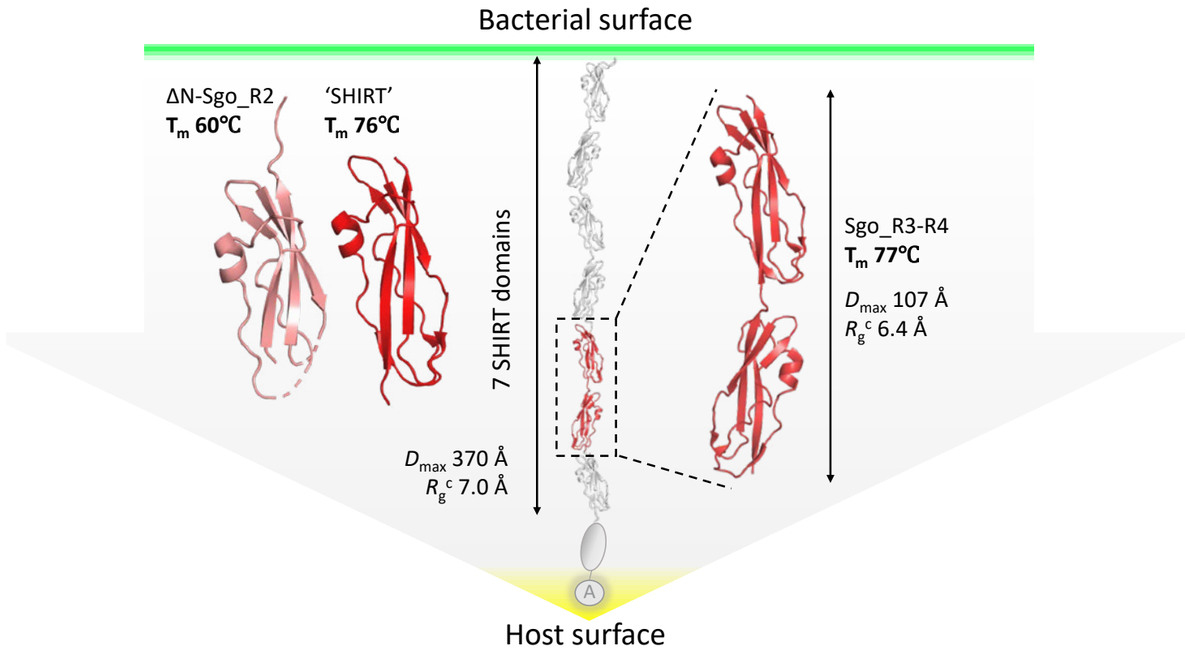

*Figure 2: Structures of N-terminally truncated (**ΔN-Sgo_R2;** PDB 7AVJ), complete (SHIRT; PDB 7AVK) and tandemly arrayed (Sgo_R3-R4; PDB 7AVH) SHIRT domains with corresponding melting temperatures (T_m). A model of 7 arrayed SHIRT domains and structure- and SAXS-determined parameters for the two lengths of tandem array (2 and 7) are also shown. C-terminal attachment to the bacterial cell wall, and the unmodelled N-terminal SHIRT domain and A domain are indicated.*

Notably, the extended nature of the tandem SHIRT structure with a short linker that would be predicted to retain rigidity and thus limit domain-domain flexibility, suggested that addition of extra repeats would result in an elongated solution conformation. To test this hypothesis, we collected Small-Angle X-Ray Scattering (SAXS) data for both the tandem and 7-repeat domain (Sgo_R2-R8) SHIRT architectures on beamline B21. This SAXS solution data revealed that for both constructs an overall rod-like solution conformation is maintained, with a conserved cross-sectional radius (Fig. 2) consistent with the tandem repeat crystal structure.

DNA sequence analyses suggested that Sgo0707, Rib and SasG (and many other bacterial surface proteins) are produced with varying numbers of repeats. If the repeat region forms a rod, as in our examples of Sgo0707, Rib and SasG, this would result in the functional (*e.g.* host colonisation) domain being projected differing distances from the bacterial cell surface. Using a memorable analogy, we called this diverse class of cell surface-anchored bacterial proteins 'Periscope Proteins'[2]. We propose that selection pressure, combined with stochastic repeat number variation enabled by high DNA repeat identity, results in enrichment of bacteria expressing short or long versions of the protein (dependent on the nature of the selection pressure)[2]. Enabled by access to Diamond Light Source, we have shown that length variation in Periscope Proteins appears to be a widespread mechanism through which pathogenic bacteria can modulate interactions with their host survival niche. Such modulated interactions could play an important role in processes during infection including host colonisation, biofilm formation and immune system evasion.

References:

1. van der Woude, M. W. *et al.* Phase and antigenic variation in bacteria. *Clinical Microbiology Reviews* **17**, 581–611 (2004). DOI: 10.1128/CMR.17.3.581-611.2004
2. Whelan, F. *et al.* Periscope Proteins are variable-length regulators of bacterial cell surface interactions. *Proceedings of the National Academy of Sciences* **118,** (2021). DOI: 10.1073/pnas.2101349118
3. Gruszka, D. T. *et al.* Cooperative folding of intrinsically disordered domains drives assembly of a strong elongated protein. *Nature Communications* **6**, 7271 (2015). DOI: 10.1038/ncomms8271
4. Whelan, F. *et al.* Defining the remarkable structural malleability of a bacterial surface protein Rib domain implicated in infection. *Proceedings of the National Academy of Sciences* **116**, 26540–26548 (2019). DOI: 10.1073/pnas.1911776116

Funding acknowledgement:
JRP, SCG and FW were funded by the British Heart Foundation (FS/12/36/29588 and PG/17/19/32862).

Corresponding authors:
Dr Samuel Griffiths, Evotec (U.K.), Sam.Griffiths@evotec.com
Dr Fiona Whelan, University of Adelaide, fiona.whelan@adelaide.edu.au

Investigating the role of metal ions in highly structured bacterial S-layers

Related publication: Herdman, M., von Kügelgen, A., Kureisaite-Ciziene, D., Duman, R., el Omari, K., Garman, E. F., Kjaer, A., Kolokouris, D., Löwe, J., Wagner, A., Stansfeld, P. J., & Bharat, T. A. M. High-resolution mapping of metal ions reveals principles of surface layer assembly in *Caulobacter crescentus* cells. *Structure* **30**, 215-228.e5 (2022). DOI: 10.1016/j.str.2021.10.012

Publication keywords: *Caulobacter crescentus*; S-layer; bacteria; Cryo-EM; cryo-ET; Fluorescence microscopy; Long-wavelength X-ray diffraction; Metal-ion-binding proteins

Surface layers (or S-layers) are present in most prokaryotic cells. They're made from a diverse family of proteins capable of forming two-dimensional arrays that encompass the entire cell. Their ability to form highly structured lattices with regular symmetry and self-healing properties makes them an attractive target for synthetic biology and studies of fundamental cell biology. To harness S-layers for synthetic biology, we need a better understanding of how they form, how they bind to the cell surface, and how they are maintained.

One of the most commonly observed features is the utilisation of metal ions by S-layers for assembly and binding to the cell surface. Researchers used the Long-Wavelength MX beamline (I23) to study how bacterial cells (from *Caulobacter crescentus*) use Ca^{2+} ions bound to the constituent S-layer protein, RsaA, to facilitate the formation of the S-layer. Their study was highly interdisciplinary and used a range of methods from microscopic to near-atomic resolution.

S-layers have a range of applications in synthetic biology, as protein-expression platforms or vaccine development systems, in bioremediation, and several other fields. S-layer biology is also a growing field with implications for fundamental prokaryotic cell biology. This study provides insight into how S-layers optimise their own biogenesis using available metal ions in the environment, which can inform the design of synthetic two-dimensional sheets with long-range order up to the micron level.

Surface layers (or S-layers) are a group of proteinaceous, two-dimensional lattices that constitute the outermost layer of many prokaryotic cell envelopes[1]. They are found in both Gram-negative and Gram-positive bacteria as well as in the enigmatic and poorly studied archaea[1]. S-layer proteins (SLPs) are highly diverse in sequence and are typically the highest-copy number proteins in expressing cells, making them one of the most ubiquitous protein groups in nature[1]. Despite the lack of obvious sequence homology, SLPs have several features that have been observed across multiple species and domains of life[1]. Of particular interest is the ability of S-layers to utilise environmentally available metal ions to facilitate their folding and retention along the cell surface, to form a regularly arranged lattice[1]. Due to this ability to self-assemble, S-layers have attracted interest due to their potential for applications in synthetic biology and for their importance in fundamental prokaryotic cell biology.

This study[2] aimed to investigate S-layer biogenesis in the model organism

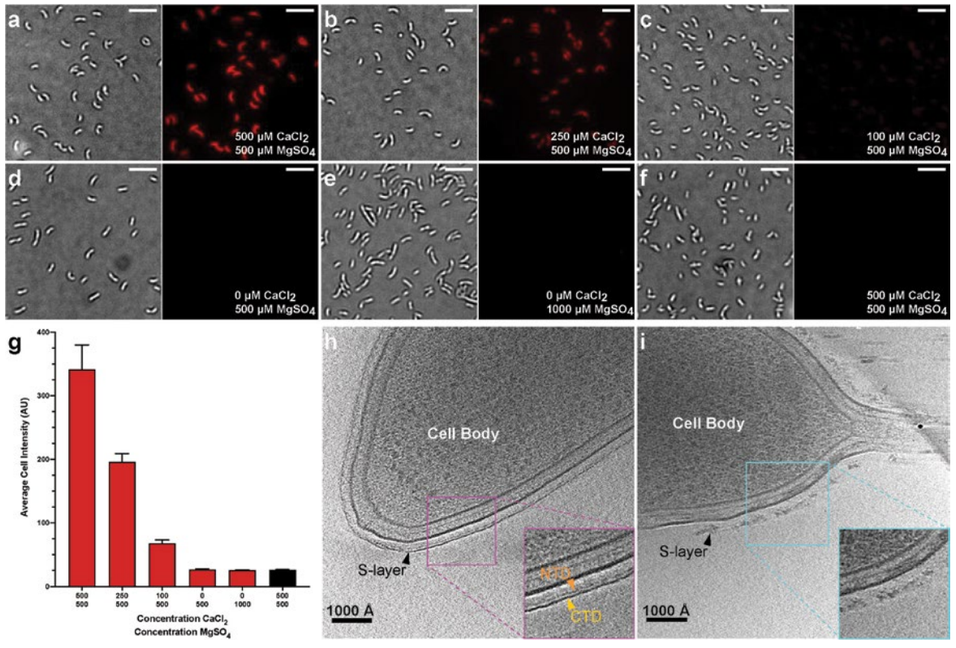

Figure 1: C. crescentus cells expressing RsaA-467-SpyTag grown in M2G media containing (A) 500 µM; (B) 250 µM; (C) 100 µM; (D) or no additional $CaCl_2$, with incubation with SpyCatcher-mRFP1; Controls included (E) 1000 µM $MgSO_4$ and no $CaCl_2$ and with SpyCatcher-mRFP1 and (F) cells grown without SpyCatcher-mRFP1. mRFP1 signal is strongest in cells grown in 500 µM $CaCl_2$ with a clear reduction at lower concentrations (scale bar: 10 µm); (H) Average cell intensity and standard deviation was quantified using ImageJ (n = 50); Slices through tomograms of cells grown in (H) 500 µM $CaCl_2$ or (I) 100 µM $CaCl_2$ M2G media, showing S-layer disruption at lower $CaCl_2$ concentrations.

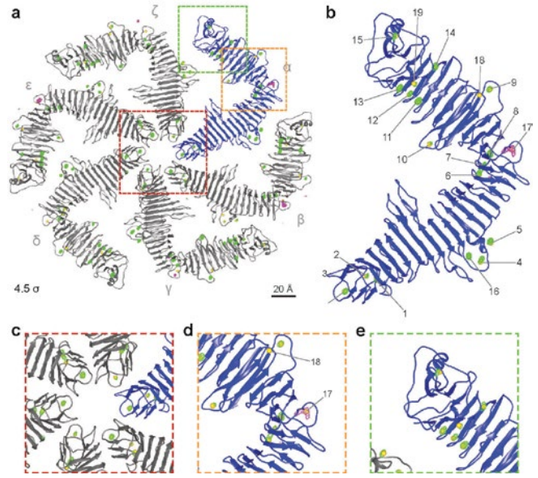

Figure 2: (A) The RsaACTD hexamer showing proposed metal-ion-binding sites (yellow spheres); Chains are identified as a-ζ. Densities in anomalous difference maps collected at X-ray energies of 4.1 and 3.7 keV represent calcium (green mesh) and potassium (magenta mesh) respectively. All maps are displayed at a contour level of 4.5 σ. Positions 1-16 and 19 are coordinated with Ca^{2+} densities, with few exceptions. Position 17 is coordinated with a K^+ ion in our three-dimensional crystals in all RsaA monomers except δ, while 18 was consistently empty; (B) Magnified chain a of the RsaA hexamer (blue); (C-E) Magnified views of RsaACTD in A.

Caulobacter crescentus, a Gram-negative bacterium with a hexagonal S-layer comprised of a single protein called RsaA. *C. crescentus* requires a high concentration of Ca^{2+} (500 µM) for optimal growth, and previous research has suggested that this high Ca^{2+} requirement is linked to the dependence of the S-layer on Ca^{2+} ions for polymerisation. Lower concentrations of Ca^{2+} result in slower growth and triggers S-layer shedding from the cell surface.

Using an engineered strain of *C. crescentus* expressing a SpyTag-peptide, the researchers irreversibly labelled the S-layer using SpyCatcher proteins conjugated with different fluorescent proteins[2]. With this approach, they were able to directly track S-layer assembly and retention as a function of Ca^{2+} concentration in the medium (Fig. 1A-G). The researchers observed that without ample Ca^{2+}, the S-layer was lost from the cell surface, confirmed using electron cryotomography (cryo-ET), indicated by large gaps along an aberrant S-layer (Fig. 1H-I).

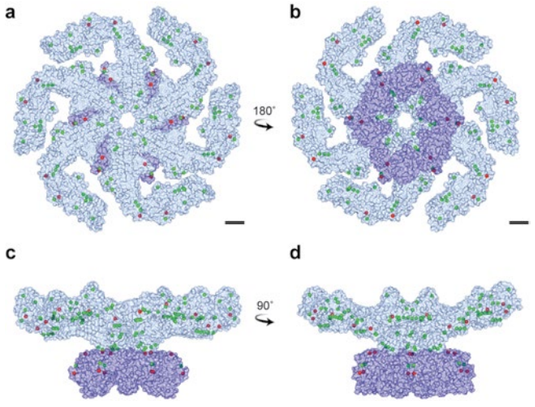

Figure 3: Surface model of the RsaA hexamer (RsaACTD displayed in blue, RsaANTD in purple) in (A) top view and (B) bottom view with associated metal ions as confirmed by experiments. Confirmed Ca^{2+} ions (positions 1-16, 19 and 21) are shown in green, metal-binding sites with unassigned or no associated ions are displayed in red, i.e. positions 17 (K^+), 18 (possibly Mg^{2+}), 20 and 22 (probably Ca^{2+}); (C-D) Orthogonal side views. Scale bar: 50 Å.

The locations of 22 metal binding sites in RsaA were previously proposed using X-ray crystallography of S-layer sheets[3]. Molecular dynamics (MD) simulations of the RsaA hexamer revealed that Ca^{2+} ions at these locations stabilised the hexameric structure of RsaA. However, two positions in RsaA, (positions 17 and 18), showed unstable Ca^{2+} binding in simulations. To unambiguously confirm these previous predictions from crystallography and MD, the in vacuum beamline I23 at Diamond Light Source was utilised. This beamline provides access to measurements below and above the X-ray absorption edges of calcium (K edge: 4.0381 keV or 3.0704 Å) and potassium (K edge: 3.6074 keV or 3.4369 Å)[4], not available anywhere else in the world.

Using measurements at the I23 beamline, the researchers were able to identify and locate the positions of the Ca^{2+} ions in the RsaA S-layer lattice[2]. Anomalous diffraction experiments showed that each monomer of the C-terminal domain of RsaA is bound to 17 Ca^{2+} ions, identified using datasets collected using X-rays with energies of 4.10 and 3.95 keV (Fig. 2), confirming their previous results. Furthermore, as suggested by MD simulations, positions 17 and 18 did not contain Ca^{2+}, satisfyingly confirmed by direct experiments. Position 17 was bound to a K^+ ion, while position 18 was neither Ca^{2+} nor K^+ (Fig. 2). Thus, long-wavelength anomalous X-ray diffraction experiments allowed them to confirm predictions made from their previous X-ray data[3] and from MD simulations, and helped them locate and identify metal ions in the RsaA lattice, of clear importance to the cell biology of *C. crescentus*.

Finally, to complement Ca^{2+} identification at I23, they were also able identify Ca^{2+} binding sites in other parts of the S-layer using Ho^{3+} substitution of Ca^{2+} ions in our previously described S-layer complex with lipopolysaccharide[5]. Ho^{3+} has a high propensity for replacing Ca^{2+} ions and cryo-EM single particle analysis of the complex produced a 4.3 Å resolution map that revealed positions of Ho^{3+} substitutions. When taken together, the cryo-EM and long-wavelength studies have allowed the researchers to confirm the positions of 108 Ca^{2+} ions in the RsaA S-layer hexamer, demonstrating the power of modern structural biology to bring atomic level insight into cell biological phenomena at the micron scale (Fig. 3).

References:

1. Bharat, T. A. M. *et al*. Molecular logic of prokaryotic surface layer structures. *Trends in Microbiology* **29**, 405–415 (2021). DOI: 10.1016/j.tim.2020.09.009
2. Herdman, M. *et al.* High-resolution mapping of metal ions reveals principles of surface layer assembly in Caulobacter crescentus cells. *Structure* **30**, 215-228.e5 (2022). DOI: 10.1016/j.str.2021.10.012
3. Bharat, T. A. M. *et al.* Structure of the hexagonal surface layer on Caulobacter crescentus cells. *Nature Microbiology* **2**, 17059 (2017). DOI : 10.1038/nmicrobiol.2017.59
4. Wagner, A. *et al*. In-vacuum long-wavelength macromolecular crystallography. *Acta Crystallographica Section D Structural Biology* **72**, 430–439 (2016). DOI: 10.1107/S2059798316001078
5. Von Kügelgen, A. *et al.* In situ structure of an intact lipopolysaccharide-bound bacterial surface layer. *Cell* **180**, 348-358.e15 (2020). DOI: 10.1016/j.cell.2019.12.006

Funding acknowledgement:
M.H. is supported by funding from the Biotechnology and Biological Sciences Research Council (BBSRC, grant number BB/M011224/1). T.A.M.B. is a recipient of a Sir Henry Dale Fellowship, jointly funded by the Wellcome Trust and the Royal Society (202231/Z/16/Z). T.A.M.B would like to thank the Vallee Research Foundation, the Leverhulme Trust, and the John Fell Fund for support.

Corresponding authors
Matthew Herdman, University of Oxford, matthew.herdman@path.ox.ac.uk
Dr. Tanmay Bharat, University of Oxford, tanmay.bharat@path.ox.ac.uk

New antibiotics with a surprising mode of action

Related publication: Kolarič, A., Germe, T., Hrast, M., Stevenson, C. E. M., Lawson, D. M., Burton, N. P., Vörös, J., Maxwell, A., Minovski, N., & Anderluh, M. Potent DNA gyrase inhibitors bind asymmetrically to their target using symmetrical bifurcated halogen bonds. *Nature Communications*, **12**, 150 (2021). DOI :10.1038/s41467-020-20405-8

Publication keywords: DNA gyrase; Antibiotics; NBTIs; Halogen bonds

Relatively few new antibiotics were developed in the late 20th Century, and overuse has led to the development of significant bacterial resistance. With some bacterial infections becoming untreatable, antibiotic discovery is now a priority.

An international collaboration, involving two academic groups in Slovenia and an academic group and a small company in Norwich, designed a series of new molecules with antibiotic potential. These new antibiotics, Novel Bacterial Topoisomerase Inhibitors (NBTIs), kill bacteria and act against a well-validated target, DNA gyrase. However, to enable the design of further molecules, the team needed to know the molecular structure of the new molecules bound to gyrase. They used state-of-the-art macromolecular crystallography beamline I04 at Diamond Light Source to investigate how these work at the molecular level.

The team evaluated the relevant potency of several NBTIs against gyrase and showed that they stabilised intermediates between the enzyme and the DNA, with a single DNA strand cleaved, which is important as it leads to bacterial killing. In addition, they solved the crystal structure of gyrase bound to one of the new inhibitors, revealing the existence of bifurcated halogen bonds between the enzyme and the inhibitor molecule - an unprecedented observation in a biological system.

This new information informs the intelligent design of new molecules based on the new biochemical and structural information. The ultimate aim is to develop new antibiotics with desirable properties for use in clinical medicine.

Novel Bacterial Topoisomerase Inhibitors (NBTIs) are a promising class of new antibacterial agents that are active against the bacterial target, DNA gyrase. By forming a complex with the enzyme and DNA, they stabilise single-strand DNA cleavage breaks, preventing the enzyme from functioning, which leads to cell death, in a manner related to the well-known quinolone antibiotics[1,2]. Since this type of antibacterial has now been known for many years, one would think that there would be little left to be discovered. Yet, the exact mechanism of NBTI-single-strand stabilisation has remained only hypothetical.

The present study started as a classical medicinal chemistry project with the in-silico design of NBTIs with innovative fragments binding to DNA gyrase, the so-called "right-hand side (RHS)" of the starting compounds. In particular, careful examination of the binding site revealed that the RHS part of the molecule could form halogen/hydrogen bonds with the backbone carbonyl oxygen of at least one of the two amino acid residues (Alanines) in gyrase. NBTIs emerging from these in-silico protocols were synthesised, their biological activity was evaluated and the exact binding mode was clarified by crystallography[3-5]. To our delight, NBTI compounds with a p-halo-substituted phenyl RHS fragment showed remarkable inhibition of *Staphylococcus aureus* DNA gyrase: $IC_{50} = 35$ nM for chloro, $IC_{50} = 7$ nM for bromo, and $IC_{50} = 11$ nM for iodo derivatives. This gave us an indication that halogen binding is likely to be behind the measured potency. Surprisingly, such excellent enzyme inhibitory potency was due to the formation of a symmetrical bifurcated halogen bond between the halogen atom and a backbone carbonyl oxygen of Ala68 from both gyrase A (GyrA) subunits (PDB ID: 6Z1A) in the heterotetrameric enzyme. It was surprising to see a symmetric bifurcated halogen bond in a biological system. Obtaining the crystal structure was not trivial, in fact, we found that bromo and iodo derivatives stabilised the ternary complex so strongly and quickly that no crystals would form. The crystal was obtained in the end, but with a chloro derivative. Serendipitously, this is the first time that such a so-called symmetrical bifurcated halogen bond has been identified in a relevant biological system where a ligand interacts with its macromolecular target.

The crystal structure had more to offer and allowed a genuine breakthrough in understanding the mechanism of action of NBTIs. Namely, since gyrase is a symmetrical enzyme, all previously reported crystal structures housed NBTIs in two orientations rotated by 180° within the same crystal. Our crystal structure is the first in which an NBTI binds in a single conformation (without static disorder), which allowed us to elucidate the mechanism of how an NBTI stabilises the gyrase-DNA complex with only one DNA strand being nicked. Indeed, the intercalation of the asymmetric NBTI causes a shift of the DNA backbone away from the cleavage site on only one side. Consequently, the scissile phosphate can get close to the catalytic metal on one side only, which is why the NBTI stabilises single-strand cleavage.

Our discovery of the mechanism of action as well as the identification of the symmetric bifurcated halogen bonds are the starting point for further structural modifications and optimisation of NBTIs. More importantly, it expands the repertoire of the medicinal chemist's interaction toolbox to design molecules of the future.

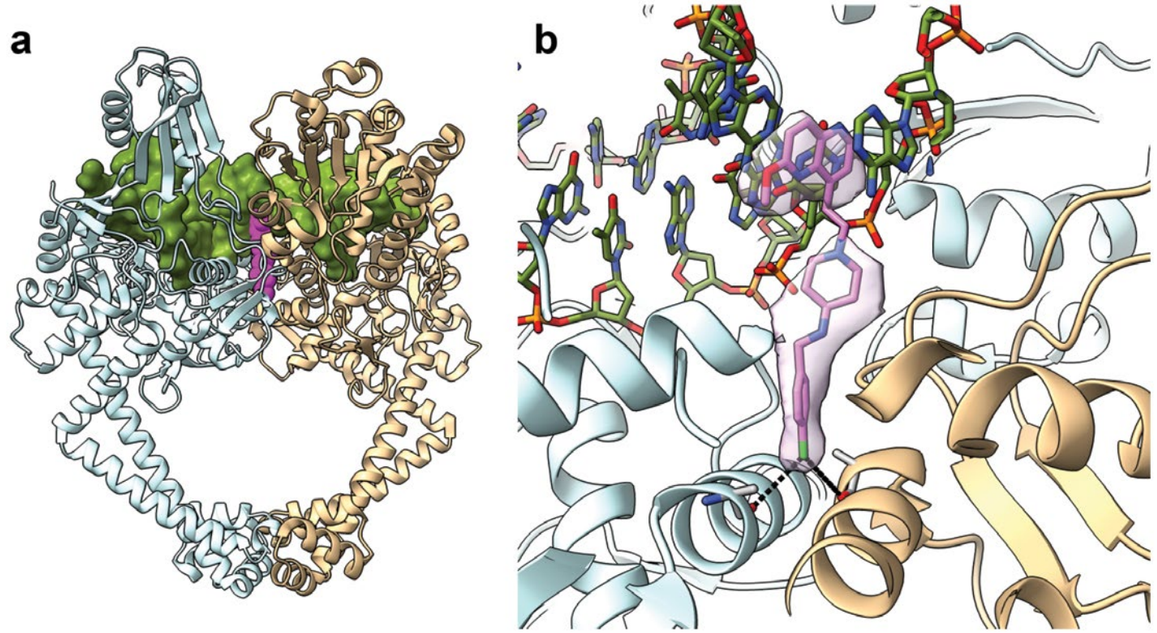

Figure 1: The crystal structure of p-chloro NBTI bound to a S. aureus gyrase-DNA complex (PDB ID: 6Z1A); (a) Overview showing gyrase in ribbons with the two halves of the complex in pale cyan and pale brown, respectively. A molecular surface for the DNA is shown in green and the inhibitor is shown as magenta van der Waals spheres; (b) Close up of the inhibitor binding site showing intercalation with the DNA at the top and the bifurcated halogen bond at the bottom that the NBTI makes with the backbone carbonyl oxygens of the two symmetry-related Ala68 residues of GyrA. Also shown as a transparent magenta surface is omit electron density for the inhibitor calculated at 2.3 Å resolution and contoured at 1.6 σ.

References:

1. Bush, N. G. *et al.* Quinolones: mechanism, lethality and their contributions to antibiotic resistance. *Molecules*, **25**, 5662 (2020). DOI: 10.3390/molecules25235662
2. Kolarič, A. *et al*. Two decades of successful SAR-grounded stories of the novel bacterial topoisomerase inhibitors (NBTIs). *Journal of Medicinal Chemistry*, **63**, 5664–5674 (2020). DOI: 10.1021/acs.jmedchem.9b01738
3. Kolaric, A. *et al*. Structure-based design of novel combinatorially generated NBTIs as potential DNA gyrase inhibitors against various Staphylococcus aureus mutant strains. *Molecular BioSystems*, **13**, 1406–1420 (2017). DOI: 10.1039/C7MB00168A
4. Kolarič, *et al*. Cyclohexyl amide-based novel bacterial topoisomerase inhibitors with prospective GyrA-binding fragments. *Future Medicinal Chemistry*, **11**, 935–945 (2019). DOI: 10.4155/fmc-2018-0472
5. Kolarič, *et al*. Potent DNA gyrase inhibitors bind asymmetrically to their target using symmetrical bifurcated halogen bonds. *Nature Communications*, **12**, 150 (2021). DOI: 10.1038/s41467-020-20405-8

Funding acknowledgement:
The financial support of this work from the Slovenian Research Agency (Grants P1-0017 and P1-0208) is gratefully acknowledged. Work in A.M.'s laboratory is supported by the Biotechnology and Biosciences Research Council (BBSRC; UK) Institute Strategic Programme Grant BB/P012523/1, and the Wellcome Trust (Investigator Award 110072/Z/15/Z); J.V.'s work was also supported by an FTMA award from BBSRC (BB/S507921/1). Diamond Light Source is acknowledged for access to beamline I04 under proposal MX18565.

Corresponding authors:
Prof. Anthony Maxwell, John Innes Centre, tony.maxwell@jic.ac.uk
Prof. David Lawson, John Innes Centre, david.lawson@jic.ac.uk

XChem fragment screening finds new binding sites on vital tubulin protein

Related publication: Mühlethaler, T., Gioia, D., Prota, A. E., Sharpe, M. E., Cavalli, A., & Steinmetz, M. O. Comprehensive analysis of binding sites in tubulin. *Angewandte Chemie International Edition* **60**, 13331–13342 (2021). DOI: 10.1002/anie.202100273

Publication keywords: Crystallographic fragment screening; Molecular dynamics simulations; Tubulin; Microtubules; Protein-ligand interactions

The tubulin protein plays an essential role in vital cell functions, including cell division. Tubulin molecules form tube-like structures, called microtubule filaments, that give cells their shape and help transport proteins and other cellular components. Tubulin can bind to many proteins and small molecules, but the total number of binding sites it has was unknown.

Researchers at the Paul Scherrer Institute and the Italien Institute of Technology used a unique combination of computer simulations and crystallographic fragment screening performed at the XChem facility and Macromolecular Crystallography (MX) beamline (I04-1) to investigate that fundamental question.

For the fragment screening, the team exposed hundreds of tubulin crystals to solutions containing fragments of molecules. Then, they used beamline I04-1 to create X-ray diffraction patterns for each soaked crystal, showing which molecule fragments have bound to the tubulin, and where.

Their results uncovered 11 previously unknown binding sites on the protein and identified 56 fragments that bind to tubulin and could be used in future drug development.

The team's approach can also be used to investigate other proteins and could help to discover new binding sites in other pharmaceutically important molecules.

Microtubules are dynamic cytoskeletal filaments, which are assembled from and disassembled into their αβ-tubulin heterodimeric building blocks (referred to as tubulin from here onwards). A fundamental property of microtubules and tubulin is their ability to bind a plethora of regulators. The main activity of these regulators is to modulate microtubule dynamics and organisation, and consequently microtubule function. In cells, an array of proteins bind microtubules to control fundamental microtubule cytoskeleton-based physiological processes in all eukaryotes ranging from cell division, cell motility, cell polarity to intracellular trafficking. In addition, a large number of chemically diverse, small molecule ligands bind to seven so far identified, distinct binding sites in tubulin. Notably, compounds that interfere with microtubule function have been very successfully used to treat human pathologies including gout and cancer, however, they are also generally employed in basic research studies aimed at understanding microtubule cytoskeleton-based cellular processes (reviewed in[1]).

The observation that tubulin can interact with a plethora of regulators raises the intriguing question of how many different binding sites do actually exist in the tubulin dimer. Here, the researchers addressed this question using a combined computational and crystallographic fragment screening approach. They initially performed a molecular dynamics simulation in explicit solvent with a high-resolution X-ray crystal structure of the tubulin dimer[2]. They then computationally identified pockets in tubulin, analysed their relative dynamics and persistency, and assessed their communication networks by tracking the exchange of atoms between adjacent pockets. With the two-fold objective to (i) validate experimentally their computational predictions, and (ii) to identify potential ligands able to bind into novel tubulin pockets, they next conducted an X-ray crystallography-based fragment screen using the XChem facility and beamline I04-1 at Diamond Light Source[3]. A fragment is a small, ~200 Da chemical entity that in combination with a crystal structure of the fragment complexed to its target has been recognised as a powerful tool for structure-based drug design[4]. They soaked individual tubulin crystals with 708 different fragments, collected 672 X-ray diffraction data sets, and solved 503 structures with a resolution of better than 4.0 Å.

The data obtained from their combined computational and experimental approach revealed a total of 27 distinct binding sites in tubulin. Remarkably, all major, previously characterised tubulin-drug binding sites (reviewed in[5]) were readily detected. Furthermore, several key contact points between tubulin dimers in microtubules as well as between tubulin and secondary structural elements of regulatory protein partners were revealed. Importantly, they found 18 sites that are not targeted by any of the antitubulin drugs that have been structurally characterised to date. 11 out of those (seven in β-tubulin and four in α-tubulin) represent completely new and thus undescribed binding sites in the tubulin dimer. They further found an intricate, dynamic communication network between different pockets located also remote from each other in both the α- and β-tubulin monomers (Fig. 1). Finally, they identified 56 chemically diverse fragments that bound to a total of 10 different tubulin pockets (Fig. 2).

Their results have important implications. For example, it is well known that the vast majority of structurally characterised tubulin-binding ligand and protein partners target β-tubulin. An open question in the antitubulin drug development field has thus been whether α-tubulin can at all be considered as a target for the development of small molecule modulators of microtubule dynamics. Their analysis now presents several sites in and fragments able to bind to α-tubulin, which can be exploited in future antitubulin ligand development campaigns. Their results further disclose several fragment binding sites in the tubulin dimer whose residue composition notably differ amongst human tubulin isotypes. This observation offers a unique basis for the design of isotype-selective antitubulin ligands. This is of particular interest in the context of chemotherapy since the upregulation of specific tubulin isotypes by cancer cells is a widely recognised resistance mechanism against antitubulin drugs. Finally, the majority of structurally characterised ligands and proteins that target tubulin typically do not share binding sites, which is rather surprising. Their experimental data now reveal four sites that are targeted by both fragments and secondary structural elements of major physiological microtubule regulators.

In conclusion, their data and analyses provide a comprehensive description of the shape, chemical property, and dynamics of small molecule-binding sites in tubulin. Until now, drug discovery efforts were directed towards interfering with microtubule dynamics. Our results not only offer a platform for the innovative design of more selective antitubulin ligands with novel mechanisms of action with respect to microtubule dynamics modulation, they also provide a structural basis for the rational design of inhibitors of tubulin-protein interactions. In more general terms, our combined computational and crystallographic fragment screening approach used in this study offers a protocol that may help identifying new ligand-binding sites in any other pharmaceutically relevant target and analyse them in terms of chemical tractability and allosteric modulation.

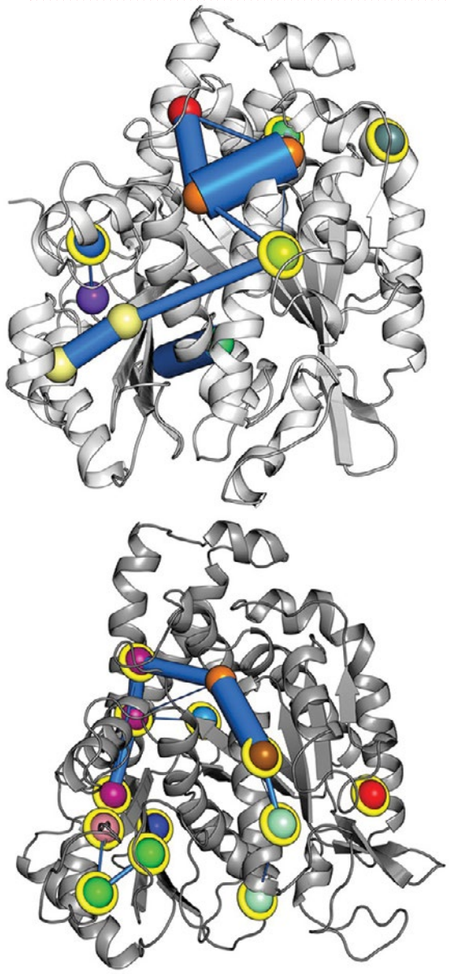

Figure 1: Tubulin pockets and their communication networks predicted by MD simulation. Predicted pockets and their communication networks in β-tubulin (top panel) and a-tubulin (bottom panel). Marine blue lines depict connected network nodes; their widths are displayed proportional to the respective communication frequency between two nodes. Spheres represent centre of masses of the pockets (corresponding to network nodes) and are shown in different colours. Identical colours indicate pockets that are often merged during the simulation. Spheres coated with yellow rings highlight novel sites identified in this study.

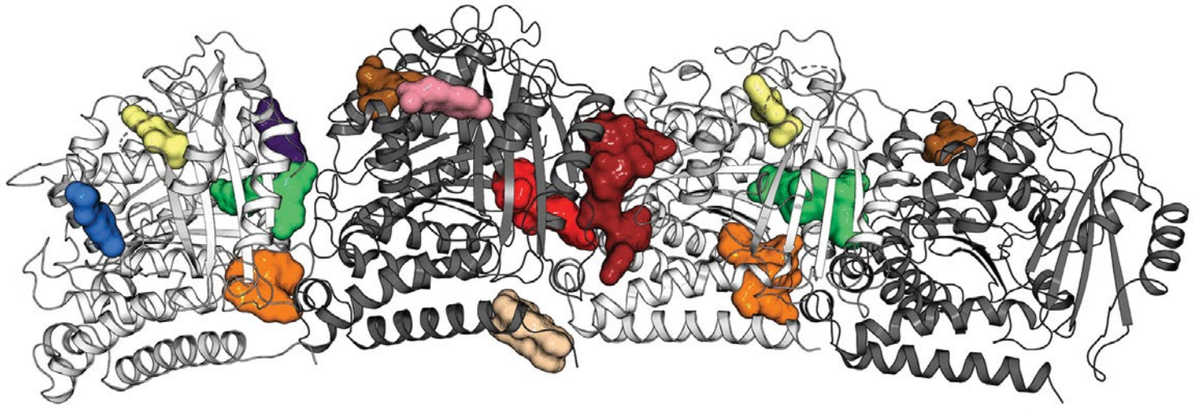

Figure 2: Fragment-binding sites in tubulin determined by X-ray crystallography. Shown are the two aβ-tubulin heterodimers as observed in their previously developed crystal system[2]. The α- and β-tubulin monomers are shown in dark and light grey ribbon representation, respectively. Fragment binding sites are highlighted in different colours.

References:

1. Dumontet, C. *et al.* Microtubule-binding agents: a dynamic field of cancer therapeutics. *Nature Reviews Drug Discovery* **9**, 790–803 (2010). DOI: 10.1038/nrd3253
2. Prota, A. E. *et al.* Molecular mechanism of action of microtubule-stabilizing anticancer agents. *Science* **339**, 587–590 (2013). DOI: 10.1126/science.1230582
3. Douangamath, A. *et al*. Achieving efficient fragment screening at XChem facility at Diamond Light Source. *Journal of Visualised Experiments* **171** (2021). DOI: 10.3791/62414
4. O'Reilly, M. *et al.* Crystallographic screening using ultra-low-molecular-weight ligands to guide drug design. *Drug Discovery Today* **24**, 1081–1086 (2019). DOI: 10.1016/j.drudis.2019.03.009
5. Steinmetz, M. O. *et al.* Microtubule-targeting agents: strategies to hijack the cytoskeleton. *Trends in Cell Biology* **28**, 776–792 (2018). DOI: 10.1016/j.tcb.2018.05.001

Funding acknowledgement:
iNEXT (PID2692), funded by the Horizon 2020 program of the European Union, the Regione Lombardia (ID 239047 NEON), and the Swiss National Science Foundation (31003A_166608 and 310030_192566).

Corresponding authors:
Prof. Michel O. Steinmetz, Paul Scherrer Institut, michel.steinmetz@psi.ch
Prof. Andrea Cavalli, Italian Institute of Technology, andrea.cavalli@iit.it

Biological Cryo-Imaging Group

Martin Walsh, Science Group Leader

The Biological Cryo-imaging Group brings together dedicated facilities for X-ray, light and electron microscopy at Diamond Light Source. The electron BioImaging Centre (eBIC) is the national centre for cryo-Electron Microscopy (cryo-EM) in the UK and provides a range of capabilities and supporting facilities for cryo-EM and Correlative Light and Electron Microscopy (CLEM). Beamline B24 hosts a full field cryo-transmission X-ray microscope dedicated to biological X-ray imaging and has also established a cryo super resolution fluorescence microscopy facility, which is a joint venture between Diamond and the University of Oxford. It provides a unique platform for correlative light and X-ray microscopy, and cryo-EM.

The Biological Cryo-Imaging group continues to grow and welcome new faces as we finalise our recruitment drive at eBIC and renew posts at B24. At eBIC two cryo-EM scientists Matt Bryne and Lorna Malone and new PhD students Emily Lacey, Frank Nightingale and Patrick Phillips, and a year in industry student (Ishika Kumar) have recently joined. In addition, the Post-Doctoral research team has expanded with the addition of two new researchers Kyprianos Hadjidemetriou and Satinder Kaur, who are funded on a new strategic ERC grant awarded to the eBIC director Peijun Zhang. At B24, Chidinma Okolo and Archana Jadhav have been appointed as beamline scientists.

Last autumn B24 underwent its first external beamline review which independently assessed the performance of the beamline to date and rated it overall as excellent and world-leading. In particular, the external panel commended the beamline team on establishing an internationally unique correlative platform combining two high-end 3D cryo-microscopy techniques (Cryo Soft X-ray Tomography (CryoSXT) and cryo Structured Illumination Microscopy (SIM)) alongside a user friendly package of protocols that encompass sample preparation methods and *in silico* procedures for data correlation and analysis.

As a result of the pandemic and with users, until recently, not being able to attend site, we continue to evolve our remote user activites and continue with developing remote training/teaching courses and material. At eBIC we have rolled out regular remote user training courses for our Block Allocation Groups and extensive new user guides for eBIC microscopes. Similarly at B24 the team has published manuals and practical guidelines for users on their webpages. B24 has also worked hard to disseminate beamline capabilities from the basics to correlative imaging through workshops (*e.g.* iNEXT-Discovery workshop "*What can Cryo Electron Tomography and Cryo Soft X-ray Tomography do?*") as well as publish beamline protocols and methodologies in peer-reviewed publications.

Highlights from eBIC's internal research programme includes the release and corresponding publication of a new software tool, IceBreaker, that helps in optimisation of particle picking and data collection[1] . The method has been developed by a joint PhD student (Mateusz Olek) between Diamond and the University of York. The aim of the method is to resolve adverse effects of variable ice thickness in cryo-EM. It consists of image segmentation and statistical analysis of the background, followed by discrete normalisation of patches. This allowed for better identification of particles irrespective of the background originating from the ice. This impacts and aids researchers to now reliably gather more structural information by analysing more protein particles. IceBreaker is now fully integrated in the eBIC single particle image processing pipeline.

Publication highlights for B24 alongside a number of instructional/ educational and review articles, include a paper in Nature Protocols which documents all steps necessary for successful sample preparation for Soft X-ray Tomography[2], work on SARS-Cov2 in partnership with eBIC and the University of Oxford[3] and further work on novel T cell-derived cytotoxic particles[4]. Finally, at B24 we have implemented automated data collection from our transmission X-ray microscope which plugs neatly into our already existing automated data reconstruction pipeline.

The partnership between Diamond and the Research Complex at Harwell (RCaH) has been strengthened by the recruitment of Michal Klosowski – who will manage the RCaH 200 keV Thermofisher Scientific Glacios electron microscope housed at eBIC. The RCaH Glacios is also currently being used to asses the Dectris SINGLA detector, a 1 Mega-pixel, hybrid pixel electron detector for micro-crystal Electron Diffraction (microED). This is carried out in collaboration with the Diamond HeXI beamline team and CCP4 where the Dials software package is being integrated to provide a data processing pipeline for the data generated.

New capabilities on the horizon at eBIC include new access routes for using the Leica cryo Correlative Light and Electron Microscope (cryoCLEM) as well as access for microED.

Coupled to this, eBIC has continued working extensively with the manufacturer Thermofisher to commission and benchmark their Selectris-X energy filter and updated Falcon 4i detectors which were brought into the user program at the start of 2022.

References

1. Olek, M. *et al.* IceBreaker: Software for high-resolution single-particle cryo-EM with non-uniform ice. *Structure* **30**, 522-531.e4 (2022). DOI: 10.1016/j.str.2022.01.005
2. Okolo, C. A. *et al.* Sample preparation strategies for efficient correlation of 3D SIM and soft X-ray tomography data at cryogenic temperatures. *Nature Protocols* **16**, 2851–2885 (2021). DOI: 10.1038/s41596-021-00522-4
3. Mendonça, L. *et al.* Correlative multi-scale cryo-imaging unveils SARS-CoV-2 assembly and egress. *Nature Communications* **12**, 4629 (2021). DOI: 10.1038/s41467-021-24887-y
4. Chang, H.-F. *et al.* Identification of distinct cytotoxic granules as the origin of supramolecular attack particles in T lymphocytes. *Nature Communications* **13**, 1029 (2022). DOI: 10.1038/s41467-022-28596-y

"Highlights from eBICs internal research program includes the release and corresponding publication of a new software tool, IceBreaker, that helps in optimisation of particle picking and data collection."

The eBIC team .

Combining synchrotron and laser light to 3D-image subcellular architecture under cryogenic conditions

Related publication: Koronfel, M., Kounatidis, I., Mwangangi, D. M., Vyas, N., Okolo, C., Jadhav, A., Fish, T., Chotchuang, P., Schulte, A., Robinson, R. C., & Harkiolaki, M. Correlative cryo-imaging of the cellular universe with soft X-rays and laser light used to track F-actin structures in mammalian cells. *Acta Crystallographica Section D Structural Biology* **77**, 1479–1485 (2021).DOI: 10.1107/S2059798321010329

Publication keywords: X-ray tomography; Water-window absorption imaging; Structured illumination; Cytoskeleton; Correlative cryo-imaging

When viewing a sample with different microscopy techniques, these often cannot be correlated because of differences in the scale and the detail of the information they capture. In the case of cells, imaging the cytoskeleton within the context of the fully hydrated cellular ultrastructure and its contents to high resolution and in 3D needs a specialised combination of microscopes that did not exist previously.

Researchers wanted to understand the distribution and architecture of filamentous actin, which represents the finest and most dynamic component of the cytoskeleton. They used the Cryo Soft X-ray Tomography beamline (B24), ensuring the capture of the native ultrastructure through vitrification without the need for chemical or mechanical modification.

The team used Cryo Soft X-ray Tomography (cryoSXT) and cryo Structured Illumination Microscopy (cryoSIM) to capture the 3D ultrastructure of the cell and the chemical localisation of filamentous actin, and to unambiguously correlate these data in 3D.

Their findings confirm the applicability of high-resolution cutting-edge 3D cryo-microscopy methods at beamline B24 in the study of biological processes. The minimal disruption approach ensures the capture of physiologically relevant information that can be used without concern over artefact induction due to sample processing.

To date, the B24 imaging platform has been used for a number of investigations into understanding basic biological mechanisms, and also for the assessment and understanding of subjects of biomedical importance such as anti-cancer drugs and vaccine development.

The subcellular universe inside living cells at physiological conditions is rich with content such as macro- and supra-molecular structures, conglomerates of vesicles and organelles alongside concentrations of inorganic and organic chemicals tethered or flowing along gradients and currents. All these constituents have a role to play (and often multiple roles) in maintaining a healthy cellular environment and responding to external stimuli as they interact with each other constantly. Because of this dynamic and multivariant subject matter, imaging one set of cellular features using one microscope invariably misses relevant features that can only be captured by different microscopy methods and the correlation of imaging data across methods becomes invaluable to fully understand context beyond localisation within an area of interest.

At beamline B24, two powerful imaging methods have been paired and used here to track and understand the role of filamentous actin in human fibroblasts[1] (Fig. 1). Cryo-Soft X-ray Tomography (cryoSXT) is a relatively young technique that has developed following progress in cryogenic sample preparation in the previous two decades with a view of preparing cellular material that retains its native ultrastructure in a form that can withstand the radiation exposure needed to capture high content high resolution 3D imaging. CryoSXT uses X-rays in the 'water window' of the spectrum where carbon-rich biological material such as membranes and vesicles absorb X-rays readily in contrast to the oxygen-rich medium that surrounds them leaving as a result an imprint of their conformation on the detector that receives the transmitted rays[2] (Fig. 2a). The principle very much reflects the application of CT in a medical setting but in this case the microscope is adapted to capture the intracellular environment. The method has proven to be an invaluable tool in assessing cellular response but lacks information on chemical localisation, namely it cannot provide the distribution of chemicals or proteins of interest. This has been achieved at B24 beamline through the combined use of fluorescence microscopy and specifically cryo-Structured Illumination Microscopy (cryoSIM) which allows the capture of chemical localisation beyond the diffraction limit through fluorescence excited via laser light. The two microscopes work synergistically and multiply the information content of the data acquired by providing direct and unambiguous 3D correlation[3] (Fig. 2b & 2c).

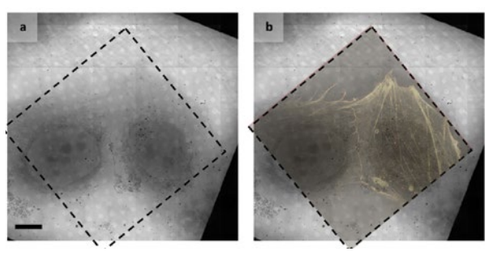

Figure 1: (a) 2D soft X-ray mosaic of vitrified human fibroblasts (two cells seen here on a perforated carbon support film; the nuclei appear as round areas of low signal with defined nucleoli while the cytoplasm shows more content such as organelles and substructures; (b) the same mosaic with filamentous actin distribution as captured with cryoSIM and clearly defining the cytoskeletal architecture that is missing from the naked SXT data. Data was collected at beamline B24. Scale bar is 10 µm.

When studying the cytoskeleton, it is often challenging to capture the finer and most dynamic most dynamic element of its components (filamentous actin) in 3D and to nanometer resolution. Although cryoSXT is an excellent tool for studying subcellular architecture, filamentous actin is difficult to decipher in an X-ray tomogram because of its low contrast profile precisely because of the finer and transient structures it creates. Using the B24 integrated imaging pipeline the authors were able to capture the chemical information needed within the cellular ultrastructure and to unambiguously localise filamentous actin structures such as supra-filaments, networks and vesicle cradles. In doing so they have established the correlative method as a valuable tool in this type of research and have enabled the gathering of information beyond what each method would be able to provide separately. From a biological standpoint, they expected filamentous actin to play an integral role in cellular functions

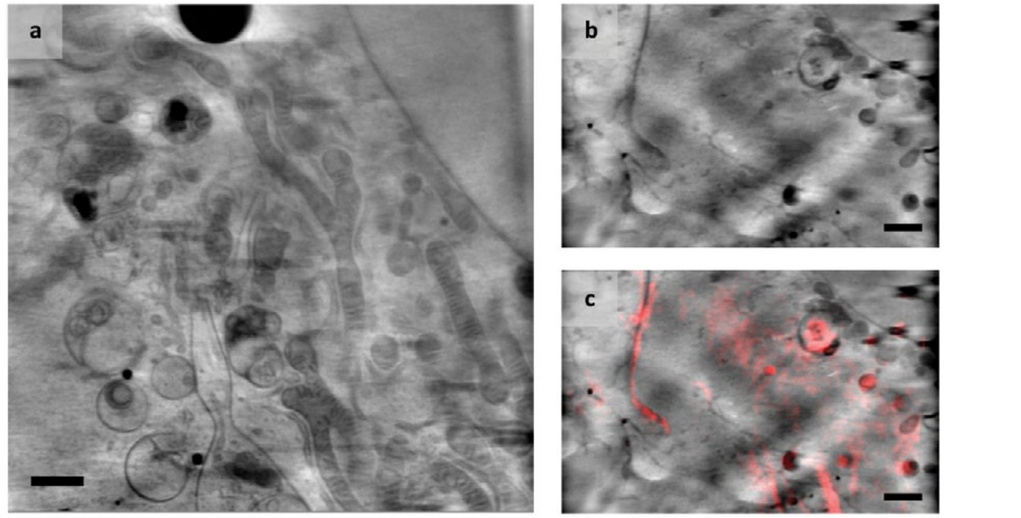

Figure 2: (a) A 2D slice from a 3D tomogram showing the perinuclear area inside a human fibroblast; Organelles visible include mitochondria, endosomes, multivesicular bodies lipid droplets and associated endoplasmic reticulum; (b) & (c); cytoplasmic area within the same cell population showing the information content of the naked SXT data (b) and the one enriched with SIM data (c); where a vesicle is clearly seen engulphed by filamentous actin (top right) and the cell-to-cell contact of neighbouring cells delineated as an edge-defining line on the upper left side of both panels.

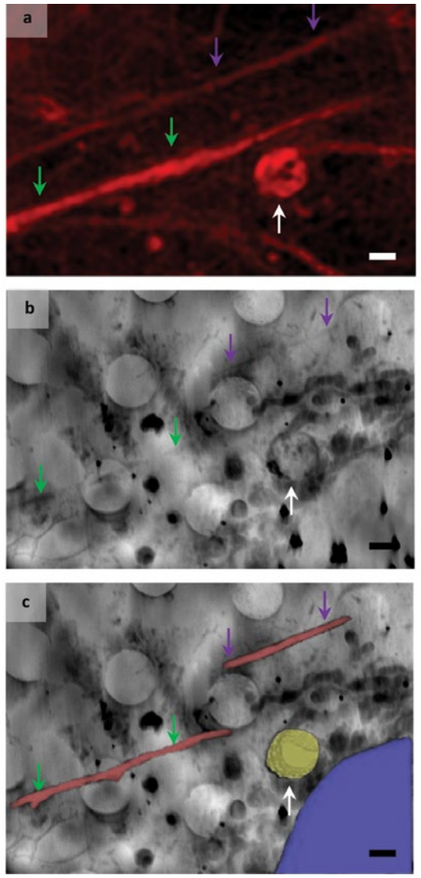

Figure 3: (a) SIM data showing actin organisation; (b) the corresponding area captured through SXT and (c) the overlay of segmented fluorescence actin signal in the context of the SXT data.

such as vesicle budding and transport, cell-to-cell contact, organelle network and substructure support as well as nuclear localisation and gene regulation[4].

Using correlated imaging they observed filamentous actin deployed in the fringes of the cell cytoplasm where contact with neighbours required the traditional actin networks that give rise to filopodia (Fig. 2c). However, its role is clearly more diverse as they examined the perinuclear area where they were able to clearly document filamentous actin-dependent vesicle transport (Fig. 3) through extensive networks of filamentous actin that connect and support organelles such as mitochondria and endosomes. It was also present within multivesicular bodies, but further work will need to be done to fully characterise this specific actin tropism, be it an incident of biological recycling or an active form of remodelling for purposes yet undisclosed.

The work presented here demonstrated the importance of technology development in the field of correlative biological cryo-imaging and has provided a proven imaging platform for the study of the cytoskeleton inside fully hydrated cells at near-physiological states.

References:

1. Okolo, C. A. A guide into the world of high-resolution 3D imaging: the case of soft X-ray tomography for the life sciences. *Biochemical Society Transactions* **50**, 649–663 (2022). DOI: 10.1042/BST20210886
2. Harkiolaki, M. *et al.* Cryo-soft X-ray tomography: using soft X-rays to explore the ultrastructure of whole cells. *Emerging Topics in Life Sciences* **2**, 81–92 (2018). DOI: 10.1042/ETLS20170086
3. Kounatidis, I. *et al.* 3D Correlative cryo-structured illumination fluorescence and soft X-ray microscopy elucidates reovirus intracellular release pathway. *Cell* **182**, 515-530.e17 (2020). DOI: 10.1016/j.cell.2020.05.051
4. Dominguez, R. *et al.* Actin structure and function. *Annual Review of Biophysics* **40**, 169–186 (2011). DOI: 10.1146/annurev-biophys-042910-155359

Corresponding author:
Maria Harkiolaki, Diamond Light Source, maria.harkiolaki@diamond.ac.uk

Understanding molecular scissors to prevent cancer cells multiplying

Related publication: Yu, J., Raia, P., Ghent, C. M., Raisch, T., Sadian, Y., Cavadini, S., Sabale, P. M., Barford, D., Raunser, S., Morgan, D. O., & Boland, A. Structural basis of human separase regulation by securin and CDK1–cyclin B1. *Nature* **596**, 138–142 (2021). DOI: 10.1038/s41586-021-03764-0

Publication keywords: Cell cycle regulation; Cohesin; Aneuploidy; Oncogene; Mitosis; Caspase

New cells form through cell division (mitosis), with two genetically identical daughter cells created from a single mother cell. Aberrant cell division can transform normal growing cells into cancer cells.

Before mitosis, the chromosomes inside the cell are duplicated. The resulting sister chromatids (identical chromosomes) are glued together through a ring-like structure named cohesin. Dissolution of the cohesin complex during cell division allows equal distribution of the sister chromatids into two daughter cells, a process called chromosome segregation.

A protein named separase acts as 'molecular scissors' and mediates the cleavage of the cohesin ring. Separase activity is tightly regulated by binding partners that inhibit cleavage activity and ensure a faithful and timely separation. As separase is often hyperactive in cancer cells, understanding the molecular mechanisms of separase regulation at an atomic level will inform future drug design to target separase activity in certain cancer types.

Researchers used Cryo-EM at the electron Bio-Imaging Centre (eBIC) to determine structures of human separase with its inhibitory binding partners - securin or the CDK1-cyclin B1-CKS1 (CCC) complex. Although the molecular mechanisms of separase inhibition are fundamentally different, both inhibitors prevent cleavage activity of the molecular scissors by occluding binding of the cohesin subunit SCC1.

The team has identified multiple binding motifs present in the substrate and inhibitor that are crucial for binding to separase. These motifs mediate binding to specific separase sites and finding new drugs to block these sites could prevent premature chromosome separation, often observed in cancer cells.

Arguably, the most fundamental task in the life of a eukaryotic cell is the ordered progression through cell division, in which one parental cell divides into two daughter cells. This process is known as mitosis. In the metaphase of mitosis sister chromatids align at the equator of the mitotic spindle before being segregated in anaphase. The transition from metaphase to anaphase is initiated by the dissolution of sister chromatid cohesion through cleavage of the cohesin complex component SCC1. Untimely and erroneous chromosome segregation leads to genomic instability and causes aneuploidy and tumorigenesis.

Separase is the protease responsible for cleavage of the cohesin ring[1]. Human separase is regulated through binding to three different inhibitors[2]. Securin, the first inhibitor identified, is conserved in all eukaryotic cells. In contrast, the CDK1-cyclin B1-CKS1 (CCC) complex seems to be vertebrate specific and interestingly, binding of the CCC complex leads to a complex in which both the kinase activity of CDK1 and the protease activity of separase are inhibited. The third inhibitory complex contains shugoshin 2-MAD2 and has only recently been identified.

While the structures of yeast[3] and worm separase[4] in complex with securin were solved in 2007, structural information on human separase remained enigmatic. By using cryogenic Electron Microscopy, the structures of the human separase-securin and separase-CDK1 cyclin B1-CKS1 complexes were determined to high resolution[5], with the use of the infrastructure at the Diamond Light Source and the Max Planck Institute of Molecular Physiology.

The structures provided insights into the regulation of separase activity by

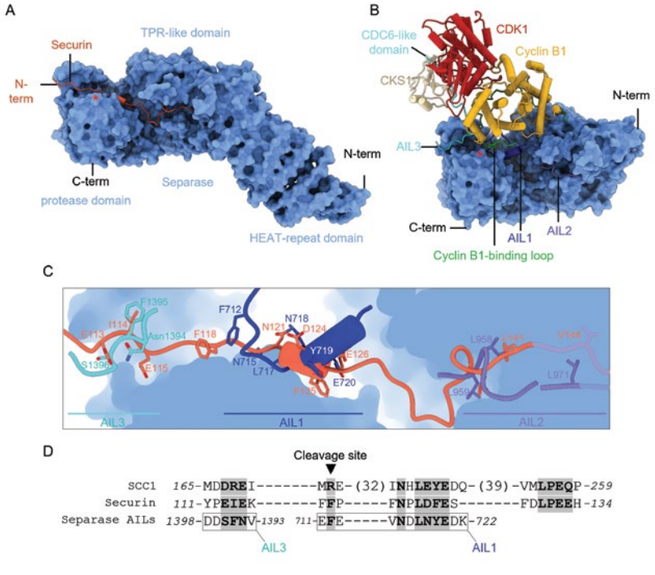

Figure 1: Cryo-EM structures of human separase complexes bound to securin or CDK1-cyclin B1-CKS1 (CCC); (a) Separase is depicted in a surface representation in blue, with domains being indicated; Securin is shown in orange; (b) CDK1 (red), cyclin B1 (yellow) and CKS1 (pale yellow) are shown as ribbon representation. The autoinhibitory loops (AILs) of separase are shown in blue (AIL1), purple (AIL2) and cyan (AIL3). The cyclin B1-binding loop containing serine 1126 is shown in green. Of note, the separase N-terminal domain is flexible and excluded in this figure; (c) Overlay of separase AILs with securin which highlights similar binding modes to separase; (d) Multiple sequence alignment between separase, securin and SCC1 reveals common separase binding motifs.

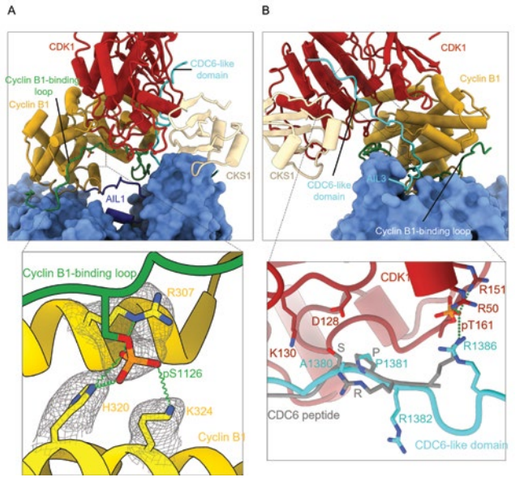

Figure 2: CDK1-cyclin B1-CKS1 (CCC) interactions with separase. Colour scheme as in Fig. 1 (a) The CCC complex binds in an interdomain cleft between the protease domain and the TPR-like domain (top). Close-up view of the phosphorylated serine 1126 (pS1126) and it's recognition by residues lining the phosphate-binding pocket of B-type cyclins; (b) Inhibition of CDK1 by the CDC6-like domain of separase (top); Close-up view of the CDC6-like domain inserted into the active site. The structure of CDK1 bound to a CDC6 peptide was superimposed onto the separase-CCC structure, revealing a similar binding mode of the CDC6-like domain (separase) to the CDC6 peptide. Importantly, the phospho-acceptor serine is replaced with an alanine (SepA1380) rationalising the inhibitory function of separase towards CDK1.

these two inhibitory partners. While both complexes abolish substrate cleavage through blocking multiple SCC1-binding sites, the molecular mechanisms underlying substrate-occlusion are fundamentally different. These novel insights into substrate- and inhibitor-binding to separase will guide future structure-based drug design studies.

During cell division the DNA content of a cell, the chromosomes, are duplicated so that each emerging daughter cell receives an identical set of sister chromatids. After duplication the sister chromatids are physically joined together through the ring-shaped cohesin complex. Subsequently, the duplicated and joint chromosomes align at the cell equator and attach to the mitotic spindle. In a final step, sister chromatid segregation and subsequent migration towards the opposite poles of the dividing cell occurs. This process needs to be tightly regulated as aberrant chromosome segregation causes aneuploidy and genomic instability, characteristics of most malignant tumour cells.

Timely separation of sister chromatids is initialised through cleavage of the cohesin subunit SCC1 by the cellular protease separase. Human separase is a large enzyme with a molecular weight of roughly 233 kDa. It consists of an N-terminal HEAT-repeat domain, a central TPR-like domain and a highly conserved C-terminal protease domain. Cleavage activity of separase is tightly regulated by different inhibitors in mammalian cells. Recent structural studies showed that securin binds to all three domains of separase and inserts itself into the active site of the protease domain using pseudosubstrate sequence, to serve as a non-cleavable substrate. Human separase is also inhibited by the heterotrimeric complex of cyclin-dependent kinase 1 (CDK1), cyclin B1 or cyclin B2, and the regulatory subunit CKS1 (CCC complex). Interestingly, binding of the CCC complex to separase was shown to be dependent on the phosphorylation of a specific serine residue in separase and results in an inactive kinase-protease complex with both enzymes inhibited. In addition, the observed pseudosubstrate sequences present in securin are absent in the CCC complex, which prompted the question how separase inhibition is mediated by this inhibitory complex.

To elucidate the molecular mechanisms of separase inhibition by securin and the CCC complex the authors used cryogenic Electron Microscopy and determined the structures of human separase bound to either securin or the CCC complex[5] (Fig. 1). The structure of separase bound to securin confirmed previous studies in which securin binds in an antiparallel extended orientation to all three domains of separase to occupy multiple binding sites and sterically block substrate recognition (Fig. 1a). The structure of the separase-CCC complex however revealed novel and fascinating aspects of separase regulation. Binding of the CCC complex to the periphery of the protease domain repositions and rigidifies several intrinsically disordered regions in separase itself. As a consequence, these loop regions now occupy binding sites used by securin or the substrate SCC1 to bind to separase and thereby occlude substrate binding. The authors therefore termed these loop segments Autoinhibitory Loops or AILs (Fig. 1b,c). A multiple sequence alignment between the inhibitor securin, the substrate SCC1, and the enzyme separase revealed that the sequence motifs present in these AILs can also be found in SCC1 and securin (Fig. 1d). In other words, these separase binding motifs have evolved multiple times and independently in evolution to occupy similar binding sites in separase.

As aforementioned, complex formation between the CCC complex and separase depends on the phosphorylation of a specific serine residue (SepS1126) in separase. This phosphoserine is recognised by a newly identified phospho-binding pocket present in B-type cyclins (Fig. 2a). The authors propose that this binding pocket represents a novel specificity site that recognises and regulates many other cell cycle proteins.

Finally, the structure of the separase-CCC complex also revealed the mutually inhibitory nature of this complex. While separase activity is abolished through autoinhibitory loop elements, a CDC6-like sequence motifs upstream of the inhibitory motif in AIL3 directly inserts into the active site of CDK1. However, the phospho-acceptor serine is replaced in this CDC6-like sequence by an alanine which prevents phosphorylation of this peptide sequence and thus subsequent dissociation (Fig. 2b). This binding results in a mutual inhibitory complex and converts the protease separase into a regulatory CDK1-inhibitor.

This work highlights the multiple and important roles of separase in cell cycle progression and illustrates the power of cryo-EM to visualise regulatory, intrinsically disordered regions that provide crucial insights into the function of enzyme regulation.

References:

1. Ciosk, R. *et al.* An ESP1/PDS1 complex regulates loss of sister chromatid cohesion at the metaphase to anaphase transition in yeast. *Cell* **93**, 1067–1076 (1998). DOI: 10.1016/S0092-8674(00)81211-8
2. Hauf, S. Two giants of cell division in an oppressive embrace. *Nature* **596**, 41–42 (2021). DOI : 10.1038/d41586-021-01944-6
3. Luo, S. *et al.* Molecular mechanism for the regulation of yeast separase by securin. *Nature* **542**, 255–259 (2017). DOI: 10.1038/nature21061
4. Boland, A. *et al.* Cryo-EM structure of a metazoan separase–securin complex at near-atomic resolution. *Nature Structural & Molecular Biology* **24**, 414–418 (2017). DOI: 10.1038/nsmb.3386
5. Yu, J. *et al.* Structural basis of human separase regulation by securin and CDK1–cyclin B1. *Nature* **596**, 138–142 (2021). DOI: 10.1038/s41586-021-03764-0

Funding acknowledgement:
This work was supported by the Swiss National Science Foundation (310030_185235) to A.B., the U.S. National Institute of General Medical Sciences (R35-GM118053) to D.O.M, and MRC (MC_UP_1201/6) to D.B.

Corresponding author:
Dr. Jun Yu, University of Geneva, Jun.Yu@unige.ch
Dr. Pierre Raia, University of Geneva, Pierre.Raia@unige.ch

Understanding how bacteria attack each other may help to develop new drugs

Related publication: Ghilarov, D., Inaba-Inoue, S., Stepien, P., Qu, F., Michalczyk, E., Pakosz, Z., Nomura, N., Ogasawara, S., Walker, G. C., Rebuffat, S., Iwata, S., Heddle, J. G., & Beis, K. Molecular mechanism of SbmA, a promiscuous transporter exploited by antimicrobial peptides. *Science Advances* **7,** (2021). DOI: 10.1126/sciadv.abj5363

Publication keywords: Antibacterial peptide; SLiPT transporter; ABC transporter; Glutamate ladder; Proton driven transporter

Bacterial species compete for access to nutrients. Many use biological weapons that target and kill closely related species. These antibacterial compounds include antibacterial peptides such as microcins which do not damage the membrane integrity (essential for bacterial survival) but inhibit specific proteins. Previous investigations have shown that while these peptides are structurally diverse, they use the same transporter (SbmA/BacA) to enter the cell. Researchers wanted to understand this process by determining its structure and molecular mechanism.

Their aim was to gain insights into the molecular mechanism bacteria use to hijack the SbmA/BacA transporter. This information could then be used to develop novel therapies that can use the same uptake process.

The team used Cryo Electron Microscopy at the electron Bio-Imaging Centre (eBIC) at Diamond Light Source to determine the structure of the transporterin a lipid-like environment that mimics the native environment of the transporter.

Determining the structure has allowed the team to identify a new family of transporters, which they have called SbmA-like peptide transporters (SLiPTs). Interestingly, the structures show similarities with another family of transporters that are usually involved in multidrug resistance, but the role of SLiPTs is to internalise multiple substrates. The scientists believe there is an evolutionary link between the two families that could allow us to understand how resistance evolved.

Microcins are small antibacterial peptides (<10 kDa) produced by enteric bacteria and target closely related species. Many microcins are known to be ribosomally-synthesised post-translationally modified peptides (RiPPs), which are produced as linear precursors and require post-translational modification in order to become biologically active (Fig. 1). Since these peptides do not damage the membrane, but instead have intracellular targets (*e.g.* DNA gyrase or RNA polymerase), they must penetrate the outer and inner membrane for internalisation. MccB17 crosses the outer membrane via the porin OmpF, whereas MccJ25 uses the ferrichrome receptor FhuA[1]. However, when it comes to crossing the inner membrane, despite their structural differences, most microcins utilise a common transporter, SbmA. The *E. coli* SbmA (EcSbmA) was identified as essential for sensitivity to thiazole-modified RiPP antibiotic MccB17 and subsequently was confirmed as the most important determinant of sensitivity to several structurally unrelated NPs from Gram-negative bacteria, including the lasso peptide MccJ25, the azole-modified peptide klebsazolicin (KLB) and the NRP-polyketide azole-containing antibiotic bleomycin (Fig. 1). While the exact natural function of EcSbmA is not established, it is a virulence factor in an avian pathogenic *E. coli* (APEC), while its *Brucella abortus* ortholog has been shown to be required for chronic intracellular infection in a mouse model. Interestingly, the *E. coli* SbmA is isofunctional with its homolog BacA from *Sinorhizobium meliloti* that is indispensable for the nitrogen-fixing symbiosis with the legume host; BacA enables the chronic intracellular infection of root nodule cells, by transporting nodule-specific defensin-like cysteine-rich peptides.

To establish the molecular mechanism of peptide transport and substrate promiscuity of EcSbmA/SmBacA, the authors determined the cryo–Electron Microscopy (cryo-EM) structure of both SbmA and BacA proteins in a lipid bilayer mimetic environment, using proteins reconstituted in nanodiscs (NDs), at 3.2 and 6 Å local resolution, respectively[2]. SbmA is a homodimer consisting of eight Transmembrane (TM) helices per protomer. SbmA consists of two TM0 domains and a core TM domain (TMD), which comprises 12 TM helices (Fig. 1). The overall structure of TMD notably resembles the TMD of ABC transporters (exporters), such as MsbA (lipid A flippase) from *E. coli*, Sav1866 (multidrug resistance) from *Staphylococcus aureus*, and Rv1819c (cobalamin transporter) from *M. tuberculosis*. Despite these similarities, the structural organisation of SbmA has not been observed in secondary transporters before. Therefore, SbmA defines a new fold for secondary transporters, named SbmA-like peptide transporter (SLiPT) fold. The SbmA dimer interface is formed between TMs 1 and 2 and 5 and 6 from one protomer and the equivalent ones from the second; TMs 1 and 2 form intermolecular contacts with TMs 5 and 6, and TMs 5 and 6 form intermolecular contacts with TMs 1 and 2. The TM0 domain of SbmA is a novel feature of SLiPT transporters, which is not present in any other known transporter structure. SbmA is trapped in an outward-open conformation ready to bind antibacterial peptides for internalisation.

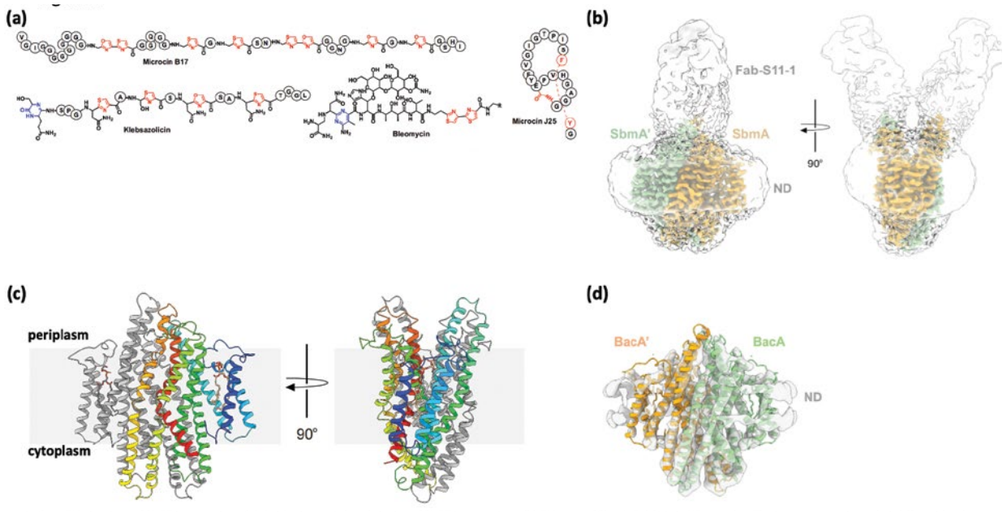

Figure 1: Cryo-EM structure of SLiPT transporters; (a) Antibiotic peptide substrates of SLiPT transporters; (b) EM map of SbmA-FabS11-1-ND complex. The two maps contoured at different levels are overlaid to represent both high-resolution (SbmA) and low-resolution (ND) parts; (c) Cartoon representation of the SbmA structure. SbmA is a homodimer consisting of two TM0 domains and a core TM domain; (d) The low-resolution EM map of BacA-ND shows fold conservation in the SLiPT transporter family; the SbmA structure has been fitted within the volume.

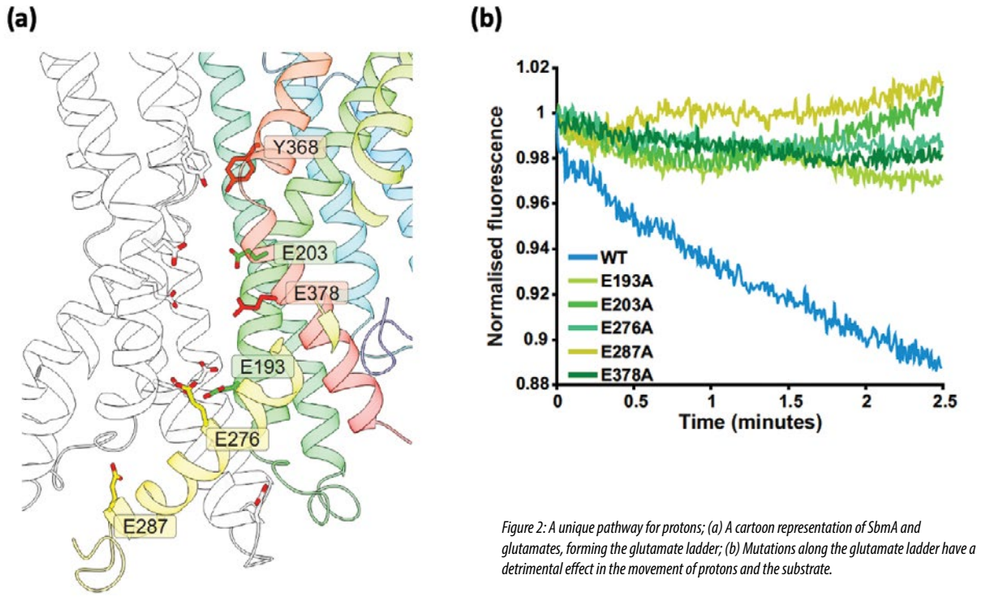

Figure 2: A unique pathway for protons; (a) A cartoon representation of SbmA and glutamates, forming the glutamate ladder; (b) Mutations along the glutamate ladder have a detrimental effect in the movement of protons and the substrate.

Considering the important biological role of BacA in symbiosis, and especially that EcSbmA is isofunctional with the SmBacA, its structure was also determined. The BacA reconstruction displays the same overall fold as SbmA; the SbmA structure can fit in the BacA map without any structural changes, suggesting that BacA also adopts a very similar fold (Fig. 1).

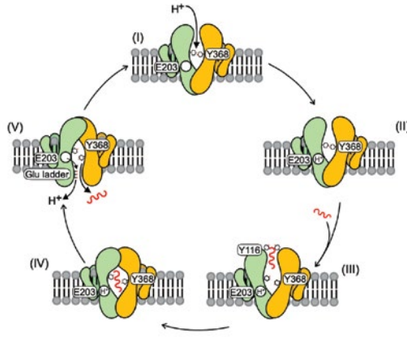

Figure 3: Molecular mechanism of SLiPT transporters.

To probe the mechanism of proton translocation, SbmA and BacA were reconstituted in liposomes; transport could only be initiated in the presence of both a proton gradient (induced by valinomycin) and the substrates bleomycin or MccB17. The SbmA cavity is lined with conserved Glu residues, forming a "glutamate ladder," suggesting a relay path for proton movement (Fig. 2). To probe their role in coordinating proton translocation, the glutamates were mutated to alanines and measured their substrate transport activity. All Glu-to-Ala mutations essentially abolished substrate transport.

In light of the structural and functional data, a mechanism for antibacterial peptide import by the SLiPT transporters SbmA and BacA has been proposed; in brief, SbmA adopts an outward-open conformation with its cavity accessible to both peptide and proton. Binding of a proton in Glu203, with subsequent movement along the glutamate ladder, and simultaneous peptide binding in the open cavity induce either a transient or a stable occluded state (Fig. 3). An inward-facing open conformation can be formed by movement of TMs 4 and 5 away from TMs 4 and 5. All fully resistant mutants are found along TM5, suggesting its important role in substrate translocation associated with conformational changes along the transport cycle. In the inward-open conformation, the antibacterial peptide and proton are released in the cytoplasm, and the transporter resets in the outward-open conformation.

References:

1. Mathavan, I. et al. Structural basis for hijacking siderophore receptors by antimicrobial lasso peptides. *Nature Chemical Biology* **10**, 340342 (2014). DOI: 10.1038/nchembio.1499
2. Ghilarov, D. *et al.* Molecular mechanism of SbmA, a promiscuous transporter exploited by antimicrobial peptides. *Science Advances* **7,** (2021). DOI: 10.1126/sciadv.abj5363

Funding acknowledgement:
Biotechnology and Biological Sciences Research Council grant BB/H01778X/1 (KB), Team program of the Foundation for Polish Science co-financed by the European Union under the European Regional Development Fund TEAM/2016-3/23 (JGH, PS), National Science Centre (NCN, Poland) grant no. 2016/21/B/CC1/00274 (OPUS 11) (ZP, DG and JGH) and 2019/35/D/NZ1/01770 (SONATA 15) (ZP, EM and DG), Chinese Scholarship Council Scheme (FQ)

Corresponding author:
Konstantinos Beis, Imperial College London, kbeis@imperial.ac.uk

Understanding the mechanism of axon degeneration

Related publication: Figley, M. D., Gu, W., Nanson, J. D., Shi, Y., Sasaki, Y., Cunnea, K., Malde, A. K., Jia, X., Luo, Z., Saikot, F. K., Mosaiab, T., Masic, V., Holt, S., Hartley-Tassell, L., McGuinness, H. Y., Manik, M. K., Bosanac, T., Landsberg, M. J., Kerry, P. S., Mobli, M., Hughes, R.O., Milbrandt, J., Kobe, B., DiAntonio, A., Ve, T. SARM1 is a metabolic sensor activated by an increased NMN/NAD+ ratio to trigger axon degeneration. *Neuron* **109**, 1118-1136.e11 (2021). DOI: 10.1016/j.neuron.2021.02.009

Publication keywords: ARM domain; NADase; TIR domain; X-ray crystallography; Allostery; Cryo-EM

SARM1 (sterile alpha and TIR motif 1) is a key player in nerve fibre (axon) degeneration and a promising new therapeutic target for prevalent neurological diseases, including peripheral neuropathies and traumatic brain injury. In healthy nerve cells, SARM1 is present but inactive. Disease and injury activate SARM1, which results in rapid breakdown of the essential 'helper molecule' nicotinamide adenine dinucleotide (NAD^+) and ultimately destruction of the axon. Defining the molecular mechanisms upstream and downstream of SARM1 enzyme activity can yield inhibitors as leads to anti-neurodegenerative disease therapeutics.

To understand the auto-inhibition and activation mechanisms of SARM1 at the molecular level, researchers needed to determine the structure of SARM1 in inactive and active states.

Using data collected at the electron Bio-Imaging Centre (eBIC for Industry), the Midlands Regional Cryo-EM Facility at the University of Leicester, and the Centre for Microscopy and Microanalysis at the University of Queensland, they determined a ~3.1 Angstrom resolution Cryo-Electron Microscopy (Cryo-EM) structure of human SARM1 in the inactive state. Using X-ray crystallography, they also determined a structure of the regulatory domain of *Drosophila* SARM1 in complex with an allosteric activator. Together these structures explain how this protein maintains an inhibited (off) state and the critical steps required for its activation. These results allowed them to propose a molecular mechanism for SARM1 activation. They also provide a molecular framework for the design of novel drugs targeting a wide range of neurodegenerative diseases.

When the normal functions of nerve fibres (axons) are compromised by insults such as trauma, transport blockade, or chemical toxicity, distinct morphological and molecular changes known as Wallerian degeneration result in cytoskeletal disassembly and granular degeneration of the axon distal to the injury site. Axon loss is a common theme shared by several neurodegenerative diseases, including neuropathies, traumatic brain injury, and glaucoma, but no treatments currently exist that effectively target axonal breakdown. The protein SARM1 is a central player in axon loss[1,2]. In healthy nerve cells, SARM1 is present but inactive. Disease and injury activate SARM1, which results in rapid breakdown of the essential 'helper molecule' nicotinamide adenine dinucleotide (NAD^+) and ultimately destruction of the axon[3-4]. Genetic knockout of SARM1 has previously been shown to prevent axon loss in models of neurological disease, including peripheral neuropathies and traumatic brain injury, whereas hyperactive SARM1 variants have recently been shown to be enriched in patients with amyotrophic lateral sclerosis. Agents that block SARM1 function could therefore be exciting therapeutic candidates for a variety of neurological conditions[5].

SARM1 consists of an N-terminal regulatory armadillo repeat (ARM) domain, two tandem sterile alpha motif (SAM) domains, and a C-terminal Toll/interleukin-1 receptor (TIR) domain with self-association-dependent NAD^+ glycohydrolase (NADase) activity. In healthy and intact axons, SARM1 activation is restrained by NMNAT2 (nicotinamide mononucleotide adenylyltransferase 2), which is an axonal enzyme that synthesises NAD^+ using NMN (nicotinamide mononucleotide) and ATP as substrates. NMNAT2 is a labile protein and is rapidly degraded after axon injury, which leads to a rise in the axonal levels of NMN. Loss of NMNAT2 causes axon fragmentation that is dependent on SARM1, suggesting that the increase in axonal NMN levels caused by the absence of NMNAT2 can activate SARM1.

In the publication, the authors first show, using a combination of cellular, biochemical and biophysical assays, that both the NADase and axon degeneration functions of SARM1 are activated by an increase in the ratio of NMN to NAD^+ and that these two metabolites directly compete for binding to SARM1's ARM domain. Next, to provide structural insight into this activation mechanism, they

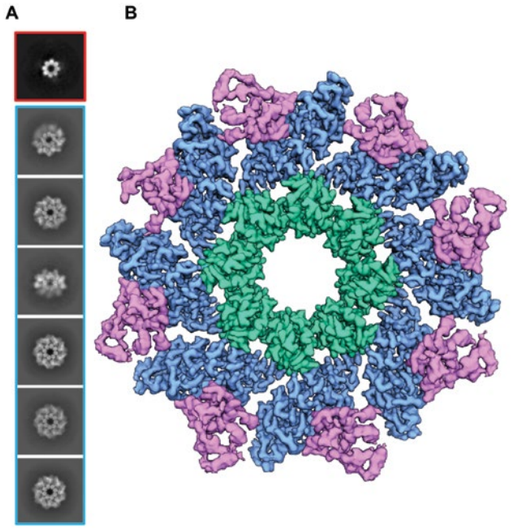

Figure 1: Overall structure of ligand-free hSARM1. (a). Representative 2D class averages of "SAM domain only" particles from initial data and "intact" particles obtained using a continuous carbon film are highlighted by red and blue boxes, respectively; (b). An electrostatic potential density map of ligand-free hSARM1 (EMD-23278); Map regions corresponding to the ARM, SAM, and TIR domains are displayed in blue, green, and pink, respectively.

determined the cryo-EM structure of human SARM1 (hSARM1) in ligand-free inactive state, and the crystal structure of the ARM domain of *Drosophila* SARM1 (dSARM1) in complex with the allosteric activator NMN.

Cryo-EM data was collected at eBIC, the Midlands Regional Cryo-EM Facility at the University of Leicester, and Centre for Microscopy and Microanalysis at the University of Queensland. From the initial EM data collected at eBIC, only features corresponding to SAM domain rings were visible in the 2D classes, suggesting that the SARM1 particles are not very stable, leading to disordered

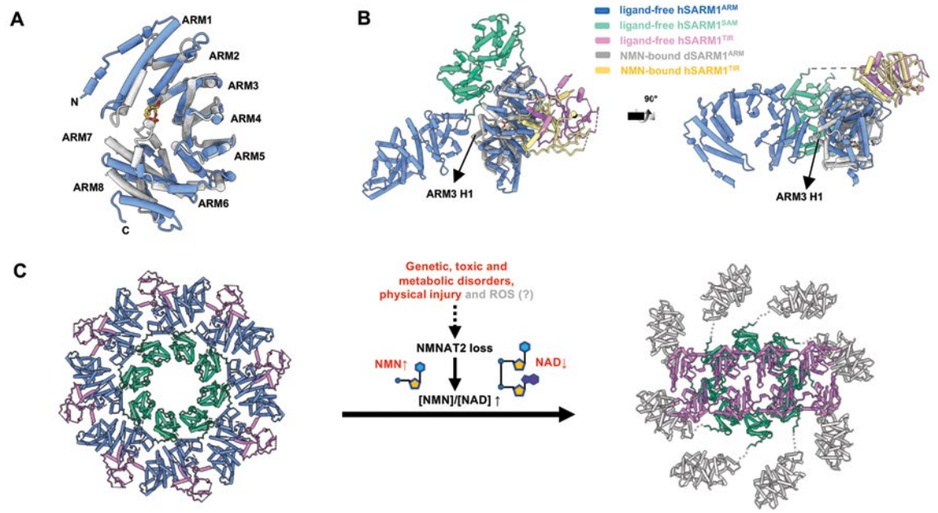

Figure 2: Model of SARM1 activation upon NMN binding; (a). Structural superposition of NMN-bound dSARM1 ARM (grey; residues 370-676) and ligand-free hSARM1ARM (blue; residues 62-400); (b). Structural superposition of ARM8 in NMN-bound dSARM1 ARM (grey) and ligand-free hSARM1ARM (blue) suggests that the ARM domain would rotate and potentially clash with the ARM domain of adjacent subunits (blue) upon NMN binding; (c). Schematic model of SARM1 activation.

ARM and TIR domains after freezing. By using grids that had been prepared with a 6 nm continuous carbon film, the quality of the sample significantly improved; intact SARM1 particles with features corresponding to the ARM and TIR domains were clearly visible in the 2D classes (Fig. 1(a), and a 3D density map with an overall resolution of 3.1 Å was obtained, which allowed modelling of the entire octameric complex (Fig. 1(b)).

The structure reveals a ring-shaped octameric protein complex (Fig. 1B). The tandem SAM domains self-associate head-to-tail to form the central inner ring. The SAM ring is surrounded by the ARM domains, each containing 8 ARM repeat motifs (ARM 1-8). The ARM domains have an open conformation in the absence of the activator NMN. This conformation is responsible of the inactive nature of the ligand-free SARM1 and is altered upon NMN binding. The TIR domains are wedged between the ARM domains on the outer periphery for the ring (Fig. 1B). The NADase activity of the TIR domains depends on their self-association, but the ARM-TIR interaction prevents such self-association.

To further elucidate the mechanism of NMN-dependant activation of SARM1, the crystal structure of NMN-bound *Drosophila* SARM1 ARM domain was determined. The ligand-free and NMN-bound ARM domain structures of the human and *Drosophila* proteins show conformational differences, with an RSMD of 2.56 Å over 292 Cα atoms. The NMN-bound structure shows the N-terminal ARM repeats 1-2 (ARM1-2), and the C-terminal ARM6-8 collapsing inwards around the ligand-binding site, resulting in a more compact conformation (Fig. 2(a)). There is no major change in the region spanning ARM3-5, which also comprises the TIR domain interface, indicating that NMN-related conformational changes do not directly affect ARM:TIR binding. Given that ARM8 is tethered to the octameric SAM ring and likely exhibits limited movement, the conformational changes upon NMN binding would translate to rotation of the ARM domain relative to the SAM octameric ring. Superimposition of ARM8 from the NMN-bound structure on the ligand-free structure shows significant movement of ARM3 towards the adjacent ARM domain, potentially leading to steric clash (Fig. 2(b)). 2D class averages of the hSARM1 octamer showing partial ARM domain rings indicate this steric clash may be responsible for disrupting the ARM:SAM interface and abolishing the ARM:TIR interaction (Fig. 1(a)).

Based on the structural analyses, the authors propose a model for SARM1 activation (Fig. 2(c)). In the ligand-free state, SARM1 is kept inactive simply by keeping the TIR domains spatially separated. Binding of the allosteric activator NMN results in collapse and rotation of the ARM domains, resulting in destabilisation of the ARM domain ring and release of the TIR domains. The TIR domains are then able to self-associate to form catalytic sites capable of cleaving NAD^+, which ultimately leads to destruction of the axon.

In conclusion, the new understanding of the molecular basis of SARM1 regulation and the identification of the allosteric NMN-binding site provide a foundation for development of therapeutics for a wide range of human neurodegenerative diseases.

References:

1. Gerdts, J. *et al.* Sarm1-mediated axon degeneration requires both SAM and TIR interactions. *Journal of Neuroscience* **33**, 13569–13580 (2013). DOI: 10.1523/JNEUROSCI.1197-13.2013
2. Osterloh, J. M. *et al.* dSarm/Sarm1 is required for activation of an injury-induced axon death pathway. *Science* **337**, 481–484 (2012). DOI: 10.1126/science.1223899
3. Essuman, K. *et al.* The SARM1 Toll/Interleukin-1 receptor domain possesses intrinsic NAD + cleavage activity that promotes pathological axonal degeneration. *Neuron* **93**, 1334-1343.e5 (2017). DOI: 10.1016/j.neuron.2017.02.022
4. Horsefield, S. *et al.* NAD^+ cleavage activity by animal and plant TIR domains in cell death pathways. *Science* **365**, 793–799 (2019). DOI: 10.1126/science.aax1911
5. Krauss, R. *et al.* Axons matter: the promise of treating neurodegenerative disorders by targeting SARM1-mediated axonal degeneration. *Trends in Pharmacological Sciences* **41**, 281–293 (2020). DOI: 10.1016/j.tips.2020.01.006

Funding acknowledgement:

The work was supported by the National Health and Medical Research Council (NHMRC grants 1107804 and 1160570 to B.K. and T.V., 1071659 to B.K., and 1108859 to T.V.), the Australian Research Council (ARC) Laureate Fellowship (FL180100109 to B.K.) and Disarm Therapeutics. T.V. received ARC DECRA (DE170100783) funding.

Corresponding author:

Prof Bostjan Kobe, University of Queensland, b.kobe@uq.edu.au
Dr Thomas Ve, Griffith University, t.ve@uq.edu.au

Structures and Surfaces Group

Chris Nicklin, Science Group Leader

The Structures and Surfaces Group includes four beamlines, each consisting of multiple end-stations that are optimised for a specific type of experiment: I05 (Angle Resolved Photoelectron Spectroscopy – ARPES), I07 (Surface and Interface X-ray Diffraction), B07 (Versatile Soft X-ray Scattering – VERSOX), and I09 (Atomic and Electronic Structure of Surfaces and Interfaces). They offer a variety of techniques to examine the atomic scale structure, chemical nature and electronic state at buried interfaces or the surfaces of materials. This year, the group has started to welcome users back for their experiments in-person, building on the strong partnerships that have developed during remote working restrictions. The group continue to benefit from many of the developments that have been realised during this period (for example enhanced automation) but recognise that many of the more complex studies rely on the expertise of the user groups, especially for sample preparation and experiment planning. It has also been a busy year for beamline upgrades (as detailed below) whilst also taking a strategic view for the future, with a focus on outlining the facilities that we plan to offer as part of the Diamond-II programme. The important role that surfaces and interfaces play in broader research areas such as battery technology, photovoltaic structures, and catalytic/electrochemical systems under *operando* conditions are key drivers for these developments.

On beamline I05, the new electron energy analyser is now installed and in routine operation, offering exceptional quality data in terms of energy resolution. The future implementation of the 'deflector mode' will enable angle resolved measurements to be recorded without having to physically move the sample and will therefore increase the speed of data acquisition and maintain the photon beam in a consistent position on the sample. The NanoARPES branch-line continues to benefit from improved flux and reduced spot size through the incorporation of a capillary mirror, with a beam of four micrometres now achievable. Excellent data quality is achieved through the ability to focus the beam onto high quality areas of the sample, which in many newly produced crystals may only be a few micrometres in size. Understanding how sample heterogeneity influences the electronic structure is now a very active focus of research on the beamline. The sample preparation and mounting facilities also continue to benefit the user programme, with the glove box and micromanipulation system enabling precise mounting and alignment of crystals that are air sensitive. The team on I05 is looking to develop a new manipulator design to integrate electrical contacts that will enable direct biasing of the sample or control of a piezoelectric device to apply mechanical strain to a crystal.

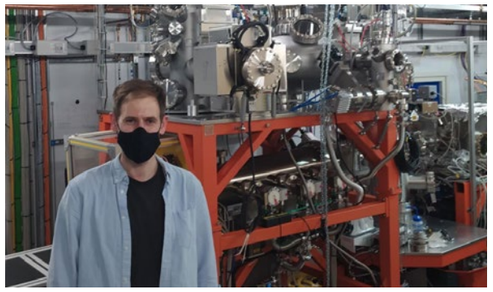

B07 Senior Beamline Scientist David Grinter with the high-throughput XPS end station.

The surface and interface diffraction facilities on beamline I07 continue to be upgraded to enhance the capabilities. Continuous scanning of the diffractometer is now implemented for single axis scans while automated fast attenuators are currently being built and installed. This will enable fast measurement of crystal truncation rods that cover many orders of magnitude changes in intensity. The next stage will be to develop trajectory scanning in reciprocal space to enable rapid acquisition of crystal truncation rods or data in arbitrary hkl directions. The Large Area Detector positioning system has been upgraded to extend the range of sample-detector distances that can be achieved, improving the implementation for grazing incidence small (wide) angle X-ray scattering (GIS(W)AXS) investigations. A new CdTe Eiger 4M detector has been purchased for these experiments, which will improve the angular resolution of the measurements and the operating efficiency at higher energies. The diffractometer upgrade has been further delayed due to lockdown restrictions, but the beamline team have commissioned the new hexapod to increase the reliability and speed of experiments. There is an ambitious plan to upgrade the optical layout of the beamline, switching from mirror focusing to making use of compound refractive lenses to provide additional tunability in the beam dimensions as well as a smaller ultimate spot size. A concurrent upgrade to the double crystal deflector (DCD) system would improve the ease of operation and improve data quality for diffraction studies from liquid surfaces. The I07 team is also moving forward with improving the software provision, in particular for visualisation of reciprocal space maps and reduction/extraction of data for crystal truncation rod analysis.

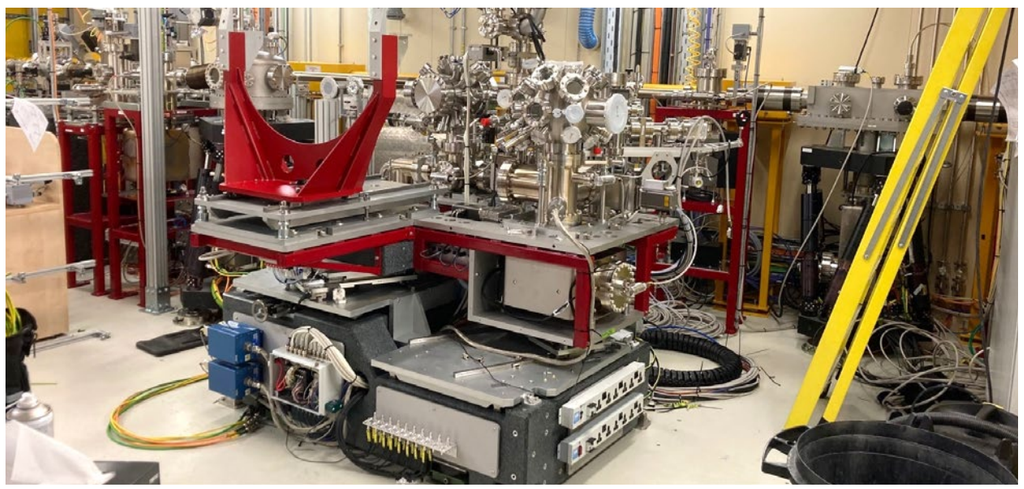

The I09 Soft X-ray ARPES end station awaiting installation of the momentum microscope electron energy analyser.

The recently installed glove box on beamline I05.

This year, the second branch (B07B) of the VERSOX beamline is scheduled to be fully open to users, with the second end-station for high-throughput X-ray photoelectron spectroscopy (XPS) studies, to enable chemical state analysis of many samples, having its first users in May 2022. The initial end-station for near edge X-ray absorption fine structure (NEXAFS) studies using soft X-rays to study processes such as molecular adsorption or catalysis has proven to be exceptionally productive. The near ambient pressure XPS (NAP-XPS) system available on Branch C of the beamline continues to work well and has been enhanced by the addition of a bespoke gas panel to enable automated exposure to pure and well controlled mixtures of gases. Full scripting of this facility through the data acquisition system enables complex studies to be semi-automated.

Beamline I09 continues to maintain a very active user programme whilst also developing new capabilities. The hard X-ray photoemission (HAXPES) system is commissioned and available for users. The end station for the soft X-ray ARPES system is now built and the momentum microscope was delivered in the early part of 2022. Integration is underway, with an extensive commissioning programme to be started in Summer 2022, that we expect to take several months due to this novel design. I09 is awaiting the delivery of a small spot ultraviolet photoelectron spectroscopy (UPS) system that will enable the commissioning to be developed whilst user experiments continue. The next stage of this project is to ensure that maintainable software is developed in collaboration with the detector manufacturer through an EPICS interface. Smaller scale hardware upgrades are also being developed, including a modified manipulator design that enables sample biasing, cooling and heating whilst still allowing sample transfer.

The group are aiming to enhance the associated infrastructure available for surface science research including the design of a new offline ultrahigh vacuum system to characterise samples, a proposal that was well received by the Scientific Advisory Committee (SAC). Design work has started as this system continues to be a high priority that will position Diamond to be able to rapidly study new samples and enhance the link between laboratory and synchrotron based experiments. We aim for this capability to be at the core of many of the joint PhD studentships that we support.

The group aim to develop its suite of instruments in a number of ways as part of the Diamond-II programme. A dedicated nanoARPES instrument to be built on a mid-straight section has been announced as one of the five flagship beamlines. An associated upgrade to I05 will ensure that the suite of ARPES facilities is optimised to deliver high energy resolution and high spatial resolution, including fast mapping capabilities. Beamline B07 is currently sourced by a bending magnet, but as part of the Diamond-II upgrade, branch C will be changed to an insertion device, increasing the flux and energy range available for the NAP-XPS experiments and opening up new science opportunities. We aim for I07 to be Diamond-II ready through the optics upgrade outlined above that will also enhance the beamline before the Diamond-II dark period. Beamline I09 requires some modest changes to its optics scheme due to a change in the source positions in the machine. We will take the opportunity to incorporate higher specification mirrors and other components that will improve the beam quality at the sample position.

The science undertaken within the group continues to be a range of underpinning fundamental surface science investigations through to using the techniques to understand the relevance to real-world applications. The user highlights include how I05 has been used to identify the spin-polarised surface states in the magnetic topological insulators $MnBi_4Te_7$ and $MnBi_6Te_{10}$ and to really in understand the interplay between the magnetic order and the topological state in the absence of magnetic dopants, opening up potential developments in the field of metrology. The report from Anthoula Papageorgiou, shows how beamline I09 has enabled X-ray Standing Wave measurements to reveal the detailed atomic structure of two similar Ru porphyrins and relate it to the catalytic activity relating to CO adsorption. Changes to the bonding height of the Ru atom caused by the CO binding are suggested as an important factor affecting the efficiency of the catalyst. Novel assembly methods for the creation of synthetic van der Waals heterostructures are the subject of the I07 highlight. The group of Prof. Feng used an on-water synthesis methods to create a 2d polymer-graphene structure where the detailed structure was investigated using GIWAXS. Beamline B07 has been used to understand key details of a catalyst used in hydrogenation/dehydrogenation reactions, by the group of Prof. Edman Tsang. They have identified the mechanism of hydrogen spillover through monitoring the ruthenium oxidation state in the catalyst and have been able to relate the pathway to oxidation of hydrogen to protons and an increase in the concentration of surface hydroxyl species.

The members of the Structures and Surfaces group are committed to continue offering the best support to our users, to ensure the highest quality scientific output from the beamlines. The combination of strong interactions and collaborations, together with continuous improvements to the instrumentation, software and technique development is key to our success. Please contact us if you would like to discuss any of the possibilities that we offer and how such synchrotron based studies could help in your research.

Investigating hydrogen spillover to improve hydrogenation catalysts

Related publication: Wu, S.; Tseng, K. Y.; Kato, R.; Wu, T. S.; Large, A.; Peng, Y. K.; Xiang, W.; Fang, H.; Mo, J.; Wilkinson, I.; Soo, Y. L.; Held, G.; Suenaga, K.; Li, T.; Chen, H. Y. T.; Tsang, S. C. E. Rapid interchangeable hydrogen, hydride, and proton species at the interface of transition metal atom on oxide surface. *Journal of the American Chemical Society* **143**, 9105–9112 (2021). DOI: 10.1021/jacs.1c02859

Publication keywords: Hydrogen spillover; Polar metal oxide; In situ characterization; Frustrated Lewis Pair

Hydrogen spillover is an atomic migration phenomenon on the catalyst surface that is crucial to the development of catalytic hydrogenation and dehydrogenation reactions at mild conditions. Typically, this takes place over a metal on the support structure where a dihydrogen molecule undergoes dissociative chemisorption to form hydrogen atoms on the metal active centre, followed by the migration of atomic hydrogen from the metal surface to the catalytic support. Despite researchers having spent tremendous efforts investigating the hydrogen spillover mechanism, there is so far no direct visualisation of this at an atomic level, and the interchangeable pathway between the various hydrogen species on the metal/support is still unknown.

In this respect, researchers from the Wolfson Catalysis Centre at the University of Oxford have precisely engineered an atomic [Ru^{2+}-O^{2-}]/MgO(111) solid-state Frustrated Lewis Pair catalyst and investigated the H spillover pathway through this material interface. They used Diamond Light Source's Versatile Soft X-ray (VerSoX) beamline (B07), which can probe the oxidation state (O.S.) change of the ruthenium in real-time as well as monitor the change in concentration of the surface hydrogenic species on the support under reaction conditions. This is critical to determining the electronic structure and the surface composition of the catalyst. The results demonstrate a spontaneous reduction in the Ru O.S. from oxidised to metallic and oxidation of H_2 to protons whereas the surface hydroxyl species concentration is found to grow massively on MgO(111) upon passing hydrogen to the catalyst. This provides the key evidence for mechanistic derivation.

To achieve fast reaction rates for hydrogenation reactions at mild conditions such as low temperature ammonia synthesis, it is essential to alleviate the hydrogen poisoning effect, which is to prevent the surface hydrogen atoms from blocking the metal active sites[1,2]. One effective means to do so is via hydrogen spillover, where the H atoms are transported from the metal sites to the catalytic support[3]. In this pioneering work, the researchers have employed a Frustrated Lewis Pair approach to construct [Ru^{2+}-O^{2-}] pairs on the polar MgO(111) support to enable labile dihydrogen activation and provide highly energetic surface oxygen sites for H atoms to migrate to.

The Transmission Electron Microscopy (TEM) image in Fig. 1a shows a high dispersion of Ru single atoms on the polar MgO(111) surface despite a high metal loading of 3.4 wt %. This is probably due to the strong surface polarity of the oxygen-terminated surface of MgO(111) that stabilises the Ru species. Atom Probe Tomography (APT) then reveals the Ru is selectively located over magnesium on the oxygen-terminated surface (Fig. 1b, c). To reconstruct the exact position of Ru on the surface, High-Angle Annular Dark-Field Scanning Transmission Electron Microscopy (HAADF-STEM) is employed in conjunction with Density Function Theory (DFT) modelling to derive a structure of a single Ru sitting on top of a 3-O hollow site with a Mg atom underneath at the next layer (Fig. 1d-g). This is further confirmed by Extended X-Ray Absorption Fine Structure (EXAFS) analysis that shows a tri-coordinated Ru-O bond for the Ru/MgO(111) sample (Fig. 1h).

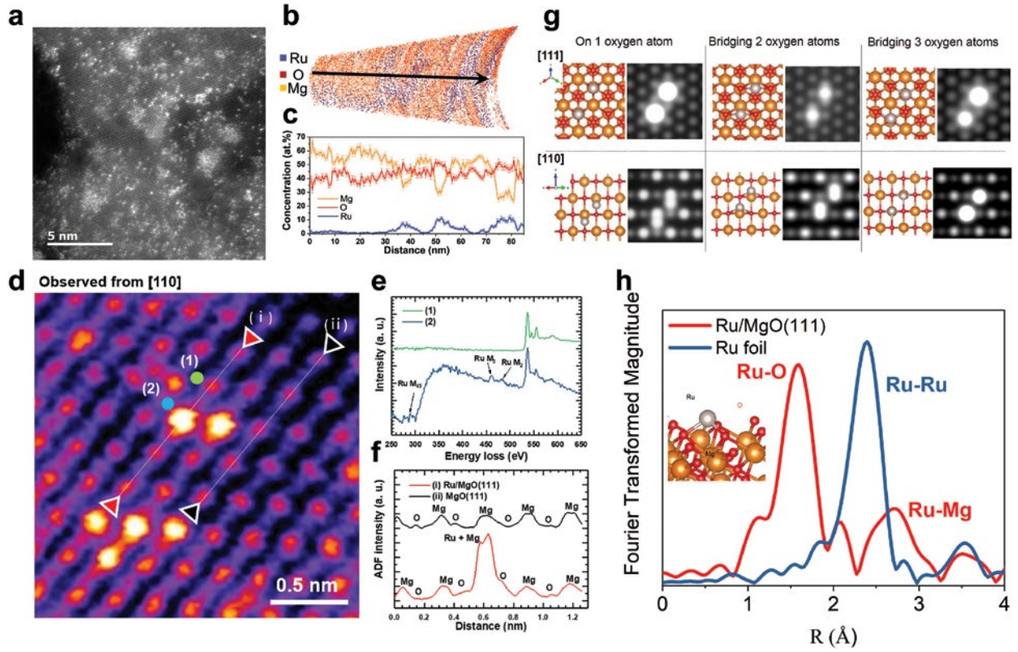

Figure 1: (a) TEM image of 3.4 wt % Ru/MgO(111); (b) APT atom map of 3.4 wt % Ru/MgO(111) (blue, Ru; red, O; orange, Mg); (c) Composition profile of Ru, Mg, and O of 3.4 wt % Ru/MgO(111) along the black line in b; (d) HAADF-STEM image of 3.4 wt % Ru/MgO(111) observed from the [110] direction; (e and f) Simultaneous acquisition (e) EELS extracted on oxygen atom (green circle in d), Ru atom (blue circle in d); and (f) HAADF acquired along the line in d; (g) Simulation of STEM images of two Ru atoms supported on different positions of MgO(111) from [111] and [110] directions. Atomic model was also provided for reference; (h) Fourier transform of k^3-weighted Ru K-edge of X-ray absorption fine structure spectroscopy (EXAFS) spectra of the post hydrogen-reduced 3.4 wt % Ru/MgO(111) measured at 300 °C. Reprinted with permission from ref [4]. Copyright 2022 American Chemical Society.

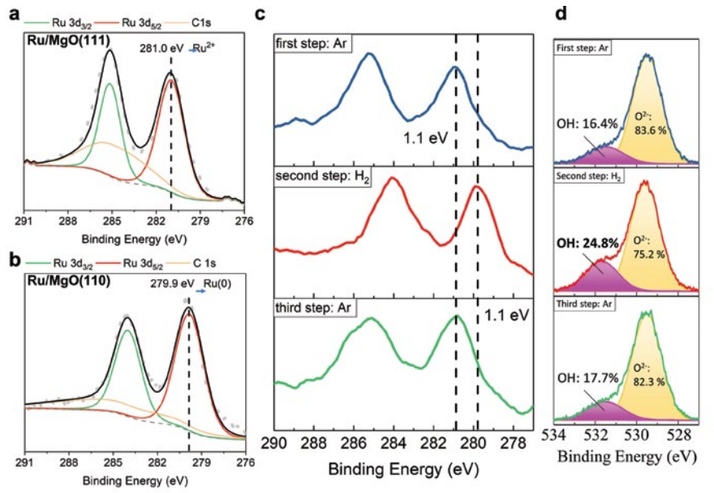

Figure 2: Ambient pressure X-ray photoelectron spectroscopy (AP-XPS) Ru 3d spectra for (a) Ru/MgO(111) and; (b) Ru/MgO(110). Measurement was performed under 1 mbar Ar at 350 °C inside an airtight sample cell after pretreatment at 1 mbar H_2 at 350 °C; (c) Ru 3d and (d) corresponding O 1s of AP-XPS spectra at 350 °C under alternative sweeping between 1 mbar Ar and 1 mbar H_2 for the Ru/MgO(111) sample. All the spectra are calibrated with reference to the internal standard Mg 2s of 88.1 eV. Reprinted with permission from ref [4]. Copyright 2022 American Chemical Society.

While imaging and X-ray absorption techniques can provide clues on structural information, high resolution *in-situ* ambient pressure X-ray Photoelectron Spectroscopy (XPS) sheds light on dynamic charge states and real-time changes of surface support compositions at reaction conditions[5]. To identify the oxidation state of Ru on MgO(111) at reaction conditions, ambient-pressure XPS was carried out at 300°C under an Ar atmosphere of 1 mbar after hydrogen pre-reduction at the same temperature. Ru is found to have an oxidation state of around +2 when it is supported on the polar MgO(111) surface whereas it is localised to a metallic state when supported on the non-polar MgO(110) surface (Fig. 2a, b). Combining this result with Bader charge calculations, a [Ru^{2+}-O^{2-}] Frustrated Lewis Pair is identified.

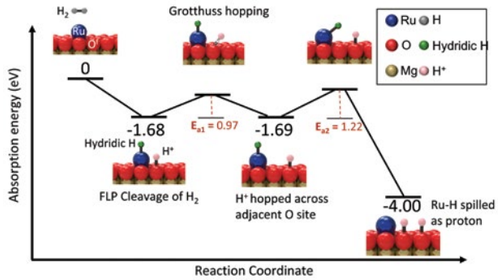

Figure 3: Proposed mechanism for hydrogen spillover on Ru/MgO(111). Reprinted with permission from ref [4]. Copyright 2022 American Chemical Society.

By switching the gas feed from Ar to H_2, the Ru 3d peaks exhibit a very significant shift of -1.1 eV that implies a spontaneous reduction from Ru (II) to the metallic state (Fig. 2c). Simultaneously, the high binding energy shoulder in the 01s spectrum, which is associated with the [OH] component, is found to increase from 16.4% to 24.8% under flowing hydrogen (Fig. 2d). This signifies the migration of H species from the metal to the MgO support as it is experimentally proven that dihydrogen cannot be dissociated on the bare support due to kinetic stability. Meanwhile, Nuclear Magnetic Resonance (NMR) has identified the co-existence of a hydridic Ru-H peak and a surface hydroxyl peak (with H-bonding) that affirms the postulation. When the gas stream is switched from H_2 back to Ar, Ru is returned to an oxidised state while the OH concentration of the support returns to its starting position, showing the reversibility of this process.

All the information combined with the DFT calculations, a reversible reaction pathway for the hydrogen spillover on the refractory oxide is proposed (Fig. 3). The dihydrogen is first activated by the surface [Ru^{2+}-O^{2-}] FLP pair on the MgO(111), followed by redox transfer of Ru-hydride to proton on O^{2-} at the metal-support interface. The fast migration is further supported by Grotthuss proton hopping with low activation barriers for the H spillover.

References:

1. Wu, S. *et al.* Removal of hydrogen poisoning by electrostatically polar MgO support for low-pressure NH_3 synthesis at a high rate over the Ru catalyst. *ACS Catalysis* **10**, 5614– 5622 (2020). DOI: 10.1021/acscatal.0c00954
2. Jiang, L. *et al.* Facet engineering accelerates spillover hydrogenation on highly diluted metal nanocatalysts. *Nature Nanotechnology* **15**, 848–853 (2020). DOI: 10.1038/s41565-020-0746-x
3. Prins, R. Hydrogen spillover. Facts and fiction. *Chemical Reviews* **112**, 2714–2738 (2012). DOI: 10.1021/cr200346z
4. Wu, S. *et al.* Rapid interchangeable hydrogen, hydride, and proton species at the interface of transition metal atom on oxidesSurface. *Journal of the American Chemical Society* **143**, 9105–9112 (2021). DOI: 10.1021/jacs.1c02859
5. Held, G. *et al*. Ambient-pressure endstation of the Versatile Soft X-ray (VerSoX) beamline at Diamond Light Source. *Journal of Synchrotron Radiation* **27**, 1153–1166 (2020). DOI: 10.1107/S1600577520009157

Funding acknowledgement:
The financial support of this work from the EPSRC research council of UK and Siemens, plc are acknowledged. S.W. would like to thank Siemens, plc, and EPSRC for a joint DPhil Studentship. We thank Diamond for the access to beamline B07.

Corresponding author:
Professor Shik Chi Edman Tsang, University of Oxford,
edman.tsang@chem.ox.ac.uk

Bio-inspired molecules have great nanotechnology potential

Related publication: Knecht, P., Reichert, J., Deimel, P. S., Feulner, P., Haag, F., Allegretti, F., Garnica, M., Schwarz, M., Auwärter, W., Ryan, P. T. P., Lee, T.L., Duncan, D. A., Seitsonen, A. P., Barth, J.V., & Papageorgiou, A. C. Conformational control of chemical reactivity for surface-confined Ru-porphyrins. *Angewandte Chemie International Edition* **60**, 16561–16567 (2021). DOI: 10.1002/anie.202104075

Publication keywords: Ab-initio calculations; CO ligands; Metalloporphyrins; Scanning probe microscopy; X-ray spectroscopy

Nature is a great source of inspiration for researchers involved in developing new materials. For example, porphyrins are a class of pigment molecules (including haem and chlorophyll) that have a flat ring shape, some with a metal atom at the centre. The past decades have seen intense interest in using porphyrins as functional building blocks, and they have great potential for use in nanotechnology. One particularly desirable application is in single-atom catalysis on solid surfaces.

The first step of catalysis is the binding of the reactant to the catalyst. A team of researchers from the Technical University of Munich investigated the reactivity of two similar Ru-porphyrins on a silver surface against carbon monoxide (CO), a chemical of interest in industrial chemistry.

To do so, they needed to characterise the relative reactivity of the Ru-porphyrins with submolecular resolution and quantify the binding strength of CO by temperature-programmed desorption. They used Diamond Light Source's Surface and Interface Structural Analysis beamline (I09) because it offers a suitable experimental method for highly accurate determination of adsorption height, *i.e.*, how close the catalytically-active atom is to the surface before and after binding. This out-of-plane information cannot be derived accurately from microscopy measurements.

Their results emphasise the crucial role of the flexibility of the Ru-porphyrin in the ligation process and the related ease of decoupling the ruthenium centre from the silver surface.

For the creation of novel materials and devices, inspiration is frequently sought in nature. Porphyrins are naturally occurring cyclic molecules that can bind metal atoms into their centre. They are widespread throughout biology, and most famously comprise haem, found in haemoglobin, that transports oxygen around the body and is a catalyst of both reductive and oxidative reactions. The flexibility, yet robustness of these cyclic molecules (Fig. 1a black structures), combined with the ability to chemically tailor their periphery (Fig. 1a grey structures) offers a unique playground to construct artificial nanosystems that exploit interactions between molecules to self-assemble, notably on surfaces[1]. Such "self-assembled monolayers" are a cornerstone of nanotechnology.

Single layer films of self-assembled metalloporphyrins, *i.e.* porphyrins with a metal atom in their centre, present well-defined and regular coordinatively unsaturated metal centres. These are provided by the generally favoured adsorption geometries with the macrocycle residing parallel to the substrate lattice. Such metal atoms can provide catalytically active sites on surfaces, suitable for heterogeneous catalysis with the inherent advantages of processing. The reactivity of individual metal atoms on surfaces is a topical issue in single-atom catalysis.

Here porphyrins stabilising Ru in the catalytically active oxidation state +2 (Fig. 1) were investigated on the atomically planar, close-packed silver surface. To elucidate the molecular events associated with the surface reactivity, an extensive array of characterisation techniques was used, including real space single-molecule imaging, diffraction, photoelectron spectroscopy, temperature programmed desorption and computational modelling. Experiments were performed under ultra-high vacuum, so as to prepare and examine samples free from any possible contaminant and solvent effects. For a correlation of structure and function, the key Normal Incidence X-ray Standing Waves (NIXSW) measurements were performed at the I09 beamline of Diamond Light Source.

The tailored functional groups, at the periphery of the porphyrin molecule, are responsible for the lateral arrangement and the conformation of the cyclic interior of the porphyrin molecule. On the Ag(111), the inspected macrocycles adopt a saddle shape (Fig. 2a) or a more planar, inverted bowl conformation

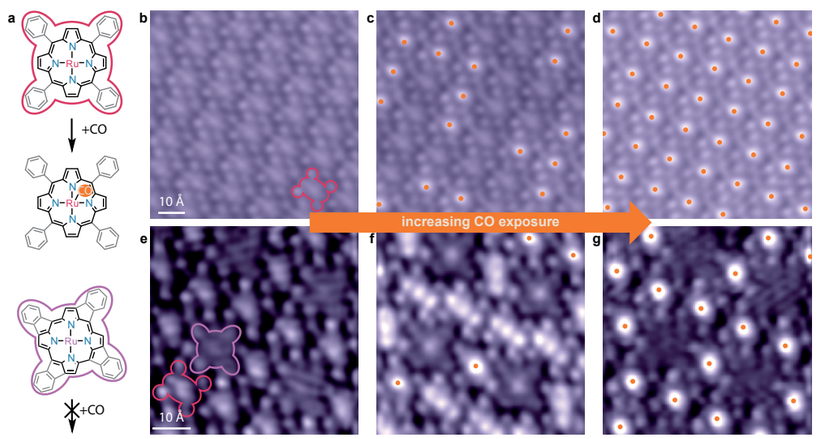

Figure 1: (a) Chemical structures of different Ru-porphyrins investigated on the Ag(111) surface. Substituents marked in grey; (b-g) STM images of progressive CO exposure in situ at 150 K of (b-c) a monolayer of saddle-shape Ru-porphyrins (outlined in raspberry) and of (e-g) a mixed layer of saddle-shape and planarised Ru-porphyrins (outlined in lila). Orange dots mark the capped molecules. CO is found only on the saddle-shape Ru-porphyrins and eventually populates all such porphyrins.

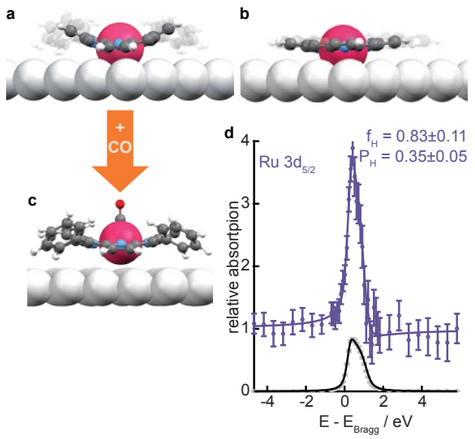

Figure 2: Ball-and-stick models of the (a) saddle-shape Ru porphyrin and (b) the bowl-shape (planarised) Ru porphyrin on Ag(111). The substituents are faded to highlight the macrocycle conformation differences[1]. (c) CO ligated saddle-shape Ru-porphyrin. Ru, C, N, O, H, and Ag in raspberry, grey, blue, red, white, and silver, respectively; (d) NIXSW photoelectron profiles and fits of the Ru $3d_{5/2}$ region in (111) reflection for saddle-shape Ru(CO)-porphyrin on Ag(111). The Ru data points in purple, the reflection of the Ag(111) substrate in grey. The data was used to determine that the Ru atoms sit 3.18 Å away from the Ag(111) surface.

(Fig. 2b). Both Ru porphyrins bind to the silver surface covalently at the Ru atom. The structural measurements at the beamline showed that the more planar molecule allowed the Ru atom to approach the surface ever so slightly more, just 0.1 Å[2].

Crucial differences were discovered in how CO binds to the Ru atoms in the porphyrin molecule, depending on the conformation of the macrocycle. Scanning Tunnelling Microscopy (STM) showed additional protrusions associated with CO, appearing solely on top of the Ru atoms hosted in the saddle-shape porphyrins (Fig. 1b-f): If the central cyclic part of the molecule had a saddle-shape, CO would bind; if, instead, the central cyclic part of the molecule was in a more planar / bowl-shape, CO would not bind. Thus, the tiny difference of the initial position of the Ru atom results in a completely different ability of the molecule to interact with the world around it.

With the CO binding to the porphyrin, the porphyrin changes its binding to the surface. The whole molecule is displaced further from the surface. NIXSW analysis determined that the Ru atoms in particular are 3.18 Å away from the Ag(111) surface (Fig. 2d): the Ru bond to the surface is elongated by 0.7 Å and significantly weakened. X-ray and ultraviolet photoelectron spectroscopies showed a significantly altered electron charge transfer between the Ru atom and the Ag surface after ligation. These can be described as a structural *trans*-effect, with both the carbonyl and the Ag surface considered as *trans* ligands to the Ru atom. In line with other observations on surface supported metalloporphyrins, the metal atom is electronically and physically decoupled from the substrate upon the inclusion of an axial ligand[3].

In addition to imaging the individual molecules on the surface, the scanning tunnelling microscope was also used to manipulate the molecules bound to the Ru atoms of the porphyrins. The tip of a scanning tunnelling microscope could be used like a scalpel to remove individual CO molecules with exquisite control (Fig. 3). Because of the binding strength these Ru pedestals exhibit (~ 0.8 eV), this operation could be performed at significantly higher temperatures than earlier studies[4] (150 K vs. 5 K). The insight gained in axial binding and manipulation of these ligands paved the way for making use of these porphyrin templated surfaces as regular pedestals for out-of-plane functional nanoarchitectures, as was indeed feasible for an organic ligand featuring a carbene anchor[5].

Future work focuses on screening substituents and surface supports to finely control the coordination of various ligands. Here again, NIXSW will provide the structural measurements necessary to reliably compare this set of systems.

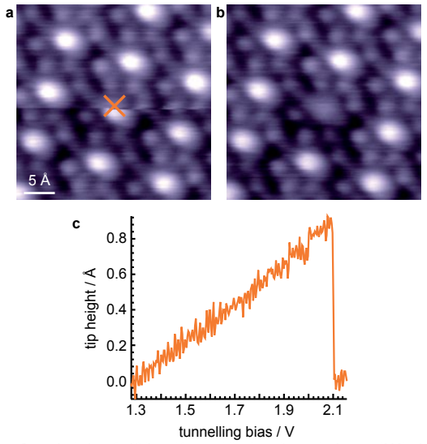

Figure 3: Manipulation of a CO ligand from saddle-shape Ru porphyrin on Ag(111) with the STM tip; (a) While scanning the surface (from bottom), a voltage pulse was applied at the position marked by the orange cross; (b) The subsequent STM image shows an uncapped saddle-shape Ru porphyrin at the same position; (c) Tip height change during the voltage pulse from 1.28 V to 2.15 V, with a current of 50 pA. The abrupt approach of the tip at ~2.1 V indicates the removal of CO.

These results will enable the bio-inspired precise engineering of the catalytic function of metalloporphyrins, akin to the optimisation of biological catalytic processes exerted by nature through Darwinian evolution.

References:

1. Auwärter, W. *et al*. Porphyrins at interfaces. *Nature Chemistry* **7**, 105–120 (2015). DOI: 10.1038/nchem.2159
2. Knecht, P. *et al.* Tunable interface of ruthenium porphyrins and silver. *The Journal of Physical Chemistry C* **125**, 3215–3224 (2021). DOI: 10.1021/acs.jpcc.0c10418
3. Flechtner, K. *et al.* NO-induced reversible switching of the electronic interaction between a porphyrin-coordinated cobalt ion and a silver surface. *Journal of the American Chemical Society* **129**, 12110–12111 (2007). DOI: 10.1021/ja0756725
4. Omiya, T. *et al.* Desorption of CO from individual ruthenium porphyrin molecules on a copper surface via an inelastic tunnelling process. *Chemical Communications* **53**, 6148–6151 (2017). DOI: 10.1039/C7CC01310H
5. Knecht, P. *et al.* Assembly and manipulation of a prototypical N-heterocyclic carbene with a metalloporphyrin pedestal on a solid surface. *Journal of the American Chemical Society* **143**, 4433–4439 (2021). DOI: 10.1021/jacs.1c01229

Funding acknowledgement:

German Research Foundation (DFG): priority programme 1928 COORNETs, Excellence Cluster e-conversion, GSC 81 International Graduate School of Science and Engineering (IGSSE) at TUM, Heisenberg professorship. Engineering and Physical Sciences Research Council (EPSRC): Centre for Doctoral Training in Advanced Characterisation of Materials (grant number EP/L015277/1). European Research Council: Consolidator Grant NanoSurfs, no. 615233. European Union H2020-MSCA-IF-2014 programme: 2DNano, no. 658070. Diamond Light Source for the award of beam time under proposal SI24320-1 and related financial support. The computing resources at the Centro Svizzero di Calcolo Scientifico (CSCS), Lugano, Switzerland, under Project uzh11. Projekt DEAL for open access of the related publication.

Corresponding author:

Dr Anthoula C. Papageorgiou, Technical University of Munich, a.c.papageorgiou@tum.de

Reliable on-water synthesis for synthetic van der Waals heterostructures

Related publication: K. Liu, J. Li, H. Qi, M. Hambsch, J. Rawle, A. R. Vázquez, A. S. Nia, A. Pashkin, H. Schneider, M. Polozij, T. Heine, M. Helm, S. C. B. Mannsfeld, U. Kaiser, R. Dong, & X. Feng. A Two-dimensional polyimide-graphene heterostructure with ultra-fast interlayer charge transfer. *Angew. Chem. Int. Ed.* **60**, 13859 (2021). DOI: 10.1002/anie.202102984

Publication keywords: Heterostructure; 2D polymer; Graphene; Charge transfer; Functional materials

Synthetic van der Waals heterostructures (vdWHs) are made by stacking different two-dimensional (2D) crystals. They are of interest for their novel functions in phototransistors, photodiodes, memory and tunnelling devices. Surface reconstruction and proximity effects between the neighbouring layers allow the opto-electrical properties of vdWHs to be tailored for tuning carrier density, enhancement of electron-hole separation and accelerated charge transfer.

2D polymers (2DPs) are a new generation of atomically/molecularly thin organic 2D materials, with repeated units linked via covalent bonds with long-range order in two distinct directions. Compared with inorganic 2D materials, 2DPs can be readily tailored to a much higher degree by using abundant building blocks and linkage chemistries. Therefore, 2DP-based vdWHs are highly attractive owing to their tunable physicochemical properties and designable functions. However, it is challenging to synthesise structurally-defined 2D polymers (2DP) and precisely assemble them with other 2D materials in a defined vdWH sequence.

Researchers have now demonstrated a general but reliable on-water synthesis and assembly strategy for preparing large-area 2D polyimide (2DPI)-graphene (G) vdWH. The team used Grazing Incidence Wide-Angle X-ray Scattering (GIWAXS) on the Surface and Interface Diffraction beamline (I07) to demonstrate the successful formation of vdWHs.

The on-water surface synthesis approach holds promise as a general method for preparing organic-inorganic vdWHs. The structures of 2DPs can be adjusted to engineer their band gaps and enhance the charge transfer.

Two-dimensional (2D) van der Waals heterostructures (vdWHs) are generated by integration of 2D materials with dangling-bond-free surfaces through the weak interlayer vdW interaction along the vertical direction[1]. 2D polymers (2DPs) have recently emerged as a new generation of atomically/molecularly thin organic 2D materials, which comprise repeated units linked via covalent bonds with long-range order in two distinct directions[2]. Owing to the homogenous, free-standing, transferable and large-area (up to cm^2) characteristics, the resultant 2DPs are attractive for the construction of 2D vdWHs.

In this work, the preparation of 2D polyimide (2DPI)-graphene (G) vdWH by the on-water surface synthesis and assembly strategy was demonstrated. The 2DPI was firstly synthesised by polycondensation between 5,10,15,20-tetrakis(4-aminophenyl)porphyrin (**M1**) and perylene-3,4,9,10-tetracarboxylic dianhydride (**M2**), as shown in Fig. 1a. The synthesis and fabrication of 2DPI-G involve 6 steps, as illustrated in Fig. 1b. The procedure from Step 1 to Step 4 deals with the synthesis of 2DPI. In Step 1, a chloroform solution of **M1** (0.1 ml, 1 mg mL^{-1}) was spread onto the water surface. After 5 min evaporation of chloroform, the Delrin barriers were driven forward to compress **M1** on the water surface at a rate of 1 mm.min^{-1} (Step 2). Then, **M2** (20 mL, 1 mg.mL^{-1}, dissolved in 1 mg.mL^{-1} LiOH aqueous solution, ~200 molar equivalents to **M1**) was gradually injected into the trough (Step 3). And the subphase was tuned to be alkaline (pH = 11). **M2** then slowly diffused to the air-water interface and got adsorbed onto the **M1** monolayer and induced the 2D polymerisation. After 30 hours of reaction, we achieved a ~20 cm x 7.5 cm thin film floating on the water surface (Step 4, Fig. 1a). Afterwards, the film was transferred onto a solid substrate and further annealed at 100˚C for 1 hour to complete the reaction of residual functional monomers and remove the water. The Atomic Force Microscopy (AFM) measurement at the film edge revealed a thickness of 0.8 nm, suggesting the single-layer feature.

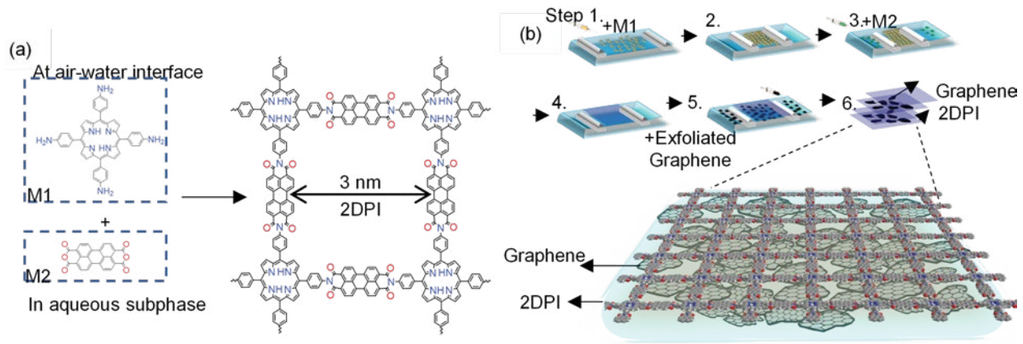

Figure 1: Reaction scheme of the 2DPI by the LB method and schematic illustration of 2DPI-G vdWH. (a) synthesis of 2DPI on the water surface and face-to-face co-assembly of graphene and 2DPI at the interface; (b) Schematic illustration of the 2DPI-G fabrication on the water surface by LB method.

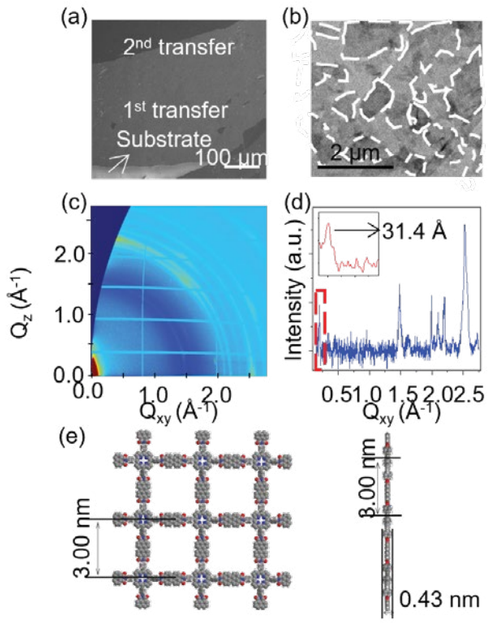

Figure 2: Morphology and structural characterisation of 2DPI-G. (a) SEM image and (b) low-magnification TEM images of 2DPI-G heterostructure after twice deposition. The edges of the graphene flakes were marked by dashed lines; (c) 2D-GIWAXS pattern of 2DPI-G; (d) The profile of integrated intensity of GIWAXS pattern with a zoom-in view of low Qxy region; (e) The model from DFT calculations, showing both top view and side view.

Following the synthesis of the 2DPI, Step 5 and Step 6 are concerned with the fabrication of the 2DPI-G vdWHs. In Step 5, an aqueous suspension of high-quality electrochemically exfoliated graphene was injected into the aqueous subphase (Fig. 1b). Graphene flakes then could attach to the bottom surface of the 2DP monolayer driven by the π-π stacking interaction. To prepare the 2DPI-G, we repeatedly transferred films to other substrates (Step 6 in Fig. 1b). As shown in Fig. 2a, the achieved vdWHs exhibited layered morphology via the repeated transfer method. The EG flakes are distributed in the 2DPI-G without significant aggregation as can be seen in Fig. 2b. We then explored the crystal structure of 2DPI-G. Grazing Incidence Wide-Angle X-ray Scattering (GIWAXS) was utilised to characterise the pristine crystal structures of 2DPI-G. Moreover, the 2DPI film is encapsulated by graphene in the case of 2DPI-G which prevents radiation damage during the measurement. The 2D-GIWAXS pattern in Fig. 2c shows diffraction rings at 0.20 $Å^{-1}$, 1.48 $Å^{-1}$, 2.21 $Å^{-1}$ and 2.53 $Å^{-1}$, which correspond to d-space values of 31.4 Å, 4.24 Å, 2.84 Å and 2.48 Å, respectively. The ring at 31.4 Å can be attributed to the 100 or 010 Bragg peaks of 2DPI (Fig. 2d), consistent with the calculated results (Fig. 2e). The peak at 4.24 Å corresponds to the layer distance of few-layer stacking graphene.[3] The peak at 2.84 Å are mainly distributed along the out-of-plane direction, which could originate from the higher-order Bragg diffraction of interlayer structure. The peak at 2.48 Å is assigned to the lattice constant of graphene ($a = b = 2.46$ Å) Moreover, this ring mainly lies in the in-plane direction, suggesting that the EG flakes prefer a face-on orientation in the vdWHs.

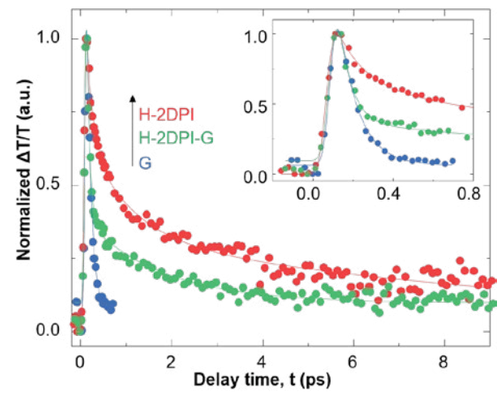

Figure 3: Dynamics of transient absorption in multi-layer graphene (blue dots), protonated 2DPI (red dots) and protonated 2DPI-G (green dots) measured using a degenerate pump-probe spectroscopy setup with fs pulses at 470 nm. The inset shows the sub-ps dynamics immediately after the photoexcitation.

The relaxation dynamics of charge carriers in 2DPI-G was characterised by the TA spectroscopy. We protonated 2DPI-G with HCl (37%wt), which is denoted as H-2DPI-G. Figure 3 presents a noticeable acceleration of the relaxation dynamics of H-2DPI-G with near-resonant excitation at 470 nm. Both fast and slow decay processes of H-2DPI-G are influenced by the charge transfer from H-2DPI to graphene. The most remarkable effect is the emergence of the pronounced fast relaxation process caused by the proximity of the graphene layer. Fitting with a bi-exponential decay function gives the relaxation time constants of the fast and slow decays in H-2DPI-G that are equal to 61.56.5 fs and 1700 100 fs. The timescale of 60 fs of the dominating relaxation defines the speed of the interlayer charge transfer in H-2DPI-G.

In summary, we demonstrated the novel on-water surface synthesis of 2DPI and its assembly with graphene for the construction of unprecedented 2DPI-based vdWHs. Guided by the strong interlayer cation-π interaction between protonated H-2DPI and graphene, the resultant H-2DPI-G exhibited remarkable ultra-fast charge transfer within 60 fs, one of the fastest in reports.

References:

1. Novoselov, K. S. *et al*. 2D materials and van der Waals heterostructures. *Science* **353**, aac9439. (2016). DOI: 10.1126/science.aac9439
2. Liu, K. Ion-water surface synthesis of crystalline, few-layer two-dimensional polymers assisted by surfactant monolayers. *Nat. Chem.* **11,** 994. (2019). DOI: 10.1038/s41557-019-0327-5
3. Wen, Y. *et al.* Expanded graphite as superior anode for sodium-ion batteries. *Nat. Commun.* **5**, (2014). DOI: 10.1038/ncomms5033

Funding acknowledgement:
We acknowledge financial support from EU Graphene Flagship (Core3, No. 881603), ERC Grants on T2DCP and FC2DMOF (No. 852909) and DFG projects (SFB-1415, No. 417590517; SPP 2244, 2DMP) as well as the German Science Council, Centre of Advancing Electronics Dresden, EXC1056 (Center for Advancing Electronics Dresden) and OR 349/1. We acknowledge Diamond Light Source for time on Beamline I07 under Proposal SI25070. Open access funding enabled and organised by Projekt DEAL.

Corresponding author:
Prof. Xinliang Feng, Technische Universität Dresden, xinliang.feng@tu-dresden.de

Investigating the electron properties at the surface of novel magnetic topological insulators

Related publication: Vidal, R. C., Bentmann, H., Facio, J. I., Heider, T., Kagerer, P., Fornari, C. I., Peixoto, T. R. F., Figgemeier, T., Jung, S., Cacho, C., Büchner, B., van den Brink, J., Schneider, C. M., Plucinski, L., Schwier, E. F., Shimada, K., Richter, M., Isaeva, A., & Reinert, F. Orbital complexity in intrinsic magnetic topological $MnBi_4Te_7$ and $MnBi_6Te_{10}$. *Physical Review Letters* **126,** 176403 (2021). DOI: 10.1103/PhysRevLett.126.176403

Publication keywords: Angle-resolved photoelectron spectroscopy; Topological insulators; Magnetism

The information technologies we currently rely on, used in (*e.g.*) cell phones and laptops, involve a significant waste of energy that is lost as heat. Our ever-growing need to access, process and store information makes it increasingly important that we develop new, more energy-efficient technologies. Current technologies are based on electron charge. One potential avenue for future information technologies is to use the electron spin - an intrinsic magnetic property of electrons - to achieve more energy-efficient information processing.

Theoretical predictions suggest that certain magnetic materials exhibit spin polarised electrons at their surface with unusual 'topological' properties. In the future, such topological surface electrons might enable information processing without heat loss in electronic devices.

An international team of researchers used Angle-Resolved Photoelectron Spectroscopy (ARPES) measurements on beamline I05 to verify the theoretical predictions. The I05 setup allows ARPES measurements with high energy resolution and a small beam spot. Their experiments confirmed that the compounds $MnBi_4Te_7$ and $MnBi_6Te_{10}$ display spin-polarised, topological surface electrons.

In the future, further optimisation of the materials could enable applications in electronic high-precision metrology (the scientific study of measurement) without the need for external magnetic fields. However, raising the temperature at which the magnetic order arises to room temperature - a pre-requisite for applications in real-world devices - still poses a significant challenge.

Topological insulators (TI) feature spin-polarised, metallic states at their surfaces while their bulk remains insulating. Here, the term "topological" refers to a special kind of "knotting" of the bulk electron wave functions, which evolves differently than in conventional insulators. The unique surface properties of a TI are a result of this non-trivial bulk topology. Over the past decade, the understanding of these materials has matured and quite a significant number of compounds have been identified to be TI[1]. Interestingly, introducing magnetic order in a TI may enable realisation of new topological phenomena[2]. One important example is the quantum anomalous Hall state, where a dissipationless flow of electronic charge is realised in the absence of external magnetic fields[3]. Another example is Majorana fermion quasi-particles, a special type of electronic excitation in a solid, that is discussed in the context of quantum computation. Yet to date, only a few Magnetic Topological Insulators (MTI) are known, *i.e.* materials that combine the presence of magnetic order and a non-trivial topology. Recently, the compound $MnBi_2Te_4$ was discovered as the first MTI that does not require doping with magnetic impurities[4].

In the present study, the compounds $MnBi_4Te_7$ and $MnBi_6Te_{10}$ were studied with the goal to directly verify the spin-polarised, metallic states at the surface. To this end, experiments based on Angle-Resolved Photoelectron Spectroscopy (ARPES) were employed using a synchrotron light source (beamline I05 at Diamond Light Source) and a laser source (HiSOR Hiroshima, Japan, and FZ Jülich, Germany). ARPES allows to directly measure the electron dispersion relation in crystalline materials with high surface sensitivity and was therefore the ideal method for the purpose of this study. In $MnBi_4Te_7$ and $MnBi_6Te_{10}$, magnetic layers, containing the element Mn, and non-magnetic layers are stacked on top of each other in a regular fashion. Depending on the stacking sequence the magnetic properties vary[5], potentially leading to interesting opportunities to manipulate the interplay of magnetic order and topology.

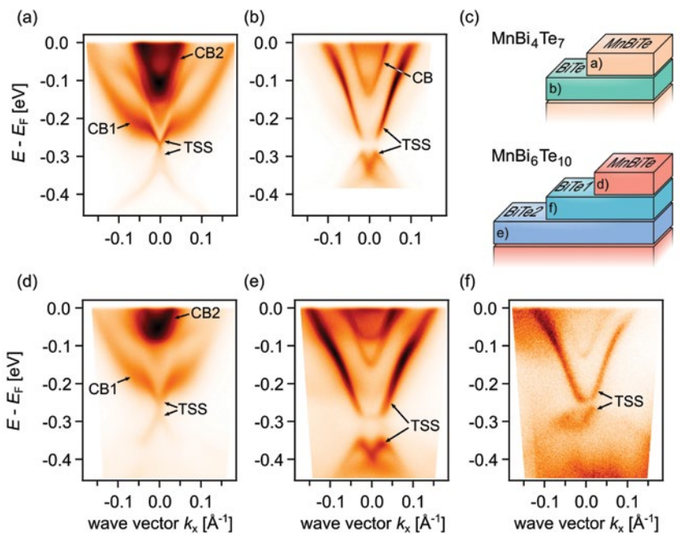

Figure 1: ARPES measurements for different surface terminations of $(Bi_2Te_3)n(MnBi_2Te_4)$ with n = 1 and 2; (a),(b) ARPES data sets for $MnBi_4Te_7$ a $MnBi_2Te_4$- and a Bi_2Te_3-terminated surface, respectively; (c) Schematic of the possible terminations of $MnBi_4Te_7$ and $MnBi_6Te_{10}$ surfaces, labelled with the panel showing the corresponding ARPES data; (d)–(f) ARPES datasets along for $MnBi_6Te_{10}$ with for different terminations

The alternating layer stacking in the crystal structure also gives rise to different possible terminations of the surface, *i.e.* surfaces with different atomic structure. Fig. 1 shows ARPES measurements of the surface states for all possible surface terminations in $MnBi_4Te_7$ and $MnBi_6Te_{10}$. It is apparent that the dispersion relations are similar for both compounds but strongly depend on the specific surface termination. The latter can be either a magnetic $MnBi_2Te_4$ layer or a non-magnetic Bi_2Te_3 layer. To further verify the topological and spin-polarised properties, more detailed ARPES experiments were carried out. In particular, spin-resolved ARPES and

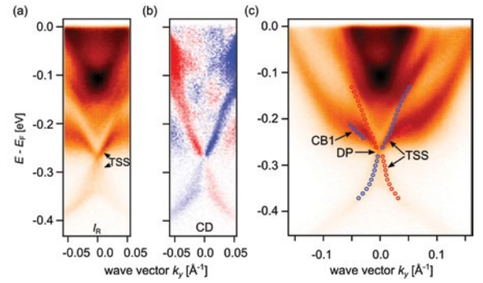

Figure 2: CD-ARPES experiments for the $MnBi_2Te_4$-terminated surface of $MnBi_4Te_7$:(a) ARPES intensity IR measured with right circularly polarised light; (b) Corresponding CD-ARPES dataset defined as the intensity difference IR – IL; (c) ARPES intensity measured with s-polarised light. The overlaid markers indicate the dispersion extracted from CD-ARPES data in (b) and the red or blue colour refers to the sign of the CD.

Circular Dichroism in ARPES (CD-ARPES) were used for this purpose. In the first case, the spin polarisation of photoelectrons is directly detected. In the latter case, the difference in photoemission cross section depending on the circular polarisation of the light used to excite the photoelectrons is measured. Fig. 2 shows CD-ARPES data for a $MnBi_2Te_4$-terminated surface. One can discern a sign change in the CD pattern at the so-called Dirac point (DP) of the surface-state dispersion, *i.e.* at the band crossing of the two surface-state branches at kx = 0. Such a sign change indicates a helicity change in the surface-state wave function across the DP, as expected for a topological surface state.

The Bi_2Te_3-terminated surface shows a particularly complex electronic structure, because the surface state strongly hybridises with the bulk valence band. To disentangle contributions from the surface and from the bulk to the photoelectron spectra, photon-energy-dependent measurements at beamline I05 turned out to be crucial. Fig. 3 shows ARPES data for a Bi_2Te_3-terminated surface measured at various photon energies. One can see that, depending on photon energy, different parts of the measured dispersion relation display high or low intensity. Through a detailed analysis, also involving theoretical calculations (Fig. 3), this effect could be traced back to a varying surface or bulk character of the electron bands as a function of wave vector. This allowed for a precise determination of the surface-state dispersion, including its hybridisation with the bulk valence band.

Overall, the study provides comprehensive evidence for the presence of spin-polarised, topological surface states in the magnetic compounds $MnBi_4Te_7$ and $MnBi_6Te_{10}$. In the future, further optimisation of these materials and their synthesis in the form of ultrathin layers could enable interesting opportunities to investigate the interplay of magnetic order and topological electronic properties.

References:

1. Bansil, A. *et al. Colloquium*: topological band theory. *Reviews of Modern Physics* **88,** 021004 (2016). DOI: 10.1103/RevModPhys.88.021004
2. Tokura, Y. *et al.* Magnetic topological insulators. *Nature Reviews Physics* **1,** 126–143 (2019). DOI : 10.1038/s42254-018-0011-5
3. Chang, C.-Z. *et al.* Experimental observation of the quantum anomalous Hall effect in a magnetic topological insulator. *Science* **340,** 167–170 (2013). DOI: 10.1126/science.1234414
4. Otrokov, M. M. *et al.* Prediction and observation of an antiferromagnetic topological insulator. *Nature* **576,** 416–422 (2019). DOI: 10.1038/s41586-019-1840-9
5. Vidal, R. C. *et al.* Topological electronic structure and intrinsic magnetization in $MnBi_4Te_7$: A Bi_2Te_3 derivative with a periodic Mn sublattice. *Physical Review X* **9,** 041065 (2019). DOI: 10.1103/PhysRevX.9.041065

Funding acknowledgement:
We acknowledge financial support from the DFG through SFB1170 "Tocotronics" (Project A01), SFB1143 "Correlated Magnetism," RE1469/13-1, SPP 1666 "Topological insulators" (IS 250/1-2 and PL 712/2-1), ERA-Chemistry Programm (RU-776/15-1), and the Würzburg-Dresden Cluster of Excellence on Complexity and Topology in Quantum Matter—ct.qmat (EXC 2147, project-id 390858490). Part of this work was carried out with the support of the Diamond Light Source, beamline I05 (Proposal No. SI22468-1). Part of the ARPES measurements were performed with the approval of the Proposal Assessing Committee of the Hiroshima Synchrotron Radiation Center (Proposal No. 19BU010). The work received funding from the DFG under Germany's Excellence Strategy–Cluster of Excellence Matter and Light for Quantum Computing (ML4Q) EXC 2004/1-390534769. J. I. F. acknowledges the support from the Alexander von Humboldt Foundation.

Corresponding author:
Hendrik Bentmann, University of Würzburg,
hendrik.bentmann@physik.uni-wuerzburg.de

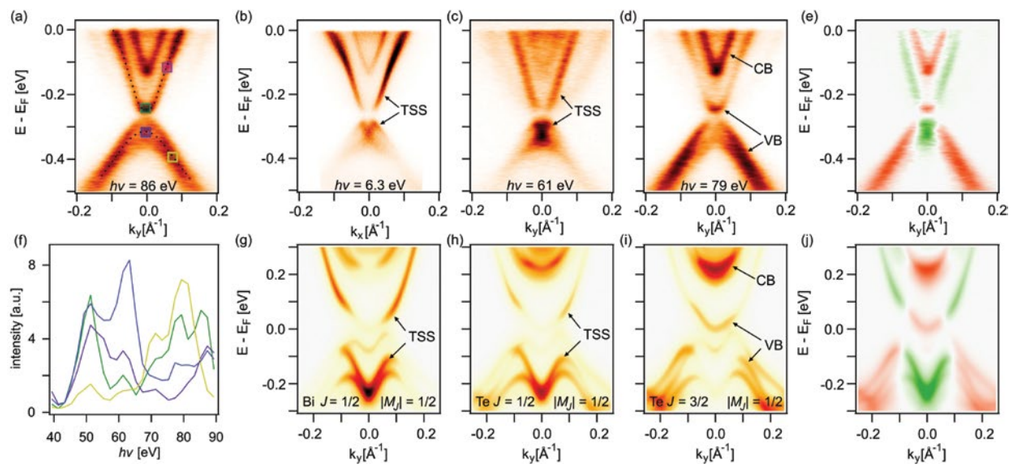

Figure 3: (a)-(d) Photon-energy-dependent ARPES data for the Bi_2Te_3-terminated surface of $MnBi_4Te_7$; (e) Intensity difference between datasets measured at photon energy hv = 61 and hv = 79 eV; (f) ARPES intensities traced as a function of hv at specific points in the band structure, indicated by boxes in (a); The colours of the boxes in (a) correspond to the respective data sets in (f); (g)–(j) Calculations of orbital-projected surface spectral densities for the Bi_2Te_3-terminated surface of $MnBi_4Te_7$; (j) Difference between the surface spectral densities projected on Bi J = 1/2 orbitals in (g) and Te J = 3/2, MJ = 1/2 orbitals in (i).

Magnetic Materials Group

Sarnjeet Dhesi, Science Group Leader

The Magnetic Materials Group (MMG) at Diamond Light Source develops and uses a range of polarised X-ray probes, including Resonant Inelastic X-ray Scattering (RIXS), Resonant Elastic X-ray scattering (REXS), X-ray Absorption Spectroscopy (XAS) and PhotoEmission Electron Microscopy (PEEM). Over the last year, our research community has used these probes to gain fundamental insights into new materials and how to tune materials to discover exotic new properties. In this contribution, we present research demonstrating how PEEM can map the antiferromagnetic textures in materials such as α-Fe_2O_3, which is under the spotlight for application in fast and energy-efficient computing. Learning how to control the formation of these textures could be the key to developing racetrack non-volatile memory for next-generation computing. Temperature-dependent REXS has uncovered a new magnetic order in ultra-thin $SrRuO_3$ films, which researchers believe corresponds to skyrmion lattice structure. This new quasi quantum particle could also soon be used for magnetic racetrack memory. We also present results reporting the successful synthesis of a 2D magnet with great potential for use in low-dissipation electronics. Combining the power of XAS and X-ray Magnetic Circular Dichroism (XMCD) allowed unambiguous determination of the atomic-scale magnetic properties of the epitaxial $CrTe_2$/graphene 2D magnets. Finally, RIXS is presently the only technique to measure magnetic excitations in momentum space from thin film samples only a few nanometers thick, a capability used here to investigate the structure of magnetic excitations in an infinite-layer nickelate (nickel oxide) superconductors. Revealing the microscopic electronic structures of the nickelate will inform the design and synthesis of new unconventional superconductors.

Racetrack memory, a concept initially proposed by IBM, uses magnetic textures to store information bits (ones and zeros) rather than charge. It involves creating tiny textures (whirls) in a uniform magnetic medium and storing or retrieving them by moving them along a magnetic track. As textures persist when there is no power, racetrack memory could be highly stable and energy efficient. The original designs for racetrack memory used ferromagnets, but recent research has shown that the textures move much faster in antiferromagnets. However, antiferromagnetic textures are harder to manipulate and even, visualise. The Nanoscience beamline (I06) gives researchers complete control over the X-ray beam properties, and using PEEM has enabled mapping of antiferromagnetic textures in exquisite detail. This is the first step towards gaining full control over the formation of these textures and their future application in fast, energy-efficient memory devices.

On the Materials and Magnetism beamline (I16), REXS has been used to search for direct evidence of magnetic skyrmions - swirls of magnetic moments - in ultra-thin $SrRuO_3$. The results showed a new magnetic order believed to be a Topological Hall effect (THE), the fingerprint of magnetic skyrmions. The unique topological properties of magnetic skyrmions make them a promising candidate for racetrack memory applications.

On I10, the Beamline for Advanced Dichroism Experiments (BLADE), XAS and X-ray Magnetic Circular Dichroism (XMCD) have been used to explore the synthesis of 2D magnets. As conventional electric and electronic devices waste energy as heat, new materials are needed to make them more energy efficient. 2D magnets are one promising option. However, producing them is challenging and understanding the synthesis process of 2D magnets and their microscopic properties is essential. The first successful synthesis of inch-scale epitaxial $CrTe_2$/graphene 2D magnets offers tremendous potential for future devices.

RIXS is presently the only technique that can extract magnetic excitations in the momentum space from thin film samples. On the RIXS beamline (I21), researchers used the high energy resolution and high photon flux to investigate the structure of magnetic excitations in $NdNiO_2$, an infinite-layer nickelate (nickel oxide) superconductor. An important focus of superconductor research at the moment is to characterise the differences and similarities between nickelate superconductors and the cuprate superconductors. This study suggests that, like cuprates, nickelates are strongly correlated electronic systems. This new information will help to design and produce new superconducting materials.

In the past year there has been considerable activity augmenting and improving the facilities of the MMG. A recent upgrade to I21 gives access to a higher energy range (~3keV) allowing, for example, RIXS studies of the complex ferroelectric and magnetic properties of 4*d* materials. The new 1.6T electromagnet facility on I10 is providing improved access to polarised spectroscopy measurements to explore trends in many samples of varying composition. On I16, the new polariser provides complete control of the X-ray polarisation down to ~3.3keV to further understand chiral magnetic materials. I06 has undergone a major upgrade with the installation of the new aberration-corrected PEEM and repurposing of the existing PEEM with a continuous-wave laser as the excitation source. The laser-based PEEM (funded by the EPSRC and developed with the Central Laser Facility) is to train the user community in using the many facilities of a PEEM, develop new sample environments and perform research through peer reviewed access. Looking to the years ahead, the MMG is developing a new beamline for Diamond-II for Coherent Soft X-ray Imaging and Diffraction. The CSXID beamline has been developed over the past two years with the help of a user working group with a final design planned for late 2022. The Magnetic Materials Group Laboratory also houses characterisation equipment allowing sample screening and inspection using SQUID magnetometry, Atomic Force Microscopy and X-Ray Diffraction and is set to expand its capabilities. Finally, the suite of MMG beamlines have migrated to a NeXus file structure allowing much richer sets of metadata to be captured which is an important first step toward automated data analysis, sample handling and data comparison between different sources.

"The goal of the Magnetic Materials Group is to operate state-of-the-art polarised X-ray beamlines with leading-edge data acquisition, data logging and data analysis software."

I21 beamline at Diamond Light Source

Magnetic excitations in infinite-layer nickelates superconductors

Related publication: Lu, H., Rossi, M., Nag, A., Osada, M., Li, D. F., Lee, K., Wang, B. Y., Garcia-Fernandez, M., Agrestini, S., Shen, Z. X., Been, E. M., Moritz, B., Devereaux, T. P., Zaanen, J., Hwang, H. Y., Zhou, K.-J., & Lee, W. S. Magnetic excitations in infinite-layer nickelates. *Science* **373**, 213–216 (2021). DOI: 10.1126/science.abd7726

Publication keywords: High Tc superconductor; Strongly correlated electronic system; Nickelate; RIXS

Since the 1986 discovery of cuprates (copper oxide materials that are superconducting at high temperatures), scientists have been searching for materials that are superconducting at closer to room temperature.

The discovery of infinite-layer nickelate (nickel oxide) superconductors has drawn a lot of attention. An important research focus is to characterise similarities and differences between the nickelates and the high-temperature cuprate superconductors.

A key question regards whether the nickelate superconductors are strongly correlated electronic systems, like cuprates. Investigating the structure of magnetic excitations in the nickelate can provide needed clarity to this question.

A team of researchers from the SLAC National Accelerator Laboratory, Stanford University and Diamond Light Source recently made the first measurements of magnetic excitations that spread through the new material like ripples in a pond.

On Diamond's Resonant Inelastic X-ray Scattering beamline (I21), they collected data using the Resonant Inelastic X-ray Scattering (RIXS) instrument. RIXS is presently the only instrument that can extract magnetic excitations in the momentum space from thin film samples. The high energy resolution and high photon flux available at I21 also played a vital role in the success of this experiment.

In undoped $NdNiO_2$, they observed a branch of dispersive magnetic excitations with a bandwidth of approximately 200 meV, suggesting that the spins are strongly antiferromagnetically coupled. These results provide a direct piece of experimental evidence that support the possible exhibition of strong correlations in infinite-layer nickelates.

This work reveals the microscopic electronic structures of the nickelate, informing the design and synthesis of new unconventional superconductors.

Understanding the rich phenomenon in high temperature superconducting cuprates is one of the important questions in condensed matter physics. Not only the mechanism of the superconductivity, but also unsolved questions such as the origin of the strange metal phase and the implication of intertwined orders have pushed the limits of established theory paradigm. To tackle these challenges, tremendous amount of effort has been spent on synthesising materials with different transition metal ions that mimic the electronic and spin structures of cuprates. This goal, however, proves to be difficult to achieve. The recent discovery of superconductivity in doped mono-valence infinite nickelate is a game-changer[1]. Their crystal structures are very similar to that of cuprates, with NiO_2 planes separated by spacer layers that only contain some rare-earth ions. They were predicted to be isoelectronic to the cuprates: monovalent Ni^{+} characterised by the same $3d9$ state as Cu^{2+} in the cuprates[2,3]. Yet, at this early stage of nickelate superconductivity research, microscopic characterisations from experiments are needed to clarify the similarity and difference between the nickelate and cuprate superconductors[4,5].

A key issue is whether the infinite-layer nickelates also exhibit strong correlation effects arising from a strong on-site Coulomb interaction U, which is known to be a critical ingredient responsible for the rich cuprate phenomenonology. One of the key signatures of a strong U is the manifestation of an intense antiferromagnetic exchange interaction *J* between neighbouring spins, like those found in cuprates. As for the infinite-layer nickelates, whether a strong U exists is considerably uncertain, as the atomic d-orbitals of monovalent Ni^{+} are more extended than those of divalent Cu^{2+}. The difference in the spatial distribution can have a substantial influence on the magnitude of U, which would consequently affect the strength and the sign of *J*. Indeed, while theories mostly predict an antiferromagnetic coupling

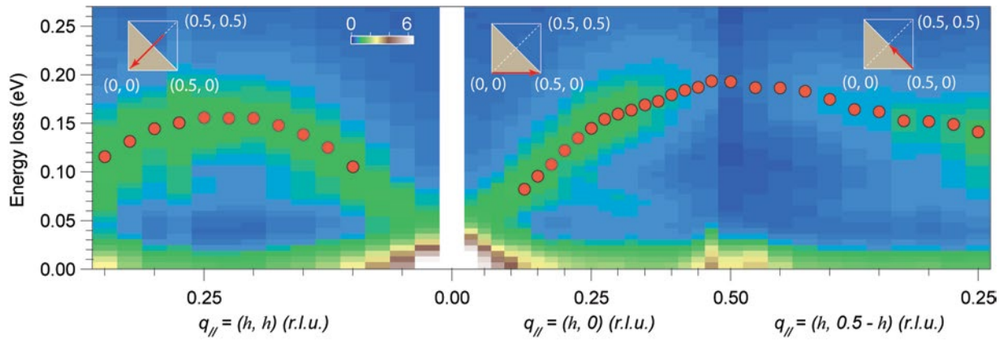

Figure 1:RIXS intensity maps versus energy loss and projected in-plane momentum transfer along three high-symmetry directions, as indicated by red arrows in the insets which show a Brillouin zone with the first AFM zone shaded. Measurements were taken at 20 K. The red circles indicate peak positions of the magnetic excitation spectra.

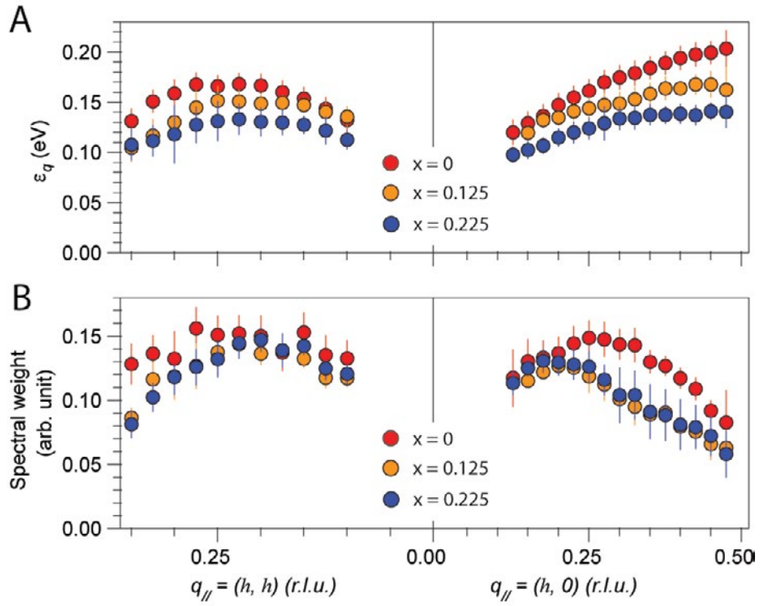

Figure 2: Summary of (A) mode energy and (B)spectral weight for three different doping concentrations.

between neighbouring spins in the infinite-layer nickelates, the energy scale of *J* did not reach a consensus: some theories suggest *J* to be one order of magnitude smaller than in cuprates owing to a large charge transfer energy, whereas some others argue differently. Thus, it is important to directly probe the magnetic structure to clarify this important issue.

The main result of this work is the direct observation of magnetic excitations in infinite-layer nickelates $Nd_{1-x}Sr_xNiO_2$. Raw RIXS intensity map taken on an undoped $NdNiO_2$ film (Fig. 1) clearly reveals a branch of magnetic excitations, which exhibit a significant dispersion in the energy-momentum space. The dispersion emanates from the zone centre and reaches maxima at (0.5, 0) and (0.25, 0.25). In addition, the spectral intensity is suppressed near (0.5, 0). Note that the magnetic excitations do not exhibit obvious dispersion along the c-axis, indicating that they are quasi-two-dimensional. The gross features of the dispersion and spectral weight bear a striking resemblance to spin-1/2 Antiferromagnet (AFM) magnons on a 2D square lattice, lending a strong support that the spin exchange interaction in the $NdNiO_2$ is indeed antiferromagnetic. Importantly, the energy scale of the band width is approximately 0.2 eV, which is comparable to that found in the parent cuprates (~ 0.3 – 0.4 eV) and notably higher than other nickelates. By fitting the dispersion to a linear spin wave theory, we obtain the nearest-neighbour coupling $J1 = 63.6 \pm 3.3$ meV, and a sizable next-nearest-neighbor coupling $J2 = -10.3 \pm 2.3$ meV.

The authors also measured doping evolution of the magnetic excitations in $Nd_{1-x}Sr_xNiO_2$ from x = 0 to 0.225, across the superconducting phase boundary. Upon doping, the mode energy (Fig. 2A) mildly softens and the spectral weight (Fig. 2B) slightly reduces, accompanied with significant broadened spectrum suggesting that the mode becomes overdamped. These behaviours are in fact consistent with spin dilution as expected in a doped Mott insulator as some spins are replaced by holes, indicating the potential relevance of Mott-physics in sculpting the electronic structures of the infinite-layer nickelates.

Overall, while the gross feature of the magnetic excitations in nickelate superconductors are similar to those in cuprates, subtle but important differences are observed. First, undoped cuprates are insulators, and the magnetic excitations are sharply defined due to the existence of a long-ranged antiferromagnetic order. In contrast, the undoped nickelate $NdNiO_2$ is metallic due to the involvement of the Nd $5d$ states, which significantly damp the magnetic excitations. In addition, whether an AFM order exists in the undoped compound remains an important open question. The authors note that the doping dependence of the magnetic excitations is also different from the paramagnon in cuprates, which they attribute this difference to a possibly less active longer-range charge dynamics in the nickelates. they anticipate that these observations can further constrain the theories. Importantly, the results establish that the nickelate superconductor possesses a strong antiferromagnetic interaction, placing the material in the strong U regime. This implies that strong correlation effects should be also at play in the nickelate superconductors, laying a foundation for future studies.

References:

1. Li, D. *et al.* Superconductivity in an infinite-layer nickelate. *Nature* **572**, 624–627 (2019). DOI: 10.1038/s41586-019-1496-5
2. Anisimov, V. I. *et al.* Electronic structure of possible nickelate analogs to the cuprates. *Physical Review B* **59**, 7901–7906 (1999). DOI: 10.1103/PhysRevB.59.7901
3. Lee, K.-W. *et al.* Infinite-layer $LaNiO_2$: Ni^{1+} is not Cu^{2+}. *Physical Review B* **70**, 165109 (2004). DOI: 10.1103/PhysRevB.70.165109
4. Mitchell, J. F. A nickelate renaissance. *Frontiers in Physics* **9** (2021). DOI : 10.3389/fphy.2021.813483
5. Botana, A. S. *et al.* Low valence nickelates: Launching the nickel age of superconductivity. *Frontiers in Physics*, **9**. (2022). DOI: 10.3389/fphy.2021.813532

Funding acknowledgement:
This work is supported by the U.S. Department of Energy (DOE), Office of Science, Basic Energy Sciences, Materials Sciences and Engineering Division, under contract DE-AC02-76SF00515. We acknowledge the Gordon and Betty Moore Foundation's Emergent Phenomena in Quantum Systems Initiative through grant number GBMF4415 for synthesis equipment.

Corresponding author:
Dr. Wei-Sheng Lee, SLAC National Accelerator Lab, leews@stanford.edu

Skyrmion lattice observation of ultra-thin $SrRuO_3$ heterostructure

Related publication: Sohn, B., Kim, B., Park, S. Y., Choi, H. Y., Moon, J. Y., Choi, T., Choi, Y. J., Zhou, H., Choi, J. W., Bombardi, A., Porter, D. G., Chang, S. H., Han, J. H., & Kim, C. Stable humplike Hall effect and noncoplanar spin textures in $SrRuO_3$ ultrathin films. *Physical Review Research* **3**, (2021). 023232. DOI: 10.1103/PhysRevResearch.3.023232

Publication keywords: Skyrmion; Magnetic texture; Topological Hall effect

The search is on for the next generation of information carriers. Ideal candidates need to be stable against external disturbances such as temperature or field fluctuations, allow for low-power manipulation and easy readout, and have a small footprint that allows for high packing densities.

Magnetic skyrmions – swirls of magnetic moments – have unique topological properties that make them promising candidates for the next generation of computer storage devices. Crystalline magnetic skyrmions are among the most promising replacements for conventional ferromagnetic computer memory.

Chiral spin structures have non-trivial Berry curvature in real space or emergent electromagnetic fields, leading to topological Hall effects. Recent studies show that chiral spin structures can exist in oxide thin film heterostructures with Dzyaloshinskii-Moriya Interactions (DMI) generated due to its Inversion Symmetry Breaking (ISB). Previous research reported progress in observing topological Hall effects in a few-layer thick $SrRuO_3$ (SRO) grown on top of a single crystal $SrTiO_3$ (001) substrate without any heavy-metal capping layer.

Researchers looking for direct evidence of the existence of magnetic skyrmions in ultra-thin $SrRuO_3$ films used temperature-dependent Resonant Elastic X-ray Scattering (REXS) on the Materials and Magnetism Beamline (I16). They observed exciting Hall effect data, the fingerprint of magnetic skyrmions.

Their results showed a new magnetic order with the same temperature dependence topological Hall effects, which they believe corresponds to skyrmion lattice structure. This new quasi quantum particle could soon be used for magnetic racetrack memory.

Skyrmions are topologically stable spin whirling configurations in magnetic materials. In addition to their importance in fundamental science, they possess high potential for future device applications. It is known that skyrmions in a magnetic system are stabilised by the Dzyaloshinskii-Moriya Interaction (DMI), forming a unique topological spin whirling texture. A notable example is $SrRuO_3$ (SRO), a prototypical ferromagnet with inversion symmetry. SRO in heterostructures was recently shown to be a platform for skyrmion formation. Here, the authors present a resonant X-ray diffraction experiment, using resonant scattering at the Ru $L_{2,3}$ absorption edge to observe the spin texture of an ultra-thin SRO system. They believe that this experiment will be a critical building block for the study of skyrmion structure in a real space system.

Illustrated in Fig. 1(a) are the electric transport results on SRO. The Topological Hall Effect (THE) exists as clear humps and disappears near the coercive field where the Anomalous Hall Effect (AHE) undergoes a sign change. The THE is a novel quantum state where electrons moving through a non-coplanar magnetic field acquire a Berry curvature and are only accessible under particular circumstances and is often formed by the swirling magnetic texture of skyrmion quasi-particles. At the lowest temperature of 2 K, the THE persists over the 0.6 - 1.6 T range, demonstrating that the THE in SRO thin films is extremely robust compared to other materials that host skyrmions over much weaker fields. The Hall effect data under the external magnetic field tilting are plotted in two different ways in Fig. 1(b), using either the total magnetic field or the perpendicular field as the variable for the plot. As we can see, the THE still exists up to 85 degrees in the in-plane geometry of the external magnetic field.

Compared to similar field-tilt experiments in EuO_2, $FeGe_2$, and GaV_4, the ultra-thin SRO shows an exceptionally wide phase diagram region of THE stability under the field tilting. Figure 1(c) represents the phase diagram at 10 K for the 4 u.c. SRO film, as deduced from the Hall effect measurement data. The two components refer to the in-plane and out-of-plane magnetic field, respectively. As presented in this phase diagram, THE area is extremely wide compared to the other Skyrmion system. Therefore, this ultra-thin SRO system is critically important to study magnetic skyrmions for real application considering this robustness.

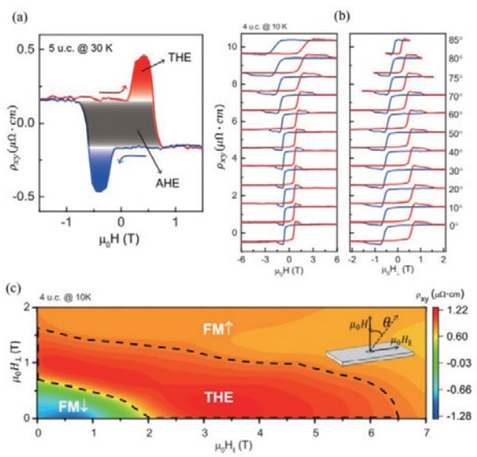

Figure 1: (a) Hall effect measured for 5 u.c. SRO at 30 K. The curves contain contributions from both AHE and THE, while the humps are due to the THE; (b) Hall resistivity at various angles of field inclination. The same data is plotted using the x-axis of total external magnetic field, and out-of-plane magnetic field; (c) Phase diagram in the plane of parallel and perpendicular components of the external magnetic field. (Inset) Schematics of our experiment with the tilt angle indicated.

A Resonant Elastic X-ray Scattering (REXS) experiment was performed at beamline I16 at Diamond Light Source. REXS was measured at the Ru L_2 absorption edge with linear polarisation. A 6-circle diffractometer allowed the authors to optimise scattering from this thin-film sample using a grazing incidence diffraction geometry around the forbidden reflection (1, 1, 1/2). The X-ray path length at this energy and angle is roughly 30 nm and in this geometry, the horizontal X-ray polarisation is ~60 degrees from the scattering plane. Air scattering was reduced with use of a helium-filled bag and an ultra-high gain, vacuum-enclosed Pilatus3-100 K area detector. A closed-cycle cryo-cooler was used to control temperature. SRO thin films were mounted directly to a copper plate using conductive silver paint. A permanent magnet was mounted directly below the plate, with a measured field on the sample H = 0.47 T, providing a steady magnetic field in order to measure the temperature dependence of the topological Hall effect in this system.

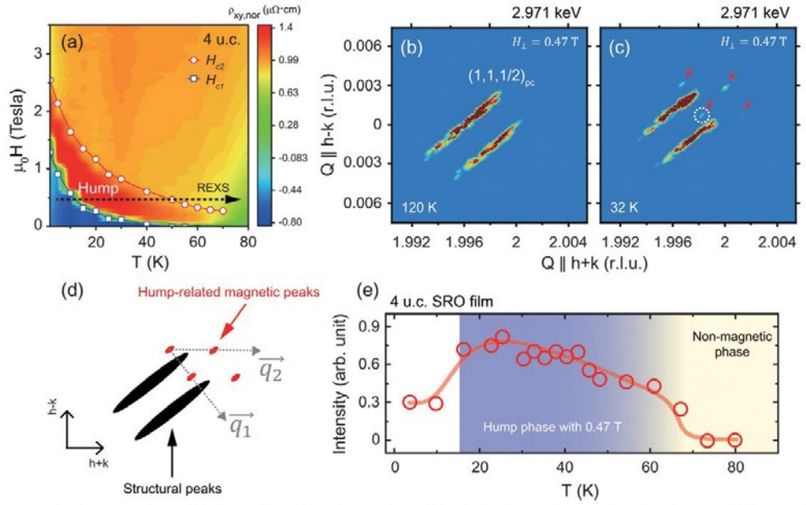

Figure 2: Hump structure related magnetic order in a SRO ultrathin film. (a) Phase diagram of 4 u.c. SRO in the (T, $\mu_0 H$) plane; Resonant Elastic X-ray Scattering (REXS) was performed as a function of temperature with $\mu_0 H = 0.47$ T; (b); (c) Reciprocal Space Mapping (RSM) of REXS around SRO (1, 1, 1/2)$_{pc}$ reflection under a magnetic field of 0.47 T at 120 and 32 K, where pc denotes pseudocubic. Additional peaks are shown at 32 K (red arrows); (d) Schematic description of REXS features around SRO (1, 1, 1/2)$_{pc}$ reflection. Black stripy (red dotted) patterns are structural (hump-related magnetic) peaks. An incommensurate magnetic modulation vector, q1, is aligned along the direction of the step terrace, whereas q2 is tilted from the step terrace; (e) Temperature-dependent intensity of hump-related magnetic peaks [white dotted circle in panel (c)].

It has been demonstrated that hump structures in Hall Effect measurement results could originate from noncoplanar spin order such as a skyrmion lattice[1]. However, there is another possibility which is inhomogeneity of Anomalous Hall Effect. Thus, if there is a real noncoplanar spin structure, hidden magnetic orders might emerge with humplike features in a 4 u.c. SRO ultrathin film. And the REXS is a powerful and critical experimental method to directly observe a magnetic order in reciprocal space[2].

Figure 2(a) represents the experimental range of the REXS measurements in the temperature-field phase diagram of Hall measurement for the 4 u.c. SRO film. Figures 2(b) and 2(c) show Reciprocal Space Mapping (RSM) results of REXS measurement under 0.47 T at 120 and 32 K, respectively. At (1, 1, 1/2) pc (pc denotes pseudocubic), the authors observed very weak and nearly temperature-independent diffraction patterns, which can originate from the crystal truncation rods or cation displacement. As shown in Fig. 2(b), only stripy patterns are observed at 120 K. The separation between the stripes in the reciprocal space is 0.0028 $Å^{-1}$ and can be converted into the distance of ~220 nm in real space, which is consistent with the width of step terraces measured by Atomic Force Microscopy. Upon decreasing the temperature to 32 K, the SRO film entered into the hump phase in Fig. 2(a). Then, extra peaks around the stripes appear in the RSM as indicated by red arrows in Fig. 2(c) and Fig. 2(d) illustrates that black and red peaks resulted from the step terraces and emergent magnetic order at low temperature, respectively. One set of magnetic wavevectors is aligned parallel to the step-terace direction and another is tilted from the step-terrace. To confirm the correlation between hump phase and the emergent magnetic peaks, the authors plotted the intensity of emergent magnetic peaks as a function of temperature (Fig. 2(e)). The phase crossover temperatures from hump to ferromagnetic and from ferromagnetic to nonmagnetic phases were approximately 15 and 60 K, respectively, with $\mu_0 H \sim 0.47$ T. At both of the crossover temperatures, they clearly observed the abrupt change of intensity of the emergent magnetic peaks. Considering the strong correlation between the hump phase and the intensity of emergent peaks, the authors propose that the emergent magnetic order is responsible for the humplike feature.

Based on this REXS observations presenting emergent magnetic order and theoretical analysis with recent XMCD imaging studies[3, 4], the authors believe that the humplike feature in Hall effect measurement is attributed to the non-coplanar spin order and can be interpreted as Topological Hall Effect.

References:

1. Yu, X. Z. *et al.* Real-space observation of a two-dimensional skyrmion crystal. *Nature* **465**, 901–904 (2010). DOI : 10.1038/nature09124
2. Zhang, S. L. *et al.* Direct experimental determination of spiral spin structures via the dichroism extinction effect in resonant elastic soft X-ray scattering. *Physical Review B* **96**, 094401 (2017). DOI: 10.1103/PhysRevB.96.094401
3. Huang, H. *et al.* Detection of the chiral spin structure in ferromagnetic $SrRuO_3$ thin film. *ACS Applied Materials & Interfaces* **12**, 37757–37763 (2020). DOI: 10.1021/acsami.0c10545
4. Sohn, B. *et al.* Hump-like structure in Hall signal from ultra-thin $SrRuO_3$ films without inhomogeneous anomalous Hall effect. *Current Applied Physics* **20**, 186–190 (2020). DOI: 10.1016/j.cap.2019.10.021

Funding acknowledgement:
This work is supported by IBS-R009-D1 through the IBS Center for Correlated Electron Systems. The work at beamline I16 of the Diamond Light Source was performed under Proposals MM22181.

Corresponding author:
Dr. Bongju Kim, Seoul National University, bongju@snu.ac.kr

The discovery of inch-scale room-temperature 2D magnets

Related publication title and DOI: Zhang, X., Lu, Q., Liu, W., Niu, W., Sun, J., Cook, J., Vaninger, M., Miceli, P. F., Singh, D. J., Lian, S.-W., Chang, T.-R., He, X., Du, J., He, L., Zhang, R., Bian, G., & Xu, Y. Room-temperature intrinsic ferromagnetism in epitaxial CrTe2 ultrathin films. *Nature Communications* **12**, 2492 (2021). DOI: 10.1038/s41467-021-22777-x

Publication keywords: 2D magnets; Ultrahigh vacuum (UHV); Molecular beam epitaxy (MBE); X-ray Magnetic Circular Dichroism (XMCD); Angle-Resolved Photoemission Spectroscopy (ARPES)

Electrical and electronic devices produce and dissipate heat, an undesirable energy loss. The search is therefore on for new materials for low-dissipation electronics. 2D magnets have great potential for this application; however, synthesising inch-scale 2D magnetic thin films is challenging. Mechanical exfoliation is a useful technique for producing research samples, but only produces micrometre scale thin films.

Therefore, an international team of researchers is investigating the synthesis process (growth recipe) of inch-scale 2D magnets and their microscopic properties. Understanding both of these is a prerequisite for developing devices based on these materials.

They successfully synthesised the first inch-scale epitaxial $CrTe_2$/graphene 2D magnets with a ferromagnetic order persisting up to room temperature. Their Ultrahigh Vacuum (UHV) based Molecular Beam Epitaxy (MBE) technique has been shown to be a critical tool for material discovery.

The team performed X-ray Absorption Spectroscopy (XAS) and X-ray Magnetic Circular Dichroism (XMCD) measurements on the Beamline for Advanced Dichroism Experiments (I10) at Diamond Light Source. I10 is equipped with a state-of-the-art XMCD end station that enabled the unambiguous determination of the atomic-scale magnetic properties of the epitaxial $CrTe_2$/graphene 2D magnets.

Devices based around 2D magnets are rapidly emerging. Their advantages include inherently sharp interfaces, ease of fabrication and low dissipation. The successful MBE growth of 2D ferromagnetic $CrTe_2$ films with room-temperature ferromagnetism opens a new avenue for developing large-scale 2D magnet-based spintronics devices. This work offers tremendous potential for future devices, as the films produced can readily reach wafer size.

Two-Dimensional (2D) magnets exhibit novel phases of quantum matter with abrupt transition in the magnon density of states in atomically thin layers. While the presence of 2D materials with intrinsic magnetism has been revealed recently[1-3], their intrinsic Ferromagnetic (FM) order is typically fragile with a low Curie temperature (T_C) as a result of the large spin fluctuation in 2D. On the other hand, most of the 2D magnets synthesised so far are thin flakes exfoliated from their bulk counterparts with a typical size of several micrometres. There is a pressing need for obtaining inch-scale epitaxial 2D magnets with intrinsic FM persisting up to high temperatures so that any devices based around these materials would become possible.

Recently we have successfully synthesised the first inch-scale monolayer $CrTe_2$ thin films on graphene in Ultrahigh Vacuum (UHV) using the Molecular Beam Epitaxy (MBE) technique. Previous work[4] has shown that MBE growth is the key to obtain the highest quality single-crystalline thin films and enable designer heterostructures in a way that is compatible with semiconductor manufacture. With the synchrotron-based X-ray Magnetic Circular Dichroism (XMCD) technique, we have unambiguously obtained a robust FM order of these $CrTe_2$/graphene thin films with an atomic magnetic moment of ~0.21 μ_B/atom and Perpendicular Magnetic Anisotropy (PMA) constant (K_u) of 4.89 $\times 10^5$ erg/cm^3 at room temperature. In-house Angle-Resolved Photoemission Spectroscopy (ARPES) studies also reveal a splitting of majority and minority band dispersions with ~0.2 eV at the gamma point.

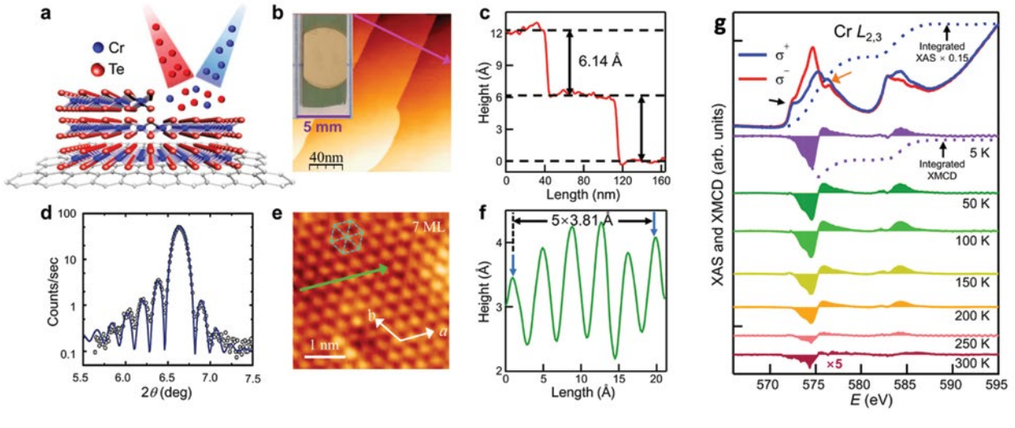

Figure 1: As-grown material characterisation and XMCD spectra. (a) Illustration of the co-evaporation process in UHV; (b) Typical in-situ STM image; (c) Step profile of (b); (d) Fitted XRD spectrum; (e) Zoom-in STM image with hexagonal features; (f) Step profile of (e); (g) XAS and XMCD spectra between 5 K and 300 K.

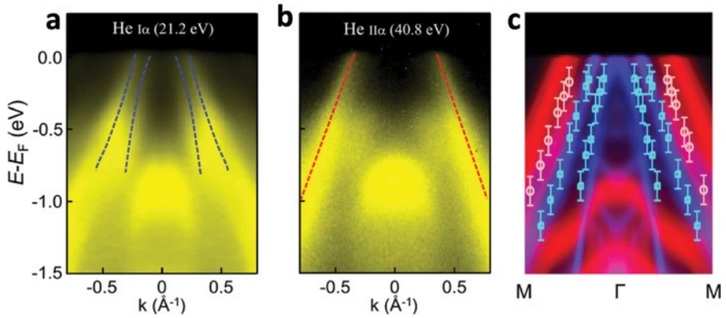

Figure 2: Valence-band dispersion near the Fermi level obtained with (a) He Ia (21.2 eV) and (b) He IIa (40.8 eV), fitted with the DFT calculated bands; (c) along the high symmetry direction M-Γ-M. The blue and red dashed lines indicate the position of hole pockets measured by He Ia and He IIa photons, respectively.

The 2D magnet $CrTe_2$ has a layered trigonal crystal structure as illustrated in Fig. 1a. Each unit cell consists of a hexagonal Cr layer sandwiched by two Te layers. The $CrTe_2$ thin films used in this work were grown on a bilayer graphene/SiC(1111) substrate in an integrated MBE-STM system with base pressure below 2×10^{-10} mbar. The bilayer graphene acts as a buffer layer to support the high-quality layer-by-layer epitaxial growth of the $CrTe_2$ films. The in-situ Scanning Tunnelling Microscopy (STM) has enabled an accurate determination of the microscopic topography of a few-layer $CrTe_2$ in their pristine state as shown in Fig. 1b-c: atomically flat terrace features can be clearly seen and a typical step height of 6.14 Å which is consistent with the thickness of the unit cell of $CrTe_2$ crystal in 1*T* phase. Note the STM characterisation performed for all thicknesses (i.e. 1-15 monolayers or MLs) of the as-grown epitaxial $CrTe_2$/graphene thin films are highly consistent, suggesting a well optimised growth process and high homogeneity of the samples.

There are various stable stoichiometries for chromium chalcogenides [*e.g.*, CrTe, $CrTe_2$, Cr_2Te_3, and Cr_5Te_8] depending on the Cr vacancies that occur in intercalation. Among them only $CrTe_2$ compounds are genuinely 2D materials. The layered surface morphology with a uniform step height obtained via STM suggests that the films are in a single phase. This is consistent with the X-ray Diffraction (XRD) 2θ-ω scans (Fig. 1e) where the perpendicular constant c = 6.13 Å agrees with the (001) crystal planes of the 1*T*-type hexagonal structure. The reflectivity curves show Laue fringes, attesting to the structural coherence of the films. Crystal structure and lattice parameters are critical information as we now know that they can alter the nature of a magnetic exchange coupling: bulk 1*T*-$CrSe_2$ with lattice constants of a = 3.39 Å and c = 5.92 Å shows an Antiferromagnetic (AFM) order,5 in contrast to the FM phase in $CrTe_2$ (a = 3.79 Å, c = 6.10 Å), for example.

The atomic scale magnetic properties of the $CrTe_2$/graphene epitaxial thin films were studied using the synchrotron-based XMCD techniques at beamline I10 at Diamond Light Source. High intensity circularly polarised X-rays were used in normal incidence with respect to the sample plane and parallel to the applied magnetic field. The XMCD was obtained by taking the difference of the XAS spectra by flipping the X-ray helicity at a fixed magnetic field of 10 kOe, under which the sample is fully magnetised with negligible paramagnetic contribution. The observed XAS spectral line shape is in line with that of spinel compounds with trivalent Cr cations on O_h sites, providing a further spectroscopic fingerprint of 1*T*-type $CrTe_2$ with predominately Cr^{3+} cations. XMCD and XAS measurements were repeated at elevated temperatures, and the dichroism of the thin film at Cr L_3 edge persists up to 300 K. The sum-rules derived spin moments (ms) of Cr exhibit a Curie-like behaviour. A remarkably large value of ms (2.85 ± 0.10 μ_B/atom) was obtained at 5 K. It retains a sizable value of 0.82 ± 0.10 μ_B/atom at 250 K and drops to 0.21 ± 0.05 μ_B/atom at 300 K.

The electronic band structure of $CrTe_2$ thin films has been mapped via an in-house ARPES measurement with two different photon energies of 21.2 eV and 40.8 eV at 107 K, and the origin of the band dispersions has been investigated by first-principle density function theory (DFT) calculations. The metallic state of the $CrTe_2$/graphene has been attributed to the hybridisation of Te-5*p* and Cr-3*d* orbitals crossing the Fermi level at the centre of the Brillouin zone. We have further studied the thickness dependencies of hole pocket features in the energy dispersion spectra. In general with the increasing film thickness, the Fermi level moves towards the valence band with the band shape invariant.

To conclude the authors have successfully synthesised the first inch-scale epitaxial $CrTe_2$/graphene 2D magnets with a FM order persisting up to room temperature. The UHV-based MBE technique has been proven to be a critical tool for material discovery and unambiguous determination of the material properties at the atomic-scale as enabled by the synchrotron. The project was an international collaboration between the teams of Royal Holloway (UK), University of Missouri (US), and Nanjing University (China). The very helpful beamline team of I10, Dr Paul Steadman, Dr Peter Bencok, Dr Raymond Fan, and Mark Sussmuth, has provided technical support to make this work possible.

References:

1. Gong, C. et al. Discovery of intrinsic ferromagnetism in two-dimensional van der Waals crystals. *Nature* **546**, 265–269 (2017).DOI: 10.1038/nature22060
2. Huang, B. *et al.* Layer-dependent ferromagnetism in a van der Waals crystal down to the monolayer limit. *Nature* **546**, 270–273 (2017). DOI: 10.1038/nature22391
3. Deng, Y. *et al.* Gate-tunable room-temperature ferromagnetism in two-dimensional Fe_3GeTe_2. *Nature* **563**, 94–99 (2018). DOI: 10.1038/s41586-018-0626-9
4. Liu, S. *et al.* Two-dimensional ferromagnetic superlattices. *National Science Review* **7**, 745–754 (2020). DOI: 10.1093/nsr/nwz205
5. Freitas, D. C. *et al.* Antiferromagnetism and ferromagnetism in layered 1*T*-$CrSe_2$ with V and Ti replacements. *Physical Review B* **87**, 014420 (2013). DOI: 10.1103/PhysRevB.87.014420

Funding acknowledgement:
This work is supported by UK EPSRC (EP/S010246/1), UK Leverhulme Trust (LTSRF1819\15\12), UK Royal Society (IEC \NSFC\181680), US National Science Foundation (NSF- DMR#1809160), National Key Research and Development Program of China (No. 2016YFA0300803, No. 2017YFA0206304.

Corresponding author:
Wenqing Liu, Royal Holloway University of London, wenqing.liu@rhul.ac.uk

Magnetic whirls join the race for new computing paradigms

Related publication: Jani, H., Lin, J.-C., Chen, J., Harrison, J., Maccherozzi, F., Schad, J., Prakash, S., Eom, C.-B., Ariando, A., Venkatesan, T., & Radaelli, P. G. Antiferromagnetic half-skyrmions and bimerons at room temperature. *Nature* **590**, 74–79 (2021). DOI: 10.1038/s41586-021-03219-6

Publication keywords: Magnetism; Spintronics,; Information technology

Racetrack non-volatile memory, developed by IBM, is one of the most innovative information technology concepts to emerge in the past two decades. It works by creating tiny 'disturbances' in an otherwise uniform magnetic medium, stored and retrieved by moving them along a track. The difficulty of stabilising the disturbances and propelling them at high speed has prevented the racetrack concept from reaching the market.

The original racetrack concept employed *ferromagnets* – materials in which the magnetic atoms all point in the same direction. However, recent research has shown that disturbances can travel much faster in *antiferromagnets* (with the magnetic atoms pointing in opposite directions).

In a previous investigation at Diamond Light Source, an international team of researchers discovered that the antiferromagnetic material α-Fe_2O_3 supports a family of vortex-like disturbances (known as antiferromagnetic textures) that are potentially very stable.

The team is now investigating how to gain full control over the formation of these textures. Antiferromagnetic textures are much more difficult to visualise than their ferromagnetic counterparts, requiring the powerful imaging techniques available at Diamond. The Nanoscience beamline (I06) delivers full control over the X-ray beam properties, allowing the researchers to map the antiferromagnetic textures in exquisite detail. Using X-ray Photo-Emission Electron Microscopy (X-PEEM), they acquired images of these textures over a field of view of a few microns.

a-Fe_2O_3 is under the spotlight for application in fast and energy-efficient computing and being able to create magnetic textures in this material easily is extremely exciting. Understanding the formation and control of such textures and their potential application in energy efficient computing represents a significant milestone in the field of information and communication technology.

The information and communication technology ecosystem has been transformed over the last 60 years due to the rapid density and cost scaling of charge-based silicon transistors, a phenomenon popularly dubbed as the '*Moore's Law*'. While this has increased computer accessibility worldwide, with ~10 billion connected devices, it consumes a lot of energy and contributes more than 2% of the world emissions (on par with aviation). With the rise of Big Data, Artificial Intelligence, Internet of Things (IoT) and mobile-computing, the overall computing energy demand is expected to a rise exponentially. This has resulted in a quest for novel 'beyond-Moore' computing paradigms, which explore energy-efficient 'normally-off' non-volatile memory, combined with unconventional processing architectures (such as logic-in-memory or brain-inspired reservoir computing).

One of the most innovative information technology concepts that emerged in the past two decades is the so-called *racetrack memory*, proposed by IBM[1] in the mid-2000's. This involved the use of *magnetic patterns* (also known as 'magnetic textures') instead of *charges* to store information bits ('0' and '1'). These textures remain stable even in the absence of external power, making them highly energy efficient. Typically, one creates tiny textures (such as magnetic walls or 'whirls') in an otherwise uniform magnetic medium, which can be stored by 'parking' them along a magnetic track and retrieved by pushing them along the same track when needed. This racetrack concept has not reached the market yet, largely due to the difficulty of stabilising the textures and propelling them at high speed. To make progress, a new concept was needed.

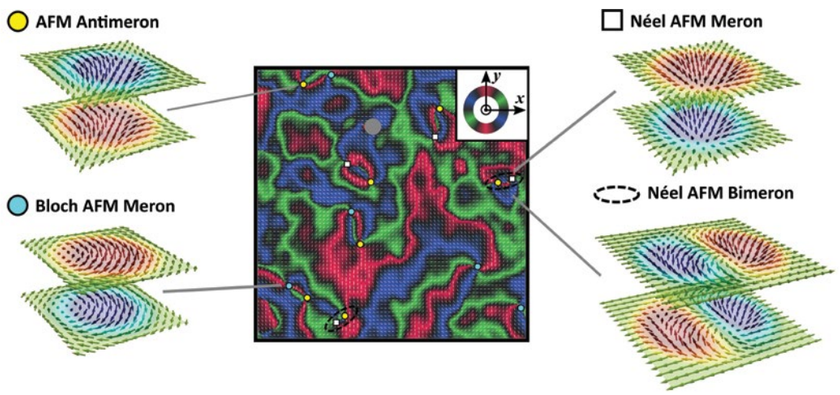

Figure 1: (Centre) X-PEEM vector map of antiferromagnetic textures at room temperature in a-Fe_2O_3. Red-Green-Blue colours represent the axis of the antiferromagnetic directions (Adapted from Ref 2). The four insets (left and right) show the schematics of magnetic arrangements in merons (blue circles and white squares), antimerons (yellow circles) and bimerons (dashed black ellipses). Their antiferromagnetic nature is shown schematically as two adjacent and oppositely aligned magnetic layers.

Figure 2: Artist's impression of whirling textures in a-Fe_2O_3 racetracks created after performing a magnetic transition analogous to the Big Bang cooling.

The original racetrack concept employed *ferromagnets* – materials in which magnetic atoms all point in the same direction. Recent research has instead focused on *antiferromagnets*, which are made of alternate atoms pointing in opposite directions (N/S/N, E/W/E etc.). This special arrangement makes antiferromagnets very stable and robust. Moreover, it has been theoretically predicted that textures in such materials (*e.g.*, antiferromagnetic whirls), would also be very scalable down to small sizes and would travel at ultra-fast speeds (up to few km/s) – making them ideal to build dense, fast and energy-efficient racetracks.

While the alternating atomic arrangement in antiferromagnets is highly beneficial, it also makes the *detection* and *control* of tiny antiferromagnetic textures very difficult via standard magnetic techniques. These are the two major barriers hindering experimental progress in this field. The recent study published in *Nature*[2] was aimed at addressing these very issues.

Firstly, to *visualise* antiferromagnetic textures the authors used the powerful X-ray microscope at the I06 Beamline to perform X-ray Photo-Electron Emission Microscopy (X-PEEM). The X-PEEM technique generates images of magnetic textures by collecting electrons emitted following the absorption of carefully polarised X-ray beams. Building on previous work[3], they exploited the full control over the X-ray beam properties and sample orientation, allowing to map out the antiferromagnetic textures in exquisite nanoscopic detail (Fig. 1).

Secondly, to *control* the formation of antiferromagnetic whirls, the authors focussed on the antiferromagnet α-Fe_2O_3, which is extremely abundant and cheap (it is a main constituent of rust). Having discovered in a previous investigation at Diamond that α-Fe_2O_3 supports a family of vortex-like textures that are potentially very stable[3], the next step was to gain reproducible control over the formation and evolution of these textures.

To realise this, the authors drew inspiration from a celebrated idea in cosmological physics, from nearly 50 years ago, developed by the British physicist Sir Tom Kibble[4]. He proposed that a phase transition in the early universe, during the cooling after the Big Bang, may have resulted in the formation of cosmic whirls. They hypothesised that the same phenomenon could be exploited to create antiferromagnetic whirls by driving α-Fe_2O_3 across its magnetic phase transition (Fig. 2). Experimentally, this involved heating ultra-high quality α-Fe_2O_3 thin films though a particular temperature, which can be conveniently chosen by slight chemical or physical alterations[2,5]. I06 images in this study confirmed that they were able to create not one but a veritable 'zoo' of whirling magnetic textures (Fig. 1). Among these, a particular variant known as *bimeron* appears to display specific 'twists' which would make it highly stable and suitable for racetrack applications. Moreover, other textures, such as *merons* and *antimerons*, could be employed in novel computing architectures inspired by the human brain. Crucially, all these textures were found to be stable at room temperature and creatable reproducibly by cycling through the magnetic phase transition.

Given that α-Fe_2O_3 has been under the spotlight for application in fast and energy efficient computing for some time, this discovery of a facile and reversible pathway to create a wide family of antiferromagnetic textures in this material is extremely exciting. The next steps are to design proof of principle devices to realise ultra-fast electrical control of the whirling antiferromagnetic family, taking the work a step closer to realistic racetracks.

References:

1. Parkin, S. S. P. *et al.* Magnetic domain-wall racetrack memory. *Science* **320**, 190–194 (2008). DOI : 10.1126/science.1145799
2. Jani, H. *et al.* Antiferromagnetic half-skyrmions and bimerons at room temperature. *Nature* **590**, 74–79 (2021). DOI: 10.1038/s41586-021-03219-6
3. Chmiel, F. P. *et al.* Observation of magnetic vortex pairs at room temperature in a planar α-Fe203/Co heterostructure. *Nature Materials* **17**, 581–585 (2018).DOI: 10.1038/s41563-018-0101-x
4. Kibble, T. W. B. (1976). Topology of cosmic domains and strings. *Journal of Physics A: Mathematical and General* **9**, 1387–1398. DOI: 10.1088/0305-4470/9/8/029
5. Jani, H. *et al.* Reversible hydrogen control of antiferromagnetic anisotropy in α-Fe203. *Nature Communications*, **12**, 1668 (2021). DOI: 10.1038/s41467-021-21807-y

Funding acknowledgement:
The work done at the University of Oxford was funded by EPSRC grant no. EP/M2020517/1. The work at the National University of Singapore was supported by the National Research Foundation under the Competitive Research Program (NRF2015NRF-CRP001-015) and by the Agency for Science, Technology and Research under the Advanced Manufacturing and Engineering Individual Research Grant (AME-IRG-A1983c0034).

Corresponding authors:
Prof Paolo Radaelli, University of Oxford, paolo.radaelli@physics.ox.ac.uk;
Dr Hariom Jani, National University of Singapore, hariom.k.jani@u.nus.edu

Imaging and Microscopy Group

Paul Quinn, Science Group Leader

The Imaging and Microscopy Group brings together eight experimental facilities (I08, I08-1, DIAD, I12, I13-1, I13-2, I14 and ePSIC) which use electrons and X-rays to image samples under different experimental conditions across a diverse range of length scales and time scales. Of note this year is that I08-1, the soft X-ray ptychography branchline, and DIAD, the dual imaging and diffraction beamline entered their first year of operations. The I08-1 and DIAD beamlines bring new world-leading capabilities in high-resolution and correlative imaging to the user community. We are are now ramping up user experiments to bring these new capabilities, and the insights they provide, to bear on a variety of exciting science problems.

The DIAD beamline for Dual Imaging and Diffraction offers two X-ray techniques, full-field radiography/tomography and micro-diffraction, used on the same sample quasi-synchronously. This setup enables *in situ* characterisation of the 3D microstructure of the material at the same time as its crystallographic phase and/or strain state. X-rays from a 10-pole wiggler are split into two independent beams and then combined at the sample position. Imaging beam can be operated in either pink or monochromatic mode; diffraction is conducted with monochromatic mode. Both beam energies can be chosen independently of each other in an energy range of 8-38 keV. In the summer, DIAD expects the delivery of a dedicated mechanical test rig with integrated tomography capabilities which will be an integral part of the end station and enable a variety of scientific experiments in engineering, materials science, biomaterials and hard tissues, geology and mineralogy. DIAD is part-funded by the University of Birmingham. The beamline is now accepting users.

The Scanning X-ray Microscopy (SXM) beamline (I08) is for morphological, elemental and chemical speciation on a broad range of organic-inorganic

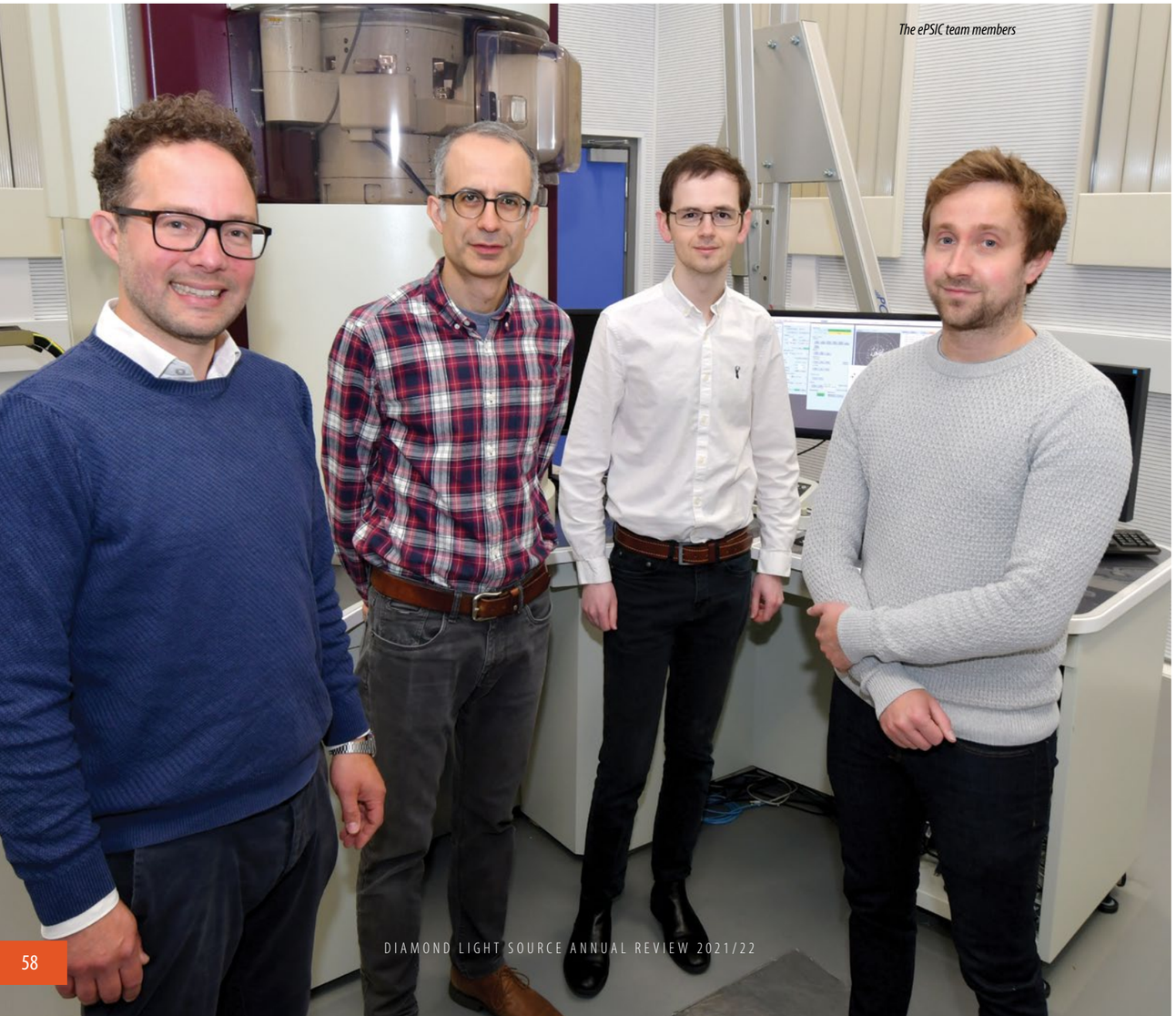

The ePSIC team members

“The new I08-1 and DIAD beamlines bring new world leading capabilities in high-resolution and correlative imaging to the user community. We are are now ramping up user experiments to bring these new capabilities, and the insights they provide, to bear on a variety of exciting science problems.”

interactions in a 250 - 4400 eV photon energy range, and sample investigations under ambient or cryogenic conditions. I08 has a range of applications including biological and biomedical sciences, earth and environmental science, geochemistry, and materials science. The new soft X-ray branchline I08-1 took first users in Oct 2020. Key developments, such as a new detector installation, are currently underway and are essential to allow the beamline to access the intended 250-2000 eV photon energy range. This will importantly provide access to the carbon for specto-ptychography studies and improve image quality and resolution. Developments to deliver cryogenic sample handling are also planned subject to operational and commissioning commitments. The resolution and contrast of I08-1 will provide a step change in imaging and spectro-microscopic performance for soft X-ray imaging at Diamond. Applications for user experiments are now accepted through our standard call.

The Joint Engineering, Environmental and Processing (JEEP) beamline (I12) uses a 4.2 T superconducting wiggler to provide polychromatic and monochromatic X-rays in the energy range 53 to 150 keV. These high photon energies provide good penetration through large or dense samples. The beamline offers beam sizes ranging from 50 x 50 μm^2 for diffraction, up to 90 x 25 mm^2 for imaging and tomography. Static objects larger than the available beam can be tomographically imaged using special scanning protocols. The beam characteristics enable the study of macroscale samples that are representative of bulk materials and processes. Another feature of I12 is the ability to use complex, enclosed sample environments without unacceptable attenuation of the beam. X-ray techniques available are radiography, tomography, energy-dispersive diffraction, monochromatic 2D diffraction and scattering. Radiography and tomography are performed predominantly with monochromatic X-rays. Polychromatic beam is reserved for energy-dispersive diffraction or non-routine special requests. I12 has a diverse user community (materials science and engineering; chemical processing; biomedical engineering; geoscience; environmental science; physics; palaeontology) who make full use of the beamline’s capabilities. The beamline’s two flexible experimental hutches allow users to bring their own rigs and sample chambers. I12 continues to support a wide range of *in situ*, time resolved experiments, notably in additive manufacturing, materials property testing and chemical processing. It is common for users to combine imaging and diffraction in the same experiment. Almost all tomography scanning is done with constant speed stage rotation, to reduce scan times. This “flyscan” technique has recently been extended to diffraction data collection, if required.

The I13 Imaging and Coherence beamline is for multi-scale imaging in the energy range of 6 -20 keV. The achievable resolution ranges from several microns to some tens of nanometers with two branchlines operating independently for this purpose. The Diamond Manchester Imaging branchline performs mainly in-line phase contrast tomography with a strong emphasis on dedicated sample environments. A new full-field microscope using Zernike phase contrast imaging over a field of view of 50-100 µm and a resolution of 50 - 100 nm is now in operation, with a growing user community, allowing us to identify nano-sized structures under dynamic conditions. A new robot arm has been installed for high-throughput and remote studies and allows measurements of up to 300 samples. It also allows for large sampling and parametric studies in a range of science areas and the possibility of sample mail-in services. The highest spatial resolution, of 30 nm, is achieved on the coherence branch with ptychographic imaging. Continuous improvements have reduced ptycho-tomography scans from days to less than an hour, and ongoing fly-scanning developments aim to reduce this even further. Ptychography has become now a standard user-friendly experiment. Instrumental upgrades for Bragg-CDI (new detector robot software) expands the experimental capabilities for studying nano-crystalline structures and has been applied successfully in combination with ptychography.

I14 is used to map chemical and structural inhomogeneities in a wide range of samples. I14 has expanded its core 2D techniques of X-ray fluorescence, diffraction, X-ray Absorption Near Edge Structure (XANES), differential phase contrast and ptychography to include tomography for volume imaging of elemental, structural and chemical states. A new state of the art nano-positioning stage, installed last year, has enabled significant progress to be made towards *in situ* experiments in liquid and gas environments. A new EIGER detector will also allow us to reduce measurement times for phase contrast and ptychography by an order of magnitude.

The electron Physical Science Imaging Centre (ePSIC) at Diamond consists of two transmission electron microscopes, a JEOL ARM 200 and a JEOL GRAND ARM 300, which were brought to Diamond through a collaboration with Johnson Matthey and the University of Oxford respectively. The ARM 200 is a state-of-the-art probe-corrected analytical microscope capable of atomic resolution electron energy loss and X-ray spectroscopy. The ARM 300 is a dedicated imaging instrument aligned across a wide range of accelerating voltages (30 - 300 keV) and is equipped with an Oxford Instruments X-Max 100 EDX detector. It is both probe and imaging corrected and has numerous detectors, including a small pixel array (512 x 512) fast direct electron detector for low voltage work and a newly installed large pixel array (4K x 4K) fast direct electron detector for high voltage imaging. These combined capabilities make this a unique resource for electron microscopy within the UK. With *in situ* sample holders, users at ePSIC can perform variable temperature measurements from 100 to 1600 K, apply electrical bias to samples during imaging and transfer samples anaerobically into the microscope. For TEM sample preparation, ePSIC runs a JEOL 4700F focused ion beam microscope with *in situ* lift out and anaerobic transfer capability. The state-of-the-art instrumentation available at ePSIC attracts both established electron microscopists looking to develop new techniques, and scientists with limited previous electron microscopy experience interested in the atomic structure of their samples. The ePSIC facility undertook a 5-year international review which recognised the outstanding work of the facility. To position the facility in the longer term, a wider engagement with the UK electron microscopy community will be undertaken in 2022 with the aim of defining a roadmap for physical science electron microscopy in the UK.

Understanding hearing loss in osteogenesis imperfecta

Related publication: de Paolis, A., Miller, B. J., Doube, M., Bodey, A. J., Rau, C., Richter, C.-P., Cardoso, L., & Carriero, A. Increased cochlear otic capsule thickness and intracortical canal porosity in the *oim* mouse model of osteogenesis imperfecta. *Journal of Structural Biology* **213**, 107708 (2021). DOI: 10.1016/j.jsb.2021.107708

Publication keywords: Brittle bone disease; *oim*; Cochlea; Otic capsule; Cortical bone; Porosity

Osteogenesis imperfecta (OI) is a hereditary (genetic) disease of collagen defects, commonly known as brittle bone disease. Progressive hearing loss starts in childhood and affects 70% of people with OI. There is no cure for OI, and the current treatments for hearing loss in this population have a low success rate.

A comprehensive understanding of the auditory system in OI will provide insights into the disease and guide the development of effective therapies to halt or reduce hearing loss. The mechanisms leading to progressive hearing loss in OI are currently unknown. Changes in the OI ear shape and internal bone structure may explain the hearing loss in this population and guide the development of new treatments.

An international team of researchers used the Diamond Manchester Imaging Branchline (I13-2) to study the 3D ear geometry of a mouse model of OI, called *oim,* suffering from hearing loss. The model needed to be visualised with high-resolution topographic images (810 nm) to reveal the cochlea and otic capsule morphology and internal porosity at the tissue and cellular level to determine any difference with the healthy inner ears.

They found outward growth of the otic capsule characterised by highly porous bone, with no change in the cochlea shape in the *oim* mouse inner ear. The disease seems to be affecting the mineralised tissue rather than the soft tissue in the inner ear.

Understanding the changes in the *oim* ears will help develop effective treatments for hearing loss in OI.

Osteogenesis imperfecta (OI or brittle bone disease) is a group of inherited genetic disorders of the connective tissues caused by mutations in the genes encoding collagen type I[1], the major protein in the human body. As such OI affects bone, ligaments, tendons, skin, eye, ears, lungs and hearts. Clinical hallmarks of OI are extreme skeletal fragility, bone deformities, joint laxity and severe functional disabilities, such as breathing disorders and hearing loss[1-4]. *Brittle bone disease* affects 1 in 10,000 children, and there is currently no cure for it[1].

About 70% of people with OI are affected by progressive hearing loss, starting in childhood[2-4]. Current treatments for ameliorating hearing loss in this population rely on standard procedures with low success rate. The hearing loss in OI may affect the middle ear alone (conductive hearing loss), or the inner ear alone (sensorineural hearing loss) or both (mixed hearing loss). Studies have found that the inner ear compartment is involved in more than half of the cases of OI hearing loss. Despite this knowledge on the auditory function in OI, little is known about the properties of ears in OI, and the mechanisms leading to the onset and progression of hearing loss.

Figure 1 represents the middle and inner ear of a mouse obtained from segmented synchrotron Microtomography images taken at I13-2. In mice, as in humans, hearing starts at the pinna. Sound waves travel along the outer ear canal and vibrate the tympanic membrane, which terminates the outer ear canal and is connected to the middle ear ossicles. The middle ear ossicles, malleus, incus, and stapes, transmit the sound induced vibrations to the inner ear or cochlea, a 3D coiled structure with the appearance of a snail. Its outer shell, the otic capsule, is bone. In the cochlea, soft tissue structures including the basilar and tectorial membrane, transform acoustically induced vibrations into trains of action potentials, which are carried to the brain and perceived as sound. Inside the cochlea three "tubes" follow the coiled structure, scala vestibuli, scala media and scala tympani. From the centre of the cochlea, the modiolus, the basilar membrane, a collagen rich soft tissue structure, spans to the cochlear wall. On top of the basilar membrane sits the organ of Corti and the tectorial membrane, delicate collagen rich soft tissue structures, which transform sound induced vibrations into action potentials along the auditory nerve, information that can be read by the brain. Architecture and composition

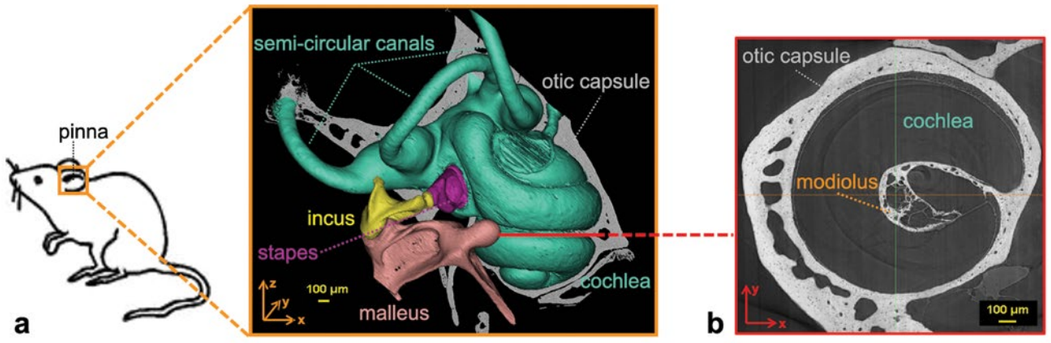

*Figure 1: (**a**) Mouse middle and inner ear as reconstructed from synchrotron X-ray Microtomographic images acquired at the I13-2 (at 1.6 um nominal resolution); (**b**) Reconstructed synchrotron X-ray Microtomographic slide at 810 nm resolution showing the cochlea ducts (dark grey), the modiolus in the centre of the cochlea and the surrounding otic capsule (grey) in a transverse plane.*

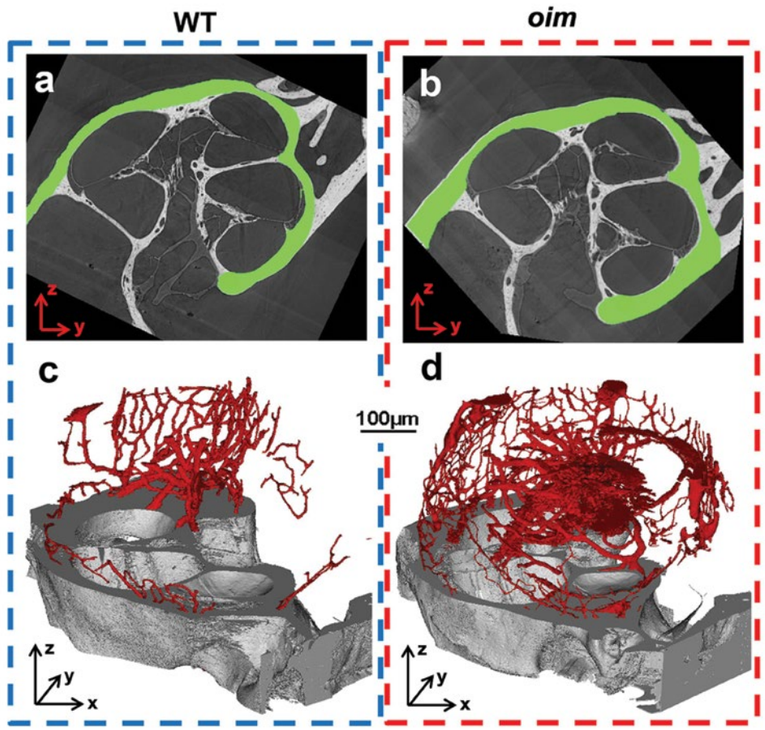

*Figure 2: (**a**, **b**) Synchrotron X-ray Microtomographic slice of healthy (wild type or WT) and osteogenesis imperfecta murine model (oim) representative otic capsule (green) showing the difference in coronal cortical thickness; (**c**, **d**) Surface render of the canal network (red) respectively within the WT and oim cochlear otic capsule (gray).*

of the different compartments of the ear play a fundamental role in determining the auditory function. Therefore, a comprehensive understanding of the properties of the auditory system in OI would provide insights into the disease and guide the development of effective therapies to halt or reduce hearing loss. However, the small dimensions of the ear compartments and their anatomical position located internal in the cranium, limit the ability to conduct a comprehensive investigation of the ear properties in living people with OI in relation to their hearing loss.

In the highlighted research we have used synchrotron X-ray Microtomography at I13-2 to investigate the morphology and porosity of the inner ear cochlea and surrounding bony otic capsule in the osteogenesis imperfecta murine model (B6C3Fe-a/aCol1a2$^{oim/oim}$ or *oim*), which also experiences hearing loss in its homozygotes mice[5]. Figure 1b shows an X-ray microtomographic slide of the cochlea in the transverse plane with its surrounding otic capsule after reconstruction. Changes in the cochlea and otic capsule architecture due to OI may adversely affect the inner ear auditory function and enhance our understanding of hearing loss in this disease.

We collected 3D images at high-resolution (810 nm nominal resolution) of *oim* and WT inner ears at 8 weeks of age, using a partially-coherent, filtered, polychromatic 'pink' beam to analyse the soft and hard (mineralised) tissue morphology, internal porosity at the tissue and cellular level, and otic capsule tissue mineral density[1]. 3D morphology was examined and morphometric parameters of the bony otic capsule volume and thickness, and its intracortical porosity (vascular canals at the tissue level and osteocyte lacunae at the cellular level) were assessed. For the cochlea, the volume in the ducts and helicotrema, and the external spiral length were quantified. Differences between the *oim* and WT inner ears were evaluated for statistical significance.

Our results show that the morphology of the cochlea is preserved in the *oim* inner ears at 8 weeks of age but their bony otic capsule is thicker and more porous, with more numerous and highly connected canals than in healthy ears (Fig. 2). These findings portray a state of compromised bone quality in the otic capsule of the *oim* mice that may change the mechanical properties of the inner ear and contribute to their hearing loss. Specifically, these alterations of the otic capsule architecture and porosity reduce bone conduction of sound in OI ears, and/or favour the formation of microcracks and fractures in OI ears, and/or alter ion and fluid balance in OI inner ears and impair function of their sensory hair cells. A full understanding of the changes in the *oim* ears will guide the development of targeted treatments to halt or reduce its hearing loss.

References:

1. Carriero, A. *et al.* How tough is brittle bone? Investigating osteogenesis imperfecta in mouse bone. *Journal of Bone and Mineral Research* **29**, 1392–1401 (2014). DOI: 10.1002/jbmr.2172
2. Pedersen, U. Hearing loss in patients with osteogenesis imperfecta *A Clinical and Audiological Study of 201 Patients*. *Scandinavian Audiology* **13**, 67–74 (1984). DOI: 10.3109/01050398409043042
3. Pillion, J. P. *et al*. Audiological findings in osteogenesis imperfecta. *Journal of the American Academy of Audiology* **19**, 595–601 (2008). DOI: 10.3766/jaaa.19.8.3
4. Ting, T. H. *et al.* Hearing in bisphosphonate-treated children with osteogenesis imperfecta: Our experience in thirty-six young patients. *Clinical Otolaryngology* **37**, 229–233 (2012). DOI: 10.1111/j.1749-4486.2012.02476.x
5. Chen, W. *et al*. Single-nucleotide polymorphisms in the COL1A1 regulatory regions are associated with otosclerosis. *Clinical Genetics* **71,** 406–414 (2007). DOI: 10.1111/j.1399-0004.2007.00794.x

Funding acknowledgement:
This work was supported by Diamond Light Source (beamtime MT9860) and National Science Foundation CBET 1829310 (A.C.).

Corresponding author:
Alessandra Carriero, The City College of New York, acarriero@ccny.cuny.edu

Understanding lattice reconstruction of 2D materials for tuning electronic behaviour

Related publication: Weston, A., Zou, Y., Enaldiev, V., Summerfield, A., Clark, N., Zólyomi, V., Graham, A., Yelgel, C., Magorrian, S., Zhou, M., Zultak, J., Hopkinson, D., Barinov, A., Bointon, T. H., Kretinin, A., Wilson, N. R., Beton, P. H., Fal'ko, V. I., Haigh, S. J., & Gorbachev, R. Atomic reconstruction in twisted bilayers of transition metal dichalcogenides. *Nature Nanotechnology* **15**, 592–597 (2020). DOI: 10.1038/s41565-020-0682-9

Publication keywords: 2D materials; Moiré superlattices; Van der Waals heterostructures

Twisting two sheets of monolayers (a layer of material one/few atoms thick) has proven to be a novel way to engineer strikingly different properties compared to their monolayer counterparts. When two Transition-metal dichalcogenide (TMD) monolayers are stacked on top of each other, two common stacking polytypes can be formed - referred to as 3R and 2H. Introducing a slight twist angle to either polytype produces a long-range periodic moiré pattern. This was expected to significantly modify the optoelectronic properties of the twisted bilayer system but had not been experimentally investigated.

Researchers used ePSIC's E02 Scanning Transmission Electron Microscopy (STEM) instrument to examine the TMD crystal lattice. The instrument's multiple detectors allowed visualisation of the domain structure from the low angle annular dark field detector (LAADF). High angle annular dark field (HAADF) imaging revealed the atomic lattice information.

Their results show that at twist angles of below around 2°, a structural transition occurs from a rigidly twisted lattice to an atomically reconstructed lattice where the energy is reduced by having regions (or domains) of commensurate (perfect) stacking separated by partial dislocations. It further demonstrated that this structural relaxation changes the electronic behaviour of the material, providing potential applications in non-volatile memory storage and quantum technologies.

The results obtained from ADF STEM combined with c-AFM suggest that this new regime of lattice reconstruction can further tailor the properties of 2D materials and broaden the scope for optoelectronic applications.

Transition-metal dichalcogenides (TMDs) are a sub-group of layered crystalline materials that can be easily exfoliated down to the monolayer thickness owing to weak inter-layer van der Waals forces. Each monolayer consists of a group VI transition metal atom sublayer sandwiched between two chalcogen atom sublayers. This study focussed on semiconducting TMDs, namely, MoS_2 and WS_2 with trigonal prismatic metal coordination. Besides graphene, TMDs are one of the most widely studied 2-dimensional (2D) materials owing to their excellent light-matter interaction, electrical properties and wide range of band-gaps that render them ideal for a host of optoelectronic applications including LEDs, transistors and sensors.

In this work, adhesion-enhanced TEM grids[2] were used to reliably fabricate clean suspended samples of twisted bilayer TMDs. The twisted bilayers were prepared in a controlled argon environment to ensure a clean interface between the layers. A modified 'tear-and-stack' method[3] was employed for twisted homobilayers to selectively determine the stacking polytype and the twist angle with high accuracy (± 0.1°). For heterobilayers (e.g. MoS_2 on WS_2), straight crystallographic edges with angles that are multiples of 30° of two dissimilar crystals were aligned with a relative twist to achieve the required small twist angle. With the latter method, there is equal probability of creating the 3R or 2H stacking polytype.

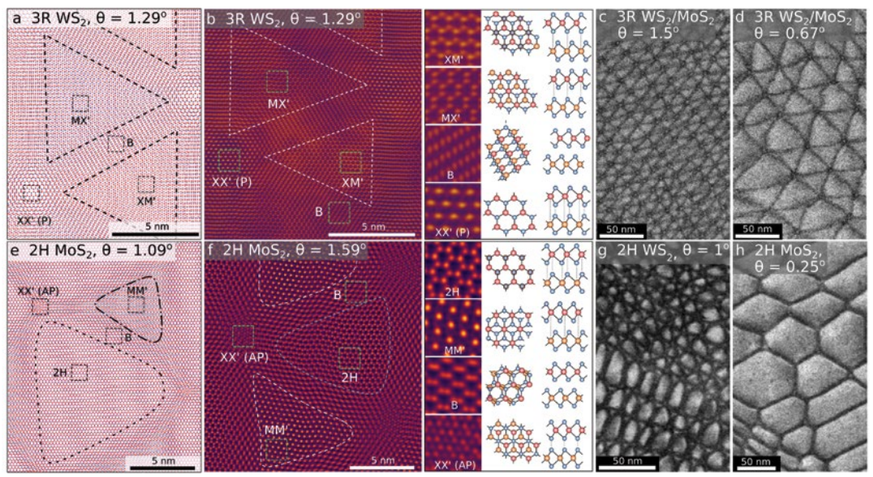

Figure 1: ADF Imaging of lattice reconstruction in twisted TMD homo- and hetero-bilayers; DFT and multiscale modelling for reconstructed (a) 3R-type and (e) 2H-type stacking domain structures. Corresponding ADF images with the four primary stacking configurations enlarged in the inset as well as atomic schematics for both (b) 3R-type and (f) 2H-type configurations. LAADF images of 3R-configuration periodically repeating triangular domains that grow equally in size with decreasing twist angle (from (c) 1.5o to (d) 0.67o) unlike the 2H-configuration that transitions from a (g) kagome-like structure to a (h) hexagonal shaped domain structure with decreasing twist angle.

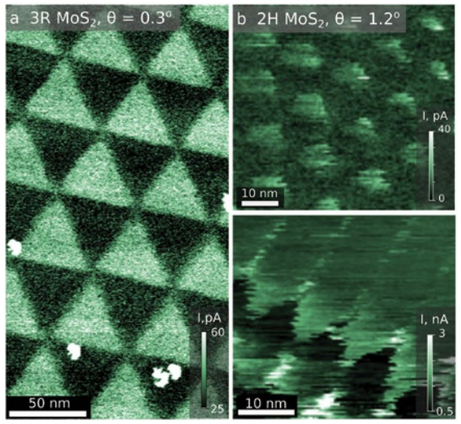

Figure 2: Conductive-AFM images of reconstructed homobilayers of MoS2 in both the 3R- and 2H- stacking configuration; (a) Map of the tunnelling current acquired on a 3R-type MoS2 homobilayer with a tip-sample bias Vb = 600 mV; (b) Map of the tunnelling current acquired on a 2H-type MoS2 homobilayer with a tip-sample bias Vb = 400 mV. In the top image, the periodically repeating bright spots correspond to regions of MM' stacking and in the bottom image the regions of higher tunnelling current correspond to both MM' as well as extended 2H/2H domain boundaries (extending to the top RHS of the image).

ePSIC's E02 Scanning Transmission Electron Microscopy (STEM) instrument was used at low accelerating voltage (60 or 80 kV) to avoid damaging the TMD crystal lattice. The instrument's multiple detectors allowed visualisation of the domain structure from the low angle annular dark field detector (LAADF) (Fig. 1c-d and g-h) as well as atomic lattice information to be revealed via high angle annular dark field (HAADF) imaging (Fig. 1b and f). Lattice reconstruction was imaged for both the 3R and 2H hetero/homobilayer crystals at the atomic scale focusing on the reconstruction that occurs when the twist angle is below ~2°

Fig. 1a-d presents the 3R-type TMD bilayers which structurally reconfigure into a triangular domain network (Fig. 1b). Periodically repeating stacking configurations were observed and identified in the image as well as corresponding insets as MX' (metal in top layer above chalcogens in lower layer), XM' (chalcogens in top layer above metals in lower layer), XX' (chalcogens/metals in top layer above chalcogens/metals in lower layer) and B (boundary- no direct alignment). Note that the MX' and XM' stackings are the identical (3R) structure 'flipped' upside down. Nonetheless, as the 3R-like atomic stacking lacks mirror and inversion symmetry, these two configurations behave differently. The triangular domains alternate between MX' and XM' stacking, while the intersections are XX' and the domain boundaries (partial dislocations) show no direct vertical alignment of the two layers. LAADF STEM revealed boundary widths of ~3 nm and that for these 3R type TMD bilayers, the tessellated triangular domains grow equally in size with decreasing twist angle (Fig. 1c-d).

In contrast, 2H-type TMD bilayers twisted close to 2° initially reconfigure into a triangular domain network, similar to that seen for 3R. However, unlike the 3R-polytype, 2H stacking has mirror/inversion symmetry. Adjacent domains of 2H (the most common TMD stacking) and MM' stacking (where the metal atoms in the top layer are directly above metal atoms in the lower layer) are observed (Fig. 1f.) The MM' stacking is a metastable-stacking configuration introduced via twisting and has not been previously observed. The domains are again separated by boundaries (3.5 nm in width) with XX' (chalcogens in the top layer above chalcogens in the bottom layer) stacking configurations at the intersections. At smaller twist angles, the domains generally increase in size, but in this case the MM' domains reach a maximum size of 5 nm for θ ~ 0.9° (Fig. 1g). At increasingly small twist angles, 2H domains eventually take on a hexagonal domain configuration in which 2H domains are adjacent to each other and the MM' stacking remains at alternating intersections (Fig. 1h). All our experimental observations agree well with complementary modelling (Fig. 1a and 1e)[4].

Complementary, conductive atomic force microscopy (c-AFM) (this work) and Kelvin probe force microscopy (KPFM) measurements[5] were used to reveal the dramatic effect such local structural relaxation has on the electronic behaviour. For the 3R-type configuration, the triangular MX' stacking domains have a higher tunnelling current than XM' domains (Fig. 2a). This is attributed to the 'layer polarised' electron wavefunction weightings of the top and bottom layers due to inversion asymmetry. In other words, the top layer has a higher probability of finding an electron than the bottom; this scenario reverses as we scan across MX' to XM' stacking domains during c-AFM measurements. A follow on study from the same group found the 3R-type domain structure to be a ferroelectric[5]. KPFM revealed an out-of-plane potential difference between oppositely polarised MX' and XM' domains and ferroelectric switching was demonstrated in prototype devices; such behaviour is ideal for non-volatile memory storage applications.

For the 2H-type configuration, c-AFM revealed regions of high tunnelling current were confined to the MM' stacking domains (with a maximum width of 5nm) and an intermediate tunnelling current at the domain boundaries (Fig. 2b). The increased tunnelling current was attributed to the piezoelectric charge induced by the localised strain, concentrated in the MM' and boundary regions. Monolayers of TMDs are known piezoelectrics; although the piezoelectric effect is expected to cancel out in 2H-type bilayers, the induced deformation at the MM' and boundary sites that is occurring in opposite directions means that piezo-charge of each layer can be added together, effectively doubling the piezoelectric induced charge confined to the MM' and B regions of the domain structure. This type of charge-confinement has the exciting potential for creating twist controlled networks of quantum dots and nanowires with novel optoelectronic properties.

References:

1. Wilson N. P. *et al*. Excitons and emergent quantum phenomena in stacked 2D semiconductors. *Nature* **599,** 383–392 (2021). DOI: 10.1038/s41586-021-03979-1
2. Hamer M. J. *et al.* Atomic Resolution Imaging of $CrBr_3$ Using Adhesion-Enhanced Grids. *Nano Letters* **20,** 6582–6589 (2020). DOI: 10.1021/acs.nanolett.0c02346
3. Kim K. *et al.* van der Waals Heterostructures with High Accuracy Rotational Alignment. *Nano Letters* **16,** 1989–1995 (2016). DOI: 10.1021/acs.nanolett.5b05263
4. Enaldiev V. V. *et al.* Stacking Domains and Dislocation Networks in Marginally Twisted Bilayers of Transition Metal Dichalcogenides. *Physical Review Letters* **124,** 206101 (2020). DOI: 10.1103/PhysRevLett.124.206101
5. Weston, A., Castanon, E.G., Enaldiev, V. *et al.* Interfacial ferroelectricity in marginally twisted 2D semiconductors. *Nat. Nanotechnol*. (2022). https://doi.org/10.1038/s41565-022-01072-w

Funding acknowledgement:
We acknowledge support from the Engineering and Physical Sciences Research Council (EPSRC) grants EP/N010345/1, EP/P009050/1, EP/S019367/1, EP/S030719/1, EP/P01139X/1, EP/R513374/1, the Centre for Doctoral Training (CDT) Graphene-NOWNANO and the Diamond Light Source for access and support in the use of the electron Physical Sciences Imaging Centre (proposal numbers EM19315 and MG21597). We also acknowledge support from the European Graphene Flagship Project, European Quantum Technology Flagship Project 2D-SIPC (820378), European Research Council (ERC) Synergy Grant Hetero2D, ERC Starter grant EvoluTEM (715502), Royal Society and Lloyd Register Foundation Nanotechnology grant.

Corresponding authors:
Dr Astrid Weston, The University of Manchester,
astrid.weston@manchester.ac.uk
Professor Sarah J. Haigh, The University of Manchester,
sarah.haigh@manchester.ac.uk

Nanofocused X-rays offer insights into the cellular life of catalytic metallodrugs

Related publication: Bolitho E. M., Coverdale J. P. C., Bridgewater H. E., Clarkson G. J., Quinn P. D., Sanchez-Cano C., Sadler P. J. Tracking reactions of asymmetric organo-osmium transfer hydrogenation catalysts in cancer cells. *Angewandte Chemie International Edition* **60**, 6462–6472 (2021). DOI: 10.1002/anie.202016456

Publication keywords: Anticancer catalysts; Bioorganometallic chemistry; X-ray Fluorescence; Organo-osmium complexes; Transfer hydrogenation

Transition metal catalysts have potential as therapeutic agents to treat cancer and other diseases. However, there is a need to improve the design of these catalysts to make them more efficient, so they can be used in lower doses, and hasten progress towards clinical use.

Researchers from the University of Warwick have designed a series of advanced organo-osmium catalysts that can transform pyruvate (an essential ketone in cell metabolism) to natural L-lactate or unnatural D-lactate inside cancer cells. This can cause selective destruction of cancer cells, but not healthy cells.

Using synchrotron X-ray Fluorescence, researchers can track the catalysts in cancer cells and observe how long they remain intact and active. The Hard X-Ray Nanoprobe beamline (I14) allowed the team to study biological samples with a range of X-ray imaging and spectroscopic techniques using a nano-focused photon beam. This allowed direct detection of metals with subcellular resolution, providing valuable insight into the distribution and chemical properties of these metal complexes inside cells.

The results obtained suggest a strategy for improving the design of catalytic organo-osmium anticancer drugs. This work also demonstrated the wider potential of experimental approaches combining simultaneous detection of ligand halogen tags and metals by X-ray based techniques for the fields of chemical biology and medicinal chemistry. This approach can contribute to the design and development of new classes of transition metal complexes as therapeutic and biotechnological tools.

Transition metal catalysts have potential as therapeutic agents to treat cancer and other diseases.[1] Such catalysts might transform multiple substrate molecules *in situ*, including exogenous prodrugs, diagnosis agents, and endogenous metabolites,[1,2] whilst requiring only low concentrations to achieve the desired activity. Therefore, therapeutic strategies based on metal catalysts might help to overcome resistance to chemotherapy and reduce unwanted side effects,[1,2] both of which are of current clinical concern.

The Sadler group has developed a chiral organo-osmium half-sandwich complex **1** structurally derived from the well-established Noyori Ru(II) industrial catalysts (Fig. 1).[3] Once inside cells, and in the presence of the non-toxic hydride donor formate, this complex catalyses the enantioselective reduction of pyruvate (an essential precursor in cell metabolism) to natural L-lactate or unnatural D-lactate (depending on the chirality of the catalyst).[2] This ability to cause metabolic perturbations in cells requires the presence of an intact catalyst, and gives rise to promising antiproliferative activity *in vitro* against a variety of human cancer cells, but not healthy cells.[2]

Yet, intracellular activity of **1** is marked by low catalytic efficiency, suggesting degradation of the complex inside cells.[2] This seems to be a common problem for most synthetic transition metal catalysts, which are normally designed to work under well-defined chemical conditions, such as in inert atmospheres or pure organic solvents.[4,5] Therefore, it is important to understand the cellular fate of synthetic catalysts to optimise their *in cellulo* catalytic and therapeutic efficiency.

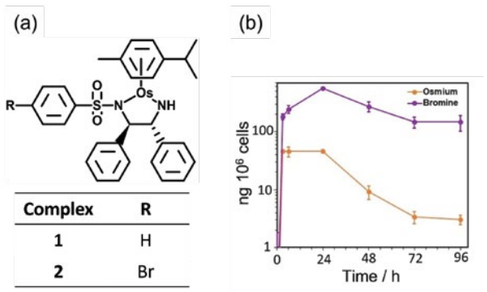

*Figure 1: (a) Structures of the organo-osmium catalysts **1** and its brominated analogue **2**. (b) Accumulation of Os and Br (ng / million cells) in cancer cells treated with **2** for different times. Reprinted with permission from DOI: 10.1002/anie.202016456 under a CC-BY License.*

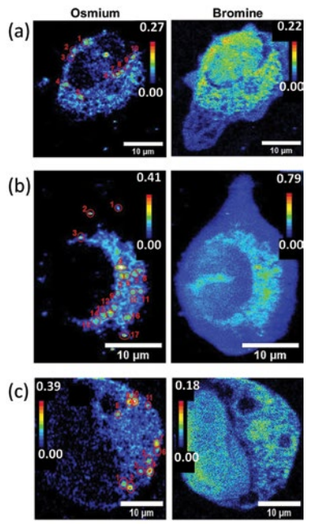

*Figure 2: XRF elemental maps of Os and Br acquired from cryopreserved and freeze-dried lung cancer cells treated with (a) 30, (b) 90 or (c) 150 µM of **2** for 24 h, showing Os-Br co-localisation in small vesicle-like areas highlighted by red circles. Maps were collected using 100 nm step size and 0.1 s dwell time. The calibration bar is in pg mm^{-2}. Reprinted with permission from DOI: 10.1002/anie.202016456 under a CC-BY License.*

The coordination sphere of metal complexes can be studied in biological environments by halogenation of selected ligands, which permits application of a range of techniques, including: ^{19}F NMR or MRI for fluorinated compounds, ICP-MS and X-ray Fluorescence (XRF) using bromine or iodine tags, or PET/SPECT imaging after radiolabelling with *e.g.* ^{131}I. As such, it is possible to probe the stability of catalyst **1** in cells by labelling its chiral chelating ligand with a bromine tag to generate the analogue complex **2** (Fig. 1). This allows comparison of the relative cellular accumulation and localisation of Os centres and Br-tagged ligands, by detecting ^{189}Os and ^{79}Br ions using ICP-MS or following XRF emissions from Os (L_3-M_5 = 8.9 keV) and Br (K-L_3 = 11.9 keV).

Such halogen substitution does not affect significantly the chemical, structural and catalytic properties of the new catalyst compared to **1**. Complex **2** shows similar biological properties to the parent complex, having the same mechanism of action and being capable of performing in-cell transfer hydrogenation. Thus, **2** is a good model to study the stability of **1** in cellular environments.

Initial ICP-MS studies show that cells accumulate more Br than Os (Fig. 1), but the cellular Br-to-Os ratio decreases when active transport is inhibited. Besides, excretion of the Os- and Br-carrying fragments seems to follow different cellular trafficking and efflux mechanisms.

Acquisition of Os and Br XRF elemental maps at the Hard X-ray Nanoprobe beamline (I14) provides a more in-depth picture of the distribution of the different fragments of **2** in cancer cells with sub-cellular spatial resolution (Fig. 2). For this, lung cancer cells were grown on silicon nitride membranes and treated with **2**, before being cryo-fixed and freeze-dried for subsequent analysis under ambient conditions using a nanofocussed X-ray beam (100 x 100 nm^2).

The XRF maps confirm that cells treated with the catalyst accumulate more Br than Os (2-7x more) after 24 h, confirmed by complementary ICP-MS experiments. Most of the intracellular Br and Os was found in regions of the cytosol (50-70% and 65-85%, respectively), although a significant amount of Br (30-50%), but not Os, also reached the nuclei of the cells. This implies that intracellular degradation of the complex is occurring, in agreement with the ICP-MS data. Nevertheless, within the cytosol, both Os and Br co-localise moderately (Pearson's Coefficient R=0.17-0.39) in small circular compartments (0.65-0.78 µm^2). These organelles are likely to be lysosomes or endosomes, since they are known to be similar in size, and the uptake of **2** occurs through active transport mechanisms such as endocytosis. Remarkably, the Br-to-Os ratio is lower in those vesicular areas than in the rest of the cell, suggesting the presence of higher concentrations of intact complex within endosomes and lysosomes, and supporting transfer hydrogenation catalytic activity in the cytosol of cancer cells.

It is also possible that catalysts might be degraded due to processes linked to their active intracellular transport. Remarkably, catalysts **1** and **2** are very stable in acidic environments, but they are degraded, and release their chiral chelated ligands, in presence of biologically relevant concentrations of thiol-containing biomolecules such as glutathione, commonly found in lysosomes. Moreover, reducing cellular levels of glutathione with low doses of L-buthionine sulfoximine, or inhibiting the activity of lysosomes in lung cancer cells with chloroquine diphosphate, leads to reduced degradation of the complex, and hence increased concentrations of intact catalyst inside cells and a significant increase in the anticancer potency of both **1** and **2**.

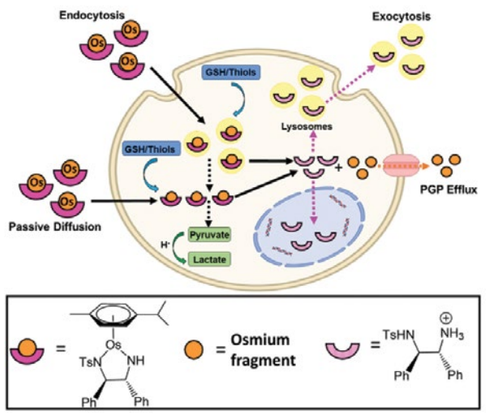

*Figure 3: Possible mechanisms proposed for the uptake, degradation and efflux of catalysts **1** and **2** in cancer cells. Reprinted with permission from DOI: 10.1002/anie.202016456 under a CC-BY License.*

Combining nanoscale synchrotron XRF mapping with ICP-MS, cellular uptake and mechanistic studies has provided new insights into the behaviour of asymmetric transfer hydrogenation catalyst **1** in cancer cells (Fig. 3). These experiments show that the catalysts are internalised by cells via a combination of both passive and active transport, reaching lysosomes, the cytosol and some other organelles. Once inside, in the presence of a hydride donor, intact catalysts facilitate the catalytic reduction of pyruvate to lactate in the cytosol, altering the metabolism of cancer cells and inhibiting their proliferation. Complex **1** also interacts with intracellular thiols. This leads to the release of Os-containing fragments and chelated ligands. The fragments generated during this degradation exhibit different cellular behaviour. Osmium-containing fragments are rapidly excreted from cells, while chelated ligands show much longer in-cell lifetimes. They are highly accumulated by cells, reaching even the cell nuclei before they are excreted. Such reactions help to explain the low intracellular turnover number (TON) observed for these catalysts.

Overall, this work demonstrates how the use of halogen tags as probes for MS and X-ray based techniques can elucidate reactions of organometallic anticancer catalysts in cells. Moreover, the reactions observed between catalyst **1** and cellular thiols provide a basis for developing new generations of therapeutic catalysts designed to have enhanced stability towards biological thiols and cause metabolic perturbations with increased efficiency in target cancer cells.

References:

1. Soldevila-Barreda J. J. *et al*. Intracellular catalysis with selected metal complexes and metallic nanoparticles: advances toward the development of catalytic metallodrugs. *Chemical Reviews* **119**, 829–869 (2019). DOI: 10.1021/acs.chemrev.8b00493
2. Coverdale J. P. C. *et al*. Asymmetric transfer hydrogenation by synthetic catalysts in cancer cells. *Nature Chemistry* **10**, 347–354 (2018). DOI: 10.1038/nchem.2918
3. Coverdale J. P. C. *et al*. Easy to synthesize, robust organo-osmium asymmetric transfer hydrogenation catalysts. *Chemistry - A European Journal* **21**, 8043–8046 (2015). DOI: 10.1002/chem.201500534
4. Bai Y. *et al*. Designed transition metal catalysts for intracellular organic synthesis. *Chemical Society Reviews* **47,** 1811–1821 (2018). DOI: 10.1039/C7CS00447H
5. Martínez-Calvo M. *et al*. Organometallic catalysis in biological media and living settings. *Coordination Chemistry Reviews* **359**, 57–79 (2018). DOI: 10.1016/j.ccr.2018.01.011

Funding acknowledgement:
The authors thank the Engineering and Physical Sciences Research Council (EPSRC grant no. EP/P030572/1), and Warwick Collaborative Postgraduate Research Scholarship and Diamond Light Source (DLS, Oxford) for a studentship for Elizabeth M. Bolitho. Carlos Sanchez-Cano thanks the Spanish State Research Agency (grant PID2020-118176RJ-I00) and the Gipuzkoa Foru Aldundia (Gipuzkoa Fellows program; grant number 2019-FELL-000018-01/62/2019) for financial support. This work was performed under the Maria de Maeztu (Grant No. MDM-2017-0720) and Severo Ochoa (Grant No. CEX2018-000867-S) Centres of Excellence Programme run by the Spanish State Research Agency. All synchrotron work was performed at the I14 Beamline (DLS, Oxford) under experiment number sp20552-1]

Corresponding authors:
Prof. Peter J. Sadler, University of Warwick, p.j.sadler@warwick.ac.uk
Dr Carlos Sanchez-Cano, Donostia International Physics Center and Ikerbasque Basque Foundation for Science carlos.sanchez@dipc.org

X-ray ptychography investigates coking of solid catalysts in 3D

Related publication: Weber, S., Batey, D., Cipiccia, S., Stehle, M., Abel, K. L., Gläser, R., & Sheppard, T. L. Hard X-ray nanotomography for 3D analysis of coking in nickel-based catalysts. *Angewandte Chemie International Edition* **60**, 21772–21777 (2021). DOI: 10.1002/anie.202106380

Publication keywords: Carbon; Methanation of CO_2; Nickel; Raman Spectroscopy; X-ray Ptychography

Catalysts speed up chemical reactions and are widely used in industrial processes. Chemical reactions involving carbon-containing species can form carbon deposits (coke) on the catalyst surface. As catalysts are typically porous materials, extensive coke formation can restrict accessibility of reactants and products through the pores, leading to so-called mass transport limitations, and can physically block the active sites of the catalyst that are responsible for facilitating the chemical reaction. While diagnosing the presence of coke is relatively simple, obtaining information on the location, chemical nature, and severity of coke formation is more complicated.

This study aimed to examine coke formation on several catalysts using X-ray ptychography. It needed a very high image resolution to visualise the catalyst sample, the pores, and possible coke deposits, all of which can occur on the scale of micrometres to nanometres. The imaging method used also had to be sensitive enough to differentiate which parts of the catalyst are coked.

The Coherence Branchline (I13-1) is specially designed for high-resolution imaging with X-ray in 2D and 3D. X-ray ptychography also allows scientists to discover the electron density of the sample, which can be used to examine where coking has occurred.

The results can be applied to study industrial catalyst samples during their life cycle, to understand the location and nature of coke deposits.

An improved fundamental understanding of catalyst deactivation is also important for catalyst design and synthesis, potentially tailoring the pore structure to withstand coking.

Catalyst coking is a major deactivation pathway of solid catalysts applied in the chemical industry. In principle, any process involving carbonaceous species might suffer from this type of deactivation, where a variety of solid carbon products may deposit on the catalyst surface. This in turn can block the catalytic active sites or fill the pores of the catalyst, inducing mass transport limitations. In the case of mass transport limitations, tailoring the catalyst pore structure by introducing hierarchical pore systems on different length scales (*e.g.*, meso-/macroporous catalysts) is one possible strategy to mitigate the effects of coking, therefore improving catalyst performance and stability[1]. Catalyst coking is often diagnosed and analysed by bulk characterisation techniques (*e.g.*, elemental analysis, IR/Raman spectroscopy, thermal analysis methods), which can provide information about the amount of coke formed or the type of coke (*e.g.*, graphitic, amorphous, activated carbon). However, conventional methods provide little information about the location of the carbon species formed, which is relevant in the context of mass transport limitations and pore blocking. A spatially resolved investigation of coke deposition should ideally be carried out on whole catalyst particles, which typically range from tens of µm (*i.e* the size of a single human hair) all the way up to the mm or cm scale in industrial applications. Considering the vast difference in length scales which are relevant for catalysis, hard X-ray imaging methods are required to investigate the whole sample without imposing limitations on beam transmission, which would be the case for soft X-ray techniques or electron microscopy. Among the currently available hard X-ray methods, X-ray Ptychography combined with tomography can retrieve quantitative 3D information about the electron density (N_e) distribution of an investigated sample[2,3]. Additionally, this method allows for high-resolution imaging (routinely below 100 nm in 3D) of extended sample volumes (tens of µm in diameter) due to the use of hard X-ray as the probe.

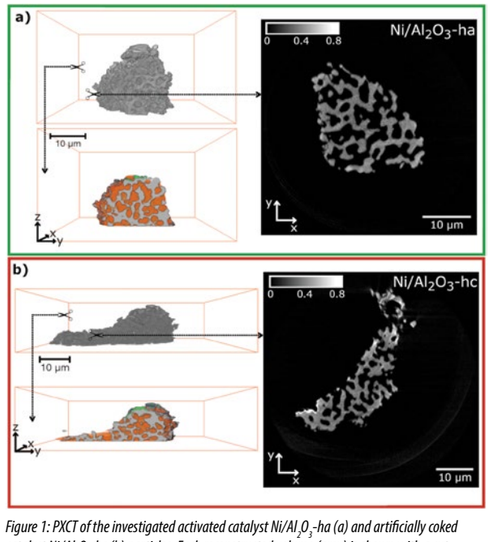

Figure 1: PXCT of the investigated activated catalyst Ni/Al_2O_3-ha (a) and artificially coked catalyst Ni/Al_2O_3-hc (b) particles. Each reconstructed volume (grey) is shown with a cut through the middle, illustrating the segmented and labelled tomograms (grey = nanoporous catalyst body, orange = pores, green = contamination) and a grayscale electron density (N_e) image of a typical slice through the volume (colour bar in N_e/e$^-$Å^{-3}, N_e offset to 0 with respect to air close to the sample).

To explore the potential of Ptychographic X-ray computed tomography (PXCT) to detect and reveal the location of coking in 3D, a hierarchically porous Ni/Al_2O_3 catalyst was selected as a case study[4]. This catalyst has applications in CO_2 methanation or CH_4 dry reforming, both of which are relevant in the context of reducing CO_2 emissions, and in storage of energy from intermittent power sources (*e.g.*, wind, solar) in chemical form. The catalyst itself exhibits a hierarchical pore structure of meso- (2-50 nm) and macropores (>50 nm). During the experiments, the catalyst was first activated using a microcapillary setup equipped with a hot-air blower, custom-made gas dosing system, and online mass spectrometer for gaseous product analysis. The activation procedure was carried out in a gas flow of 25% H_2/He (20 mL.min^{-1}) at about 700 °C followed by reaction conditions of 20% H_2/5% CO_2 / He at 400 °C to obtain an activated catalyst sample (Ni/Al_2O_3-ha). An artificially coked sample (Ni/Al_2O_3-hc) was obtained by a subsequent coking step in 4% CH_4/He at 400 °C after reaction conditions, while the formation of coke during the latter step was confirmed by operando Raman spectroscopy.

Selected particles of the Ni/Al_2O_3-ha and Ni/Al_2O_3-hc samples (around 30 to 50 µm diameter) were then mounted on Al tomography pins using a dual-beam focused ion beam scanning electron microscope (FIB-SEM) with Pt deposition.

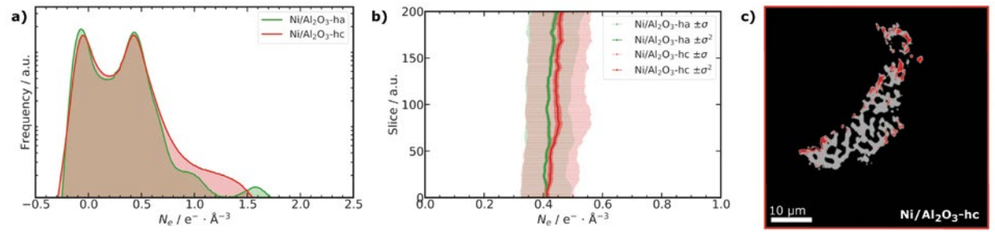

Figure 2: Global electron density (N_e) distribution from PXCT of the activated and artificially coked catalyst particle labels of Ni/Al_2O_3-h (a). Mean, standard deviation (a) and variance (σ^2) in N_e of the segmented catalyst body label in a selected slice range (b). Segmented tomogram slice of Ni/Al_2O_3-hc (c) showing less electron dense (grey, assigned to uncoked catalyst body) and higher density (red, assigned to coked catalyst body) regions by binary thresholding of the normalised N_e distribution.

The Ni/Al_2O_3-ha and Ni/Al_2O_3-hc samples were then studied by PXCT at beamline I13-1 of Diamond Light Source, which is specialised in coherent hard X-ray imaging methods such as ptychography. For each sample, 1,000 2D-projections were acquired over an angular range of 180°, followed by image reconstruction to obtain tomograms (3D digital volumes) of the complex refractive index (δ). From the δ tomograms, the electron density (N_e) tomograms of the catalysts can be directly calculated[2,3]. The N_e tomograms (Fig. 1) in the present work have an isotropic voxel size of ca. 37 nm and an estimated resolution of 74 to 83 nm based on Fourier shell correlation. The tomograms readily show the connected macropore network of Ni/Al_2O_3-ha and Ni/Al_2O_3-hc, but the resolution is not sufficient to directly resolve the mesopores.

For further analysis, the tomograms were segmented and labelled based on the N_e distribution into regions containing pores (orange), nanoporous catalyst body (grey) and contamination (green) (Fig. 1), following which the N_e distribution of the whole catalyst particles was determined (Fig. 2a). The contamination mainly originates from Pt used to mount the sample particles on the pins during FIB-SEM preparation, which can be selected and discarded from the 3D volumes before further analysis. Comparing the N_e distribution for the whole catalyst particles, a shoulder with increased N_e can be observed on the nanoporous catalyst body peak at $N_e > 0.5$ e$^-$Å^{-3} for the Ni/Al_2O_3-hc sample. This is additionally illustrated by plotting the mean N_e with the standard deviation (σ) of the nanoporous catalyst body label depending on the tomography slice number (Fig. 2b). Over the whole slice range, the mean N_e of Ni/Al_2O_3-hc is larger than for Ni/Al_2O_3-ha, while the σ value also highlights the increased contribution from regions of higher N_e.

The normalised N_e distribution of the whole nanoporous catalyst labels of Ni/Al_2O_3-ha and Ni/Al_2O_3-hc were used to critically select a threshold for segmentation of the Ni/Al_2O_3-hc into coked and uncoked labels (Fig. 2c). No obvious coke formation was detected inside the macropores of the Ni/Al_2O_3-hc catalyst. Based on the distribution of the coked label (Fig. 2c), it is postulated that coke forms in mesopores within the catalyst body, with a pronounced coke distribution at the exterior of the particle. Similar observations were recently reported by X-ray holotomography for fluid catalytic cracking particles with a 3D spatial resolution of ca. 200 nm[5]. However, in the present case further studies at different coking stages should be performed to validate this conclusion. In principle, the electron density distribution and thus the results of PXCT are sensitive to any changes of the atomic configuration in 3D space, requiring careful interpretation of the results. In the present study, it is reasonable to attribute the observed N_e increase to coking. Other possible factors such as Ni nanoparticle sintering can be neglected, due to the comparison of similar treatment and activation conditions at high temperatures for both samples, with only a short coking time (30 min) at the reaction temperature.

In conclusion, X-ray Ptychography allows routine analysis of catalyst particles up to tens of µm in diameter with sub-100 nm resolution. At this level of performance however the method is currently only feasible at dedicated synchrotron beamlines for coherent hard X-ray microscopy, such as I13-1 of Diamond Light Source. This is due to the high coherent photon flux required for such measurements. On the other hand, the quantitative electron density contrast available from PXCT can not only be used to analyse coking of catalysts, but also to directly visualise the location of coke deposits. Based on this knowledge, the methodology presented here has great potential to provide fundamental knowledge on catalyst deactivation for various use cases. Obtaining such information at the nanoscale on extended sample volumes is hardly possible with any other currently established method. Understanding and mitigating catalyst deactivation is a crucial component in future knowledge-based tailoring of catalyst synthesis methods as well as structural properties (*e.g.*, pore networks) to increase the catalyst stability, improve the efficiency and lifespan particularly for industrial applications. With the current shift towards next generation diffraction limited synchrotron light sources, such as Diamond-II, it is anticipated that the resolution, performance, and applications of hard X-ray imaging will stand to gain quite dramatically in future.

References:

1. Wang, G. *et al.* Rational design of hierarchically structured porous catalysts for autothermal reforming of methane. *Chemical Engineering Science* **65**, 2344–2351 (2010). DOI: 10.1016/j.ces.2009.09.079
2. Dierolf, M. *et al*. Ptychographic X-ray computed tomography at the nanoscale. *Nature* **467**, 436–439 (2010). DOI: 10.1038/nature09419
3. Diaz, A. *et al*. Quantitative x-ray phase nanotomography. *Physical Review B* **85**, 020104 (2012). DOI: 10.1103/PhysRevB.85.020104
4. Weber, S. *et al*. Porosity and structure of hierarchically porous Ni/Al_2O_3 Catalysts for CO_2 Methanation. *Catalysts* **10**, 1471 (2020). DOI: 10.3390/catal10121471
5. Veselý, M. *et al.* 3-D X-ray nanotomography reveals different carbon deposition mechanisms in a single catalyst particle. *ChemCatChem* **13**, 2494–2507 (2021). DOI: 10.1002/cctc.202100276

Funding acknowledgement:

Funded by the Deutsche Forschungsgemeinschaft (DFG, German Research Foundation) – 406914011. This work was partly carried out with the support of the Karlsruhe Nano Micro Facility (KNMF), a Helmholtz Research Infrastructure at Karlsruhe Institute of Technology (KIT), which provided access to FIB instruments via proposal 2019-022-026980. This work was carried out with the support of Diamond Light Source, instrument I13-1 (proposal MG24079-1). We acknowledge KIT and DFG for financing the Raman spectrometer system (INST121384/73-1). Open access funding enabled and organised by Projekt DEAL.

Corresponding authors:

Sebastian Weber, Karlsruhe Institute of Technology (KIT), sebastian.weber@kit.edu
Dr. Thomas L. Sheppard, Karlsruhe Institute of Technology (KIT), thomas.sheppard@kit.edu.

Bright light emission from composite glasses

Related publication: Hou J., Chen P., Shukla A., Krajnc A., Wang T., Li X., Doasa R., Tizei L. H. G., Chan B., Johnstone D. N., Lin R., Schülli T. U., Martens I., Appadoo D., Ari M. S., Wang Z., Wei T., Lo S.-C., Lu M., Li S., Namdas E., Mali G., Cheetham A. K., Collins S. M., Chen V., Wang L.-Z., Bennett T. D. Liquid-phase sintering of lead halide perovskites and metal-organic framework glasses. *Science* **374**, 621–625 (2021). DOI: 10.1126/science.abf4460

Publication keywords: Metal-organic framework glass; Metal halide perovskite; Sintering

Lead halide perovskites are a family of synthetic semiconductor materials that can be used for solar panels, LEDs, displays, sensors, and many other applications. However, these materials have limited stability over time and can leach toxic chemicals into the environment. $CsPbI_3$, for example, is sensitive to temperature, air, light, and commonly encountered chemicals like water, limiting its practical applications.

An international team of researchers has addressed this challenge by encapsulating $CsPbI_3$ in a matrix made of a new type of glass derived from a class of materials known as metal-organic frameworks. The composite showed orders of magnitude higher efficiency for light emission and significantly enhanced stability, providing high-quality light for more than a year. They turned to advanced tools to understand how and why this new material works the way it does.

Using the E02 microscope at the electron Physical Science Imaging Centre (ePSIC) made it possible to see individual nanometre scale crystals and determine the type of crystal within the glass. They used a type of transmission electron microscopy that takes diffraction data from less than 5 nm of material without damaging materials that are otherwise very easily changed when exposed to high energy electrons.

Microscopic observations enabled the team to document how the glass preserves and locks in the correct, light-emitting perovskite crystals. Together with many other measurements with collaborators worldwide, the results explain how to make long-lasting light-emitting glass composites, preventing toxic lead leaching while simultaneously improving the mechanical properties of the material to prevent breakage.

Extensive research in the last 10-15 years on lead halide perovskites (LHPs) has resulted in record developments for photovoltaics, light-emitting diodes (LEDs), radiation detection, and thermometry. LHPs exhibit tunable band gaps, high charge carrier mobilities, and bright, narrow-band photoluminescence (PL), but the widespread industrial use of LHPs is still hampered by several factors, including (i) their decomposition when exposed to polar solvents, oxygen, heat, and light, (ii) their inherent polymorphism, (iii) the presence of deep trap states, and (iv) the phase segregation and leaching of toxic heavy metal ions. The high-temperature pseudo-cubic 'black' phases (α-, β- and γ-phases) of $CsPbI_3$, for example, exhibit strong optical absorptivity and direct band gaps, making them excellent for photovoltaics and red-light emitting LEDs. Under ambient circumstances, however, they rapidly change into a thermodynamically stable, non-perovskite 'yellow' δ-phase, leading to almost complete loss of their optoelectronic properties (Fig. 1).[1]

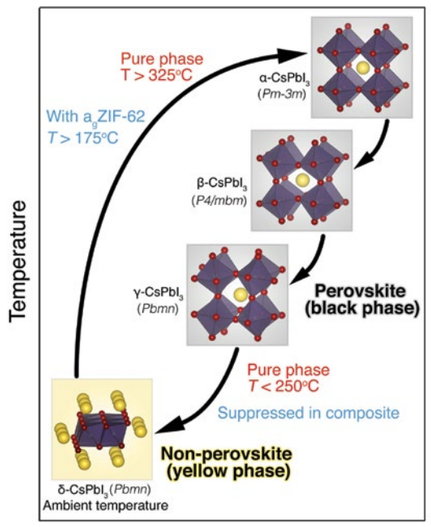

Figure 1: Phase transition of $CsPbI_3$ in its pure phase and within the composites.

Figure 2: Photoluminescence spectra for $(CsPbI_3)0.25(agZIF\text{-}62)0.75$ composites fabricated at different sintering temperatures and cryogenic quenching.

The creation of LHP composites offer a route to address these difficulties. The ionic character of LHPs, however, is not generally favourable to composite production. A critical step is to create low-cost, processable, stable, environmentally friendly, and scalable LHP composites that can be used in real-world applications. Zeolitic imidazolate frameworks (ZIFs) are a kind of metal-organic framework (MOF) that consists of metal tetrahedra (e.g., Zn2+/Co2+) coordinated by imidazolate ligands. Recent improvements in ZIF materials have given access to stable ZIF liquids that can be quenched to produce microporous glasses. These ZIF glasses are a promising host for many other functional materials because the ZIF glasses can be modified to offer many desirable properties, from chemical control to mechanical properties.[2]

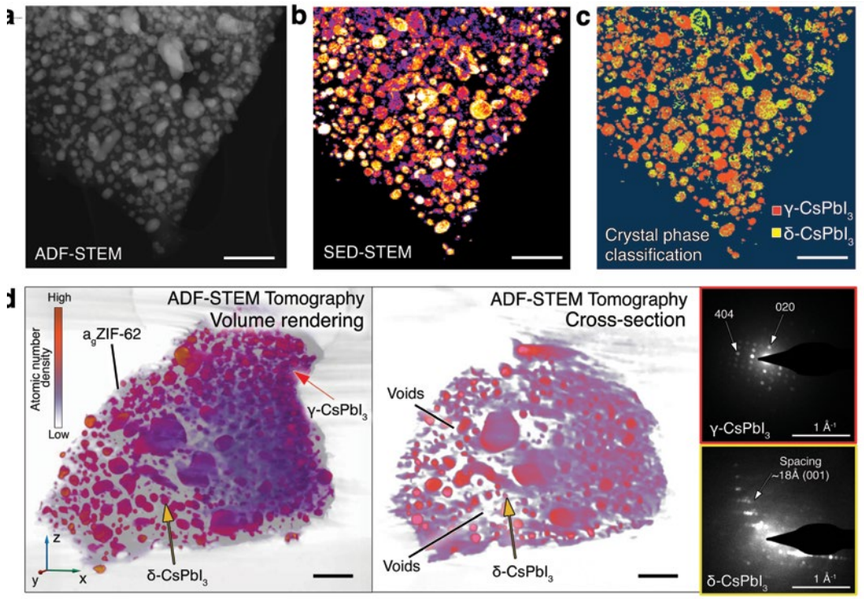

Figure 3: Phase distribution for the $(CsPbI_3)0.25(agZIF\text{-}62)0.75$ composite fabricated with 300 °C sintering. (a) ADF-STEM image, (b) SED-STEM mapping and (c) $CsPbI_3$ crystal phase classification results for $(CsPbI_3)0.25(agZIF\text{-}62)0.75$ composite. (d) Volume rendering of a tomographic reconstruction of $(CsPbI_3)0.25(agZIF\text{-}62)0.75$ and a single cross-sectional plane extracted from the volume. Colour-coded arrows highlight the regions where electron diffraction data were collected. Scale bars in (a-d) are 250 nm.

In order to translate these principles to LHPs, a technique known as liquid phase sintering was applied to combine a preformed ZIF glass powder and LHP materials to create a single material in a carefully controlled heat treatment. This is the first demonstration of liquid phase sintering, an industrial powder processing technique, applied to the material systems of LHPs and ZIF glass. More specifically, ZIF glass {agZIF-62 (Zn[(Im)1.95(bIm)0.05] (Im: imidazolate; bIm: benzimidazolate))} and $CsPbI_3$ were synthesised via ball milling directly from the precursors, and then homogenised at a weight ratio of 3:1. The mixture was pelletised and then sintered at a rate of 20 °C/min at different temperatures under the protection of an inert Argon atmosphere. To minimise any undesirable thermal decomposition, the sintering process was quenched using liquid nitrogen. The fabricated composites were referred to as for $(CsPbI_3)0.25(agZIF\text{-}62)0.75$.

The $(CsPbI_3)0.25(agZIF\text{-}62)0.75$ started to show intense and narrow red PL emission after being heated to 175 °C (Fig. 2). The narrow-band emission is a strong indication that the metastable, optoelectronically active phase of $CsPbI_3$ was created and preserved within the composite. Further increasing the sintering temperature enhanced the PL intensity, with the strongest PL achieved by sintering at 275 °C. Notably, the PL intensity of the sintered composite was over 200 times higher than the sample consisting of the mixed powder pellet prior to sintering, referred to as $(CsPbI_3)(agZIF\text{-}62)(25/75)$.

To understand the detailed microstructure and crystal phase information, Scanning Transmission Electron Microscopy (STEM) was used to examine the $(CsPbI_3)0.25(agZIF\text{-}62)0.75$ composite with nanometre spatial resolution, the critical length scale for $CsPbI_3$ nanocrystals. Using annular dark field STEM (ADF-STEM) imaging clearly distinguished the atomic number contrast between the two phases (Fig. 3), and the predicted elemental distribution was further corroborated by mapping the composite using X-ray Energy-Dispersive Spectroscopy (STEM-EDS). By taking an electron diffraction pattern at every point in the image, a technique known as Scanning Electron Diffraction (SED), maps were constructed of the crystalline areas corresponding to the $CsPbI_3$ nanocrystals (Fig. 3b). Classification in terms of the active and optically inactive $CsPbI_3$ phases was retrieved from the SED data through a machine learning approach, using a convolutional neural network. This classification demonstrated that the optoelectronically active phase was the main crystalline component in the composite (Fig. 3c). To look inside the three-dimensional structure of the composite, tomography in ADF-STEM (Fig. 3d) unveiled the interfacial contact as well as voids characteristic of the liquid phase sintering process. Electron diffraction captured from single $CsPbI_3$ crystal grains confirmed that active γ-$CsPbI_3$ crystals were found in the regions of the composite with the most interfacial contact and dense packing of the ZIF glass around the $CsPbI_3$ grains.

Subsequently, to examine the practicality of these materials, the stability of the composites was tested by soaking in water for over 10,000 h, sonicating in various nonpolar, polar protic, and polar aprotic organic solvents, and under exposure to constant laser excitation (ca. 57 mW/cm^2) for over 5,000 seconds. The composite showed satisfactory stability in all of these challenging environments. The ZIF glass composite approach was further extended across the inorganic lead halide perovskite family (Cl, Br, I and mixed halide ions), generating emission from blue to red. Through suitable selection of colour combinations, these materials were ultimately demonstrated in a white light LED device.

References:

1. Steele J. *et al*. Thermal unequilibrium of strained black $CsPbI_3$ thin films. *Science* **365**, 679–684 (2019). DOI: 10.1126/science.aax3878
2. Hou J. *et al*. Metal-organic framework crystal-glass composites. *Nature Communications* **10**, 2580 (2019). DOI: 10.1038/s41467-019-10470-z

Funding acknowledgement:
The authors acknowledge financial support from the Australian Research Council (DE190100803, DP180103874, DE190101152 and FL190100139); The University of Queensland (UQECR2057677); the Royal Society and Leverhulme Trust for a University Research Fellowship (UF150021) and Philip Leverhulme Prize (2019). The authors gratefully acknowledge the Leeds EPSRC Nanoscience and Nanotechnology Facility (LENNF) for support & assistance in this work, and the Diamond Light Source for access and support in the use of the electron Physical Sciences Imaging Centre (MG21980, MG25140).

Corresponding author:
Dr. Jingwei Hou, University of Queensland, Jingwei.hou@uq.edu.au

Visualising dendrite-induced cracking in lithium anode solid-state batteries

Related publication: Ning, Z., Spencer Jolly, D., Li, G., de Meyere, R., Pu, S. D., Chen, Y., Kasemchainan, J., Ihli, J., Gong, C., Liu, B., Melvin, D. L. R., Bonnin, A., Magdysyuk, O., Adamson, P., Hartley, G. O., Monroe, C. W., Marrow, T. J., & Bruce, P. G. Visualizing plating-induced cracking in lithium-anode solid-electrolyte cells. *Nature Materials* **20**, 1121–1129 (2021). DOI: 10.1038/s41563-021-00967-8

Publication keywords: Solid-state batteries; Imaging techniques; Materials for energy

High energy density solid-state batteries, with ceramic solid electrolytes and lithium metal anodes, promise to address the range anxiety and safety issues of electric vehicles. However, practical application of solid-state batteries is limited by electrolyte cracking and short circuits at high charging rates due to the propagation of lithium filaments called dendrites through the ceramic electrolyte.

Observing how lithium dendrites penetrate solid electrolytes and correlating this with crack propagation will guide the design of better ceramic electrolytes that can enable fast-charging solid-state batteries. Researchers used Diamond Light Source's Joint Engineering, Environmental and Processing (JEEP) beamline (I12) to image dendrite-induced cracks using high spatial resolution X-ray Computed Tomography (XCT) and located lithium dendrites by spatially mapped X-ray diffraction. Combining XCT and diffraction provided reliable evidence of the correlation between cracks and dendrite growth into the cracks.

At high charging rates, lithium dendrite ingress into the ceramic electrolyte induces spallations (conical 'pothole'-like cracks) in the ceramic adjacent to the lithium electrode. Further lithium plating into the spallation cracks drives the propagation of transverse cracks across the electrolyte by widening the cracks from the rear. During charging, lithium plates into the dry transverse cracks, ultimately causing short-circuiting of the battery.

Preventing lithium dendrites is key to enabling fast-charging solid-state batteries. This work suggests that an effective way to prevent dendrite growth in solid-state batteries is to inhibit the development of dry cracks in the ceramic electrolyte. Therefore, strategies that toughen the ceramic electrolyte, such as fibre reinforcement and transformation toughening, may help to enable fast-charging, safe and highly energy-dense solid-state batteries.

Solid-state batteries pairing a lithium anode with a ceramic solid electrolyte are being considered for next-generation batteries as they promise to revolutionise the energy density and safety of cells[1]. Electric vehicles are an important market for next-generation batteries, and a key requirement is fast charging. However, charging at practical rates in the mA/cm^2 range proves challenging, as dendrites (filaments of Li metal) are observed to penetrate across the ceramic electrolyte, leading to short-circuit and cell failure[2].

In order to develop solid-state batteries that are able to charge at high rates, it is important to understand the mechanism by which dendrites grow into the ceramic electrolyte during the charging process. However, despite decades of research into this problem there is no clear consensus in the literature as to how soft Li metal can propagate dendritic cracks through ceramic electrolytes which have shear moduli that are orders of magnitude higher than that of Li metal[3].

In this study, *in situ* X-ray Computed Tomography (XCT) with high spatial resolution and phase contrast was combined with spatially mapped X-ray Diffraction (XRD) to follow the penetration of Li dendrites into the ceramic electrolyte of a solid-state battery during cycling. Imaging the dendrite as it grows provides new observations as to how dendritic cracks initiate and propagate into the ceramic electrolyte, giving new insights as to the mechanism of dendrite growth.

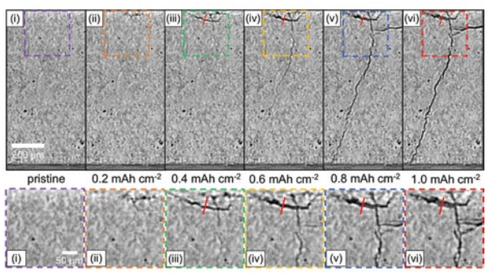

Figure 1: In situ propagation phase-contrast XCT virtual cross-sections during a single plating of a Li/Li$_6$PS$_5$Cl/Li cell. Cross-sections show (i) the pristine cell and (ii) after 0.2 mAh cm^{-2}; (iii) 0.4 mAh cm^{-2}; (iv) 0.6 mAh cm^{-2}; (v) 0.8 mAh cm^{-2} and (vi) 1.0 mAh cm^{-2} of charge passed; plated electrode at the top. The red line across the crack corresponds with the greyscale analysis in Fig. 2a. Adapted by permission from Springer Nature: Nature Materials, Visualizing plating-induced cracking in lithium-anode solid-electrolyte cells, Z. Ning, D. Spencer Jolly, G. Li et al., Copyright 2021.

For this study, a solid-state symmetric cell consisting of Li electrodes and an argyrodite-type Li$_6$PS$_5$Cl electrolyte was chosen, as Li$_6$PS$_5$Cl is a leading candidate solid electrolyte due to its high ionic conductivity. XCT was used to track crack propagation as a function of the state of charge of the cell. Early in the charging process, XCT revealed that a crack forms (Fig. 1ii), developing into a conical, 'pothole'-like crack, termed a spallation crack, at the surface of the ceramic electrolyte near the interface with the plated electrode (Fig. 1iii). As more charge is passed, this surface cracking worsens and the spallation crack is observed to widen (Fig. 1iv). Analysis of the greyscale within the spallation crack shows that the grey-level within the crack gradually increases as a function of charge, revealing that Li is plating within the spallation, filling and widening the crack (Fig. 2a).

As more charge still is passed, a crack which is perpendicular to the electrode/electrolyte interface, termed the transverse crack, is observed to propagate across the ceramic electrolyte from the position of the spallation crack. The transverse crack advances across the solid electrolyte, finally reaching the counter electrode after passing 0.8 mA·h/cm^2 of charge (Fig. 1v). Interestingly, even after passing 1 mA·h/cm^2 capacity the cell was not observed to short-circuit, indicating that the crack traversing the electrolyte was not completely filled with Li, but rather was propagating ahead of the Li metal. This conclusion was strengthened by further analysis of the greyscale within the crack after passing 1 mA·h/cm^2 (Fig. 2b-c), revealing that whereas Li has started to plate into the top of the transverse crack near to the spallation (blue), the lower region of the crack near the counter electrode contained no Li metal (yellow).

The implication of these results is that dendrite propagation through the solid electrolyte is driven by the plating of Li not at the crack tip, but at the rear of the crack. As a result, cracks can traverse the electrolyte without the cell short-circuiting, but will critically fail once Li fills the cracks. These observations are contrary to some previous models for the formation of dendrites, and therefore considerably narrow the possible mechanisms for dendrite growth through ceramic electrolytes.

The relationship between spallation cracking and dendrites was further investigated using spatially resolved XRD mapping to identify the location of Li dendrites. Diffraction was carried out with the X-ray monochromatic beam perpendicular to the Li/Li$_6$PS$_5$Cl interface, and the intensity of the diffraction peak corresponding to Li {110} was mapped onto the area of the ceramic electrolyte to identify where Li metal was present within the ceramic (Fig. 3a). This map of dendrite locations could then be superimposed on the XCT reconstruction of the ceramic electrolyte, revealing that Li dendrites had only penetrated into the ceramic at positions where surface spallations were observed. This result demonstrates that transverse dendritic cracks typically initiate from spallation cracks.

That Li dendrite growth into ceramic electrolytes initiates with spallation cracking at the interface, and that these spallations develop into transverse cracks propagating across the electrolyte driven by Li plating at the rear of the crack rather than at the tip, are new observations that inform understanding of how solid-state batteries fail at high rates of charge. These insights lay the foundations for preventing dendrite growth during fast-charging using

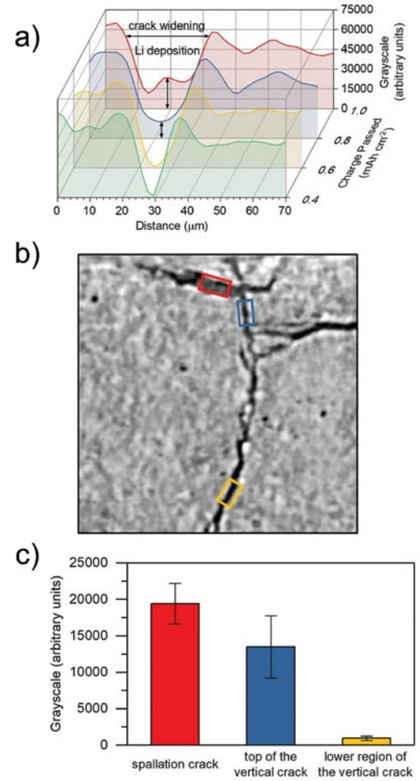

Figure 2: a) Measured greyscale profiles across the crack at the region indicated by the red lines in Fig. 1 b) Magnified image from Fig. 1(vi) showing where the greyscale values were determined for the spallation crack (red box) and different parts of the vertical crack (blue and yellow boxes) after passage of 1.0 mAh cm^{-2}; c) Greyscale analysis showing the amount of lithium in the regions of the crack identified by the boxes after passage of 1.0 mAh cm^{-2}. Adapted by permission from Springer Nature: Nature Materials, Visualizing plating-induced cracking in lithium-anode solid-electrolyte cells, Z. Ning, D. Spencer Jolly, G. Li et al., Copyright 2021.

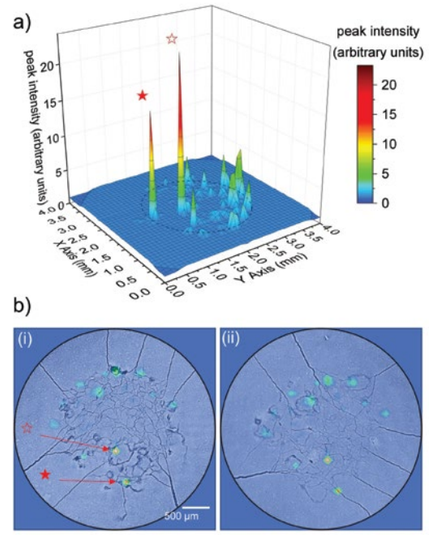

Figure 3: Diffraction mapping showing distribution of lithium dendrites and their association with the spallation cracks. a) Diffraction intensity of lithium {110} peak revealing the distribution of lithium dendrites. The dashed black circle marks the position of the electrodes in the cell; b) XCT image slices from planes in the electrolyte parallel and adjacent to the two electrodes, (i) and (ii). The two most intense lithium peaks are marked with stars. Adapted by permission from Springer Nature: Nature Materials, Visualizing plating-induced cracking in lithium-anode solid-electrolyte cells, Z. Ning, D. Spencer Jolly, G. Li et al., Copyright 2021.

strategies such as engineering the ceramic electrolyte by transformation toughening and fibre reinforcement to block the propagation of dry-cracks. This study also reveals the power of synchrotron X-ray techniques such as *in situ* XCT and XRD mapping for revealing the failures occurring within a solid-state battery.

References:

1. Janek, J. *et al.* A solid future for battery development. *Nat. Energy* **1**, 16141 (2016). doi: 10.1038/nenergy.2016.141
2. Kerman, K., *et al.* Review - Practical challenges hindering the development of solid State Li ion batteries. *J. Electrochem. Soc.* **164**, A1731–A1744 (2017). DOI: 10.1149/2.1571707jes
3. Pasta, M. *et al.* 2020 Roadmap on solid-state batteries. *J. Phys. Energy* **2**, 0–52 (2020) DOI: 10.1088/2515-7655/ab95f4

Funding acknowledgement:
P.G.B. is indebted to the Faraday Institution All-Solid-State Batteries with Li and Na Anodes (FIRG007, FIRG008), as well as the Engineering and Physical Sciences Research Council, Enabling Next Generation Lithium Batteries (EP/M009521/1), the University of Oxford experimental equipment upgrade (EP/M02833X/1) and the Henry Royce Institute for Advanced Materials (EP/R0066X/1, EP/S019367/1, EP/R010145/1) for financial support. G.L. and C.W.M. acknowledge the Faraday Institution Multiscale Modelling (FIRG003) and the UK Industrial Strategy Challenge Fund: Materials Research Hub for Energy Conversion, Capture, and Storage, under grant EP/R023581/1, for financial support. J.I. is supported by the Swiss National Science Foundation (no. PZ00P2_179886). We thank Diamond Light Source (beamline I12, experiment no. EE20795-1) and the Paul Scherrer Institute (TOMCAT beamline X02DA, experiment no. 20182142) for beamtime, as well as technical and experimental support.

Corresponding author:
Dominic Spencer Jolly, University of Oxford, dominic.spencerjolly@materials.ox.ac.uk;
Peter G. Bruce, University of Oxford, peter.bruce@materials.ox.ac.uk

Organic carbon preservation linked to carbon chemistry and sediment mineralogy

Related publication: Curti, L., Moore, O. W., Babakhani, P., Xiao, K.-Q., Woulds, C., Bray, A. W., Fisher, B. J., Kazemian, M., Kaulich, B., & Peacock, C. L. Carboxyl-richness controls organic carbon preservation during coprecipitation with iron (oxyhydr)oxides in the natural environment. *Communications Earth & Environment* **2**, 229 (2021). DOI: 10.1038/s43247-021-00301-9

Publication keywords: Organic carbon; Iron (oxyhydr)oxides; Coprecipitation; Soils; Sediments; Preservation

Organic carbon preservation in soils and sediments helps control atmospheric carbon dioxide concentrations. Previous studies suggest that organic carbon can be preserved by becoming associated with soil and sediment minerals. With a better understanding of the carbon-mineral interactions, it may be possible to predict spatial and temporal patterns of carbon preservation that may help explain the evolution of climate over Earth's history and be used to help mitigate current climate change.

Researchers from the University of Leeds investigated the mechanisms responsible for organic carbon preservation in soils and sediments at a micro scale. They used the Diamond's Scanning X-ray Microscopy Beamline (I08), one of the only beamlines that can spatially and chemically analyse organic carbon at micro scale resolution. Their results showed that the binding of organic carbon to minerals in soils and sediments is strongly controlled by the chemistry of the carbon and the type of minerals available.

Organic carbon that is rich in carboxyl functional groups binds more strongly and more stably to iron minerals than molecules that are poor in carboxyl groups. This implies that carboxyl-richness provides an important control of organic carbon preservation in natural environments.

The findings suggest that increasing the carboxyl-richness of the carbon and the quantity of iron minerals in soils could improve organic carbon storage and help store organic carbon in soils where it is locked away from the atmosphere.

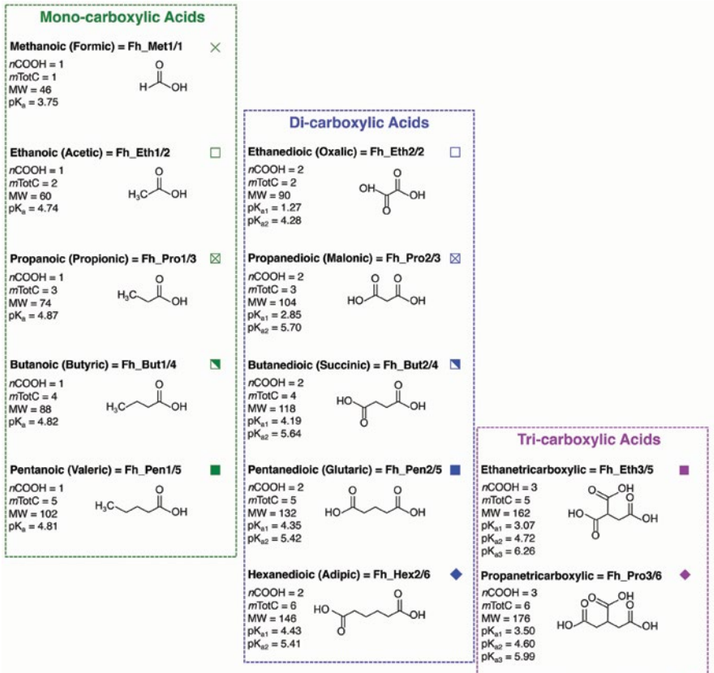

Figure 1: Carboxylic acids coprecipitated with ferrihydrite. Mono-, di- and tri-carboxylic acids, including systematic name, common name in parentheses, coprecipitate nomenclature and data symbol; number carboxyl functional groups (nCOOH); number total carbon atoms (mTotC); Molecular Weight (MW); and pK_a of carboxyl functional groups. Influence of number of carboxyl groups (n) at constant number of total carbon atoms (m) on carbon affinity and stability investigated by comparing acids across columns (sequentially increasing n). Influence of number of total carbon atoms (m) at constant number of carboxyl groups (n) on carbon affinity and stability investigated by comparing acids down columns (sequentially increasing m).

The preservation of organic carbon in soils and sediments is an important control on atmospheric carbon dioxide and oxygen[1]. Despite decades of research however, the controls on carbon preservation are still poorly understood[2]. The factors controlling the preservation of carbon are complex, but in order for carbon to become preserved, it must escape microbial remineralisation which oxidises it back into carbon dioxide[3]. One leading hypothesis for carbon preservation asserts that carbon bound with soil and sediment minerals is less accessible to microbes and thus protected from microbial attack[4]. Work to date identifies that carbon that is rich in carboxyl functional groups might bind very strongly to iron (oxyhydr)oxide minerals and be protected from microbial remineralisation[5]. Whether and to what extent the carboxyl-richness of carbon can control carbon binding and stability however, is unknown.

This work takes a direct mechanistic approach to test whether the carboxyl-richness of carbon can control carbon binding, stability and hence persistence with iron (oxyhydr)oxide minerals. Macro scale binding and stability experiments are combined with micro scale synchrotron spectroscopy analyses to determine the affinity of carboxyl-rich carbon for iron (oxyhydr)oxide minerals and the stability of bound carbon against chemical remineralisation. Carboxyl-rich carbon is represented by simple carbon compounds that are found prevalently in soils and sediments and serve as model compounds for more complex forms of carbon. Iron (oxyhydr) oxide minerals are represented by ferrihydrite which is found ubiquitously in soils and sediments and is commonly associated with carbon. Affinity, stability and persistence are investigated with respect to the number of carboxyl groups (*n*) at constant number of total carbon atoms (*m*), and the number of total carbon atoms (*m*) at constant number of carboxyl groups (*n*) (Fig. 1, comparing across (sequentially increasing *n*) or down columns (sequentially increasing *m*)). The corresponding coprecipitates are denoted Fh_acid*n*/*m*_C:Fe, where Fh is ferrihydrite, acid indicates the first three letters of the compound name, followed by *n* carboxyl groups and *m* total carbon atoms, and C:Fe is the molar C:Fe ratio of the solid phase.

To investigate the affinity of the acids with ferrihydrite, each acid was coprecipitated with ferrihydrite at a sequentially increasing initial carbon and fixed initial iron concentration. The data show that as the number of carboxyl groups increases, the molar amount of carbon bound with the ferrihydrite increases. Thus carboxyl-richness likely provides an important control on carbon affinity with iron (oxyhydr) oxides in soils and sediments. To investigate the stability of the acids with ferrihydrite against release and chemical remineralisation, coprecipitates were exposed to solutions typically used to either release or oxidise carbon from iron (oxyhydr)oxides. The data show that as the number of carboxyl groups increases, the molar amount of carbon released or oxidised from ferrihydrite decreases. Thus carboxyl-richness likely provides an important control on carbon stability with iron (oxyhydr) oxides in soils and sediments.

To determine the mechanisms responsible for the increased affinity and stability of carboxyl-rich carbon with ferrihydrite, Scanning Transmission X-ray Microscopy (STXM) coupled with Near Edge X-ray Absorption Fine Structure (NEXAFS) Spectroscopy was used on I08. The spectra show that the carboxyl peak for all the coprecipitates is reduced in amplitude and broadened compared to their respective standards (Fig. 2). This indicates that carboxyl-rich carbon binds to ferrihydrite via a carboxyl group ligand exchange adsorption mechanism, occurring between the hydroxyl part of a carboxyl group and the hydroxyl part of a ferrihydrite adsorption site. The spectra also show that as the number of carboxyl groups increases in the coprecipitates, the carboxyl peak is increasingly shifted to lower energy compared to the respective standards (Fig. 2). This indicates that as the number of carboxyl groups increases in the coprecipitates, the number of carboxyl ligand exchange bonds between each adsorbing acid molecule and the ferrihydrite particles increases (Fig. 2). Thus carboxyl-rich carbon binds to ferrihydrite via a multi-carboxyl ligand exchange adsorption mechanism.

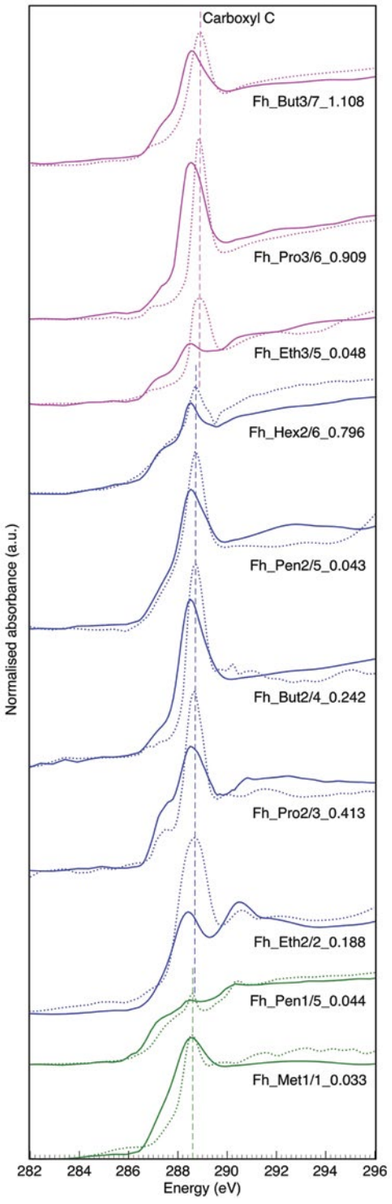

Figure 2: Carbon 1s NEXAFS spectra for carboxylic acids coprecipitated with ferrihydrite. Spectra for carboxylic acid standards (dotted lines) and carboxylic acid ferrihydrite coprecipitate samples (solid lines) plotted as energy (eV) vs. normalised absorbance (arbitrary units). Green, blue and purple colour codes depict mono-, di- and tri-carboxylic data, respectively. The coprecipitate nomenclature is given in Fig. 1. Spectra are stacked with an arbitrary offset for clarity. Carboxyl carbon peak positions for the unreacted mono-, di- and tri-carboxylic acid standards are shown with vertical dashed green, blue and purple lines, respectively.

Overall this work indicates that the increased affinity and stability of carboxyl-rich carbon with iron (oxyhydr)oxides results from a multi-carboxyl ligand exchange adsorption mechanism, in which carboxyl-rich carbon forms more bonds with ferrihydrite particles and is subsequently more difficult to release and oxidise. In soils and sediments carboxyl-rich carbon and iron (oxyhydr) oxides are prevalent and their association likely imparts a strong control on carbon persistence in natural environments and thus an important control on carbon cycling and atmospheric carbon dioxide and oxygen.

References:

1. Berner, R. A. The phanerozoic carbon cycle, (2004). DOI: 10.1093/oso/9780195173338.001.0001
2. Arndt, S. *et al*. Quantifying the degradation of organic matter in marine sediments: A review and synthesis. *Earth-Science Reviews* **123**, 53–86 (2013). DOI : 10.1016/j.earscirev.2013.02.008
3. Hedges, J. I. *et al.* Sedimentary organic matter preservation: an assessment and speculative synthesis. *Marine Chemistry* **49**, 81–115 (1995). DOI: 10.1016/0304-4203(95)00008-F
4. Keil, R. G. *et al.* Sorptive preservation of labile organic matter in marine sediments. *Nature* **370**, 549–552 (1994). DOI: 10.1038/370549a0
5. Kaiser, K. *et al.* The role of DOM sorption to mineral surfaces in the preservation of organic matter in soils. *Organic Geochemistry* **31**, 711–725 (2000). DOI: 10.1016/S0146-6380(00)00046-2

Funding acknowledgement:
This research project has received funding from the European Research Council (ERC) under the European Union's Horizon 2020 research and innovation programme (Grant agreement No. 725613 MinOrg). Royal Society Wolfson Research Merit Award (WRM/FT/170005) is gratefully acknowledged. Diamond Light Source provided access to Beamline I08 (STFC grant numbers SP21323, SP20839 and MG23049) that contributed to the results presented here.

Corresponding author:
Prof. Caroline Peacock, University of Leeds, C.L.Peacock@leeds.ac.uk

Crystallography Group

Joe Hriljac, Science Group Leader

The Crystallography Group comprises the High-Resolution Powder Diffraction beamline (I11), the Extreme Conditions beamline (I15), the X-ray Pair Distribution Function (XPDF) beamline (I15-1), and the Small-Molecule Single-Crystal Diffraction beamline (I19). Having these beamlines together in one science group allows us to fully exploit the technical and scientific expertise within its teams to provide the basis for future development and pioneering experiments.

The past year was a second challenging one with the continuing COVID-19 pandemic, but especially so for beamlines that were undergoing large upgrades that started pre-pandemic such as I11 and I15-1. These both did progress significantly and are near to completion, but many delays occurred due to staff shortages and supply chain issues and the knock-on effects these had on project planning. Thankfully these did not impact the purchase, installation and commissioning of new detectors and so those for I15 and I19 went more to plan and are now fully operational. The other project that has been delayed is the upgrade to the I15/I15-1 wiggler as engineers were not able to come from abroad to do the intended works. Parts have arrived and the upgrade should be completed in summer of 2022. Due in large part to the hard work and dedication of the beamline and technical staff to continue supporting remote user experiments, the user programmes on all beamlines have moved closer to pre-pandemic levels and 185 papers were published during the 2021 calendar year from data attributed to the four beamlines.

I11 update

The high brightness beamline uses monochromatic X-rays in the range of 6 - 25 keV for high-resolution and time-resolved powder diffraction experiments in the first Experimental Hutch (EH1) or for Long Duration Experiments in EH2. The varied science programme supports a wide range of studies by chemists, physicists, materials scientists and environmental scientists in particular for non-ambient applications and experiments requiring unusual hardware setups such as toxic/corrosive gas absorption studies at cryogenic temperatures, resonant diffraction at high temperature and time-resolved in operando lithium-ion (Li-ion) battery work.

After running for over ten years, many components such as the monochromator, diffractometer and Multi-analyser Crystal (MAC) detector began to show signs of wear. An upgrade plan, endorsed by the Scientific Advisory Committee (SAC) and the Diamond Industrial Science Committee (DISCo) at the end of 2017 to replace these components started in 2019 and the new Newport diffractometer was partly installed when site was shut in March 2020. During the course of the remainder of 2020 the installation and commissioning resumed when possible under the COVID-19 working protocols. Finally in January 2021 the last stage, commissioning of the robot sample changer, was completed and the beamline became operational again. Since that point a large number of more routine experiments have been conducted by remote user access with beamline staff assistance and, more recently, users have returned to site. When all restrictions have been removed the full experimental programme will resume – until now some experiments are still not scheduled as they require setups that require too many people in small, enclosed spaces. The construction of a new PSD using Mythen3 technology is well underway with hopes for completion, testing and commissioning in 2022. This will lead to the ability for even faster collection of powder patterns for, e.g., time-resolved studies.

I15 update

The Extreme Conditions beamline, I15, employs high energy X-rays to explore the structure of materials at high pressures, high and low temperatures, as well as other *in situ* and *in operando* conditions. The beamline receives an X-ray continuum from the superconducting wiggler; this allows for experiments that require monochromatic X-rays between 20 and 80 keV, as well as polychromatic beam. I15 was originally designed to serve the mineral physics community, which it has, whilst also assisting material scientists, chemists and solid-state physicists with their structural investigations, at pressure or otherwise.

I15 continues to offer extensive capabilities and support to users to assist their high-pressure studies. I15 users have pre-experiment access to bespoke assistance and training from our highly skilled staff in diamond anvil cell (DAC) preparation and loading, as well as the usage of beamline DACs for novice users for I15 experiments. The high-pressure gas loader available at I15 offers users the choice of many possible gases to use as their pressure transmitting media (PTM), allowing them to optimise for hydrostaticity with helium or neon, or choosing a PTM based on desired interactions with the sample at pressure. Work is underway to add hydrogen to our gas loading capabilities, originally scheduled for 2020 this has had to be pushed back into 2022 due to the pandemic. The recent addition of the laser heating system adds a further unique capability – the I15 system is capable of quickly ramping the laser power to perturb a sample without delivering too much heat to the bulk. A DECTRIS PILATUS3 X CdTe 2M arrived in late 2020 and is now in routine use with 14 user experiments having used it in 2021. It provides much greater sensitivity to high-energy X-rays and the capability for much faster data collections. The quality of data has led to a resumption of the development of high-pressure single crystal data collection including the project of a Diamond PhD student. Further upgrades to I15 to take full advantage of fast hardware-based scanning and mapping are planned.

I15-1 update

The XPDF beamline, I15-1, is dedicated to producing high-quality X-ray scattering data for Pair Distribution Function (PDF) analysis. Operational since 2017, I15-1 has illuminated samples from diverse fields, from Earth sciences to pharmaceuticals, as well as material science and chemistry. XPDF receives X-rays from the inside edge of the wiggler fan, and this light is monochromated and directed to the end station in three energies: 40, 65 and 76 keV. PDF data are collected at high energies to produce the low sample absorption and high Q-range required for successful interpretation. Gaining structural information on amorphous samples is a primary goal of many XPDF experiments, but crystalline samples can also display local structure variations such as defects and disorder, which can be studied via PDF analysis. PDF data collections are rarely available at home institutions, so in order to allow more people to exploit this powerful technique I15-1 complements the standard proposal route with popular Rapid and Easy Access routes, where PDF data can be collected via a mail-in procedure.

Consisting of a sample position, with an optional sample-changing magazine, and two large area detectors, the end station is highly flexible and has been adapted to many *in situ* and *in operando* experiments, including variable temperature, gas flow, hydrothermal synthesis and electrochemical cycling. For more routine measurements, the 15-position sample changer has been a popular choice, allowing automatic data collection. Further upgrades, including a new end station and a sample-changing robot with 400 positions, progressed during 2021 and these are now in use. The final aspect of the current upgrade is a new detector based on CdTe sensors that will be much more sensitive at high energy and with faster electronics for data readout. Construction has progressed and the detector is currently in the testing stage with an expectation that it will be commissioned on the beamline in 2022. These upgrades will be a synergistic addition to the existing autoprocessing infrastructure and will allow users to collect better data with less manual intervention.

The Crystallography Science Group members.

I19 update

The Small-Molecule Single-Crystal Diffraction beamline, I19, uses X-rays in the 5 – 25 keV energy range to determine the structures of small-molecule and extended three-dimensional systems, e.g. Metal-Organic Frameworks, with single-crystal diffraction techniques. These methods can be applied to the characterisation of novel materials or for investigating the variation in the structure of a crystalline material under an external physical influence such as a change in temperature, the exposure to a gas, photo-excitation or through the application of high-pressure.

The use of the robotic sample changer, and remote access, is now well established in Experimental Hutch 1 (EH1) of the beamline, where premounted samples are sent to Diamond under cryogenic storage, and users then run their beamtime from their home institutions. This mode of operation makes it possible to carry out chemical crystallography studies in a more responsive manner as beamtime can be scheduled in more regular, and shorter, periods. We now schedule individual shifts, rather than whole one-day (three shifts) blocks of beamtime, for those wishing to run their beamtime via the remote access route. For Experimental Hutch 2 (EH2), we have recently developed a cell which allows a high static electric field to be applied to the sample crystal. The application of electric fields to materials can result in a variety of responses that may have important technological applications, spanning electronic and ionic conductivity to piezo- and ferro-electricity.

In 2021, the original mirrors were replaced with much improved quality ones that were no longer needed on I04. These are giving much improved performance in both beam focus and positional stability. During 2021 a DECTRIS EIGER2 X CdTe 4M was installed in EH2 and this is now in regular use producing vastly superior data over the older system.

Structural insight into the photocatalytic water-splitting activity of N-TiO_2

Related publication: Foo C., Li Y., Lebedev K., Chen T., Day S.J., Tang C., Tsang, S. C. E. Characterization of oxygen defects and nitrogen impurities in TiO_2 photocatalysts using variable-temperature X-ray powder diffraction, *Nat. Commun.* **12**, 661 (2021). DOI: 10.1038/s41467-021-20977-z

Publication keywords: Water splitting; Photocatalysis; Oxygen vacancies; X-ray diffraction

TiO_2-based powder materials have been widely studied as efficient photocatalysts for water splitting due to their low cost, photo-responsivity, abundance, and chemical and thermal stability. Nitrogen-doping TiO_2 enhances the presence of structural defects and dopant impurities at elevated temperatures and results in a material with impressive visible-light absorption for photocatalytic activity. Although the electronic and optical properties of these materials have been extensively studied, the structure-activity relationship and photocatalytic mechanism remain ambiguous.

Using the High-Resolution Powder Diffraction beamline (I11), researchers at the University of Oxford have detailed the structure of nitrogen-doped TiO_2. The high collimation and angle-rejection on I11 can lead to very high real-space resolution. The ease of variable-temperature environments and the reasonable exposure time on I11 were also paramount for this investigation.

They found that an unusual anisotropic thermal expansion of the anatase phase can reveal the intimate relationship between sub-surface oxygen vacancies, nitrogen-doping level and photocatalytic activity. They also identified a new cubic titanium oxynitride phase for highly doped anatase, which provides important information on the fundamental shift in absorption wavelength, leading to excellent photocatalysis using visible light.

These results show that visible light can drive efficient photocatalytic water-splitting over nitrogen-doped TiO_2, yielding plentiful hydrogen gas at elevated temperatures. Crucially, the absorption profile is shifted to longer wavelengths relative to undoped TiO_2, which usually absorbs primarily in the UV region. Strong absorption of visible light enables more complete utilisation of the solar spectrum.

TiO_2-based powder materials have been widely studied as efficient photocatalysts for water splitting due to their low cost, photo-responsivity, earthly abundance, chemical and thermal stability, etc. In particular, the recent breakthrough of nitrogen-doped TiO_2, which enhances the presence of structural defects and dopant impurities at elevated temperatures, exhibits an impressive visible-light absorption for photocatalytic activity. Although their electronic and optical properties have been extensively studied, the structure-activity relationship and photocatalytic mechanism still remain ambiguous.

Previous research within the Tsang group at the University of Oxford has shown that nitrogen-doped TiO_2 can be an exemplary photocatalyst for water-splitting, and hence the production of hydrogen. This report details the structural characterisation, primarily by X-ray powder diffraction. Data was collected at the High-Resolution Powder Diffraction beamline (I11) at Diamond Light Source, as well as supplementary collections at BL02B2 at SPring-8, Japan. The authors report an in-depth structural study of rutile, anatase and mixed phases (commercial P25) with and without nitrogen-doping by variable-temperature synchrotron X-ray powder diffraction (SXPD). An unusual anisotropic thermal expansion of the anatase phase can reveal the intimate relationship between sub-surface oxygen vacancies, nitrogen-doping level and photocatalytic activity. For highly doped anatase, a new cubic titanium oxynitride phase is also identified which provides important information on the fundamental shift in absorption wavelength, leading to excellent photocatalysis using visible light.

Efficient photocatalysts must utilise the highly abundant visible part of the solar spectral-irradiance. In the publication, the authors have shown that visible light can drive efficient photocatalytic water-splitting over nitrogen-doped TiO_2, yielding plentiful hydrogen gas at elevated temperature. Crucially, the absorption profile is shifted to longer wavelengths relative to pristine TiO_2, which usually absorbs primarily in the UV region. Strong absorption of visible light enables more complete utilisation of the solar spectrum. In additional work, It has also been shown that the temperature requirements of the reaction can also be provided by solar energy through the concentration of light in a light furnace with no electrical heating[1].

The photoactivity of TiO_2 is well-known to be linked with the oxygen vacancy concentration at a given temperature. The formation of an oxygen vacancy as 'hole' is accompanied by the release of two electrons. Usually these are thought to reside at Ti^{4+} sites forming Ti^{3+} (electron). In N-doped TiO_2, these high energy

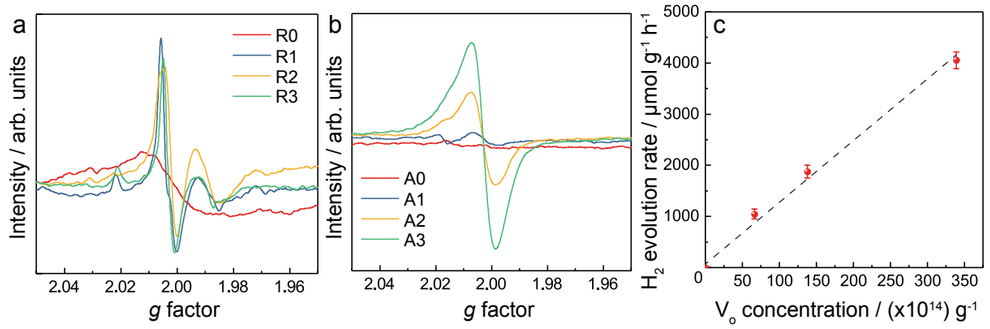

Figure 1. EPR spectra for (a) rutile and (b) anatase materials; (c) Hydrogen evolution of anatase catalysts under visible light against EPR-derived oxygen vacancy concentration. Error bars indicate the standard deviation.

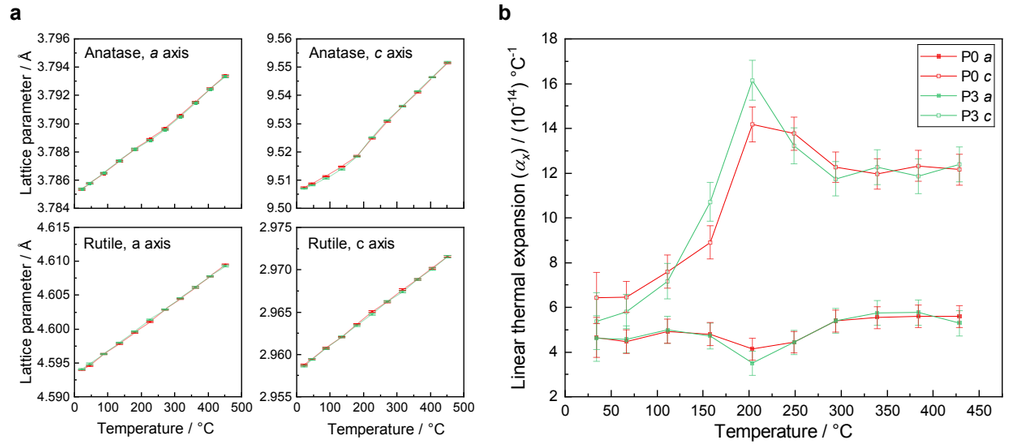

Figure 2. (a) Lattice parameters of anatase and rutile phases for P0 and P3 from room temperature to 500 °C; (b) Linear thermal expansion coefficient a for the a-axis and c-axis of the anatase phase in P0 and P3. Error bars indicate the standard deviation.

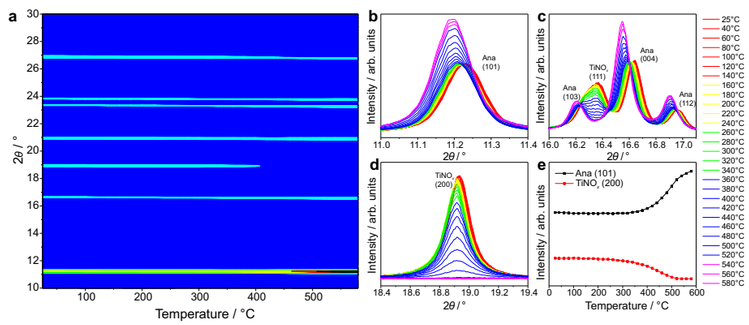

Figure 3. (a) In-situ VT-SXPD patterns; (b–d) enlarged regions showing the decomposition of $TiNO_x$ and increase in anatase intensity; (e) intensity of anatase (101) and TiN (200) plotted against temperature (negligible standard deviation not plotted).

electrons can also be localised at nitrogen impurity sites, which significantly decreases the energy of formation for oxygen vacancies. The high concentration leads to linearly increasing rate of photocatalytic hydrogen evolution, as shown by EPR in Fig. 1. However, structurally there is a lack of information about the location of the nitrogen impurity, and the coordination effects of the absence of oxygen and the presence of undercoordinated titanium.

The insight into the system lies in the unusual thermal expansion of TiO_2 and N-TiO_2. The high resolution of the I11 instrument, leads to very high real-space resolution. This, coupled with the ease of use of variable-temperature environments and fast exposure times was also paramount to the success execution of this investigation. Though known to be non-linear, this degree of correlated anisotropic thermal expansion is a novel observation. There is a significant change in the c-axis lattice expansion in anatase under elevated temperature, resulting in a unique non-linear expansion due to the Jahn-Teller effect (Fig. 2). However, as surface oxygen vacancies are formed at temperatures above 200°C, a concomitant decrease in the c-axis expansion in lattice is observed, which have been shown to be correlated to photocatalytic activity. The authors demonstrate oxygen-vacancy mobility from the disordered surface to form ordered sub-surface vacancies, as resolved by SXPD. The technique indicates that the effects of the large quantities of oxygen vacancies and Ti^{3+}, which facilitate photocatalysis in anatase, extends beyond the surface trilayer and into the bulk material, particularly in comparison to the inactive rutile polymorph which experiences no anisotropy. The inclusion of nitrogen can clearly increase the quantity of sub-surface oxygen vacancies and stabilise the anatase phase as reflected by the different degrees of observed unit-cell distortion.

By doping high levels of nitrogen into anatase, a new cubic titanium oxynitride phase is identified. This phase was markedly different to standard titanium nitride in its (1) lattice parameter, (2) thermal stability, and (3) excess electron density. Firstly, while lattice parameters for the anatase component of the powder agreed with the known values, the value refined for $TiNO_x$ is much lower than expected (exp. 4.1843 Å vs. lit. 4.235 Å). Secondly, the phase is only stable to 240°C, after which the reflections are no longer observed at 520°C (Fig. 3). This is a remarkably low thermal stability compared to non-oxygen-doped titanium nitride which only reaches full degradation at 1,000°C[2].Thirdly, the real-space Fourier difference maps for the Rietveld phase showed excess electron density at the tetrahedral hole of the framework. This phase identification provides an additional component in the effort to achieve a more complete fundamental understanding of the bandgap modification in N–TiO_2 materials and will inform wider hypotheses and perspectives on this system.

In summary, the authors present important links for the first time between structure, sub-surface oxygen vacancies, nitrogen-doping, and photocatalytic activity of anatase catalysts at various temperatures. Ultimately, the authors report the influence of well-characterised structural modifications on electronic phenomena in this photocatalytic hydrogen-evolution powder catalyst.

References:

1. Li, Y. *et al.* Photocatalytic water splitting by N-TiO2 on MgO (111) with exceptional quantum efficiencies at elevated temperatures. *Nature Communications*, **10**, 4421 (2019). DOI: 10.1038/s41467-019-12385-1
2. Hou, X.-M. *et al.* Kinetics of thermal oxidation of titanium nitride powder at different oxidizing atmospheres. *Journal of the American Ceramic Society* **94**, 570–575 (2011). DOI: 10.1111/j.1551-2916.2010.04084.x

Funding acknowledgement:
This work is supported by the EPSRC (1947428) and Diamond Light Source, both of whom are thanked for the joint DPhil Studentship undertaken by C. Foo.

Corresponding author:
Professor Shik Chi Edman Tsang, University of Oxford,
edman.tsang@chem.ox.ac.uk

High-energy X-rays reveal non-equilibrium battery chemistry

Related publication: Hua, X., Allan, P. K., Gong, C., Chater, P. A., Schmidt, E. M., Geddes, H. S., Robertson, A. W., Bruce, P. G., & Goodwin, A. L. Non-equilibrium metal oxides via reconversion chemistry in lithium-ion batteries. *Nature Communications* **12**, 561. (2021) DOI: 10.1038/s41467-020-20736-6

Publication keywords: Lithium-ion batteries; Metal oxides; Non-equilibrium phases; Pair distribution function

Concerns such as global warming and the depletion of fossil fuel reserves are driving up demand for lithium-ion batteries in the automotive industry. Developing next-generation batteries with improved performance requires new, affordable materials.

A class of transition metal oxides (M_xO_y) provides cost-effective electrode candidates. However, we have a limited fundamental understanding of how these materials change during battery cycling, a complex process involving multiple highly nanostructured (or amorphous) phases.

Researchers from the University of Oxford used X-Ray Pair Distribution Function (XPDF) beamline (I15-1) to characterise the nanoscopic phases present in these battery materials. The beamline's high flux and high energy X-rays, together with its optimised *in operando* electrochemistry setup, allowed the researchers to collect high-quality pair distribution function (PDF) data. This was crucial for investigating any nanostructured components and their phase behaviours in real time.

Their results showed that the mechanisms of these metal oxides have a metal dependence and their reactions follow a topotactic pathway, contradicting the commonly-presumed mechanism via a complete structure de- and reconstruction. This new mechanistic understanding of how these materials react rationalised the origin of their slow electrochemical performances, providing insights into effective strategies for further development.

In addition, this study also reported the experimental observation of the non-equilibrium metal monoxide polymorphs for the first time. This opens up exciting new avenues for electrochemically assisted synthesis to explore non-native metal oxides with new functionalities.

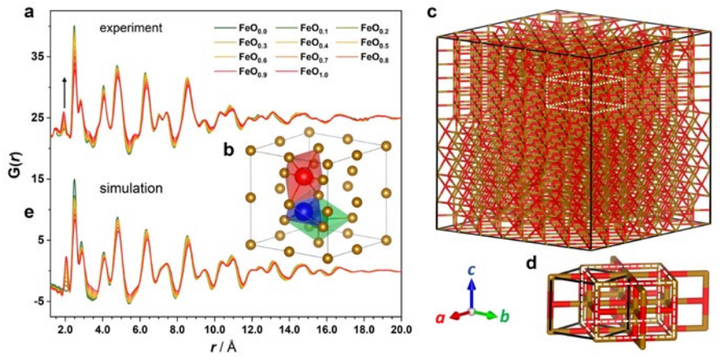

Figure 1: In operando PDF data of (a) the Fe oxides upon charge and (b) modelling analysis. The results gave rise to a (c) bcc-FeO structure with well-ordered domains resembling (d) distorted rs-FeO. (e) Simulations using the derived structure models show an excellent agreement with the experiment. Copyright 2021, Nature Publishing Group.

The conventional electrode materials for lithium-ion batteries operate via *insertion* chemistry[1], whose reversibility is restricted by the homogeneity range of materials' crystal structures upon charge and discharge, limiting capacity. In the search for the next-generation electrode materials, *conversion*-type binary metal oxides (M_xO_y) have attracted considerable interest. These materials were believed to undergo a complete structure de- and re-construction upon battery cycling and involve a full reduction of the metal centre ($2y\text{Li} + M_xO_y \leftrightarrow xM + y\text{Li}_2\text{O}$), thus resulting in a large capacity. Despite significant synthetic efforts giving rise to a library of M_xO_y systems with diverse nano-morphologies[2], a mechanistic understanding of these materials' reversible battery chemistry remains poor. Consequently, critical issues such as low power and energy efficiency persist, hindering their practical use. To conceive viable strategies for further development requires fundamental knowledge of these materials' phase behaviours underpinning their unique reactivities within a battery.

In this work, a series of Fe and Mn oxides (Fe_xO_y and Mn_xO_y) were selected as model compounds because they are the most attractive candidates of M_xO_y due to their low cost and facile syntheses. The metal oxides' battery chemistry is heterogeneous and nanoscopic in nature making it challenging to study via traditional crystallographic methods, so instead the pair distribution function (PDF) technique was employed in-operando on the I15-1 beamline. I15-1 allowed the local structure of these materials to be studied and tracked in real time during battery cycling.

Based on the acquired PDFs of the reversible cycles, the patterns between the Fe_xO_y and Mn_xO_y series are notably different, indicating their metal dependent phase behaviours. However, the peak evolution within the same Fe or Mn series shows a single common trend among different species, implying that the reversible reaction mechanism of the same M_xO_y family is independent of the composition and the initial crystal structure of the oxide species.

For the Fe oxides (represented by *a*-Fe_2O_3), the PDFs (Fig. 1a) surprisingly show subtle peak shifts with slight peak broadening and intensity reduction upon charge, suggesting that the α-Fe lattice with a body-centred cubic (*bcc*) ordering is retained without transformation to the rocksalt *(rs)* FeO as commonly believed. Remarkably, while most of the PDF peak intensities progressively decrease upon charge, a peak at 1.9 Å that corresponds to the Fe-O atom pair continues to grow (Fig. 1a), implying oxygen insertion into the α-Fe lattices to form *bcc*-FeO phases. To determine their crystal structures, a series of *bcc*-FeO_x models ($0 \leq x \leq 1$) were constructed. These models include octahedrally-coordinated oxygen concerning its lower energy than the

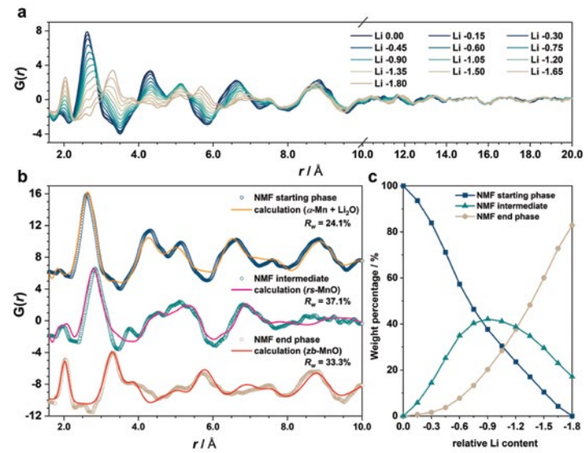

Figure 2: In operando PDF patterns for (a) the Mn oxides during the first charge. The NMF analysis gave rise to (b) three distinct components and (c) the evolution of the associated phase ratios. Copyright 2021, Nature Publishing Group.

tetrahedral counterpart (Fig. 1b). For the selected *x* values, local structure relaxation was introduced by using a Metropolis Monte Carlo algorithm to incorporate O-O interactions. The results showed that upon increase of the oxygen concentration, the *bcc*-FeO_x system experiences a disorder-to-order transition regarding the O distribution and eventually transforms to a structure with locally ordered domains (Fig. 1c) that mirror the tetragonally-distorted *rs*-FeO, hinting at an underlying link between the *bcc*- and *rs*-FeO (Fig. 1d). Using these derived structures, their PDF patterns were calculated (Fig. 1e) and showed an excellent agreement with the experimental data, confirming the reliability of this modelling analysis.

In contrast to the Fe series, the PDFs of the Mn oxides (represented by Mn_3O_4, Fig. 2a) show a drastic change in peak profiles reflecting a significant Mn atomic rearrangement during the reversible reactions. The short structure coherence lengths (< 20 Å) of the PDF patterns persist, indicating that the average grain sizes of Mn-containing species remain small (or near amorphous) upon cycling. Given the practical challenges to study highly nanoscopic structures, as well as the analytic uncertainties concerning the intermediate, a recently-developed method[3] based on Metropolis non-negative matrix factorisation (NMF)[4] was employed, allowing for robust deconvolution of complex mixtures without *a priori* knowledge of the number and nature of the constituent components. The analysis incorporated three members representing the starting, intermediate and end phases, and gave rise to distinct PDF patterns that could be respectively modelled by using α-Mn, distorted *rs*-MnO, and zincblende (*zb*) MnO structures (Fig. 2b). Their corresponding phase ratios (Fig. 2c) also supported the presence of an intermediate.

Although a one-step *conversion* reaction from M to *rs*-MO has been widely accepted as the charge reaction pathway, our study showed that both Fe and Mn oxides exhibit a two-step mechanism forming *bcc*-FeO and *zb*-MnO phases. Based on the structure coherence among the constituent phases, the charge reaction in Mn_xO_y manifests as insertion of Mn^{2+} into the face centred cubic (*fcc*) O sublattice, whereas a different pathway based on O^{2-} insertion into the *bcc*-Fe sublattice was observed in the Fe system (Fig. 3). These topotactic reactions highlight a *displacement*-like mechanism, which is subjected to a path hysteresis due to the mobility differences amongst displaced species. This new insight rationalised the distorted voltage polarisations observed within the reversible cycles of M_xO_y, and on the one hand, pointed to future strategies to improve their kinetic performances by employing displaced species with fast mobilities.

It is important to note that this study also reported the first experimental observation of the non-equilibrium *bcc*-FeO and *zb*-MnO polymorphs. Their formation under well-defined electrochemical conditions is likely stabilised by substantial surface energies of very finite particle sizes, suggesting electrochemical devices may offer an alternative synthesis strategy to explore non-native metal monoxides with new functionalities.

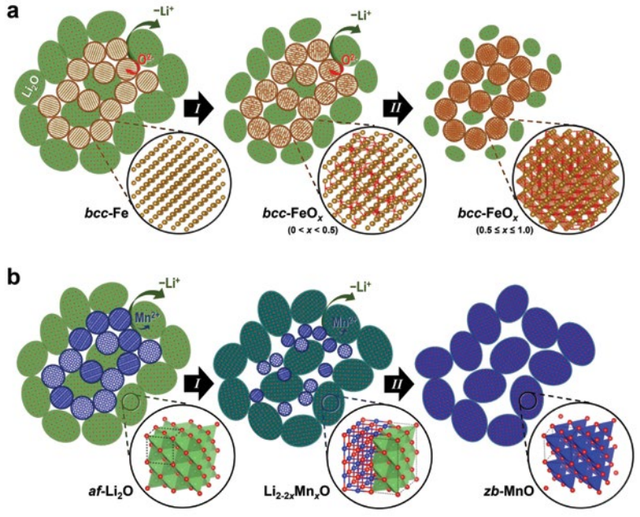

Figure 3: Illustrated charge reaction pathways of (a) Fe_xO_y and (b) Mn_xO_y. Copyright 2021, Nature Publishing Group.

References:

1. Cabana, J. *et al*. Beyond intercalation-based Li-Ion batteries: the state of the art and challenges of electrode materials reacting through conversion reactions. *Advanced Materials* **22**, E170–E192 (2010). DOI: 10.1002/adma.201000717
2. Ren, Y. *et al*. Ordered mesoporous metal oxides: synthesis and applications. *Chemical Society Reviews* **41**, 4909 (2012). DOI:10.1039/c2cs35086f
3. Geddes, H. *et al.* Structural characterisation of amorphous solid dispersions *via* metropolis matrix factorisation of pair distribution function data. *Chemical Communications* **55**, 13346–13349 (2019). DOI: 10.1039/C9CC06753A
4. Lee, D. D. *et al*. Learning the parts of objects by non-negative matrix factorization. *Nature* **401**, 788–791 (1999). DOI: 10.1038/44565

Funding acknowledgement:

This project was supported by the European Commission via M.S.C.A. (Grant 798169), the E.R.C. (Grant 788144), the Henry Royce Institute (Grant ref EP/R010145/1) and a Birmingham Fellowship.

Corresponding author:

Dr Xiao Hua, Lancaster University, x.hua1@lancaster.ac.uk

Weaving a molecular knot

Related publication: Leigh, D. A., Danon, J. J., Fielden, S. D. P., Lemonnier, J.-F., Whitehead, G. F. S., & Woltering, S. L. A molecular endless (7_4) knot. *Nature Chemistry*, **13** 117–122 (2021). DOI: 10.1038/s41557-020-00594-x

Publication keywords: Supramolecular chemistry; Interwoven grids; Molecular knots

Knots have been used for thousands of years to create tools and materials. The ability to knot molecular-sized threads, approximately 100,000 times thinner than a human hair, should allow us to make incredibly strong novel materials. However, methods of knotting such small threads are lacking, so researchers have developed a new technique for weaving at the molecular scale.

They investigated different molecular strand designs to ensure they were the correct shape to be woven together into a grid. They had to find a suitable template, a metal compound that could control the weaving process by guiding the strands into a grid structure.

The woven grid is far too small to be seen by the naked eye, so they had to use X-ray diffraction on the Small Molecule Single Crystal Diffraction beamline (I19) to probe the relative positions of molecular strands.

Their experiment revealed that the molecular strands had indeed woven together to give a grid structure. It allowed them to determine the distances and angles between the strands and templates and show how the weaving process was controlled. They also showed that the strands were of the correct length so their ends could be connected to give a molecular knot.

Molecular knots have unique molecular structures that have been shown to catalyse chemical reactions, act as sequestering agents and kill cancer cells. Interwoven molecular grids can be connected to each other to give extended 2D materials with high stiffness that can act as molecular-sized nets.

Knots play an important role at the nanoscale. Knots are found in DNA and proteins, where they profoundly impact the stability and biological activity of these macromolecules. Synthetic polymer chains also spontaneously tie into knots; the resulting entanglements determine macroscopic material properties such as stiffness and viscosity. The ways that a strand can be tied into a knot are practically limitless; there are billions of tabulated knot types. However, it remains extremely difficult to tie a molecular strand precisely into a specific type of knot[1]. This means systematic studies into the implications and applications of tying a molecule into a knot are currently scarce.

For this study, inspiration was taken from the macroscopic weaving of threads to develop a new strategy to access molecular knots. This approach involves the self-assembly of organic polytopic ligands and metal salts into an interwoven grid[2]. If the ends of the ligands are connected to each other, a molecular knot is obtained. Specifically, a 3×3 interwoven grid was targeted in order to obtain a molecular 'endless knot' (7_4 by Alexander Briggs notation)[3]. Such a structure would result from the self-assembly of six ligands around an array of nine co-planar metal ions. The crossing points (entanglements) of the knot are generated using the thiazolo[5,4–d]thiazole unit to ensure the ligand adopts a zig-zag conformation when coordinating to metals in the grid architecture.

After several design iterations, a suitable ligand containing three binding pockets with the correct spacing, geometry and electron donating ability was found. Combining this ligand with $Fe(II)(BF_4)_2$ or $Zn(II)(BF_4)_2$ in organic solvent leads to the near-quantitative formation of a molecular 3×3 interwoven grid (Fig. 1). Whilst these assemblies could be studied using $^1H/^{13}C$ nuclear magnetic resonance and electrospray ionisation mass spectrometry, the most compelling proof of the interwoven nature of the grid was provided by single crystal X-ray diffraction. The data for this experiment were obtained at the I19 beamline at Diamond Light Source. The X-ray structure (Fig. 2) shows the desired interwoven arrangement of ligands around an array of metal ions was indeed present.

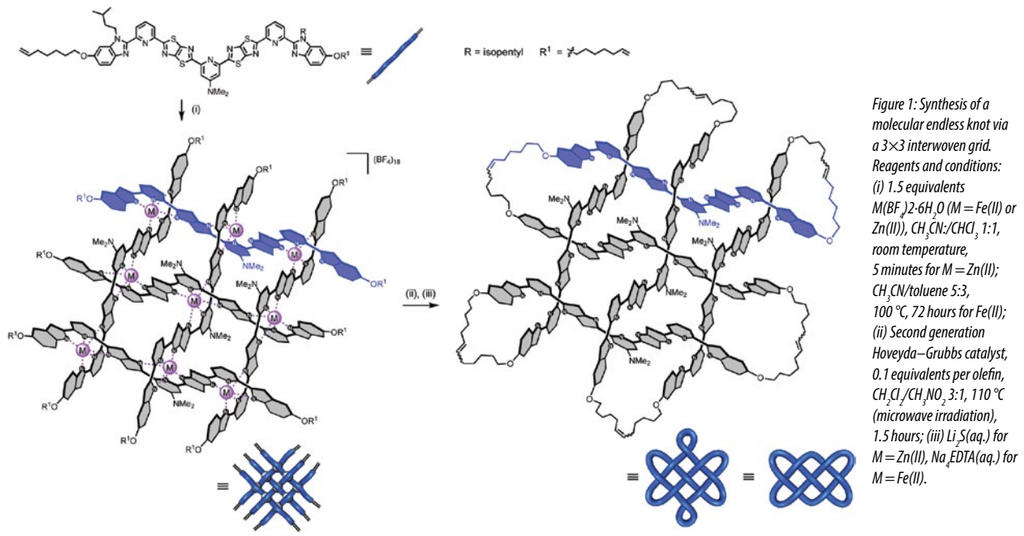

Figure 1: Synthesis of a molecular endless knot via a 3×3 interwoven grid. Reagents and conditions: (i) 1.5 equivalents $M(BF_4)2\text{-}6H_2O$ (M = Fe(II) or Zn(II)), CH_3CN:/$CHCl_3$ 1:1, room temperature, 5 minutes for M = Zn(II); CH_3CN/toluene 5:3, 100 °C, 72 hours for Fe(II); (ii) Second generation Hoveyda–Grubbs catalyst, 0.1 equivalents per olefin, CH_2Cl_2/CH_3NO_2 3:1, 110 °C (microwave irradiation), 1.5 hours; (iii) Li_2S(aq.) for M = Zn(II), Na_4EDTA(aq.) for M = Fe(II).

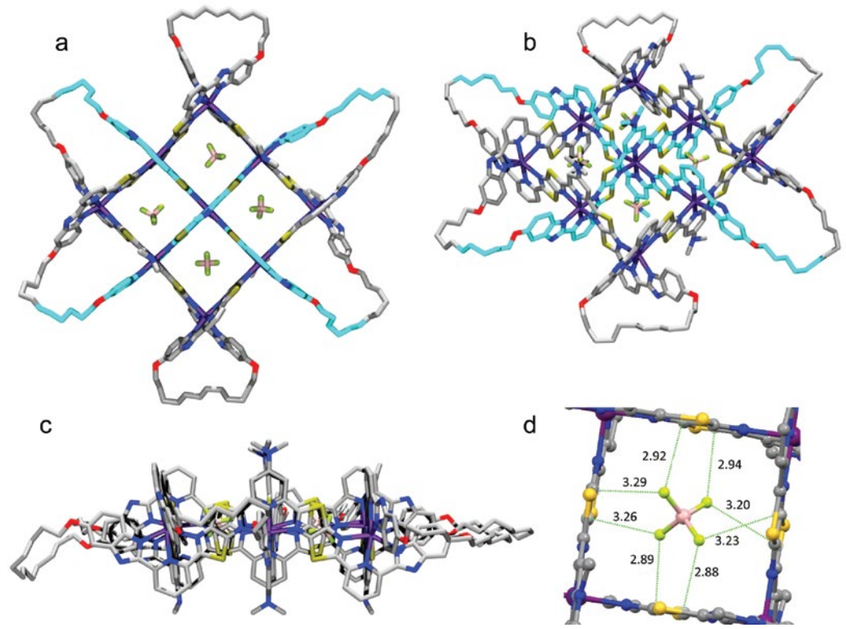

Figure 2: X-ray crystal structure of 3×3 interwoven grid containing Fe(II), in which the disordered olefin-terminated chains are replaced by cyclised end groups modelled by a Merck molecular force field; a) Viewed orthogonally to the plane of the nine Fe(II) ions. b) Angled view showing the planarity of the weft and warp strands and the directionality of the anion–π and anion–Fe(II)interactions of the BF_4^- templates; c) Viewed along the plane of the Fe(II) ions. d) One of the square cavities formed between the criss-crossed strands. Distances in Å.

Unexpectedly, it was found in preliminary studies that the counter anions of the templating metal cations also played a role in the self-assembly process. The use of tetrafluoroborate salts was necessary to produce a 3×3 grid; other salts gave simpler complexes such as squares and dimers. The unanticipated role played by tetrafluoroborate ions was revealed in the X-ray structure. A BF_4^- ion is found bound within each of the four-square cavities formed between ligands placed at right angles. The B–F bonds of these anions point towards the templating metal ions situated at the corners of the square, whilst the fluorine atoms are in close contact with the centres of the thiazole rings. This suggests the driving force for grid self-assembly is partially derived from a combination of charge-dipole and anion-π interactions.

Adjacent ligands of the grid were connected using olefin metathesis. After the metal ions were removed a wholly organic endless knot, containing seven crossings in a loop 258 atoms long, was isolated. It was found that the sequence of ligand closures dictated the product outcome – if olefins were not connected in a perfect alternating pattern other cyclic species are formed: either a Solomon link (doubly interlocked rings) or unknot (non-entangled macrocycle). The endless knot could be remetallated with $Zn(II)BF_4$ to again form the planar grid complex.

The endless knot has significant symbolic relevance in several ancient and modern civilisations: it is the smallest Chinese knot, one of the eight auspicious symbols of Buddhism and Hinduism and is often found in Celtic knotwork. From a chemist's perspective, the ability to precisely synthesise hitherto inaccessible knots opens the door for studies that give deeper understanding to the role of knotting at the molecular scale. Whilst it has been known for at least 50 years that molecular entanglement has profound impact on material properties, explanations to the molecular origins for such effects remain elusive. Routine access to a variety of molecular topologies will provide the missing link to allow the specific molecular entanglement sequences to be exploited. In addition, tessellation of molecular grids provides a new strategy to access 2D interwoven materials[4].

References:

1. Fielden, S. D. P. *et al*. Molecular knots. *Angewandte Chemie International Edition* **56**, 11166–11194 (2017). DOI: 10.1002/anie.201702531
2. Hubin, T. J. *et al.* Template routes to interlocked molecular structures and orderly molecular entanglements. *Coordination Chemistry Reviews* **200–202**, 5–52 (2000). DOI: 10.1016/S0010-8545(99)00242-8
3. Alexander, J. W. *et al*. On types of knotted curves. *Annals of Mathematics* **28**, 562-586 (1926). DOI: 10.2307/1968399
4. August, D. P. *et al*. Self-assembly of a layered two-dimensional molecularly woven fabric. *Nature* **588**, 429–435 (2020). DOI: 10.1038/s41586-020-3019-9

Funding acknowledgement:
We thank the Engineering and Physical Sciences Research Council (EPSRC; EP/P027067/1), the European Research Council (ERC; Advanced Grant no. 786630), and East China Normal University for funding; the EPSRC National Mass Spectrometry Service Centre for high-resolution mass spectrometry; the Diamond Light Source for synchrotron beam time on Beamline I19 (XR029); networking contributions from the COST Action CA17139. David Leigh is a Royal Society Research Professor.

Corresponding author:
Dr Stephen Fielden, University of Birmingham, s.fielden@bham.ac.uk

Using pressure and X-ray diffraction to reduce uncertainty in the modelling of Ti-6Al-4V

Related publication: MacLeod, S. G., Errandonea, D., Cox, G. A., Cynn, H., Daisenberger, D., Finnegan, S. E., McMahon, M. I., Munro, K. A., Popescu, C., & Storm, C. v. The phase diagram of Ti-6Al-4V at high-pressures and high-temperatures. *Journal of Physics: Condensed Matter*, **33** 154001 (2021). DOI: 10.1088/1361-648X/abdffa

Publication keywords: Ti-6Al-4V; X-ray diffraction; High-pressure; High-temperature; Phase transition; Equation-of-state

Ti-6Al-4V is a titanium alloy used in a wide range of commercial and industrial applications. Its superior strength-to-weight ratio, resistance to corrosion and ease of machinability are desirable material properties. Ti-6Al-4V is particularly attractive to the aerospace, automotive and defence sectors. Design engineers in these industries require accurate experimental data to improve their materials models to meet the constant demand to improve performance.

Researchers wanted to study the crystal structure of Ti-6Al-4V at high pressures and temperatures, to generate a pressure-temperature phase diagram for Ti-6Al-4V.

They used the Extreme Conditions beamline (I15). This beamline is dedicated to high-pressure research and provides all the technical expertise and ancillary equipment needed for a successful outcome. The X-ray micro-focus of 20 microns is essential for studying materials properties up to Mbar pressures in diamond anvil cells (DACs). The research team used the experience gained performing DAC experiments at I15 over many years to help develop their resistive heating capability, working closely with the beamline staff.

As a result, the team was able to study Ti-6Al-4V up to 93 GPa and ~850 K using DACs, X-ray diffraction and resistive heating. From the diffraction patterns collected and analysed, they produced an experimental pressure-temperature phase diagram for Ti-6Al-4V and used the data to constrain their theoretical model for Ti-6Al-4V.

The a-phase of titanium is hexagonal-close-packed at ambient conditions (see Fig. 1). Ti-6Al-4V (90% by weight titanium, 6% by weight aluminium, and 4% by weight vanadium) is an alloy created to stabilise the α-phase character of titanium. Ti-6Al-4V crystallises predominantly in the α phase, with a small amount of β-phase, or body-centred-cubic structure, around the a grain boundaries. Alloying aluminium and vanadium with titanium, in the presence of impurities oxygen, carbon and iron, produces a metal possessing a greater hardness, yield strength and tensile strength than pure titanium. Since the mechanical properties are strongly influenced by the underlying crystal structures, defects, impurities, and grain boundaries, design engineers require models that accurately represent all of these properties. However, without quality experimental data to constrain and validate these models, design uncertainties will not improve. Surprisingly, the crystal structures of Ti-6Al-4V have rarely been studied at the extreme pressures and temperatures commercial and industrial designs may be exposed to during operation, for example aerospace vehicles during the various stages of flight. This paucity of data impedes the development of a truly predictive Ti-6Al-4V model. The structural pathway for pure titanium and Ti-6Al-4V is shown in Fig. 1. At room temperature, and under compression, α-titanium transitions to a hexagonal but more brittle ω-phase structure at 3-11 GPa[1]. The α-β-ω triple point, where all 3 phases can coexist at equilibrium conditions, is estimated to occur at 7.5 GPa and 913 K[2]. Since Ti-6Al-4V is strengthened in the more desirable α-phase, the aim of this work was to investigate how much the structural pathway of Ti-6Al-4V diverged away from titanium.

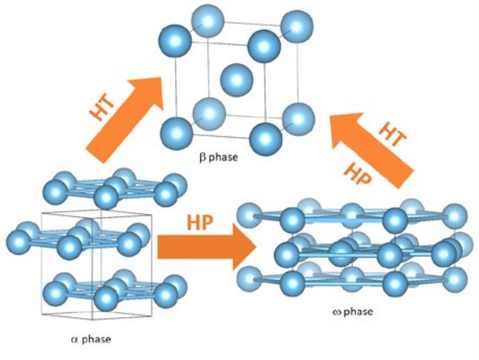

Figure 1: The transformation pathway for titanium and Ti-6Al-4V at high-pressure and high-temperature.

The diamond anvil cell (DAC) is a device for studying materials at static high pressures. It comprises two back-to-back diamonds with a metal gasket between them to form a pressure chamber. Driving the diamonds together reduces the chamber volume and increases the pressure on the material in the chamber. DACs are frequently used to study the equations-of-state (EoS) of materials. The EoS of a material can be described as the variation of its pressure as a function of atomic volume and temperature and is best studied at a dedicated high-pressure synchrotron beamline.

Ti-6Al-4V samples were loaded into several DACs, alongside materials known as pressure gauges, whose thermal EoSs have been previously characterised[3]. Resistive heaters wrapped around the DACs ensured samples could be heated to ~900 K. K-type thermocouples monitored the temperature. Under compression, isotherms were collected at 298 K, 418(2) K, 517(2) K, 586(2) K, 642(3) K, 713(1) K, 844(5) K, and 886(2) K to study the $\alpha + \omega$ transition. The highest pressure reached was 93 GPa at ~850 K. The waterfall plot of integrated angle-dispersive X-ray diffraction patterns in Fig. 2 shows typical results for the isotherm collected at 642(3) K. The $\alpha \rightarrow \omega$ phase transition occurs at ~29 GPa, with both phases coexisting until the transition to the w phase is completed at ~40 GPa. Thermal EoSs were generated for the α and ω phases of Ti-6Al-4V. The bulk moduli (or compressibility) were found to be 110(2) GPa for α and 115(8) GPa for ω, in good agreement with titanium, which is 114(3) GPa for α and 107(3) GPa for ω[4]. In parallel with the DAC study, a large volume press (LVP) experiment, which measured a change in electrical resistivity rather than X-ray diffraction to signify a phase change, determined the $(\alpha+\beta) \rightarrow \beta$ transition at high temperatures. Resistivity changes were

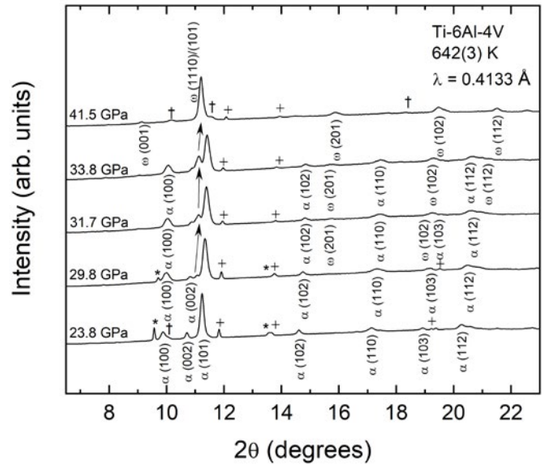

*Figure 2: A waterfall plot of integrated ADXRD patterns showing the $\alpha \rightarrow \omega$ transition in Ti-6Al-4V at 642 K. The a and w phase peaks are all indexed according to their X-ray scattering planes. The arrow at 29.8 GPa points to the emergent dominant w phase (101)/(110) peaks. * represents reflections from NaCl, + from Cu, and † from the gasket material.*

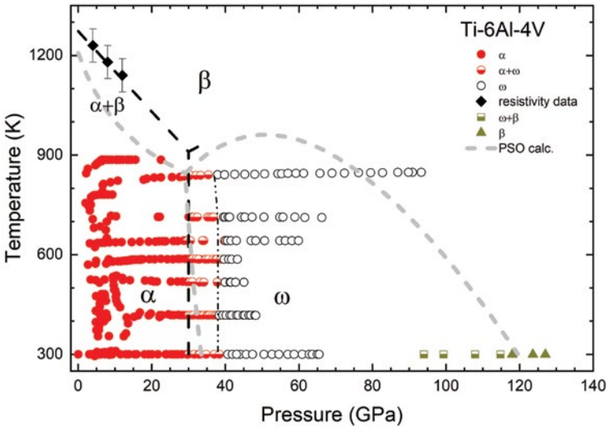

Figure 3: Phase diagram of Ti-6Al-4V, constructed from DAC isotherms and the LVP data, and showing the range of the desirable a phase. Red circles represent: a; half-red half-white circles, mixed phase ($\alpha+\omega$); white circles ω; black diamonds, phase changes using Bridgman cell. Data from previous work: half-dark yellow half-white squares mixed phase ($\omega+\beta$) [5]; dark yellow triangles β [5]. Black dashed lines are a visual guide for proposed $\alpha-\omega$ and $(\alpha+\beta)-\beta$ phase boundaries. Black dashed-dot line indicates complete transition to ω from $(\alpha+\omega)$. Grey dashed lines represent solid-solid phase boundaries calculated using particle swarm optimisation.

detected at 1,230(30), 1,180(30), and 1,140(30) K, and at pressures 4.0(2), 8.0(2) and 12.0(2) GPa respectively.

Data from the DAC and LVP experiments were combined to produce the pressure-temperature phase diagram shown in Fig. 3. Extrapolating the LVP and DAC data suggests the α-β-ω triple point occurs at ~30 GPa and ~910 K. An almost vertical α-ω phase boundary, with slope ~550 K GPa^{-1}, coupled with an $(\alpha+\omega)$ phase coexistence of 8-10 GPa up to 844 K is indicative of a weak temperature dependence on the kinetic barrier to the transition to the ω-phase. This data was then used, along with previous experimental data collected at room temperature[5], to constrain a calculation using the particle swarm optimisation (PSO) method, represented by the grey dashed lines in Fig. 3.

Although this work represents the first time the alloy Ti-6Al-4V has been studied at high-pressure and high-temperature using synchrotron X-rays, there is still much work to do in gaining a better understanding of the phase diagram, for example, confirmation of the α-β-ω triple point, measuring the ω-β phase boundary and the melt curve. Extending our experimental reach should lead to improvements in our modelling capability and have real-world impact. Future DAC experiments planned at I15 will incorporate a new resistive heater capable of reaching 2,000+ K. In addition, the existing laser heating apparatus will be used to study melting.

References:

1. Errandonea, D. *et al.* Pressure-induced transition in titanium metal: a systematic study of the effects of uniaxial stress. *Physica B: Condensed Matter*, **355** 116–125 (2005). DOI: 10.1016/j.physb.2004.10.030
2. Zhang, J. *et al*. Experimental constraints on the phase diagram of titanium metal. *Journal of Physics and Chemistry of Solids*, **69** 2559–2563 (2008). DOI: 10.1016/j.jpcs.2008.05.016
3. Dorogokupets, P. I. *et al*. Equations of state of MgO, Au, Pt, NaCl-B1, and NaCl-B2: Internally consistent high-temperature pressure scales. *High Pressure Research*, **27** 431–446 (2007). DOI : 10.1080/08957950701659700
4. Zhang, J. *et al*. Thermal equations of state for titanium obtained by high pressure—temperature diffraction studies. *Physical Review B*, **78** 054119 (2008). DOI: 10.1103/PhysRevB.78.054119
5. MacLeod, S. G. *et al*. Experimental and theoretical study of Ti-6Al-4V to 220 GPa. *Physical Review B*, **85** 224202 (2012). DOI: 10.1103/PhysRevB.85.224202

Funding acknowledgement:
We thank Diamond Light Source for access to beamline I15 (EE8176 and EE9366).

Corresponding author:
Dr Simon MacLeod, AWE Plc, simon.macleod@awe.co.uk

Spectroscopy Group

Sofia Díaz-Moreno, Science Group Leader

The Diamond Spectroscopy Group consists of four beamlines; the Microfocus Spectroscopy beamline (I18), the Core EXAFS beamline (B18), and the two independently operating branches of the Versatile X-ray Absorption Spectroscopy beamline, I20-Scanning and I20-EDE. These spectrometers are highly complementary, most notably in the energy ranges they cover, the size of their focussed beam spots, and the time resolutions they are able to reach. This complementarity means that they can support research across many different scientific disciplines, from chemistry and catalysis through materials science, condensed matter physics, environmental and life science, and cultural heritage.

Two new flagship beamlines will be added to the portfolio of instruments of the Spectroscopy Group as part of the Diamond-II programme. SWIFT (Spectroscopy WithIn Fast Timescales) is a high flux beamline optimised for the study of samples under *operando* conditions, and with the added potential to investigate sample heterogeneities at the 20 µm length scale. The design of the beamline is progressing very well. The conceptual design review took place successfully in December 2021, and we are now preparing the technical design review. BERRIES (Bright Environment for X-ray Raman, Resonance Inelastic and Emission Spectroscopies), that will be built as part of phase-II of the upgrade programme, will be offering two new techniques to the Diamond user community: pink-beam X-ray Emission Spectroscopy (pink-XES) and X-ray Raman Scattering (XRS).

Last year has seen the return to normal operations for the spectroscopy beamlines, with most of the experiments performed with users on-site, although with limited numbers. This has been challenging at times, especially for those experiments that require permanent on-site supervision. Maintaining the momentum acquired during operations in 2020, efforts have continued towards enhancing the level of automation on the beamlines.

Aside of supporting the user programme, many technical developments and improvements have also been realised on the beamlines over the last year. New detectors procured for B18 and I20-EDE have enhanced the capabilities of the beamlines to collect complementary XRD data. The photon-in/photon-out capabilities of the group will significantly expand with the on-going development of the emission spectrometers for I20-Scanning and I18. This year has also seen the integration of the IR-DRIFTS instrument into B18 and I20-EDE, to complement the time-resolved X-ray Absorption Spectroscopy (XAS) measurements performed on these instruments.

I18 update

The Microfocus Spectroscopy Beamline, I18, uses a focussed beam, variable between 2 µm to 50 µm in size, to study heterogeneous samples with a variety of experimental techniques such as X-ray Fluorescence (XRF) and X-ray Diffraction (XRD) imaging, micro X-ray Absorption Spectroscopy (microXAS), and XRF and XRD micro-tomography (microCT).

A new in-house designed double-crystal monochromator (DCM) was installed and commissioned last year. The monochromator has not only improved significantly the positional stability of the micron-size beam at the sample position, but the additional Si(311) crystal set will enable the collection of spectroscopy data with enhanced energy resolution. We are currently working towards implementing continuous scanning with the new monochromator, enabling fast XAS measurements that will reduce damage in sensitive samples caused by the X-ray beam. The monochromator has been designed so it will be compatible with operations after the Diamond-II upgrade, including the extension of the operational energy range of the beamline to 27 keV, that will be achieved by using the additional crystal set.

Another major beamline upgrade has been the installation of the new motorised sample motion stages, allowing faster and reliable operations. The high speeds that the new sample stages can operate at (up to 5 mm/sec) together with the increased translation ranges enable scanning large sample areas very quickly. The throughput of the beamline is significantly increased when combined with the XRF and XRD detector data collection rates of up to 1kHz and up to 200 Hz, respectively. This is especially relevant for time-consuming measurements such as tomography and XANES mapping.

In the upcoming year, the capabilities of the beamline will be enhanced by the addition of a new X-ray emission spectrometer based on a 0.5m diameter Rowland circle, that operates in the Johann configuration in the vertical plane. This instrument will expand the photon-in/photon-out capabilities of the group towards the tender energy regime, and the small focal spot of the beamline will enable spatially resolved measurements

B18 update

The Core EXAFS beamline, B18, is optimised for the efficient collection of XAS data over all elements heavier than phosphorous. The focussing optics and the capability of the monochromator for continuous scanning, together with a flexible experimental space that supports a large range of sample environment equipment, make this beamline ideal for experiments that are performed under *in situ* and *operando* conditions

During the last year, efforts at B18 have been focussed on enhancing automation of the beamline. A 6-axis compact industrial robot is now fully integrated into the beamline data acquisition system. The robot is able to handle more than 300 samples and has a small footprint, so it does not interfere with the diverse sample environments available on the beamline. Another important step towards automation has been the motorisation of the fluorescence detector, that will enable measuring samples in fluorescence detection mode with different concentrations without the need of manual intervention. In parallel,

Joshua Elliott - Post doctoral research associate (Spectroscopy Computational Scientist).

Diego Gianolio - Principal Beamline Scientist at B18.

work has been done to support the increased rate of data collection, improving data analysis automation. A system of automatic experimental logs, including scan parameters, averaging of multiple repetitions, and data processing using larch and jupyter notebooks is being implemented and will soon be accessible on a dedicated webpage.

The monochromator crystal cage based on direct water cooling has been successfully replaced last December. The new cage, where the crystals are indirectly cooled, will enhance the reliability of the device, avoiding the need for regular interventions to change the failing water seals. The new crystal cage has been operating since January, showing solid performance in terms of thermal stability and energy resolution.

A new Pilatus 300KW detector has been procured for acquisition of X-ray diffraction/scattering data. The new detector will replace the Mythen microstrip, offering an improved signal to noise ratio and wider sensor area. The capability of faster readout, with further integration, will also enable collection of XRD images while continuously scanning the monochromator in the future, introducing the possibility to perform DAFS experiments.

I20-Scanning update

The Scanning branch of I20, I20-Scanning, exploits the high flux provided by the wiggler source through two different end-stations. The XAS end-station is optimised to examine the structure of very low concentration samples. The X-ray Emission Spectroscopy (XES) end-station is dedicated to the performance of high-energy resolution studies of the electronic structure of samples. The year has been a busy one with the beamline fully scheduled, mainly with users doing their experiments in person but with only limited numbers allowed per experiment. We also conducted several remote experiments, particularly for users from overseas who found it difficult to travel to the UK.

The project to replace the current 3 analyser crystal emission spectrometer with a 14-crystal instrument has moved from the design phase to the build phase late in 2021. The 14 multi-axis stages that will move the analyser crystals have been built and work is continuing on the rest of the assembly before a programme of motion and software testing begins in late spring 2022. This new instrument will enable faster data collection times and substantially reduce the concentration of samples that can be studied. The instrument is due to be installed in the experimental hutch at the end of 2022.

In order to reach higher energies on I20-Scanning, an innovative new first crystal has been designed for the four-bounce monochromator. The design aims to minimise any distortion in the crystal surface when the high-power X-ray beam produced by the wiggler source hits the surface. This crystal has now been procured and will be thermally tested in spring 2022 to determine if the expected performance matches the calculations.

I20-EDE update

The Energy Dispersive EXAFS (EDE) branch of I20 uses a polychromator to perform XAS experiments in a dispersive geometry. It is designed for *in situ* and *operando* studies with time resolutions ranging from seconds down to milliseconds or even microseconds.

Due to the nature of the research programme, remote experiments are not possible on I20-EDE but, with the return of users on-site, the regular experimental programme has been restarted.

During the last year, a Mar345 imaging plate detector has been repurposed from the crystallography group and integrated into the beamline, allowing the collection of complementary XRD data. This is particularly useful for the high-pressure users of the beamline, but will also be useful for the materials scientists looking at material developments such as metal-organic framework synthesis.

Community support and development

Aside of supporting the beamlines and the operational science programmes, the Spectroscopy Group has continued its effort to support the development of the spectroscopy user community.

The annual three-day X-ray Absorption Spectroscopy workshop was run remotely for the first time in June 2021, due to the restrictions imposed by the COVID pandemic. As was the case in previous years, the workshop was in high demand, with more than 180 applications, although required staff to student ratios limited the successful applications to 36 participants. Although the hands-on sessions were not as productive as when the workshop takes place in person, the feedback received was very positive.

Diamond, through the Spectroscopy Group, together with the University of Newcastle, are the principal partners of the COllaborative NEtwork for X-ray Spectroscopy (CONEXS), an Engineering and Physical Sciences Research Council (EPSRC) funded network that aims to bring together experimentalists and theoreticians who are working in the area of X-ray spectroscopy. The network aims to improve members’ abilities to fully exploit and interpret experimental data. As part of the activities of the network, the third Summer School was organised in the last week of March 2022, immediately before the third international conference. Both events were run at Newcastle University, and they were very well attended. The network also runs monthly webinars where international speakers give an overview of the fundamentals of X-ray spectroscopy from the experimental and theoretical points of view. The webinars have proven to be very popular, with more than 1,000 visits to our YouTube channel.

To increase the group’s capabilities on advanced data analysis, Joshua Elliott, an expert in ab-initio modelling, has joined the Spectroscopy Group this year. This will help us better support the spectroscopy users with the interpretation of their data.

Biomass-derived low cost and scalable catalysts for oxygen reduction

Related publication: Feng, J., Cai, R., Magliocca, E., Luo, H., Higgins, L., Romario, G. L. F., Liang, X., Pedersen, A., Xu, Z., Guo, Z., Periasamy, A., Brett, D., Miller, T. S., Haigh, S. J., Mishra, B., & Titirici, M. Iron, Nitrogen Co-doped carbon spheres as low cost, scalable electrocatalysts for the oxygen reduction reaction. *Advanced Functional Materials* **31,** 2102974 (2021). DOI: 10.1002/adfm.202102974

Publication keywords: Oxygen reduction reaction, Non-PGM catalysts, Anion exchange membrane fuel cell

Hydrogen and fuel cells play a vital role toward reaching 2050 net-zero carbon emissions targets. However, the oxygen reduction reaction (ORR) occurring at the fuel cell cathode is slow, reducing energy conversion efficiencies, and the platinum-based catalysts currently in use are expensive.

Significant progress has been made in the development of non-precious metal catalysts for ORR electrocatalysis. Catalysts based on iron atoms coordinated to nitrogen and supported on carbon offer promising performance in the ORR.

A team of scientists used Diamond Light Source's Core EXAFS beamline (B18) to investigate the local coordination of iron within the free-standing carbon electrodes and confirm nitrogen-iron catalytic active sites. The bending magnet source at B18 allows for high sample throughput and a wide range of detection capabilities, ideal for the Extended X-ray Absorption Fine Structure (EXAFS) studies required in this investigation. Furthermore, the remote operation capabilities of B18 and the generous support of the beamline staff allowed this experiment to be performed remotely during the COVID-19 pandemic.

The quality of the data from B18 allowed for the successful determination of the Fe-N_4 active site on the electrode. It also highlighted the presence of iron carbide nanoparticles, which were later confirmed using X-ray Photoelectron Spectroscopy (XPS) and High-Angle Annular Dark-Field Scanning Transmission Electron Microscopy (HAADF-STEM). The study revealed the local coordination environment and the oxidation state around the iron centres. It also showed that the oxidation state of the iron precursor influences the oxidation state of the Fe-N site in the obtained catalysts, which in turn influences the catalytic activity. This work provides a new perspective on understanding the catalytic active sites.

Great progress has been made to date in designing non-precious metal-based catalysts for fuel cell cathodes, specifically for the sluggish oxygen reduction reaction (ORR) based on Fe, Co, Mn with acceptable yet inferior catalytic performance to the noble-metal catalysts[1-3]. The M-N-C catalysts (where M is a transition metal single atom) are among the most promising electrocatalysts for ORR. The key characteristic of these catalysts is the presence of M-N_x, which has shown high stability and high catalytic activity[4]. Fe-N-C catalysts have shown superior performance among various metals, which has attracted considerable recent attention from the research community. Various aspects, including the local structure of the Fe-N sites, synergetic performance of different iron species, stability of the Fe-N coordination structures, active site evolution from raw precursors into the final carbon materials during carbonisation, and the oxygen reduction reaction (ORR) pathways have been investigated. Although great progress has been made, there are still challenges in establishing the exact structure-to-property correlation in such catalysts, which is essential for the rational design and synthesis of new catalysts with tailored activities for wide ranges of electrocatalytic processes[4].

In this work, a facile route to construct scalable, low-cost iron nitrogen-doped carbon spheres as high-performance ORR catalysts were prepared. Firstly, hydrothermal carbon spheres with abundant oxygen functionalities were synthesised. The obtained hydrothermal carbon spheres were then impregnated with iron precursors ($FeCl_2$ or $FeCl_3$) and a nitrogen precursor (melamine), followed by two-step carbonisation under inert N_2 gas. Iron and nitrogen were hybridised into the carbon support during the carbonisation process, followed by acid treatment to remove any free metallic iron species formed on the surface, allowing only Fe-N_x complexes to remain (Fe@NCS-A, where A represents acid). Samples impregnated with $FeCl_2$ or $FeCl_3$ are denoted as Fe^{2+}@NCS-A and Fe^{3+}@NCS-A, respectively, where -A refers to acid wash. Gram scale of Fe@NCS catalyst (≈51 wt% yields) can be easily obtained in one batch, demonstrating the scalability of this reaction.

To obtain an overview of the morphology for the obtained electrocatalysts, high-resolution High-Angle Annular Dark-Field Scanning Transmission Electron Microscopy (HAADF-STEM) was employed. As shown in Fig. 1a-b, both obtained electrocatalysts showed a size range of 200-500 nm. Most of the formed carbon spheres have uniform brightness, with only a small portion showing the presence of the nanoparticles. Energy-Dispersive X-ray Spectroscopy (EDS) was performed to map the presence of Fe species, where most carbon spheres showed a well-distributed Fe signal, suggesting that Fe may exist in the form of isolated sites within the carbon matrix.

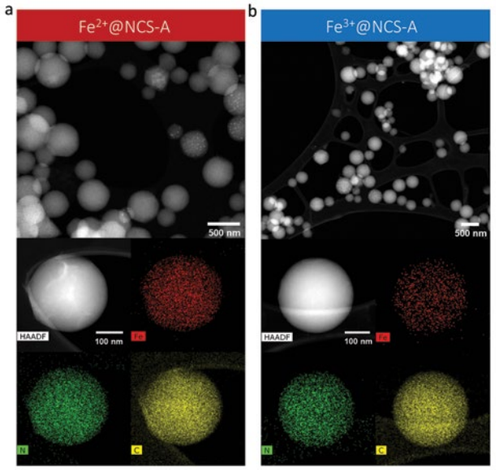

Figure 1: a) top HAADF-STEM image of Fe^{2+}@NCS-A, bottom EDS mapping results of Fe^{2+}@NCS-A; b) top HAADF-STEM image of Fe^{3+}@NCS-A, bottom EDS mapping results of Fe^{3+}@NCS-A.

X-ray Absorption Near Edge Spectroscopy (XANES) and Extended X-ray Absorption Fine Structure (EXAFS) data were collected on the B18 to study the chemical configuration of Fe-N single sites. To reveal the local structure of catalysts, XANES signals were compared with theoretical XANES spectrums reported by Zitolo *et al.*[5], where FeN_4 without additional ligand gave the best match for both catalysts. Moreover, the best fit values for EXAFS fittings (Fig. 2a-b) of Fe^{2+}@NCS-A give an average coordination number of 4.0 ± 0.4 for Fe-N at 2.10 ± 0.01 Å and 2.4 ± 0.4 Fe-C at 1.92 ± 0.01 Å. Meanwhile, the average coordination numbers for Fe^{3+}@NCS-A were found to be 3.4 ± 0.1 Fe-N at 2.08 ± 0.01 Å and 1.2 ± 0.3 Fe-C at 1.90 ± 0.01 Å. In addition, Fe-Fe bonding with a coordination number of 0.5 ± 0.1 was required to fit Fe^{3+}@NCS-A. The Fe-C and Fe-Fe signal was found to be due to the presence of Fe_3C in these samples, as later confirmed by HAADF-STEM and EDS analyses. The absence of the Fe-Fe signal in Fe^{2+}@NCS could be either due to minimal Fe_3C content or a much smaller average particle size of Fe_3C. Therefore, we propose that the iron existed primarily as Fe-N_x on the carbon substrate for Fe^{2+}@NCS-A and Fe^{3+}@NCS-A, with Fe^{2+}@NCS-A being a fully stoichiometric Fe-N_4 species.

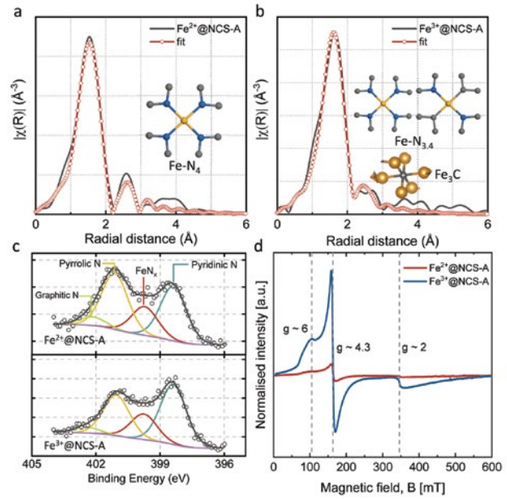

Figure 2: The magnitude of EXAFS FT k2-weight Fe K-edge spectra and fitting curve of a) Fe^{2+}@NCS-A; b) Fe^{3+}@NCS-A; c) high resolution N1s XPS spectrum of Fe^{2+}@NCS-A (top) and Fe^{3+}@NCS-A (bottom); d) X-band EPR of Fe^{3+}@NCS-A and Fe^{2+}@NCS-A.

The deconvoluted N1s spectra from X-ray Photoelectron Spectroscopy (XPS) (Fig. 2c) show four types of nitrogen species for both samples, in which the peak at 399.9 eV can be assigned to FeN_x complexes. Further, Electron Paramagnetic Resonance (EPR) was performed to investigate the electronic structure of Fe^{3+}@NCS-A and Fe^{2+}@NCS-A. EPR results shown in Fig. 2d reveal that Fe^{3+}@NCS-A has a stronger response than Fe^{2+}@NCS-A, suggesting greater Fe^{3+} content in Fe^{3+}@NCS-A. Fe content was analysed by Inductively Coupled Plasma Mass Spectrometry (ICP-MS), XPS and EDS, where Fe content in Fe^{2+}@NCS-A is higher than that in Fe^{3+}@NCS-A. Thus the missing Fe signal in EPR suggests a higher Fe^{2+} content in the Fe^{2+}@NCS-A than Fe^{3+}@NCS-A. This difference in iron oxidation states is due to the iron precursors ($FeCl_2$/$FeCl_3$) that could be further responsible for a different catalytic activity.

Linear Sweep Voltammetry (LSV) was carried out to assess the performance of the obtained electrocatalysts (Fig. 3a). The Fe^{2+}@NCS-A shows the most promising ORR activity due to its more electroactive iron species. LSV (Fig. 3a) curves of Fe^{2+}@ NCS-A show a pronounced peak for oxygen reduction, whose onset potential (0.94 V, the potential at −0.1 mA cm^{-2}) is more positive than Fe^{3+}@NCS-A (0.91 V). Fe^{2+}@NCS-A also displays a half-wave potential of 0.79 V, which is 30 mV more positive than Fe^{3+}@NCS-A (0.76 V), suggesting a better catalytic activity in Fe^{2+}@NCS-A. Chronoamperometry testing was performed to check the stability of Fe^{2+}@NCS-A. After 10 000 s at 0.7 V, due to the Fe-N singles sites, nearly 85% of the current was retained for Fe^{2+}@NCS-A, whilst Pt/C only showed 76% current retention (Fig. 3b). To further explore the performance of Fe^{2+}@NCS-A in real operating devices, the electrochemical performance in Anion Exchange Membrane Fuel Cells (AEMFCs) was also tested (Fig. 3c-d). The operating AEMFCs were fed with H_2 and O_2 gases. The Fe^{2+}@NCS-catalyst achieved high open-circuit potentials at 0.96 V in the operating AEMFC compared to other M-N-C catalysts. Although it is still lower than Pt-based catalysts tested under similar conditions, it shows great potential after further electrode optimisation.

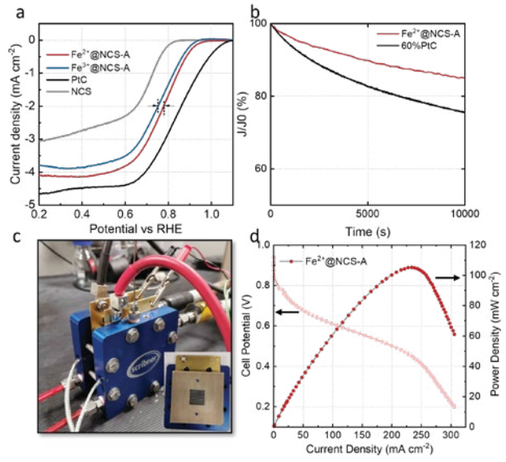

Figure 3: a) LSV curves at 1600 rpm, 10 mV s^{-1} scan rate; b) chronoamperometric responses of Fe^{2+}@NCS-A and Pt/C at 0.7 V and 1600 rpm. RDE/RRDE tests were performed in O_2-saturated 0.1 M KOH, background N_2 current was extracted. Reference electrode: Hg/HgO, counter electrode: graphite rod. Catalyst loading: 0.28 mg cm^{-2}, Pt loading 0.021 mg cm^{-2}; c) Photo image of AEMFC under testing; d) AEMFC performance of Fe^{2+}@NCS-A cathode (red line corresponds to power density, pink line corresponds to cell potential).

To conclude, the researchers demonstrated scalable electrocatalysts synthesis, applied them in AEMFC, and determined the Fe in the obtained electrocatalysts exist mainly in Fe-N_4 sites with the help of synchrotron techniques. The influence of iron precursors was also studied; however, more experiments are needed to reveal the mechanism of how the Fe oxidation state influences the electrocatalysis steps.

References:

1. Lefèvre, M. *et al.* Iron-based catalysts with improved oxygen reduction activity in polymer electrolyte fuel cells. *Science* **324,** 71–74 (2009). DOI: 10.1126/science.1170051
2. Pedersen, A. *et al.* Dual-metal atom electrocatalysts: theory, synthesis, characterization, and applications. *Advanced Energy Materials* **12,** 2102715 (2022). DOI: 10.1002/aenm.202102715
3. Xie, X. *et al.* Performance enhancement and degradation mechanism identification of a single-atom Co–N–C catalyst for proton exchange membrane fuel cells. *Nature Catalysis* **3,** 1044–1054 (2020). DOI: 10.1038/s41929-020-00546-1
4. Fei, H. *et al.* General synthesis and definitive structural identification of MN_4C_4 single-atom catalysts with tunable electrocatalytic activities. *Nature Catalysis* **1,** 63–72 (2018). DOI: 10.1038/s41929-017-0008-y
5. Zitolo, A. *et al.* Identification of catalytic sites for oxygen reduction in iron- and nitrogen-doped graphene materials. *Nature Materials* **14,** 937–942 (2015). DOI: 10.1038/nmat4367

Funding acknowledgement:
The authors thank Giannantonio Cibin and Nitya Ramanan from the B18 (SP26201) and Andy Smith from the I22 beamlines (SM27900) at Diamond Light Source to support and assist the measurements. T.S.M. thanks the EPSRC for support via EP/P023851/1 and EP/S01800X/1. J.Y.F., Z.X., and Z.Y.G. thank the support from Chinese Scholarship Council. R.C. and S.J.H. thank EPSRC EP/P009050/1. The authors want to thank Prof. John Varcoe's group for providing the membrane and the ionomer.

Corresponding author:
Prof Maria-Magdalena Titirici, Imperial College London, m.titirici@imperial.ac.uk

Unraveling the chemistry of bimetallic Metal-Organic Frameworks (MOFs)

Related publication : Ronda-Lloret, M., Pellicer-Carreño, I., Grau-Atienza, A., Boada, R., Diaz-Moreno, S., Narciso-Romero, J., Serrano-Ruiz, J. C., Sepúlveda-Escribano, A., & Ramos-Fernandez, E. v. Mixed-valence Ce/Zr metal-organic frameworks: controlling the oxidation state of Cerium in one-pot synthesis approach. *Advanced Functional Materials* **31,** 2102582 (2021). DOI: 10.1002/adfm.202102582

Publication keywords: Metal-Organic Frameworks; Mixed-valence; One-pot synthesis; X-ray absorption

The synthesis of metal organic framework (MOF) materials made of metal species that can exchange their oxidation state upon varying conditions is crucial for MOFs to evolve from a laboratory curiosity to real applications. For that reason, researchers are developing synthetic routes to prepare bimetallic MOFs with redox properties. However, the preparation and characterisation of these mixed-metal MOFs are far from trivial. In order to understand the success of the synthesis and the MOFs' properties, the local structure of the metal must be fully understood. X-ray Absorption Spectroscopy is the most appropriate technique to define the local structure of the metal.

Diamond Light Source's I20-Scanning beamline has high photon flux and high spectral purity, making it ideal for investigating samples with relatively low concentrations of the metal to be analysed. I20-Scanning also has facilities that allow measurements *in operando*.

Using their results from I20-Scanning, the team has found a synthetic route to prepare true-mixed metal MOFs, which uses a modulator to modulate the crystal morphology and the electronic nature of the metal cations. By using the modulator appropriately, they can prepare samples with only Ce(III) cations, a mixture of Ce(III)/Ce(IV) cations, or Ce(IV) cations.

Their results give us a new way to prepare bimetallic redox MOFs, which have the potential to be applied as catalysts in many different reactions, including selective hydrogenation, oxidation or Meerwein-Ponndorf-Verley reactions.

The presence of metal species that can easily exchange their oxidation states is of paramount importance in the field of catalysis, sensors and photocatalysis, among others. A classic example is ceria (CeO_2), in which Ce(IV) can readily be reduced to Ce(III) under suitable conditions, and vice versa. The major drawback of CeO_2 for being applied as a catalysis is that only the surface of the crystallites is used in the catalytic event. Therefore, most of the cerium and oxygen atoms of the lattice are not used. One promising alternative to better take advantage of ceria properties is the dispersion of CeO_2 nanoparticles on an inert support, as the authors and others have already demonstrated. Another approach might be the fabrication of porous solids made of molecularly dispersed cerium oxide clusters that allow reactants to reach the clusters. In this sense, Metal-Organic Framework (MOF) materials are ideal candidates, since cerium-based MOFs might be constructed.

Although there have been some attempts to prepare Ce-containing MOFs, their stability is limited. Stock's group and others have reported the preparation of Ce MOFs in which Ce(IV) is introduced. The presence of the Ce(IV)/Ce(III) redox pair has been demonstrated by de Vos. However, the presence of the

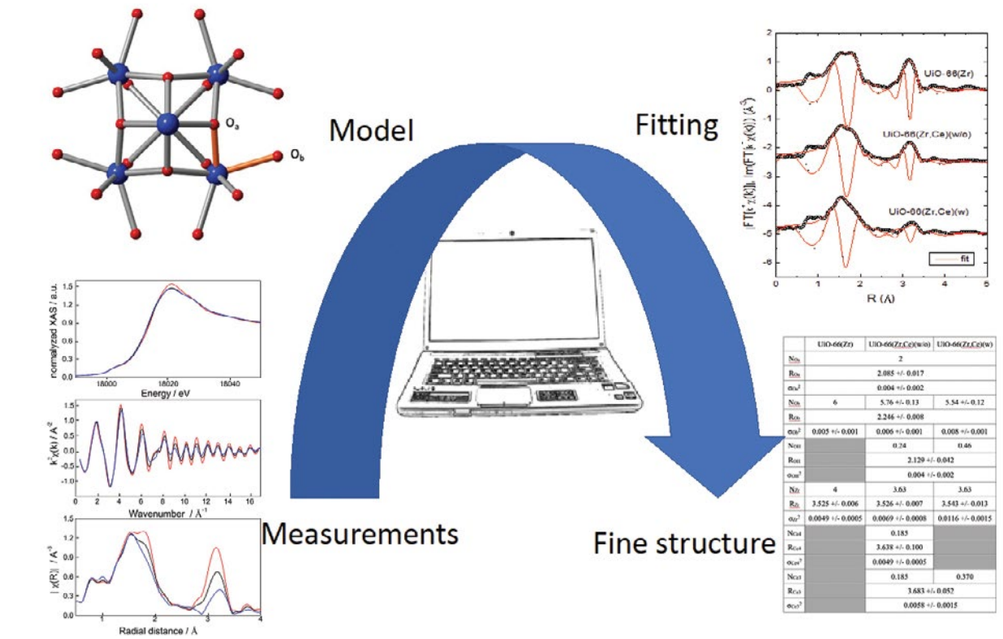

Figure 1: Schematic representation of the work done.

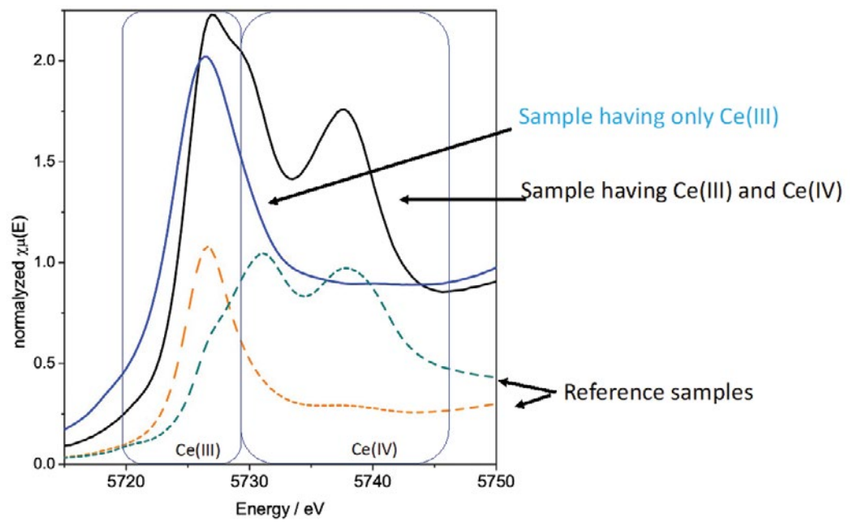

Figure 2: Ce L3-edge XANES spectra of two selected Ce(III) and Ce(IV) containing samples and reference compounds

redox pair is induced during the reaction but it is not present in the pristine MOF[1,2].

The main drawback of Ce-based MOFs is their low thermal stability that limits their practical applications to low temperature processes (<100 °C). However, the stability and the redox behaviour can be enhanced by introducing Zr cations in the same cluster with Ce, in a way that the atomic arrangement found in ceria-zirconia mixed oxides is replicated at smaller scale in the cluster. Another important point is the tailoring of the oxidation state of the Ce cations that are present in the MOF. In that respect, it is worth mentioning that the preparation and characterisation of these mixed-metal MOFs is far from trivial. Indeed, aiming for getting clusters containing both cations, *i.e.*, a true mixed-metal MOF, different undesired scenarios regarding the arrangement of the elements can be found such as the formation of segregated Ce-MOF and Zr-MOF crystalline phases or the formation of mono-elemental clusters in the same crystallite.

Besides the true mixed-metal nature of the MOF, it is also crucial to control the oxidation state of the Ce cations. Ce(III) and Ce(IV) are both stable at ambient conditions depending on the environment, and both of them have the same coordination number with carboxylic acid groups, although their ionic diameter is different; thus, both can be used for producing MOFs with the same topology. The tailoring of the oxidation state of the Ce cations is expected to lead to a fine control of the redox properties.

In this work, a one-pot synthesis method that enables the preparation of true (Zr,Ce) mixed-metal UiO-66 with tailored redox properties has been developed. This method allows the preparation of mixed-metal MOFs having only Ce(III), Ce(IV), or even mixed-valence MOFs with Ce(III)/Ce(IV). The designed synthetic method makes use of a modulator to finely control the oxidation state of the cerium cations.

The X-ray Absorption Spectroscopy (XAS) measurements performed at I20-Scanning[3] enabled the acquisition ofw detailed information of the local environment of both Zr and Ce. The Zr K-edge XAS revealed that the first and second coordination spheres of Zr were distorted upon the incorporation of a Ce atom (see Fig. 1).

In order to understand the role of the Ce species in the bimetallic MOF, the Ce L3-edge XAS was also measured. Surprisingly, it was discovered that depending on the synthesis conditions it was possible to tailor the oxidation state of the Ce cations (III, IV) (Fig. 2). With this data in hand, the synthetic routes were modified to design and synthesise the desired bimetallic MOF.

The new synthetic method developed has opened a new way of understanding MOF synthesis and the use of modulators in it. With this work, the scientific community has been provided with a new technique to prepare bimetallic MOFs with cations with the desired oxidation state. This opens the door to produce bimetallic MOFs with the desired electronic properties, multiplying the number of possible applications (catalysis, sensors, adsorption etc)[4].

References:

1. Smolders, S. *et al.* Unravelling the redox-catalytic behavior of Ce^{4+} metal-organic frameworks by X-ray absorption spectroscopy. *ChemPhysChem* **19**, 373–378 (2018). DOI: 10.1002/cphc.201700967
2. Wu, X.-P. *et al.* Cerium metal–organic framework for photocatalysis. *Journal of the American Chemical Society* **140**, 7904–7912 (2018). DOI: 10.1021/jacs.8b03613
3. Diaz-Moreno, S. *et al.* I20; the versatile X-ray absorption spectroscopy beamline at Diamond Light Source. *Journal of Physics: Conference Series* **190**, 012038 (2009). DOI: 10.1088/1742-6596/190/1/012038
4. Rogge, S. M. J. *et al.* Metal–organic and covalent organic frameworks as single-site catalysts. *Chemical Society Reviews* **46**, 3134–3184 (2017). DOI: 10.1039/C7CS00033B

Funding acknowledgement:
Authors acknowledge financial support by MINECO (Spain) through projects, MAT2017-86992-R, MAT2016-80285-P and Ministerio de Ciencia e innovación" (PID2020-116998RB-I00). EVRF acknowledges MINECO for his Ramón y Cajal fellow RYC-2012-11427. We also would like to thank Diamond Light Source (I20-Scanning beamline) for the beamtime given at the proposal SP19114 and SP16337.

Corresponding author:
Dr. Enrique V. Ramos-Fernández, Universidad de Alicante, enrique.ramos@ua.es

Upgrading zeolite catalysts to improve propene production

Related publication: Lin, L., Fan, M., Sheveleva, A. M., Han, B., X., Tang, C. C., Carter, J. H., da Silva, I., Parlett, C. M. A., Tuna, F., McInnes, E. J. L., Sastre, G., Rudić, S., Cavaye, H., Parker, S. F., Cheng, Y., Daemen, L. L., Ramirez-Cuesta, A. J., Attfield, M. P., Liu, Y., Tang, C. C., Han, B., Yang, S. Control of zeolite microenvironment for propene synthesis from methanol. *Nature Communications*, **12** 822 (2021). DOI: 10.1038/s41467-021-21062-1

Publication keywords: Methanol-to-propene; Hetero-atomic zeolite; Microenvironment; First carbon-carbon bond

Propene is a key compound used in the production of a wide range of polymers and chemicals. With rapidly growing demand for propene, the world faces a shortage of this crucial ingredient unless more efficient production methods can be developed.

Commercial methanol-to-propene (MTP) plants use the ZSM-5 and SAPO-34 zeolite catalysts to produce propene from methanol. However, this process is poorly understood and produces a range of products. Fundamental investigations of the process and the development of more selective and stable catalysts are both challenging goals for MTP research.

A team from the University of Manchester synthesised an MFI-zeolite within tantalum(V) and aluminium(III) centres in the framework. Using Diamond Light Source's Energy Dispersive EXAFS beamline (I20-EDE), they studied the interaction of methanol with the Tantalum(V) centre during the MTP reaction. They also used complementary measurements on the High-Resolution Powder Diffraction beamline (I11) to examine the configurations of adsorbed methanol molecules in zeolite pores.

Their results show that the new zeolite offers remarkable propene selectivity (51%), propene/ethene ratio (8.3) and catalytic stability (>50 hours) at full methanol conversion. Combining *in situ* synchrotron X-ray powder diffraction and X-ray absorption spectroscopy at Diamond and inelastic neutron scattering at ISIS with DFT calculations, the team was able to uncover key details of the process to add to our fundamental understanding.

This work will help develop sustainable manufacturing techniques for propene and other light olefins, using renewable resources such as biomass and CO_2.

Propene is a versatile building block for many important polymers, intermediates and fine chemicals[1]. It is predicted that the rapidly growing demand for propene will lead to a global propene shortage[2]. Methanol-to-propene (MTP) processes is a promising route to alleviate this short fall. This process has been commercialised by using ZSM-5 or SAPO-34 zeolites as catalysts[3], but many by-products such as alkanes, aromatics, and coke, form via complex reaction pathways, resulting in low propene selectivity and rapid deactivation of the catalysts owing to the coke formation. Thus, the development of new catalysts with the merit of the balance in "propene selectivity-propene/ethene ratio-catalytic stability" attracts much attention from academia and industry. Moreover, in academia, more than 20 different, sometimes controversial, formation mechanisms of the first carbon-carbon bond have been postulated to date[4]. Thus, unravelling the explicit mechanism and developing efficient catalysts remain unsolved problems[5].

Recently, a new hetero-atomic zeolite (denoted as TaAlS-1) was designed and synthesised by direct hydrothermal method to catalyse the MTP process. The Ta(V) and Al(III) centres were readily incorporated into the framework by adding Ta(V) and Al(III) sources in the mixture during the synthesis, resulting in a new zeolite material with dual-metal-decorated pores. Electron Paramagnetic Resonance (EPR) spectroscopy has confirmed the successful incorporation of Ta(V) and Al(III) into framework sites. The pyridine-adsorption infrared spectroscopy and ammonia temperature-programmed desorption show that the introduction of Ta(V) and Al(III) centres alters the acidity of the resultant zeolite, and thus it provides a unique microenvironment for the conversion of methanol. A remarkable propene selectivity (51%), propene/ethene ratio (8.3) and catalytic stability (>50 hours) at full methanol conversion were achieved simultaneously over the TaAlS-1 zeolite. Its catalytic performance compares favourably with that of all state-of-the-art catalysts for MTP reactions (Fig. 1).

The binding domains of methanol molecules within TaAlS-1 zeolite were determined by *in situ* Synchrotron X-ray Powder Diffraction (SXPD). For comparison, the same investigations on HZSM-5 and TaS-1 (the isostructural

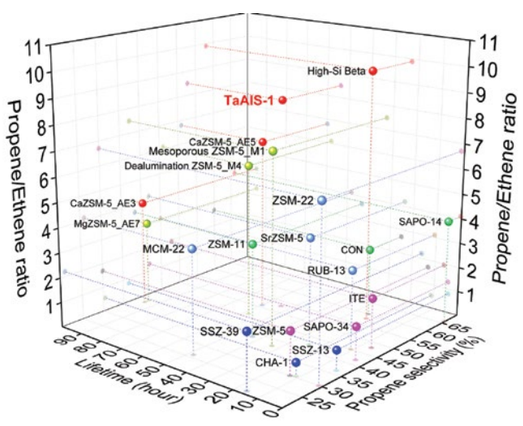

Figure 1: Comparison of propene selectivity-propene/ethene ratio-catalytic stability of selected MTP catalysts.

analogue without Al sites) zeolites were also performed. Adsorbed methanol molecules show three distinct spatial orientations within the framework of HZSM-5, TaAlS-1 and TaS-1 (Fig. 2a-c), indicating the presence of varying host-guest interactions. $MeOH^{II}$ and $MeOH^{IV}$ in TaAlS-1 interact with bridging O(H)-centres through its C-OH groups via hydrogen bonds (Fig. 2d). $MeOH^{I}$ interacts with $MeOH^{II}$ and $MeOH^{IV}$ to assemble a $\{MeOH\}_3$ trimer that favours the formation of trimethyloxonium (TMO) as the reaction intermediate. The TMO-type configuration is also observed in HZSM-5 (Fig. 2e), but not in TaS-1 due to lack of Brønsted acid sites (Fig. 2f). $MeOH^{III}$ is located close to $MeOH^{IV}$ in both TaAlS-1 (Fig. 2g) and HZSM-5 (Fig. 2h), and it interacts with Ta(V) sites in TaAlS-1 (Fig. 2g), which is potentially crucial for the activation of the C-O bond and thus to the formation of the first C-C bond.

To understand the effect of active Ta(V) sites, their local environment was interrogated through Ta L3-edge X-ray Absorption Spectroscopy (XAS).

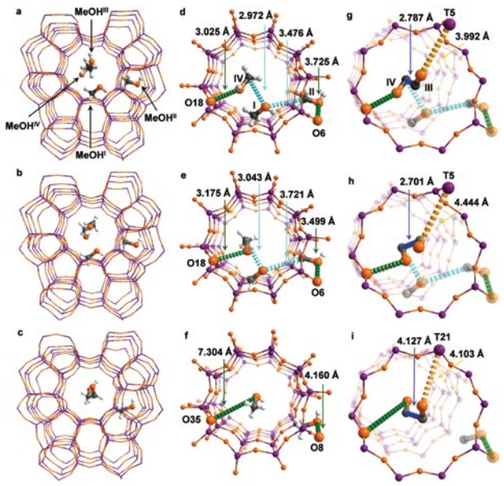

Figure 2: Views of crystal structures of MeOH-loaded TaAlS-1, HZSM-5 and TaS-1. Four distinct binding sites (I to IV) for MeOH have been observed in the channels. (a) TaAlS-1·MeOH; (b) HZSM-5·MeOH; (c) TaS-1·MeOH; Only three binding sites were observed in TaS-1. Detailed views of $MeOH^{I,II,IV}$ (d,e,f) and $MeOH^{III}$ (g,h,i) in TaAlS-1, HZSM-5 and TaS-1, respectively. Ta/Al/Si, violet; C, grey; O, orange; H, white.

Temperature programmed operando XAS revealed that the degree of methanol adsorption decreased with increasing reaction temperature (Fig. 3a,b). At the reaction temperature, adsorbed methanol molecules were revealed at the Ta(V) sites. This indicates that the adsorbed methanol molecule is activated by Ta(V) sites and then released for reaction to form products, resulting in "open" Ta(V) sites for next reaction cycle. Thus, the framework Ta(V) sites are ideal active sites for adsorption, activation and desorption of methanol substrates.

The detailed reaction mechanism was investigated by combined Inelastic Neutron Scattering (INS) and DFT calculations. Adsorbed methanol on Brønsted acid sites reacts with one weakly-adsorbed methanol molecule to form dimethyl ether (DME). Then DME reacts with a third methanol molecule to form TMO as a key intermediate which was clearly observed by INS (Fig. 3c, 365 cm^{-1}). Further, a fourth methanol molecule adsorbed on Ta(V) sites attacks the TMO intermediate to form the first carbon-carbon bond, resulting in the formation of olefins (Fig. 3d).

In conclusion, the new hetero-atomic zeolite with Ta(V) and Al(III) centres in the framework shows unique microenvironment that is ideally suited for the conversion of methanol to propene. Ta(V) sites in zeolite framework play a vital role in adsorbing and activating methanol molecules to form the first carbon-carbon bond. The formation of the first carbon-carbon bond between TMO and activated methanol molecule was evidently revealed. This will inform the design of future catalytic systems in these challenging industrial processes.

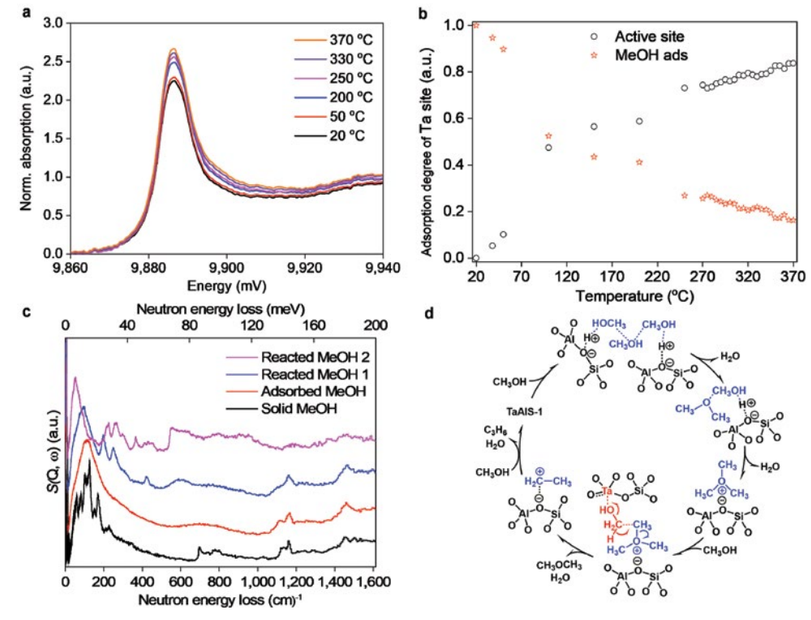

Figure 3: XAS and INS spectra for TaAlS-1 zeolite and proposed reaction mechanism for MTP; (a) Operando XAS spectra at the Ta L3 edge of TaAlS-1 zeolite during the conversion of methanol, only selected spectra shown; (b) Deconvolution of XAS via linear combination fitting to activated and adsorbed species. (c) INS spectra for TaAlS-1 on the adsorption and catalytic conversion of methanol; (d) Proposed reaction mechanism for the conversion of methanol in the induction period over TaAlS-1.

References:

1. Torres Galvis, H. *et al.* Supported iron nanoparticles as catalysts for sustainable production of lower olefins. *Science*, **335** 835–838 (2012). DOI: 10.1126/science.1215614
2. Grant, J. T. *et al.* Selective oxidative dehydrogenation of propane to propene using boron nitride catalysts. *Science*, **354** 1570–1573 (2016). DOI: 10.1126/science.aaf7885
3. Tian, P. *et al.* Methanol to olefins (MTO): from fundamentals to commercialization. *ACS Catalysis*, **5** 1922–1938 (2015). DOI: 10.1021/acscatal.5b00007
4. Yarulina, I. *et al.* Recent trends and fundamental insights in the methanol-to-hydrocarbons process. *Nature Catalysis*, **1** 398–411 (2018). DOI: 10.1038/s41929-018-0078-5
5. Olsbye, U. *et al.* Conversion of methanol to hydrocarbons: how zeolite cavity and pore size controls product selectivity. *Angewandte Chemie International Edition*, **51** 5810–5831 (2012). DOI: 10.1002/anie.201103657

Funding acknowledgement:
We thank EPSRC (EP/P011632/1), the Royal Society, National Natural Science Foundation of China (21733011, 21890761, 21673076), and the University of Manchester for funding. We thank EPSRC for funding the EPSRC National Service for EPR Spectroscopy at Manchester.

Corresponding author:
Dr. Sihai Yang, University of Manchester, Sihai.Yang@manchester.ac.uk.

The impact of applying a biostimulant on selenium enriched wheat

Related publication: Xiao, T., Boada, R., Llugany, M., & Valiente, M. Co-application of Se and a biostimulant at different wheat growth stages: Influence on grain development. *Plant Physiology and Biochemistry*, **160** 184–192 (2021). DOI: 10.1016/j.plaphy.2021.01.025

Publication keywords: Wheat biofortification; Se speciation; Functional food; Plant biostimulant

Selenium is an essential nutrient for human health. The selenium-biofortification of crops is increasingly common in selenium-deficient regions. However, issues remain regarding the observed toxicity to the plant.

Using a plant biostimulant can significantly reduce the stress experienced by wheat plants during selenium-biofortification processes. However, little was known regarding the effect of the plant biostimulant over the selenium metabolisation pathways, as the plant transforms inorganic selenium into more bioavailable organic forms (seleno-amino acids).

To assess the success of combining the plant biostimulant treatment with the selenium-biofortification process, researchers investigated the chemical species of selenium present in the wheat grains (i.e., the ratio of the seleno-amino acids).

The Microfocus Spectroscopy beamline (I18) offered the possibility of getting information, at the microscopic level, about the distribution of the elements and the chemical species present on the wheat grain section.

Their study proves that the biostimulant has a key role in enhancing both the number of grains produced per spike and their dry biomass without hindering the selenium enrichment process, either by diminishing the selenium concentration or massively disrupting the selenium species present in the wheat grain.

Based on the successful results on wheat plants, similar enrichment studies are envisaged on other vegetal systems (e.g., alfalfa). The team aims to better understand the spatial distribution of selenium-bioavailable species and the toxic effects of selenium for the plant upon different biofortification conditions.

This information will be useful to minimise both plant toxicity and economic cost and move towards more effective and plant-healthy selenium supplementation.

Selenium (Se) is an essential trace mineral of fundamental importance to human health. In terms of the human metabolism, Se substitutes sulphur (S) in the amino acid groups forming antioxidant enzymes such as glutathione peroxidase (GPx), thioredoxin reductase (TrxR) and iodothyronine deiodinase (IDD) which are important, among other things, for protecting against oxidative stress and for regulating the thyroid hormone metabolism. Se, as many other nutrients, is introduced into the human body via food intake. For instance, food derived from plants is a natural source of Se since plants can transform inorganic Se species (e.g., selenium salts) present in the soil into organic ones (e.g., seleno-amino acids) which are the desired chemical form of Se for human diet since they are much more bioavailable than inorganic ones. Thus, Se level in the soil usually has a direct influence in the concentration of Se present in food and, subsequently, in the Se level found in the human body. Hence, regions with low Se level in soils would yield Se deficient diets. This is a major issue nowadays since up to 14% of the population worldwide suffers from having an inadequate dietary Se intake with the associated risk of developing several chronic degenerative diseases[1].

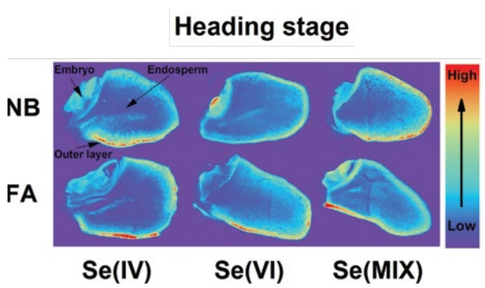

Figure 1: X-ray fluorescence mapping of Se in wheat grains grown under different treatments applied at heading growth stage: No Biostimulant-NB and Foliar Application-FA, in combination with the Se treatments described in the text (sodium selenite, Se(IV); sodium selenate, Se(VI); or a 1:1 mixture of both, Se(MIX)).

To achieve the appropriate Se level in the body, Se supplementation has been extensively used. For instance, soil fertilisation with Se has been applied in Finland since 1984 to increase Se concentration of food in regions with Se-deficient soils. However, the presence of high concentration of Se in soil induces stress to the plant and may hamper its normal development[2]. To overcome this issue, genetic engineering has been proposed as a strategy to enhance Se accumulation, volatilisation and/or tolerance in plants[3]. However, this approach has serious potential risks since it might promote the presence of new allergens in food, and the accumulation of other undesired heavy metals in the plant[4]. Alternatively, the application of a plant biostimulant as anti-stressor to alleviate the Se-induced toxicity in the plants emerges as a promising solution.

In our work, we used wheat as a model crop since it is a widely used food for human food and livestock feed. The plants were grown on hydroponic cultivation to set the basis for future studies on soil cultures. We applied three different Se treatments (sodium selenite, Se(IV); sodium selenate, Se(VI); or a 1:1 mixture of both, Se(MIX)) together with the biostimulant (Fyto-fitness by BIO Fitos). The biostimulant was applied at two growing stages, tillering (when the plant has three or four leaves) or heading (when the spike begins to emerge), until harvesting the grains once matured.

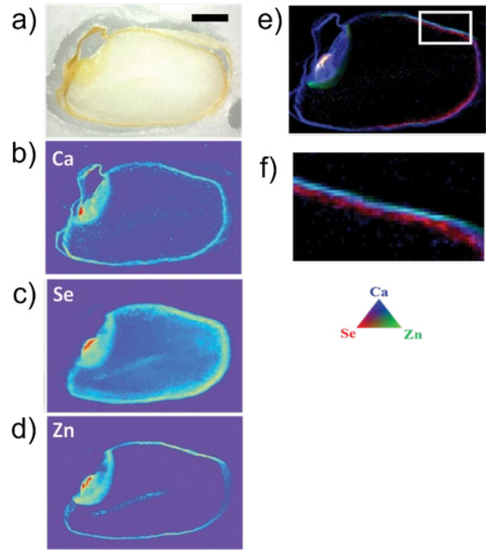

Figure 2: Optical image (a) and normalised μXRF elemental maps for Ca (b), Se (c) and Zn (d) of the wheat grain section for Se(VI) treatment applied at heading stage. Warmer colours indicate higher element concentration. Tricolour map image displaying the colocation of Ca, Se and Zn (e) and zoom on the bran region of the wheat grain (f). Horizontal scale bar in panel (a) denotes 1mm.

The total Se levels found in grains for the different treatments indicated that Se-biofortification of grains was achieved with values within the range of 37–100 $\mu g.g^{-1}$ and of 75–138 $\mu g.g^{-1}$ for heading and tillering stages, respectively. In addition, our results showed that the biostimulant have a key role increasing both the number of grains produced per spike and their biomass without diminishing the total amount of Se achieved by the biofortification processes. When the Se treatment is applied at the heading stage, the Se toxicity is less severe than when applied at the tillering stage. This can be attributed to the longer duration of the Se treatment in the case of the tillering stage.

In that respect, the elemental mapping performed at beamline I18[5] via micro X-ray Fluorescence (μXRF) imaging allowed us to get detailed information about the Se distribution in the grain (Fig. 1). The maps showed that Se is unevenly distributed in the grain (warmer colours indicate higher Se concentration). The higher concentrations of Se are mostly found in the germ and outer layer regardless of the treatment applied. This is related to the fact that the outer layer, mostly the aleurone and the germ, are the main regions containing proteins and, therefore, the Se-proteins assembled from seleno-aminoacids are in those regions. Regarding the co-location with other micro and macronutrients, the analysis of the μXRF maps for the different elements indicated that aleurone and scutellum are major storage tissues for macro (e.g., P, K, Ca and Mg) as well as micro (e.g., Fe, Zn, Cu and Mn) nutrients (Fig. 2). This distribution does not get affected by either Se species supplied in the treatment or the application of plant biostimulant at either of the two different growth stages considered.

However, it is not the amount of the Se accumulated but the chemical state of the Se which drives its bioavailability for humans. Therefore, determining the chemical state of Se is of crucial importance to assess the health benefits of the biofortification procedure. The chemical speciation analysis of Se performed by collecting micro X-ray Absorption Near-Edge Structure (μXANES) spectra at the regions of interest showed that the amount of organic Se species was always larger than 90% when the treatment was applied at the tillering stage, whereas for heading stage they were lower than 80% in most of the cases.

The effect found in the grain is that the total Se content decreases together with the total organic Se, and that there is an increase of C–Se–C (e.g., selenomethionine) respect to the total organic Se found in the heading group. Although both C–Se–C and selenocysteine species are seleno-amino acids that can be incorporated into proteins in place of methionine and cysteine, leading to toxicity, C–Se–C species have less harmful effects. Indeed, elemental Se, Se(0), is only detected in the heading stage group of grains and it is negligible in the tillering ones. Se(0) is one of the products derived from SeCys via the action of a selenocysteine lyase (SL). Elemental Se is comparatively innocuous for the plant, therefore this could be a potential Se detoxification mechanism by the plant. In the heading group, the abiotic stress caused by Se when the grain spike is just appearing may stimulate the expression of SL to enhance Se tolerance and maintain the growth cycle.

These results confirmed that the application of the plant biostimulant does not affect either the Se distribution or the Se speciation in the wheat grain and that the Se-biofortification from the heading stage is less toxic to the wheat plant than applications at earlier stages (e.g., tillering).]

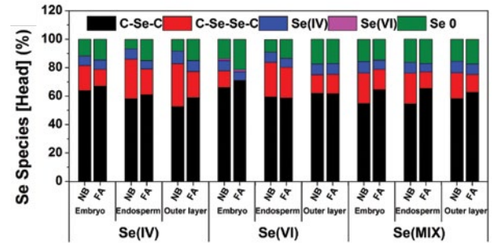

Figure 3: Results from the Se speciation analysis performed with the μXANES spectra collected at different parts of the wheat grain for biostimulant treatment applied at heading stage.

References:

1. Rayman, M. P. The importance of selenium to human health. *The Lancet*, **356** 233–241(2000). DOI: 10.1016/S0140-6736(00)02490-9
2. Guerrero, B.*et al*. Dual effects of different selenium species on wheat. *Plant Physiology and Biochemistry*, **83** 300–307 (2014). DOI: 10.1016/j.plaphy.2014.08.009
3. Progress in botany. *Nature*, **194** 1023–1023 (1962). DOI: 10.1038/1941023a0
4. Buchanan, B. B. Genetic engineering and the allergy issue. *Plant Physiology*, **126** 5–7 (2001). DOI: 10.1104/pp.126.1.5
5. Mosselmans, J. F. W. *et al*. I18 – the microfocus spectroscopy beamline at the Diamond Light Source. *Journal of Synchrotron Radiation*, **16** 818–824 (2009). DOI: 10.1107/S0909049509032282

Funding acknowledgement:
This research was supported by the Spanish CTM2015-65414-C2-1-R project from MINECO. We acknowledge Diamond Light Source beamtime no. SP18671-1 at I18 beamline. R. Boada acknowledges funding support from the European Union's Horizon 2020 research and innovation program under the Marie Skłodowska-Curie grant agreement No. 665919. T. Xiao acknowledges the grant from China Scholarship Council (201608330235).

Corresponding authors:
Mercè Llugany, Universitat Autònoma de Barcelona, merce.llugany@uab.cat
Roberto Boada, Universitat Autònoma de Barcelona, roberto.boada@uab.cat

Soft Condensed Matter Group

Robert Rambo, Science Group Leader

The Soft Condensed Matter (SCM) Group is comprised of the High Throughput SAXS (B21), the Multimode Infrared Imaging and Microspectroscopy (MIRIAM) (B22), SAXS and Diffraction (I22) and the Circular Dichroism Microspectroscopy (B23) beamlines, co-located in sectors 3 and 4 of Diamond. This unique portfolio of instruments enables studies of non-crystalline materials at nano- to meso-scale resolutions that include two-dimensional thin-films (photovoltaics, OLEDs), living mammalian cells, three-dimensional matrices (*e.g.* metal-organic frameworks, gels and waxes) and nano-particles in non-crystalline states. SCM science is "*the science that underpins continued improvements to quality of life*" and was critical to the rapid development of the COVID vaccines from Pfizer-BioNTech and Moderna. These vaccines are lipid nanoparticles encapsulating a modified messenger RNA stabilised in a non-crystalline environment. The SCM user community is international, providing 69.9% of our peer-reviewed allocated beamtime to users from the United Kingdom where the remaining time is shared largely between member states of the European Union, United States, China, Canada, Japan, Israel, and Australia.

In the last year, the SCM Group contributed to 144 scientific publications covering a broad range of disciplines including chemistry, material science, chemical engineering, physics and astronomy, biochemistry, genetics and molecular biology and engineering. Experiments on metal-organic frameworks from our group showed diverse applications including the emergence of hierarchical structures from disordered MOF mixtures, binding and separation of carbon and sulfur dioxide gases from hetero-metallic MOFs, and catalytic decomposition of noxious nitrogen dioxide. In healthcare, controlled drug release investigations were studied by TeraHertz radiation that measured the interaction between proteins and metallodrugs, whereas SAXS characterised the process of nanoparticle precipitants and lipidic cubic phases in drug release. More importantly, studies on I22 characterised bone-quality changes across the nano- to micron length scales showing the effects of steroids on osteoporosis. Across the group, material science studied self-assembly properties of diblock copolymer mixtures and gels producing stimulus-responsive, shape-shifting materials. More importantly, on B23, circular dichroism studies using the new Mueller Matrix Polarimeter (MMP) end-station discovered emergence of a new type of chiral-optical properties in solid-thin films. The MMP is world-leading, with unique capabilities making it ideal for studying thin-film materials with applications in flexible electronic and opto-electronic devices.

The 2021 COVID-19 working restrictions posed many challenges for our scientific community. B21 operated entirely as a mail-in service throughout 2021 whereas B22, B23 and I22 provided mixed access pending national working guidelines. At the start of the 2021 academic year, a new cohort of students joined our existing SCM doctoral students which now include the Universities of Pisa (Italy), Surrey and Chalmers, Southampton, College London, Imperial, Sheffield, Reading, Leeds and Durham. SCM provided several training workshops via online platforms including the popular S4SAS meeting led by I22. B22 organised an advanced training workshop with SOLEIL using machine learning software (Quasar) in infrared image analysis and B21 hosted a series of online, small group data analysis sessions for users which is now a routine part of our user programme. However, we were able to restart our annual in-person, bioSAXS training course hosted in Oulu, Finland in November 2021. The workshop featured users from Finland, Sweden and Denmark with keynote speaker Jan Skov Pedersen from Aarhus University.

B21 update

B21 studies noncrystalline, randomly oriented particles using high-throughput approaches. SAXS measurements can be made on any type of sample and in any physical state. The life sciences community comprises our largest user group since such measurements provide the opportunity to study biological machines in conditions that are comparable to their liquid, hydrated environment. B21 commissioned the design and manufacturing of a new sample environment unit (SEU) that provides an on-axis camera for sample viewing, and three interrogation ports for probes to enable light activation or heating. This will allow B21 to examine light sensitive soft matter materials during data acquisition. The project was driven by Beatrice Jones, a member of our PhD studentship programme from University of Cambridge. Her project is examining azobenzene compounds as a method to store solar energy through chemo-mechanical isomerisations.

BioSAXS measurements provide a structural snapshot of the thermodynamic ensemble. The measurement is over 1000s of billions of macromolecules and over a time-domain that is too long to inform on macromolecular dynamics. Furthermore, in the interpretation of bioSAXS data, flexibility is often inferred by a combination of molecular modelling (*i.e*, more than one model is required for model fitting) or by an interpretation of a semi-quantitative Kratky plot. To address the gap in dynamic studies of polymers at synchrotron X-ray sources, we have been developing expertise in Diffracted X-ray Tracking (DXT) and X-ray Foot-printing Mass Spectrometry (XFMS) for studies in the micro- to milli-second time domains. In 2021, we have completed the design of a prototype XFMS end-station that will allow for X-ray footprinting studies of polymers in the solution state. XFMS is a covalent modification of the residue through radiolysis of water molecules. This experimental modality will allow us to validate, at a residue level, atomistic models from molecular dynamics based simulations as well as structural hypothesis from bioSAXS investigations. XFMS can uncover structural waters, cavities, validate antibody-antigen complexes, and complement structure-function studies. Unlike hydrogen-deuterium (HD) exchange where side-chain exchange rates are too fast for detection, solvent accessibility of residues by XFMS will not go undetected. XFMS is a productive technique with a notable publication detailing disordered compact state of the estrogen receptor transactivation domain and GPCR receptor G-protein complex assembly[1,2]. We anticipate our first users in summer 2022.

B22 update

The Multimode Infrared Imaging and Microspectroscopy (MIRIAM) beamline, B22, is used to assess the molecular composition and microscopic spatial distribution of a sample at the highest, optically-achievable resolution in the infrared (IR). B22 operates two end-stations for scanning IR spectro-microscopy and IR imaging, with a suite of single and 2-D detectors that seamlessly cover the whole IR range, from near-IR to mid-IR and further into THz. B22 has been used in the analysis of inorganic-organic combinations in biomineralogy or composite materials, chemical degradation in conservation and archaeology, as well as studying live mammalian cells under the IR microprobe for *in situ* drug response, an important tool in anti-cancer research. This past year, B22 provided nano- and micro-spectroscopy imaging experiments studying corrosion resistance of steel in seawater, superlubricity of long-chain alcohols, varied applications of MOFs, metabolism in living mammalian cells and electrochemistry.

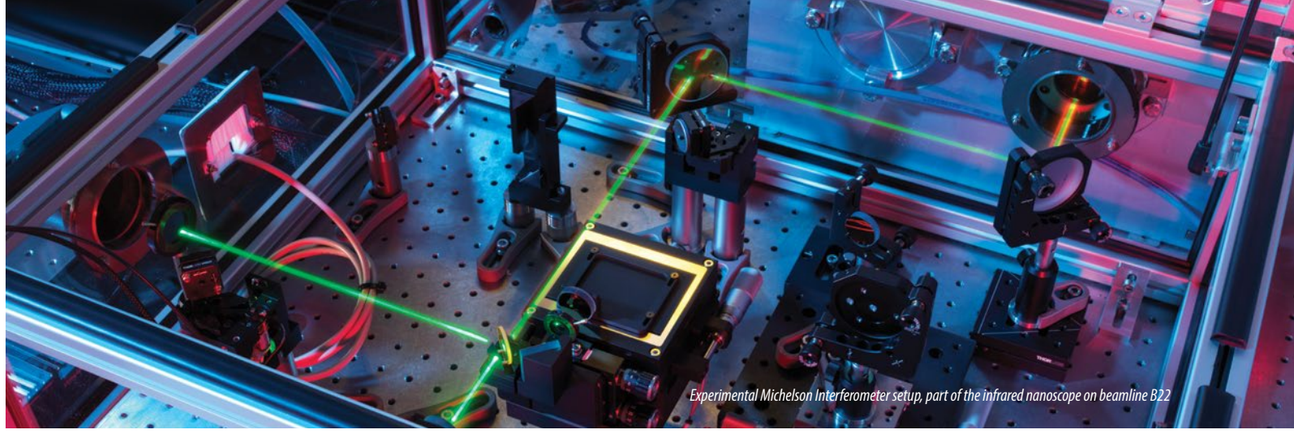

Experimental Michelson Interferometer setup, part of the infrared nanoscope on beamline B22

The beamline successfully installed its new end-station upgrade, a modern, Atomic Force Microscopy for AFM couple IR measurements. B22 pioneered the first photothermal AFM-IR measurements and will now provide two additional AFM-IR capabilities, namely tapping and s-SNOM. Collaborative calls for IR nanospectroscopy in photothermal, tapping and scattering-SNOM AFM-IR will be issued during the commissioning of the end-station and will be supported by a new dedicated support scientist. This cutting edge end-station is suitable for molecular analysis of submicron to micron scale organic matter and biomaterials - from mammalian cells to microplastic - with exceptional sub-micron resolution (i.e. up to 100 times below the IR wavelength scale). In addition, B22 finished a prototype gas-microreactor design for studying small volumes using IR microscopy. The device will increase sample throughput, position stability and be resistant to corrosive gases such as NOx up to 300 °C.

B23 update

B23 synchrotron radiation Circular Dichroism (CD) beamline uses circularly polarised light to characterise the structure-architecture of complex chiral materials in solution and in solid-state thin films. Chiral materials have a handedness like our right and left hands that are not superimposable and absorb differently the circularly polarised light generating CD fingerprint ID spectra. The beamline operates two end-stations: module A and B to accommodate a variety of sample environments. Module A operates in the 170-500nm region (125- 500nm for gas phase) utilising an automated 6-cell turret for protein UV denaturation and/or thermal stability assays, a motorised XY stage to accommodate either microfluidic chips for the separation of proteins by diffusion or a custom made 96-cell multiplate to characterise the biomolecules conformational behaviour and ligand binding screening. Since 2020, module B operating in the 190- 650nm spectral region is equipped with the Mueller Matrix Polarimeter (MMP) to study the optical (linear dichroism (LD), circular birefringence (CB)) and chiroptical properties (circular dichroism (CD), and circular birefringence (CB)) of thin films of chiral materials such as polymer, biopolymers, optoelectronics, hydrogels, and twisted liquid crystals. For optoelectronic materials, the measurement of CD at 50micron of spatial resolution can inform about the homogeneity of the supramolecular structure, which is strictly related to their efficacy. For biological samples, CD is also used to monitor in microfluidic chips structural changes, drug binding, protein instabilities as a function of temperature, pressure, ionic strength, surfactant, pH, ligand interactions, and ageing.

Pioneered by the B23 team, CD Imaging (CDi) technology exploits a highly collimated, synchrotron microbeam for scanning thin-films of solid materials. Unlike absorption, CDi can inform on the homogeneity of the chiral supramolecular structure. CDi at B23 is the only synchrotron-based instrument with the required sensitivity to guide the researchers on how to improve the properties of chiral materials. Combined with Diamond high-resolution microscopy, B23 is the unique worldwide facility for material and life sciences. B23 through collaborative calls is developing novel applications for CDi.

During COVID pandemic, B23 was one of the few beamlines operational within four weeks of the start of the pandemic in the United Kingdom. The beamline provided automated CD-thermal denaturation studies using the automated 6-cell turret sample holder and automated use of the novel 96-well sample measurement plate. These studies have inspired a new, limited mail-in service coordinated with B21 users in 2021.

I22 update

The Small Angle Scattering and Diffraction beamline (I22) offers combined Small and Wide Angle X-ray Scattering (SAXS and WAXS) studies on a range of low order biological, natural and synthetic samples. I22 excels at providing structural information on partially ordered materials ranging from colloidal nanoparticles and thin-films to large hierarchical structures such as bone.

Informed by remote and mail-in operations during COVID pandemic, I22 began an automation project that will use robotics to measure samples stored in a sample hotel co-located at the beamline. This automation project will store ~5000 samples in capillaries or DSC pans and take advantage of camera lengths during unsociable hours. Users often require different camera lengths depending on the hierarchical scale under investigation. In some cases, on-site users may have a camera length configuration required by a queued sample and the automation will be designed to efficiently take advantage of on-site user specific camera configurations. The automation project is expected to be completed October 2022. The quality of the source has been improved through completion of the Beam Conditioning Optics (BCO) project and an upgrade of our original monochromator (DCM). The BCO project allows for precise and stable control of a microfocus X-ray beam whereas the DCM upgrade replaced the original 2007, phase-I monochromator. The new monochromator is compatible with Diamond-II. In addition, we installed an in-vacuum, Pilatus 2M WAXS detector specifically designed for I22. This has allowed us to provide simultaneous "2D" WAXS measurements with the highest sensitivity. The new microfocus set-up improved our low q capability significantly from 0.25nm^{-1} (25nm) to 0.03nm^{-1} (~210nm), with the additional benefit of significantly lower background scatter over the previous microfocus configuration I22 also welcomed a new member to its group, Dr. Thomas Zinn, a senior support scientist with extensive experience in USAXS and XPCS experiments.

The I22 Principal Beamline Scientist Dr Nick Terrill, in collaboration with Prof Michael Rappolt from the School of Food Science and Nutrition at the University of Leeds, manage an Engineering and Physical Sciences Research Council (EPSRC) grant to support an offline SAXS facility at Diamond. The Multi-User Facility for SAXS/WAXS (DL-SAXS) provides a Xenocs Xeuss 3.0 instrument operating with an Eiger-2R 1M detector. The facility is now accepting Peer-reviewed Panel (PRP) proposals for 25% of its available time with the remaining time dedicating to University of Leeds and sample environment development.

1. Peng, Y. *et al*. A metastable contact and structural disorder in the estrogen receptor transactivation domain. *Structure* **27**, 229-240 (2019), DOI: 10.1016/j.str.2018.10.026
2. Du, Y. *et al*. Assembly of a GPCR-G protein complex. *Cell* **177**, 1232-1242 (2019). DOI: 10.1016/j.cell.2019.04.022

3D printable plastics that break down pollution

Related publication: Zhang, W. H., Day, G. J., Zampetakis, I., Carrabba, M., Zhang, Z., Carter, B. M., Govan, N., Jackson, C., Chen, M., & Perriman, A. W. Three-dimensional printable enzymatically active plastics. *ACS Applied Polymer Materials*, **3,** 6070–6077 (2021). DOI: 10.1021/acsapm.1c00845

Publication keywords: Nanocomposite; Nanomorphology; Functional bionanomaterials; Enzyme; Nanoconjugate; 3D printing; Melt electrowriting

Some pollutants - such as the organophosphates used in pesticides and chemical weapons - persist in the environment. Self-decontaminating materials could alleviate environmental pollution or form smart personal protective equipment.

Incorporating enzymes into solid materials would allow us to take advantage of their fast and efficient reaction kinetics. However, current strategies, such as surface immobilisation of enzymes or the use of biomimetic hydrogels, are not always successful.

Researchers have developed a method to modify the surface of a native enzyme with a mixture of anionic and cationic polymer surfactants. This enhances the thermal resilience of the modified enzymes as well as enabling their dissolution in organic solvents to make co-dispersions with plastic polymers.

To investigate the compatibility of these constructs with additive manufacturing fabrication techniques, the authors studied the protein structure to ensure the enzyme remained folded and active under the conditions required for material fabrication.

The unique B23 beamline facilities offered the power and reliability to measure Circular Dichroism (CD) of the samples sandwiched between two fused silica windows held horizontally to assess the protein secondary structure of the solvent-free enzymes. The beamline also allowed accurate characterisation of the thermal dependent unfolding transition of the melts above 100 °C up to 250 °C, unattainable with bench-top CD instruments.

Temperature-dependent Wide-Angle X-ray (WAXS) studies were also conducted on beamline I22 at Diamond Light Source to investigate the transition of the conjugates from lyophilised powders to annealed melts.

This research demonstrated that the fabrication methods of organophosphate degrading enzymes through 3D printing, thermal moulding, and melt electrowriting retaining their active structure were reproducible, the *sine qua non* condition for any commercial application.

Organophosphates (OPs), found in nerve agents and pesticides, pollute the environment and can persist for several years in industrial materials, such as polymer paint coatings or tar roads[1]. Accordingly, the display or incorporation of hydrolytic enzymes into novel materials offers a route to imbuing such materials with self-decontaminating properties to counteract subsequent expose routes. Enzymes are an attractive option, as they often exhibit rapid reaction kinetics, function under green conditions, and can be modified to tailor their activities towards specific toxic compounds. Accordingly, there has been a focused research effort to integrate enzymes into solid materials through surface immobilisation or *via* the development of biomimetic hydrogels. However, there are limitations that reduce their widespread industrial utility. For example, surface-immobilised enzymes may be denatured, depleted or fouled and thus require a tailored environment to preserve surface activity, whereas enzymes immobilised in hydrogel matrices typically have limited mechanical and environmental stability, and can require specific conditions

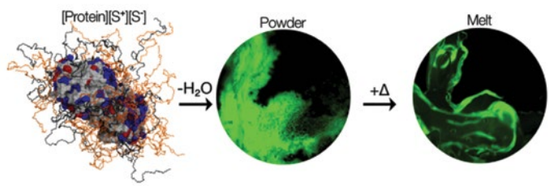

Figure 1: Schematic demonstrating the formation of the solvent-free protein melt. The surface of the enzyme (arPTE) or protein (sfGFP) is modified via the sequential addition of cationic and anionic polymer surfactants and is then lyophilised to create a dry powder. Upon heating, the powder melts form a solvent-free liquid. Crucially, this does not inhibit the biological function, as shown by the retention of sfGFP fluorescence.

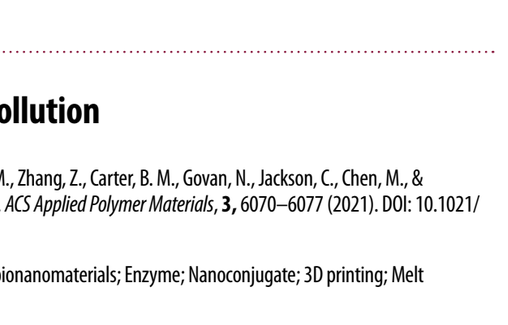

Figure 2: The absorbance at 230 nm as a function of temperature of the unmodified arPTE in aqueous solution (blue) compared to the [arPTE][S⁺][S⁻] melt showing that the melt has an enhanced thermostability.

to retain their gel phase[2]. A key advance would be to successfully incorporate enzymes into more ubiquitous structural materials that have widespread utility. Our strategy involves re-engineering the surface of an enzyme such that it is readily dispersible in a hydrophobic medium; to provide a route towards their integration with suitable feedstock materials (e.g., polymers or plastics) for the fabrication of "smart" solid-state structures. In this scenario, the enzyme exists as an integral component within the material, which could even present new active surfaces through tuneable material degradation profiles, thus overcoming the issues of denaturation or fouling.

Previously, we have reported on the electrostatic conjugation of polymer surfactant molecules to the surface of an enzyme to form an enveloping, dynamic corona[3]. This corona provides an interface with a polarity compatible with the desired dispersion media and also acts as a surrogate hydration shell to support correct protein folding and dynamics. Moreover, a well-designed corona has the potential to even improve the performance of enzymes by increasing the rate of substrate and product transport, by varying the dielectric constant in the vicinity of the active site[4]. In our present study, cationic and anionic polymer surfactants (S^+ and S^-, respectively) were sequentially conjugated to phosphotriesterase from *Agrobacterium radiobacter* (arPTE). The resulting aqueous protein-polymer surfactant nanoconjugates, [arPTE][S^+][S^-], were lyophilised and thermally annealed to form solvent-free protein "melts": dense, tacky biofluids composed purely of enzyme and surfactant (Fig. 1). Differential scanning calorimetry (DSC) performed on these biofluids revealed an endothermic melting transition at 33.9 ± 0.1 °C, which was corroborated by a loss of crystalline features when measured by temperature-dependent Synchrotron Radiation Wide-Angle X-ray Scattering (SR–WAXS), confirming a midpoint melting transition temperature of approximately 33.6 °C.

Demonstrating compatibility of these hybrid materials with modern high-resolution fabrication techniques is key for their adoption as a viable and practical material. Accordingly, the folding and thermostability of the arPTE in the melt was assessed by measuring its secondary structure content *via* Synchrotron Radiation–Circular Dichroism (SR–CD). The low sample volume, its inherent protein concentration and hyper-thermal stable properties required the superior signal-to-noise ratios, narrow pathlengths and large variable temperature range offered through beamline B23 at Diamond Light Source, compared to conventional CD apparatus. Notably, SR–CD revealed a midpoint denaturation temperature (T_m) of 102.4 ± 2.0°C for the [arPTE][S^+][S^-] melt, a significant increase in the thermal stability compared to aqueous native arPTE enzyme (T_m = 71.2 ± 0.6°C; Fig. 2). This midpoint protein denaturation temperature indicated that the biofluid could tolerate the high temperatures applied during material fabrication without denaturation of the enzyme and loss of function.

The polymer surfactant layer facilitated the dispersion of the nanoconjugate in a range of organic solvents, a necessary step to incorporating the enzyme with material feedstocks. Chloroform was used to produce co-dispersions of [arPTE][S^+][S^-] and polycaprolactone (PCL). PCL was of interest as it is biocompatible, biodegradable, and can be thermally extruded or moulded at *ca.* 60°C, thus was compatible with [arPTE][S^+][S^-]. Removal of the solvent from these co-dispersions gave solid enzymatically active plastic materials. The [arPTE][S^+][S^-]–PCL enzyme plastics could also be directly fabricated using thermal extrusion or moulding of the solid matrix after removal of the solvent. This provided access to 3D printed filaments and thermally moulded monoliths, allowing for the fabrication of larger structures. Significantly, 3D printed [arPTE][S^+][S^-]–PCL rings (1% enzyme w/w) exhibited enzymatic activity, persisting beyond 650 hours. Furthermore, the high resolution 3D fabrication technique Melt Electrowriting (MEW) was used to extrude precise "micro-meter" resolution structures at 70 °C from [arPTE][S^+][S^-]–PCL and analogous superfolder green fluorescent protein co-dispersions, [sfGFP][S^+][S^-]–PCL, such as fabric meshes with ultrafine threads (<5 µm, 0.1% enzyme w/w; Fig. 3). Interestingly, Quantitative Nanomechanics (QNM) mapping of the MEW plastic fibres revealed that the identity of the guest protein (arPTE or sfGFP) impacted upon the morphology and mechanical properties of composite materials. When compared with the neat PCL, both [sfGFP][S^+][S^-]–PCL and [arPTE][S^+][S^-]–PCL exhibited morphologies with increased levels of ordered structure that was indicative of high order molecular orientation and crystallinity, and the overall statistical average modulus of these materials were found to be 26.2 ± 11.6 MPa, 133.7 ± 49.8 MPa and 499.6 ± 182.0 MPa for PCL, [sfGFP][S^+][S^-]–PCL, and [arPTE][S^+][S^-]–PCL, respectively.

In conclusion, we showed that functional bionanomaterials comprising enzymes and synthetic polymers provide an attractive opportunity to increase the diversity of chemical environments encountered by protein-based components. Our methodology for re-engineering the native protein surface by the sequential conjugation of anionic and cationic polymer surfactants can yield hyperthermal stable nanoconjugate melts capable of dispersion in a range of dielectric media. These melts could be co-dispersed with polymers, such as PCL, to yield feedstocks compatible with a range of modern fabrication techniques, including 3D printing and melt electrowriting, to fabricate bespoke, enzymatically active solid structures with tuneable degradation profiles and mechanical properties. Specifically, we utilised the phosphotriesterase arPTE to manufacture enzyme–plastics capable of hydrolysing organophosphorus compounds and exhibited catalytic activity persisting across multiple assays and throughout prolonged exposure to an aqueous environment.

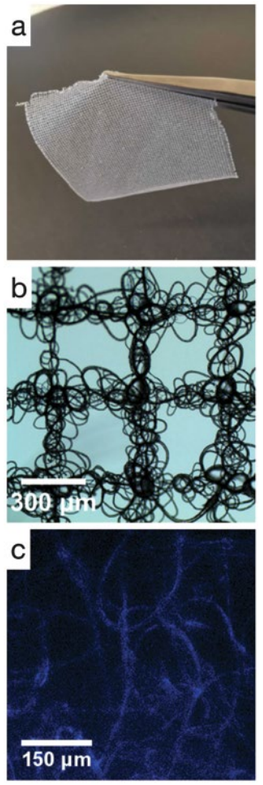

Figure 3: Melt electrowriting prints fine PCL threads. (a) active enzyme-PCL fabrics ([arPTE][S^+][S^-]–PCL); Fabric shown is 3 cm² in size; (b) Close examination of the [arPTE][S^+][S^-]–PCL fabric with widefield microscopy shows that it is comprised of tight tangles of enzyme–PCL threads arranged in a discrete repetitive pattern (fibres <5 µm in thickness); (c) Enzymatic activity of the material is retained after the melt electrowriting process, as shown through widefield fluorescence microscopy of the fabric in the presence of Coumaphos, a phosphothioate that is hydrolysed by arPTE into the fluorescent product chlorferon (excitation wavelength 355 nm, emission peak 460 nm).

References:

1. Jang, Y. J. *et al.* Update 1 of: destruction and detection of chemical warfare agents. *Chemical Reviews* **115,** PR1–PR76 (2015). DOI: 10.1021/acs.chemrev.5b00402
2. Basso, A. *et al.* Industrial applications of immobilized enzymes–A review. *Molecular Catalysis* **479,** 110607 (2019). DOI : 10.1016/j.mcat.2019.110607
3. Brogan, A. P. S. *et al.* Enzyme activity in liquid lipase melts as a step towards solvent-free biology at 150 °C. *Nature Communications* **5,** 5058 (2014). DOI: 10.1038/ncomms6058
4. Zhang, W. H. *et al.* Sequential electrostatic assembly of a polymer surfactant corona Increases activity of the phosphotriesterase arPTE. *Bioconjugate Chemistry* **30,** 2771–2776 (2019). DOI: 10.1021/acs.bioconjchem.9b00664

Funding acknowledgement:
This research was funded by the EPSRC (EP/N026586/1) that was awarded in collaboration with the Defence Science and Technology Laboratory (Dstl).

Corresponding author:
Dr Graham J. Day, University of Bristol, gd15316@bristol.ac.uk
Prof. Adam W. Perriman, University of Bristol, chawp@bristol.ac.uk

Synchrotron TeraHertz spectroscopy and neutron scattering pave the way to understanding chemoresistance

Related publication: Batista de Carvalho, L. A. E., Mamede, A. P., Batista de Carvalho, A. L. M., Marques, J., Cinque, G., Rudić, S., & Marques, M. P. M. Metallodrug-protein interaction probed by synchrotron terahertz and neutron scattering spectroscopy. *Biophysical Journal*, **120** 3070–3078 (2021). DOI : 10.1016/j.bpj.2021.06.012

Publication keywords: Anticancer drugs; Human serum albumin; Metallothionein; Synchrotron THz spectroscopy; Inelastic neutron scattering spectroscopy; Fourier transform infrared spectroscopy

Metallodrugs are pharmaceutical drugs that contain metals such as silver or platinum. The low bioavailability and toxicity of metallodrugs, and the development of resistance to them, are still severe handicaps in cancer treatment. These factors drastically restrict chemotherapy success and affect millions of patients.

To overcome these drawbacks, we must thoroughly understand the mechanisms underlying drug transport and resistance, which control the agent's biodistribution and availability at its pharmacological target. Intracellular inactivation of the drug via coordination to biomolecules apart from the target (DNA) is one such mechanism involving metallothioneins (MTs).

The Multimode InfraRed Imaging and Microspectroscopy (MIRIAM) beamline B22 has been established as an invaluable tool to monitor biomolecular binding and conformational rearrangements, and researchers used a combination of coherent synchrotron-radiation TeraHertz spectroscopy and inelastic neutron scattering to investigate two platinum (Pt)- and palladium (Pd)-polyamine agents that have yielded promising results toward some types of human cancers.

Their results revealed an impact of the Pt- and Pd-agents on protein structure, conformational behaviour and overall flexibility, similar to former observations on the effect of this type of metallodrugs on DNA.

These findings are expected to contribute to a better understanding of the drug's mode of action, particularly of the inactivation processes associated with drug-protein linkage prior to DNA binding that underlie resistance and toxicity. This will assist in the design of improved platinum- and palladium-derived anticancer agents with higher bioavailability at the target, lower acquired resistance and decreased adverse side effects, thus enhancing chemotherapy effectiveness.

Cancer is still a major public health problem worldwide. Numerous cytostatic agents have been developed over the years, aiming at an improved antineoplastic activity coupled to decreased acquired resistance and deleterious side effects, including Pt- and Pd-based compounds introduced upon the discovery of cisplatin. Among these, Pt(II) and Pd(II) polynuclear chelates with polyamines (Fig. 1A) constitute a specific class of DNA-damaging anticancer agents[1].

However, low bioavailability, toxicity and acquired resistance of metallodrugs are still severe handicaps in oncology practice. Intracellular inactivation of the drug via coordination to biomolecules apart from the target (DNA) is one of the mechanisms underlying acquired resistance, namely involving metallothioneins (MTs). These ubiquitous cysteine-rich proteins are linked to cellular protection against metal toxicity and have a high affinity for soft transition metal ions such as Pt^{2+} and Pd^{2+}, thus being involved in cisplatin´s resistance through the formation of Pt-thiolate clusters. Human Serum Albumin (HSA) is the most abundant protein in human serum, playing a key role in the transport and metabolism of exogenous compounds. Pt-based agents, in particular cisplatin, are known to reversibly bind to HSA upon intravenous administration, yielding stable adducts that circulate in the bloodstream. This will help to elucidate the drug´s pharmacokinetic profile, specifically the competition between S- or N-donor ligands from proteins and DNA´s purine bases.

Fourier Transform Infrared (FTIR) spectroscopy coupled to synchrotron radiation constitutes an unmatched tool for studying biological systems[2]. In addition, terahertz (THz) absorption spectroscopy, covering the 3 – 100 cm^{-1} frequency range, is particularly sensitive to very low frequency vibrational modes. THz measurements on proteins are highly sensitive to intra- and intermolecular interactions, providing reliable information on protein´s conformational rearrangements, average flexibility and functionality. The use of a high-flux terahertz Coherent Synchrotron Radiation (CSR) emission at the B22 beamline ensures a greatly enhanced intensity of the exciting beam which, coupled to highly sensitive broadband detectors, provides a much better quality of the acquired data. In particular, the low-alpha mode available at Diamond allows to probe the very low frequency spectral range (10 – 65 cm^{-1}).

Inelastic Neutron Scattering (INS) spectroscopy performed in the TOSCA spectrometer at the ISIS Neutron and Muon Source is a non-optical technique complementary to THz spectroscopy that has proved to be extremely useful for monitoring drugs' impact on biological samples[3]. INS enables the observation of all the fundamental vibrational modes, overtones and combination bands of a system, and is especially sensitive to hydrogenous materials particularly in the low energy range (0 – 400 cm^{-1}). This complementarity between THz absorption and neutron scattering allows to probe the same energy modes of a sample in two completely different ways – respectively **via** an optical method (subject to selection rules) and **via** inelastic scattering (according to the nuclear cross section).

The present study aimed at studying the interaction between the anticancer agents Pt_2Spm, Pd_2Spm and cisplatin, and the proteins HSA and MT. Two crucial processes for drug activity were investigated: (i) drug transport through the blood stream, for these types of intravenously administered chemotherapeutic agents – using a drug–HSA model; (ii) acquired resistance, due to drug binding to sulphur-containing intracellular proteins such as MT – using a drug–MT model.

The measurements performed covered the 10 – 660 cm^{-1} (0.3 – 20 THz) spectral range, with special emphasis to the low energy excitations (below 65 cm^{-1}). This region comprises global collective vibrational modes of the biopolymer, which are strongly dependent on the protein´s overall conformation and are prone to be affected by the drug-protein interplay see Fig 1B. Therefore, any changes in these conformational preferences will be clearly reflected in the corresponding

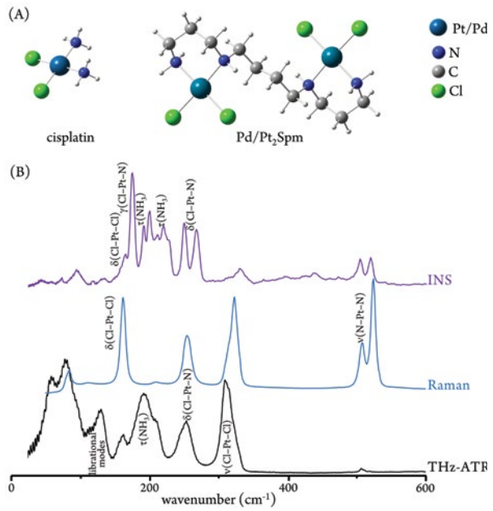

Figure 1: (A) Structural representation of cisplatin and Pt/Pd_2Spm; (B) Vibrational spectra – THz-ATR, Raman and INS (below 600 cm^{-1}) – of the anticancer agent cisplatin.

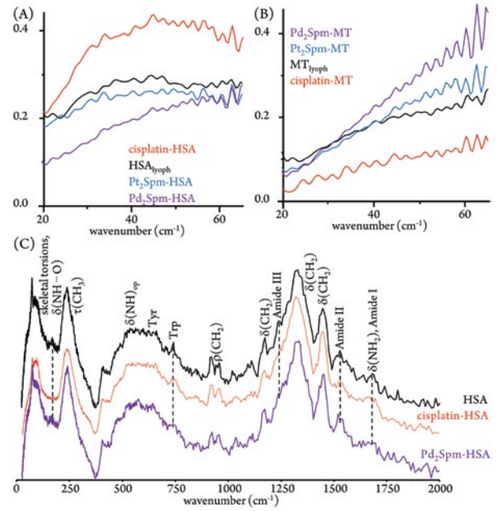

Figure 2: (A) CSR-THz-ATR spectra (acquired in low-alpha mode) of human serum albumin (HSA) and its drug adducts; (B) CSR-THz-ATR spectra (acquired in low-alpha mode) of metallothionein (MT) and its drug adducts; (C) INS spectra (at 10 K) of human serum albumin (HSA), cisplatin-HSA and Pd_2Spm-HSA (0 – 2000 cm^{-1}).

THz profile. While for the HSA systems the absorbance increased with frequency up to ca. 40 cm^{-1} then becoming nearly constant, mainly for the Pt-containing systems (Fig. 2A), for the MT conjugates there was an almost linear increase from 20 to 65 cm^{-1} (Fig. 2B). This slope increment, more pronounced for the drug-protein conjugates as compared to the free proteins (particularly for the Pd_2Spm adducts), reveals a conformational rearrangement of the protein consistent with an enhanced flexibility, giving rise to a greater density of low energy vibrational modes. This plasticity enhancement within a protein due to binding to an external ligand has been previously reported, namely regarding the interaction of the anticancer drug methotrexate with its target enzyme dihydrofolate reductase[4].

Each of the currently tested metallodrugs induced distinct conformational changes in either HSA or MT. The effect of the dinuclear agents Pt_2Spm and Pd_2Spm followed a similar trend for each of these biomolecules, with either a lower or higher intensity relative to free HSA and MT, respectively. In turn, the mononuclear agent cisplatin was found to have opposite impacts on HSA as compared to MT, and always inverse to the effects of the Pt- and Pd-spermine compounds. Also, Pd_2Spm showed a more significant influence on MT relative to HSA, and an overall stronger impact on both proteins as compared to its Pt-counterpart.

Regarding the INS profile, clear changes of the drug-HSA conjugates relative to both the free protein and the isolated Pd-agent were detected (Fig. 2C), revealing the perturbation on protein´s conformation due to drug-binding which takes place via metal coordination to the N and S sites from HSA´s histidine and methionine residues. A drug impact on HSA´s skeletal torsions (Amide VII mode) and NH ··· O interactions within the peptide backbone, responsible for signals centered at ca. 160 cm^{-1}, was evidenced in the cisplatin-adducts for which these features virtually disappeared – this may be due to drug-elicited protein aggregation. Additionally, the band from tryptophan (ca. 750 cm^{-1}) slightly lowered its intensity upon drug interaction, this variation being more significant for the Pd_2Spm-HSA system.

Similarly to former observations on the effect of this type of metallodrugs on DNA, a clear impact of the Pt- and Pd-agents on protein´s structure, conformational behaviour and overall flexibility, both for HSA and MT was revealed. Furthermore, drug effects on proteins often lead to aggregation via cross-linking interactions, as previously reported for lysozyme and HSA[5]. This type of protein aggregation has been identified as one of the pre-DNA binding mechanisms responsible for acquired drug resistance.

Coupled to previous data on the impact of Pt- and Pd-spermine compounds on human cancer cells and DNA, the present results are expected to contribute to a better understanding of the drug´s mode of action, particularly of the inactivation processes associated to drug-protein linkage prior to DNA binding, which underlie resistance and toxicity. This will assist in the design of improved platinum- and palladium-derived anticancer agents, with higher bioavailability, lower acquired resistance and decreased adverse side effects, thus enhancing chemotherapy effectiveness.

References:

1. Farrell, N. P. Multi-platinum anti-cancer agents. Substitution-inert compounds for tumor selectivity and new targets. *Chemical Society Reviews,* **44,** 8773–8785 (2015). DOI : 10.1039/C5CS00201J
2. Batista de Carvalho, A. L. M. *et al.* Anticancer drug impact on DNA – a study by neutron spectroscopy coupled with synchrotron-based FTIR and EXAFS. *Physical Chemistry Chemical Physics,* **21,** 4162–4175 (2019). DOI: 10.1039/C8CP05881D
3. Marques, M. P. M. *et al.* A new look into the mode of action of metal-based anticancer drugs. *Molecules,* **25,** 246 (2020). DOI: 10.3390/molecules25020246
4. Balog, E. *et al.* Direct determination of vibrational density of states change on ligand binding to a protein. *Physical Review Letters,* **9,** 028103 (2004). DOI: 10.1103/PhysRevLett.93.028103
5. Pinato, O. *et al.* Platinum-based drugs and proteins: Reactivity and relevance to DNA adduct formation. *Journal of Inorganic Biochemistry,* **12,** 27–37 (2013). DOI: 10.1016/j.jinorgbio.2013.01.007

Funding acknowledgement:
The author thanks financial support from POCentro, COMPETE 2020, Portugal 2020 and European Community through the FEDER and the Portuguese Foundation for Science and Technology (UIDB/00070/2020 and PhD Grant SFRH/BD/137001/2018). Diamond Light Source (UK) and the STFC Rutherford Appleton Laboratory are thanked for access to the B22/MIRIAM beamline (SM21620) and to neutron beam facilities (TOSCA/RB2010013, DOI 10.5286/ISIS.E.RB2010013).

Corresponding author:
Dr Ana Batista de Carvalho, University of Coimbra, almbc@uc.pt

Understanding how cells communicate could help treat cancer

Related publication: Zeronian, M. R., Klykov, O., Portell i de Montserrat, J., Konijnenberg, M. J., Gaur, A., Scheltema, R. A., & Janssen, B. J. C. Notch–Jagged signaling complex defined by an interaction mosaic. *Proceedings of the National Academy of Sciences* **118,** (2021). DOI: 10.1073/pnas.2102502118

Publication keywords: Receptor; Ligand; Complex; Cell signalling; SAXS; Structure; X-ray diffraction

Communication between cells is essential for the development and stability of tissues and prevents diseases, including cancer. The Notch and Jagged transmembrane proteins interact to regulate communication between cells in all multicellular animals. Defining these interactions is critical to understanding Notch-associated disorders. However, while structural studies have focused on short regions of both proteins, it remained unclear how their entire extracellular domains collectively engage to activate signalling.

Researchers used Small-Angle X-Ray Scattering (SAXS) measurements on the High-throughput SAXS beamline (B21) to probe the low-resolution properties of the Notch1 and Jagged1 ectodomain. SAXS turned out to be very useful to show that the proteins have conformational flexibility. They also used the Macromolecular Crystallography beamline I03 for X-ray diffraction on crystals of a smaller Notch1 segment.

Their results identified several unreported, interacting regions in the Notch1–Jagged1 full extracellular complex. The Notch1 and Jagged1 ectodomains are flexible and not fully extended. Notch1 and Jagged1 interact through more sites than previously thought, and regions of importance, *i.e.*, for Notch1 activation, are in direct contact in the Notch1-Jagged1 complex.

Knowing which parts in the Notch1-Jagged1 complex are interacting will help in the design of tools to interfere with this interaction. This may be useful for new therapeutics in the fight against cancer. This interaction network redefines our knowledge on Notch activation and provides avenues for therapeutic advances.

The cell-surface receptor Notch1 is an important factor in the communication between cells and controls the development and function of tissues. Interactions between Notch1 and the ligand Jagged1 regulates cell differentiation in multicellular animals including humans[1]. Notch1 dysfunction often leads to developmental disorders and cancers, and as such, Notch1 is a sought-after therapeutic target[2].

Notch1 signaling is initiated by Jagged1 binding. Jagged1 binding triggers a conformational change in Notch1, exposing sites for proteolytic processing in the C-terminal membrane proximal domain, releasing the Notch1 intracellular segment that can then travel to the nucleus to regulate transcription of target genes[3]. Jagged1 interaction can also inhibit Notch1 signaling when the proteins are expressed on the same cell. How Notch1 and Jagged1 interact is not entirely resolved. Notch1 and Jagged1 are large proteins, with 40 and 19 domains on the extracellular side, respectively, of which epidermal growth factor (EGF) repeats make up a large part. The extracellular segments are believed to be conformationally flexible, although this has only been experimentally determined for a few smaller portions in the extracellular segments[4]. Work during the past three decades has focused on two sites in this signalling pair, the EGF8-EGF12 region in Notch1 and the C2-EGF3 region in Jagged1. Recent crystal structure data has shown that these segments interact in an antiparallel fashion[5]. How other sites contribute to Notch1-Jagged1 interaction in the context of the full extracellular segments is unknown. Also, the coupling of Jagged1 binding to Notch1 EGF8-EGF12 and the subsequent conformational change in the Notch regulatory region (NRR) separated by 24 EGF repeats is not resolved. Structural studies on the full ectodomains have been hampered due to their large size, extensive N- and O-linked glycosylation, numerous disulfide bonds – 119 in Notch1 – and concomitant difficulty in producing purified samples.

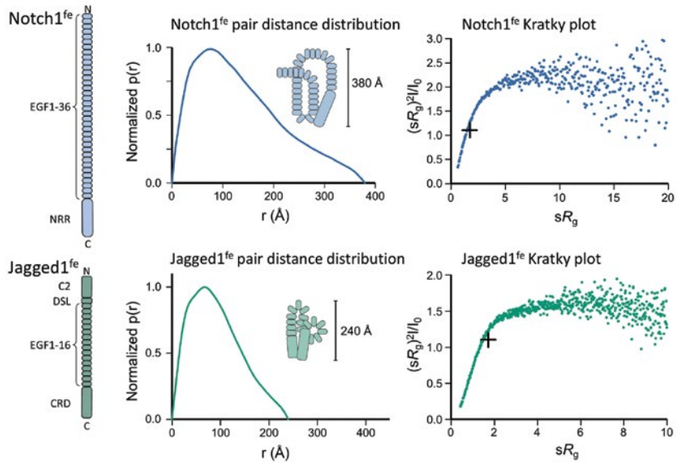

Figure 1: SAXS analysis of the full-extracellular segments of Notch1 and Jagged1 reveal conformational flexibility. Left, schematic of the 40 extracellular domains of Notch1 and the 19 extracellular domains of Jagged1. Pair-distance distribution analysis (middle column) and normalised Kratky plots (right column) of the SAXS data indicate the proteins are conformationally flexible. The crosshairs in the Kratky plots indicate the peak position expected for a globular protein.

By using human embryonic kidney (HEK293) cell suspension culture at multi-litre scale it was possible to obtain sufficient full ectodomain Notch1 and Jagged1 sample for Size Exclusion Chromatography Small Angle X-ray Scattering (SEC-SAXS) experiments. SEC-SAXS on these purified samples, measured at Diamond Light Source beamline B21 and ESRF beamline BM29, revealed that the ectodomain conformations of Notch1 (Notch1^{fe}) and Jagged1 (Jagged1^{fe}) are flexible and not fully extended (Fig. 1). The maximum dimension (D_{max}) of the Notch1 ectodomain is 380 Å, whereas that of Jagged1 is 240 Å. If both proteins would be fully extended, as schematically drawn in Fig. 1 (left), the D_{max} would have been 1,027 Å for Notch1^{fe} and 585 Å for Jagged1^{fe}. Considering the flexibility and size of the samples, more detailed structural studies on the full ectodomains were predicted to be challenging. Instead, smaller segments were analysed by X-ray diffraction and batch SAXS.

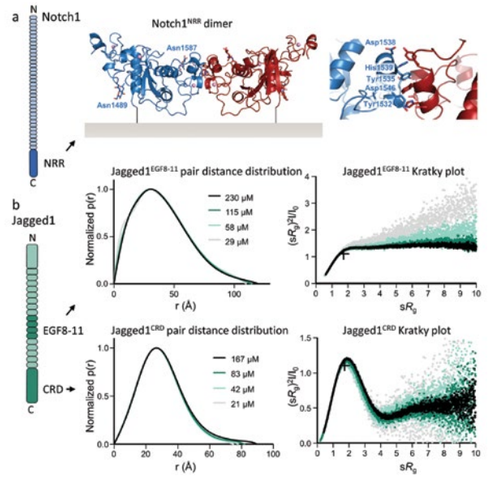

Figure 2: Segments of the Notch1 and Jagged1 ectodomain have different properties; (a) Crystal structure of Notch1NRR, consisting of three small Lin12/Notch repeats and a heterodimerisation domain, reveals a dimer compatible with Notch1 homodimerisation in cis; N-linked glycans and interface residues are indicated; (b) Batch SAXS pair-distance distribution and Kratky plot indicate the Jagged1 EGF8-11 segment has conformational flexibility whereas the Jagged1 CRD is compact and globular. The crosshairs in the Kratky plots indicate the peak position expected for a globular protein.

A crystal structure of Notch1 NRR, determined from 2.1 Å diffraction data collected at Diamond beamline I03, revealed a dimer that is compatible with Notch1 dimerisation as a full-length protein on the cell surface (Fig. 2a). The dimerisation of Notch1^{NRR} was confirmed in solution by Size Exclusion Chromatography Multi-Angle Light Scattering (SEC-MALS). Batch SAXS analysis, at Diamond beamline B21, of two smaller Jagged1 segments at a range of concentrations showed both segments do not change their oligomeric state in solution (Fig. 2b). The four-domain EGF8-11 segment of Jagged1 has conformational flexibility whereas the Jagged1 cysteine-rich domain (CRD) is globular and compact. The flexibility and the size of the Notch1 and Jagged1 ectodomains may enable them to interact through multiple sites.

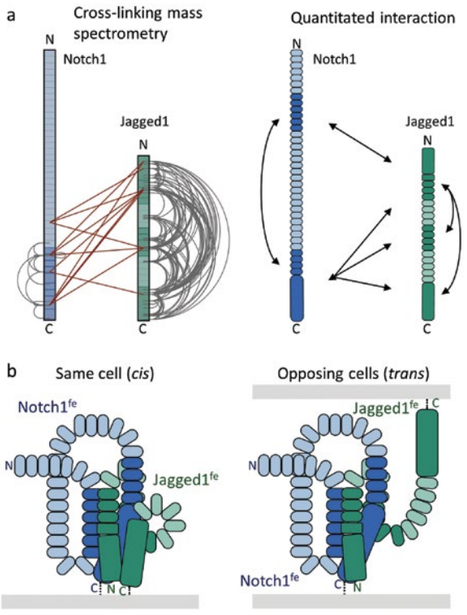

Figure 3: Inter- and intra-molecular interactions in the Notch1 – Jagged1 complex; (a) XL-MS analysis indicates that several sites in Jagged1 are in close proximity to the Notch1 EGF33-NRR C-terminal region; The intra- and inter-molecular interactions are confirmed in quantitative interaction experiments (SPR and MST) using targeted sites; (b) Two schematic representations indicating the architecture of the Notch1 – Jagged1 complex in a cis-setting and in a trans setting

Cross-Linking Mass-Spectrometry (XL-MS) analysis on the Notch1^{fe} – Jagged1^{fe} complex indicated that the C-terminal region of Notch1^{fe}, centred on the EGF33-NRR segment, played a role in interaction with three regions in Jagged1; C2-EGF3, EGF8-11 and CRD (Fig. 3a). In addition, a multitude of crosslinks in Jagged1^{fe} suggested substantial intramolecular interactions within the Jagged1 ectodomain. The proximity of Notch1$^{EGF33\text{-}NRR}$ to Jagged1$^{C2\text{-}EGF3}$ in the complex is remarkable as this could implicate a more direct role for Jagged1 binding to Notch1 NRR activation. Quantitative interaction experiments, *i.e.* Surface Plasmon Resonance (SPR) and Microscale Thermophoresis (MST) of smaller targeted segments, confirmed the intermolecular and intramolecular interactions indicated by the XL-MS analysis. In addition, direct interaction of Notch1$^{EGF8\text{-}EGF13}$ and Notch1^{NRR} showed that these two functionally important segments are likely much closer within Notch1 than previously thought. These data, on conformational flexibility and a mosaic of interaction sites, suggest that Notch1 and Jagged1 can interact intimately, and that the interaction mode is, most likely, dependent on their setting on the same cell (in *cis*) or on opposing cells (in *trans*) (Fig. 3b). The identification of previously unreported Notch1 and Jagged1 interactions sites opens the possibility for the development of new therapeutics that target these sites to prevent Notch1 activation in cancers.

References:

1. Bray, S. J. Notch signalling in context. *Nature Reviews Molecular Cell Biology* **17,** 722–735 (2016). DOI: 10.1038/nrm.2016.94
2. Aster, J. C. *et al.* The varied roles of Notch in cancer. *Annual Review of Pathology: Mechanisms of Disease* **12,** 245–275 (2017). DOI: 10.1146/annurev-pathol-052016-100127
3. Kovall, R. A. *et al.* The canonical Notch signaling pathway: structural and biochemical insights into shape, sugar, and force. *Developmental Cell* **41,** 228–241 (2017). DOI: 10.1016/j.devcel.2017.04.001
4. Weisshuhn, P. C. *et al.* Non-linear and flexible regions of the human Notch1 extracellular domain revealed by high-resolution structural studies. *Structure* **24,** 555–566 (2016). DOI: 10.1016/j.str.2016.02.010
5. Luca, V. C. *et al.* Notch-Jagged complex structure implicates a catch bond in tuning ligand sensitivity. *Science* **355,** 1320–1324 (2017). DOI: 10.1126/science.aaf9739

Funding acknowledgement:
This project was supported by the European Research Council (ERC) under the European Union's Horizon 2020 research and innovation programme with grant agreement No. 677500 (to B.J.C.J.); the research programme TA with project number 741.018.201 (to R.A.S.), which is partly financed by the Dutch Research Council (NWO); and the European Union Horizon 2020 programme INFRAIA project Epic-XS project 823839 (to R.A.S.). This work benefited from access to the Amsterdam NKI, an Instruct-ERIC centre, with financial support provided by Instruct-ERIC (PID 10025). This work has been supported by iNEXT (PID 6764), funded by the Horizon 2020 programme of the European Union.

Corresponding author:
Dr. Bert Janssen, Utrecht University, b.j.c.janssen@uu.nl

Controlling the strength of muscles

Related publication: Hill, C., Brunello, E., Fusi, L., Ovejero, J. G., & Irving, M. Myosin-based regulation of twitch and tetanic contractions in mammalian skeletal muscle. *ELife*, **10,** (2021). DOI: 10.7554/eLife.68211

Publication keywords: Skeletal muscle; Muscle regulation; Muscle contraction; X-ray diffraction

Skeletal muscles connect to bones and allow a wide range of movements and functions, and muscle weakness caused by disease and ageing significantly impacts quality of life. Although these changes are generally associated with loss of muscle mass, the intrinsic strength of a given mass of muscle is also reduced.

The basic mechanical response of a skeletal muscle cell to the electrical stimulus it receives from the central nervous system is called a twitch. The force produced by a twitch is much smaller than the maximum force that the muscle cell can produce when the motor proteins that drive contraction are fully activated.

As the motor proteins in muscles are organised into regular (almost crystalline) arrays, the structural changes that control muscle activation can be followed by measuring the diffraction of X-rays by the motor arrays. However, muscles diffract X-rays very weakly, and these experiments require an extremely bright X-ray source combined with a sensitive X-ray video camera that can record 200 diffraction patterns every second. The Small Angle Scattering and Diffraction beamline (I22) at Diamond Light Source is one of few facilities worldwide that meet these demanding requirements.

The discovery of the molecular structural factors that limit the strength of skeletal muscle in its normal twitch response allows those structures to be used to design and test potential drugs that could increase muscle strength. Almost identical mechanisms operate to limit the strength of the heartbeat and could be targeted to treat heart failure.

Muscle contraction is driven by sliding between two types of protein polymer filaments – the actin and myosin filaments. The former acts as a track for myosin motors to 'walk' along, stepping between actin monomers. In resting muscle, the actin monomers are not available for myosin motors to bind because regulatory proteins in the actin filaments block the binding sites. Activation of the muscle by an electrical signal from the central nervous system removes that block through a well-characterised signalling pathway mediated by a transient increase in the calcium concentration in the muscle cell.

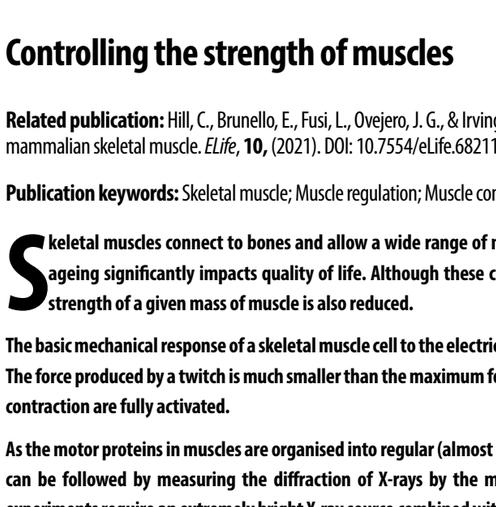

*Figure 1: Schematic of the myosin and actin filaments and X-ray diffraction patterns recorded at rest (**a** & **c**) and in a tetanus (**b**, **d**); The helical tracks of myosin motors (yellow) (**a**) generate the first-order myosin layer line reflection (ML1) (**c,** red box); In the tetanus (**b, d**), some actin-attached myosin motors (purple) and non-actin-attached partner myosin motors (magenta), intensify the M3 reflection (**d**, green box); Isotropic motors (light pink) do not contribute to the diffraction patterns.*

However, there is a second block on the interaction between myosin and actin in resting muscle: nearly all the myosin motors are locked into helical tracks on the surface of the myosin filaments (Fig. 1a; yellow motors), producing a characteristic 'layer line' reflection in the X-ray pattern from resting muscle (Fig. 1c, 'ML1'). When the muscle contracts the motors leave the helical tracks and bind to actin (Fig. 1b; purple motors), producing a brighter reflection on the vertical axis of the pattern (Fig. 1d, 'M3').

These characteristic X-ray reflections were used to determine how the strength and speed of the muscle response to a single electrical stimulus from the brain is controlled. It was known that this force response - called a twitch (Fig. 2a; blue) - is much smaller than the maximum force the muscle can produce when activated repetitively by a train of stimuli, called a tetanus (Fig 2a; navy). However, it was also known that the calcium transient in a twitch is large enough to saturate all the regulatory sites to which it binds in the actin filaments. This suggests that the size and speed of the twitch might be limited by the fraction of myosin motors that leave the helical tracks. To test that idea, X-ray patterns like those in Fig. 1c,d were recorded every five milliseconds during twitch and tetanic contractions using a Pilatus 2M detector at the I22 beamline[1]. The brightness of the ML1 reflection, shown in Fig. 2b as its amplitude (AML1), which is proportional to the fraction of myosin motors in the helical array (yellow motors in Fig. 1a), decreased rapidly at the start of contraction, in both a twitch (blue) and a tetanus (navy). However, the decrease in the twitch was rapidly reversed, so that it never became as large as in a tetanus.

These results, supported by similar analyses of the changes in other parts of the diffraction patterns, were used to create a structural model of the movements of the myosin motors during a twitch and a tetanus (Fig. 3). In resting muscle (Fig. 3, lower panel 1) nearly all the myosin motors are locked into helical tracks, and both filaments can be considered to be switched off, coded in the diagram as a white filament backbone. At the peak response to a tetanus (Fig. 3, navy), both the actin and myosin filaments are maximally switched on, coded by the red and green filament backbones respectively (panel 3), although some motors remain in the helical tracks. At the peak of the twitch (blue, panel 2), the actin filament is fully on (red), but the myosin filament is only partly activated (light green); a large fraction of the myosin motors stay in their helical tracks. Thus, the strength of muscle in its unitary response to electrical stimulation- the twitch- is limited by the fraction of myosin motors that are activated. The speed of force development is limited by the rate of motors binding to the actin filaments rather than by the speed of actin filament activation, and the speed of relaxation is determined by the rate of detachment of the motors, which is again much slower than the inactivation of the actin filaments.

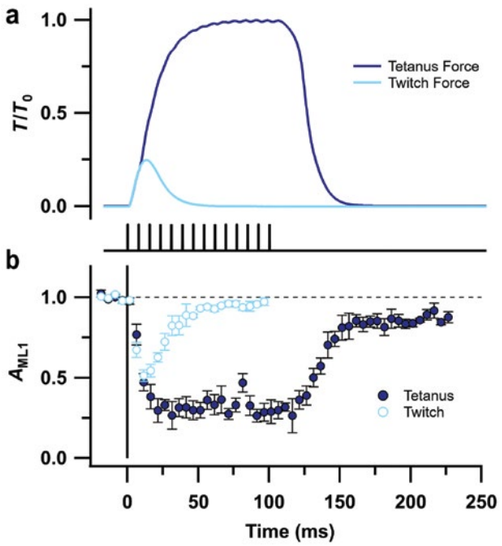

*Figure 2: (**a**) Time-course of isometric force production relative to maximal tetanic force (T/T_0) for two stimulation protocols (black trace) in response to a single stimulus (twitch; blue) or a 100ms train of electrical stimuli (tetanus; navy); (**b**) Time-course of the amplitude of the ML1 reflection (A_{ML1}) normalised to the mean resting value for the twitch (open, blue) and tetanus (filled, navy). Mean ± SEM for n=5 muscles for tetanus and n=4 muscles for twitch.*

These results challenge the previous focus on the actin filaments and the calcium transient as targets for therapeutic intervention in muscle weakness and heart disease, suggesting that the myosin filament may be a more functionally relevant target. The I22 beamline with a Pilatus 2M detector is ideally suited to build on these results to exploit that therapeutic strategy. The next steps in the programme would be to investigate the structural mechanisms of myosin filament activation and relaxation, of the adaptation of the myosin motors to the variable external loads that muscles experience in the body, and of the enhanced response of muscles that have been recently stimulated, called post-tetanic potentiation.

References:

1. Hill, C. *et al.* Myosin-based regulation of twitch and tetanic contractions in mammalian skeletal muscle. *ELife*, **10** (2021). DOI: 10.7554/eLife.68211

Funding acknowledgement:
Diamond Light Source beamtime at I22 was granted on project SM21316-1. This work was funded by the Medical Research Council MR/R01700X/1 and Diamond Light Source. EB and JGO were supported by a British Heart Foundation Intermediate Basic Science Research Fellowship awarded to EB (FS/17/3/32604). LF was funded by a Sir Henry Dale Fellowship awarded by the Wellcome Trust and the Royal Society (210464/Z/18/Z). The funders had no role in study design, data collection and interpretation, or the decision to submit the work for publication.

Corresponding author:
Dr Cameron Hill, King's College London, cameron.hill@kcl.ac.uk

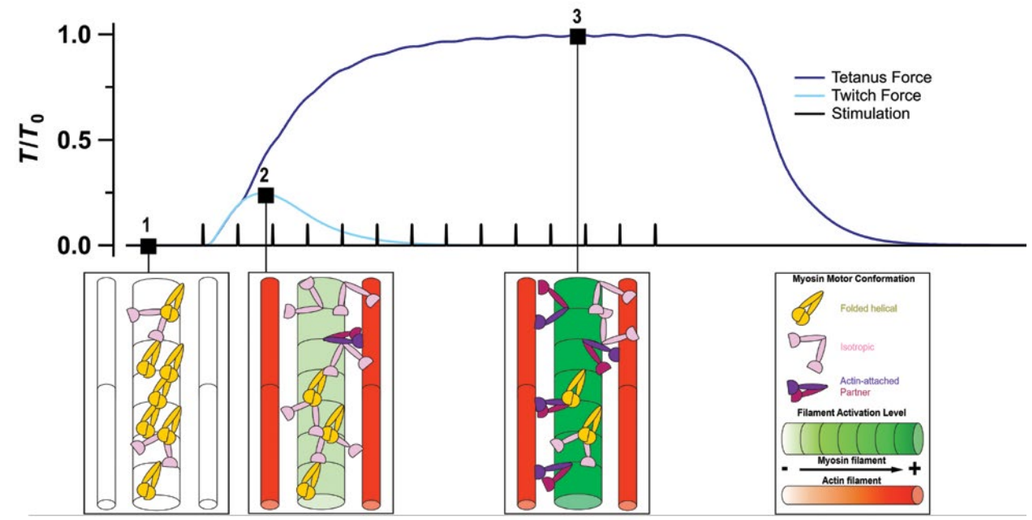

Figure 3: Motor conformations and activation level of the myosin (green cylinder) and actin (red cylinder) filaments for the twitch (blue) and tetanus (navy); Panel 1, rest; panel 2, peak twitch force; panel 3, peak tetanus force. The darker the colour of the filament, the higher its activation level.

Integrated Facilities and Collaborations

As a world-leading centre for synchrotron science and a cornerstone of a world-class site for scientific discovery and innovation at Harwell, Diamond Light Source has powerful synergies with its neighbouring research institutes and beyond the campus, through collaborations and shared visions. The integrated facilities at Diamond present academic and industrial users with a one-stop-shop for research opportunities, enabling them to combine cutting-edge techniques and capabilities to advance their studies. Diamond participated in 20 grants in the fiscal year 2021 – 2022, and Diamond researchers show a greater interest in collaborative grants. You will find in this section some highlighted collaborations.

Integrated Facilities

The Membrane Protein Laboratory (MPL)

The Membrane Protein Laboratory (MPL), led by Dr Andrew Quigley at Diamond Light Source, has been awarded £1.5m of Wellcome funding to support the laboratory's research for a further five years. The MPL is one of Diamond's integrated user facilities and is located within the Research Complex at Harwell. Its focus is understanding the structure of membrane proteins through the delivery of high-quality samples to Diamond's beamlines and microscopes. This new funding from Wellcome, a shareholder of Diamond, will enable wider sample support to further Diamond beamlines and microscopes and form a foundation for integrative membrane protein structural biology.

Membrane proteins are found at the junctions between the outside world and the inner workings of the cell. Multicellular organisms such as humans use membrane proteins for communication, to acquire nutrients and detect threats. Membrane proteins are important targets for biomedicine, with over half of all medicines altering membrane protein function. Understanding the structure and function of these proteins in isolation as well as within the wider cellular context will help us to develop new therapeutics to tackle disease.

Visiting scientists to the MPL can spend anywhere between a day and a year in its labs, supported by state-of -the art equipment and its experienced support scientists. Recently published work in *Nature Communications*[1] details the molecular basis of regulation of bacterial capsule assembly by Wzc. Wzc is the regulator behind the formation of extracellular polysaccharides that help bacteria to evade the human immune response. The authors show that dephosphorylation of Wzc leads to the assembly of an octomer. This is the molecular switch that enable Wzc to cycle through on and off states controlling the passage of lipid linked polysaccharides.

In other work, MPL scientists have collaborated with researchers from Protein Production UK (PPUK) at the Rosalind Franklin Institute supporting a systematic study looking at the small-scale transient expression of Eukaryotic membrane proteins in Expi293F cells[2]. Small-scale screening allows the rapid optimisation of samples that can be used for cryo-electron microscopy and crystallisation. Detailed protocols were published in *Methods in Molecular Biology*.

1. Yang, Y., Liu, J., Clarke, B.R. *et al.* The molecular basis of regulation of bacterial capsule assembly by Wzc. *Nat Commun* **12,** 4349 (2021). https://doi.org/10.1038/s41467-021-24652-1
2. Krasnoselska GO, Dumoux M, Gamage N *et al*. Transient Transfection and Expression of Eukaryotic Membrane Proteins in Expi293F Cells and Their Screening on a Small Scale: Application for Structural Studies. Methods Mol Biol. 2021;2305:105-128. doi: 10.1007/978-1-0716-1406-8_5.

XChem

Alongside the full return of the XChem user programme, including welcoming our users back on-site, the XChem team has continued to support the COVID Moonshot, a global open science, structure enabled drug discovery campaign targeting the SARS-CoV2 main protease. By leveraging crowdsourced medicinal chemistry design, high throughput structural biology, machine learning and exascale molecular simulations, the collaboration discovered a novel chemical scaffold and developed it into orally bioavailable inhibitors with clinical potential within two years. These inhibitors are currently being evaluated in pre-clinical studies funded by an £8 million award from Wellcome on behalf of the COVID-19 Therapeutics Accelerator (https://www.diamond.ac.uk/Home/News/LatestNews/2021/27-09-21.html). All compound designs, structural data, assay data and synthesised molecules have been shared rapidly and openly, creating a rich, intellectual property free knowledge base that can be exploited by the wider scientific community.

MPL Laboratory in RCaH.

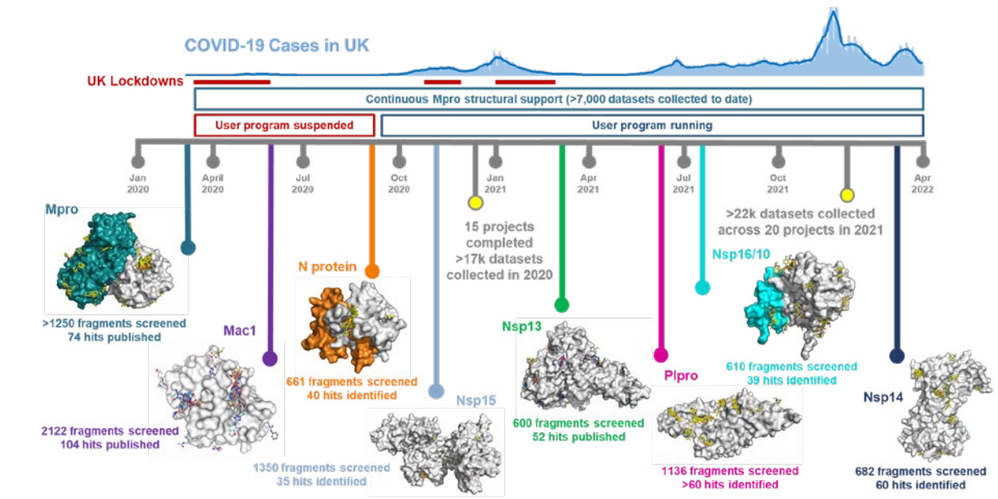

XChem campaigns on SARS-CoV-2 targets.

To enable increased throughput of XChem to both meet user demand for ultra-high-throughput fragment screening and to exploit new experimental modalities, such as screening membrane proteins and producing data to drive machine learning and artificial intelligence approaches, it has been proposed as part of the Diamond-II project to build a new beamline capable of underpinning the next revolution in rational drug discovery over the coming decade. This new beamline, K04, will be a flagship project of Diamond-II with building taking place in the run up to the Diamond dark period, minimising the downtime of a key UK infrastructure.

Highlighted publications:

- The COVID Moonshot Consortium. Open science discovery of oral non-covalent SARS-CoV-2 main protease inhibitor therapeutics. *bioRxiv*, (2021) DOI: 10.1101/2020.10.29.339317
- Singh, A. K. *et al.* Sliding of HIV-1 reverse transcriptase over DNA creates a transient P pocket - targeting P-pocket by fragment screening. *Nat Commun*. **8**, (2021). DOI: 10.1038/s41467-021-27409-y
- Piticchio, S. G. *et al*. Discovery of novel BRD4 ligand scaffolds by automated navigation of the fragment chemical space. *J. Med. Chem*. **64**, 17887–17900 (2021). DOI: 10.1021/acs.jmedchem.1c01108
- Bajusz, D. *et al.* Exploring protein hotspots by optimized fragment pharmacophores, *Nat Commun.* **12**, 3201 (2021). DOI: 10.1038/s41467-021-23443-y
- Mahy, W. *et al*. 5-Phenyl-1,3,4-oxadiazol-2(3H)-ones are potent inhibitors of notum carboxylesterase activity identified by the optimization of a crystallographic fragment screening hit. *J. Med. Chem.* **63,** 12942–12956 (2020). DOI: 10.1021/acs.jmedchem.0c01391

XFEL Hub

The X-ray Free Electron Laser (XFEL) Hub at Diamond continues to provide expertise and support to the UK community engaged in serial crystallography and XFEL-related life science research. This ranges from experimental conception to beamtime proposals, through sample preparations and testing, to XFEL data collection, analysis, and publication. Our Diamond-based activities continue to include organising and running the block allocation group "Dynamic Structural Biology at Diamond and XFELs" for serial crystallography and time-resolved studies at various MX beamlines at Diamond.

This fiscal year, members of the Hub participated in 13 XFEL experiments at the LCLS in the USA, PAL-XFEL in Korea, or the European XFEL in Germany, mostly by remote access and with reduced scientific scope. Two XFEL experiments at PAL-XFEL were cancelled due to the pandemic. In March 2022, several members of the XFEL Hub travelled to the LCLS to participate on-site in experiments in time-resolved Serial Femtosecond Crystallography (tr-SFX) correlated with X-ray Emission Spectroscopy (tr-XES).

Highlighting the synergistic overlap and technology transfer between XFEL and synchrotron facilities, the XFEL Hub continued two major projects at Diamond that will establish methods for time-resolved serial crystallography studies using on-demand sample delivery and reaction initiation strategies that can be correlated with tr-XES too. The plans also include a deeper collaboration with one or more XFEL facilities, including SwissFEL, which may also host the sample delivery capabilities developed at Diamond. The Hub has been testing prototypes for sample delivery and XES data collection with von Hamos geometry at Diamond beamline VMXi. Orders have been placed for analyser crystals to enable XES from copper- and/or iron-dependent metalloenzymes. Commissioning activities for these two projects are anticipated later in the year and further.

Highlighted publications:

- Rabe, P. *et al*. X-ray free-electron laser studies reveal correlated motion during isopenicillin N synthase catalysis, *Science Advances* **7**, (2021). DOI: 10.1126/sciadv.abh0250
- Butryn, A. *et al.* An on-demand, drop-on-drop method for studying enzyme catalysis by serial crystallography, *Nature Communications* **12**, 4461 (2021). DOI: 10.1038/s41467-021-24757-7

Collaborations

The Rosalind Franklin Institute

The Diamond-Franklin collaboration in electron imaging and diffraction methods is moving from strength to strength. This past year has seen the delivery of the Franklin's first Titan Krios microscope, *Dorothy*, and the second-generation plasma focused ion beam (pFIB), called *Franklin* to enable large volume cellular tomography using novel sample geometries as part of a close collaboration with Thermo Fisher Scientific. The developments are funded by Wellcome through the Electrifying Life Science grant that also funds the development of the HeXI dedicated electron diffraction beamline. The Dorothy microscope was delivered in July 2021, commissioned by Diamond and Franklin staff throughout the

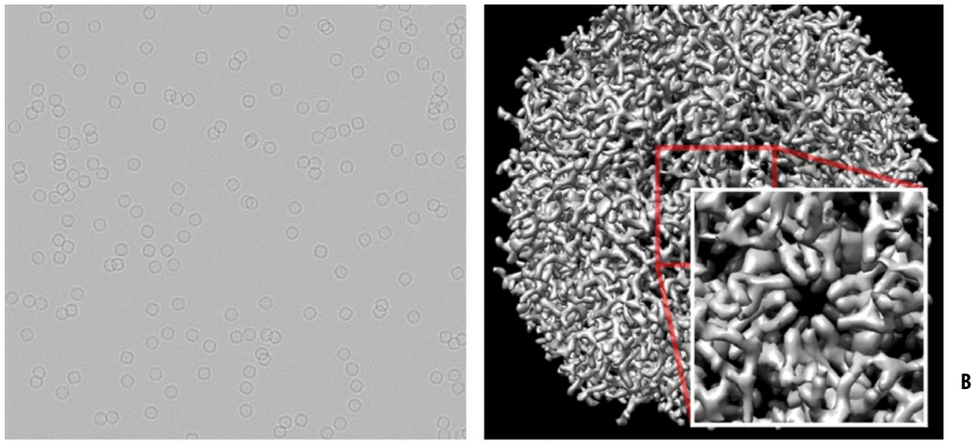

Figure 1 (a) Digital twin of large planar lamella containing apoferritin particles. (b) Reconstruction of single apoferritin molecule from +/- 90 degree tilt series.

summer and is now fully operational in the Rosalind Franklin Institute Hub building offering state of the art capability to Franklin and Diamond scientists.

Another key aspect of this collaboration is the development of the Parakeet software suite[1] that can create a comprehensive digital twin of an electron microscope, a biological sample, and a detector to perform a simulated cryo-electron tomography experiment. The simulated data can be analysed in the same way as *real* tomography data (see Figure 1) and allows scientists to study the relative benefits of critical decisions in sample preparation, data collection strategy and even the hardware choices in the construction of a microscope.

Highlighted publication

1. Parkhurst, J. M. *et al.* Parakeet: a digital twin software pipeline to assess the impact of experimental parameters on tomographic reconstructions for cryo-electron tomography. *Open Biology* **11**, (2021). DO: 10.1098/rsob.210160

Research Complex at Harwell (RCaH)

The Research Complex at Harwell (RCaH) is a joint venture between Diamond Light Source and the UK research councils, now UKRI, and provides a research hub on the Harwell campus for the physical and life sciences. It currently hosts more than 180 researchers from universities across the UK working in a mix of wet and dry laboratory space supported by research grants. In addition, there is a mix of research facilities or consortia based at RCaH *e.g.* Diamond's Membrane Protein laboratory (MPL, funded by Wellcome), the Central Laser Facility (CLF), CCP4 and CCP-EM. This rich environment of research facility hubs welcomes around 500 scientific visitors and users yearly.

The platform underwent a major upgrade at the start of 2022 thanks to a successful bid to the Medical Research Council (MRC) to enhance and extend the capabilities of the facility. This includes a new imaging hotel equipped with Ultra-Violet and multi-fluorescence imaging that facilitates detection of protein crystals, robotics for optimisation of crystallisation hits (the Formulatrix formulator®) and a Mosquito® Lipidic Cubic Phase (LCP) for automated crystallisation of soluble and membrane proteins. The Membrane Protein Laboratory has been successfully re-funded by Wellcome for a further five years and the first membrane protein structure determined using cryo-EM supported by access to the MPL was published by the Naismith group[1]. On the cryo-EM front, RCaH again with support from the MRC and in partnership with Diamond, have installed a ThermoFisher scientific Glacios™ 200 kV cryo-transmission electron microscope equipped with a falcon IV detector. The microscope has been installed at eBIC and provides Harwell groups with a state-of-the-art cryo-TEM for structural projects. This is complemented by dedicated facilities for cryo-EM sample preparation including the use of micropatterning to facilitate precise positioning of cells for cryo-electron tomography. Time-resolved structural biology is conducted at all five XFELs around the world, as well as at Diamond microfocus beamlines. These efforts include scientists from universities, industry, Diamond, and the XFEL Hub. A variety of strategies are available to initiate enzyme reactions within microcrystal slurries, and some of these include the use of anaerobic chambers in the Orville and Carr groups.

The massive push to SARS-CoV-2 research aided by the Research Complex remaining open during the pandemic has led to further work on the SARS-CoV-2 proteases (Walsh) and the use of nanobodies directed against the SARS-CoV-2 spike protein (Naismith, Owens). The XFEL Hub (Orville) has helped with probing protease catalysis through a series of on-going time-resolved experiments at various XFEL sources around the globe. Finally, the XChem facility (Von Delft) continues to apply fragment-based approaches to SARS-COV-2 targets, having screened well in excess of 22,000 crystals across eight different targets at the close of 2021, following on from the success of the COVID Moonshot project which remains on track to commence preclinical trials for an orally available antiviral targeting the main protease of SARS-CoV-2. The latter initiative sprang from the very substantial fragment campaign that was rapidly executed at Diamond and the Research Complex at the start of the pandemic in 2020.

Highlighted publication

1. Yang, Y. *et al.* The molecular basis of regulation of bacterial capsule assembly by Wzc. *Nat Commun* **12,** 4349 (2021). https://doi.org/10.1038/s41467-021-24652-1

Catalysis Hub

Since 2013 the UK Catalysis Hub has had a Block Allocation Group for X-ray Absorption Spectroscopy (XAS) at the XAS beamline (B18). The BAG aims to increase the user base within the catalysis community and is designed to encourage new users with a dedicated team at Harwell who will work with them to develop proposals and to guide and train users in the analysis of data. Through the operation of the XAS BAG, XAS has become one of the most important analytical tools available at Diamond for catalysis research. The frequent and rapid access to beamtime enables measurements to be completed on a short timescale, which is especially useful when completing publications. Over 80 publications have directly resulted from the B18 BAG with recent highlights including the study of aqueous phase reforming (APR) of glycerol which is an important reaction utilising renewable feedstocks such as biomass for the renewable production of hydrogen. These technologies are increasingly important in the move to net-zero CO_2. Studies have included catalysis including Pt-Sn nanoparticles allowing deeper understanding of the Pt environment in active catalysts crucial to designing more active catalysts with improved lifetimes. Perovskite structured catalysts were also investigated for these reactions and it was discovered Pt/$LaAlO_3$ and Pt/$LaNiO_3$ showed higher stability and activity than other metals. XAS investigations helped show this is due to Pt redistribution and Pt/Ni alloy formation. Based on the results, intentionally prepared Pt/$LaCO_3OH$ catalysts were found to be active and stable in the APR reaction and the stability of materials warrants further study.

The XAS BAG is managed by the UK Catalysis Hub, supported by Diamond staff, and is open to every academic working in catalysis in the UK. Time is awarded based on scientific merit and feasibility and with particular emphasis on proof-of-concept studies and exploration of new areas of catalysis science. Recently, the UK Catalysis Hub has been awarded a further BAG, this is for X-ray Pair Distribution function analysis (XPDF) at I15-1. This total scattering technique is complementary to XAS and provides both *ex situ* and *in situ* data with recently completed studies including studies of singly supported Pd atoms on MOFS and an *in situ* study of the formation of ruthenium nanoparticles on a silica substrate. As with the BAG for B18, the new XPDF BAG aims to introduce new users to XPDF and to develop a broad user base from within the UK Catalysis community.

Active Materials Laboratory

In late 2019 Diamond was awarded a grant by the Engineering and Physical Sciences Research Council (EPSRC) under the second National Nuclear User Facility scheme (NNUF II) to build a laboratory on-site to enable users to handle active samples while doing experiments at the synchrotron. The building construction finished in July 2021 and all the equipment for users has now been procured.

The Active Materials Laboratory (AML) consists of four main rooms. There are two laboratories for experimental use. The wet lab has a recirculating fume cupboard, centrifuge, anaerobic Coy chamber, a small oven and high precision balances. The dry lab has two anaerobic glove boxes – one with an optical microscope and front face partially made of lead glass, the other will tolerate solvents -, a vented fume hood, a 1,200 °C tube furnace; an optical microscope; pellet press and high precision balance. Portable beamline equipment just as UV and IR spectrometers can be imported into the AML if a user has need for them.

The AML has a characterisation room with a gamma spectrometer and a liquid scintillation counter and there is also a storage room, with safes, fridges and a freezer for samples to be stored when not in use in the labs or beamline. The lab is open for use in normal working hours on weekdays, though samples in the storage room can be accessed at any time. Access is designed principally for those with beamtime at Diamond, but can also be obtained without beamtime through the offline facilities scheme. Access is free for non-proprietary research via either route, but currently extra support funding is available through the NNUF II scheme.

The University of Manchester at Harwell

The University of Manchester at Harwell (UoMaH) is hosted by Diamond as part of the partnership. UoMaH provides the interface with the Harwell national facilities, enabling UoM researchers to access world-class research at Diamond and all the Science and Technology Facilities Council (STFC) facilities at Harwell, including the ISIS Neutron and Muon Source (ISIS), Scientific Computing Department (SCD) and the Central Laser Facility (CLF). UoMaH is comprised of core administrative and technical teams and research fellows and their groups.

The core technical team specialises in developing sample environments and equipment in support of experiments, involving high risk materials and extreme sample environments, fielded at the national facilities. In early 2021 UoMaH expanded its core team capabilities with the recruitment of a Data Analysis manager. UoMaH plans to grow its data analysis group in the coming years. The group's purpose will be to work with National Facilities to facilitate users' data reconstruction and analysis, with the aim to reduce the time it takes for users to publish their findings.

UoMaH research fellows are affiliated with different departments within the University's Faculty of Science and Engineering and pursue research in critical themes to both the University and the facilities. Currently, UoMaH has a growing contingent of fellows based at Harwell; two fellows working on resilience and catalysis are sponsored by Diamond, one fellow working on fusion is sponsored by ISIS, one fellow working on data science is sponsored by STFC/SCD and one "extreme science" fellow, currently in the recruitment stage will be sponsored by US office of Scientific research. Alongside them, six further fellows and their groups are based in Manchester. The fellows strengthen the University's link with Harwell by bringing their research, networks and new users from industry and faculty academics to Diamond.

In May 2021, UoMaH partnered with Diamond, CLF, UCL, the Health and Safety Executive (HSE) and the UK Health Security Agency (UKHSA) to support the National Core COVID-19 PROTECT Transmission and Environment Study. The research project was funded for a second year in April 2022; with the research in this last year focusing on using X-ray and laser imaging techniques to image the COVID-19 Alpha and Kappa variant. UoMaH is also being funded to programme manage, for HSE, the COVID-19 PROTECT Transmission and Environment Study during the study's final year and transition to UKRI.

InFUSE Prosperity Partnership

Climate Change is the single biggest threat to present and future generations. To meet the ambitious targets for net-zero CO_2 set out by the UK government, and in line with the Paris Climate Agreement, requires technological mobilisation on an unprecedented scale – with action required in both rapid development and deployment of new approaches. A paradigm shift in the UK's research and development capabilities is needed to reduce time to market for novel and sustainable solutions for energy production and consumption. Successful rapid translation requires deep and coherent interactions between academia and industry, along with a shared vision and commitment.

Across the range of proposed technological strategies for CO_2reduction - either at source or via post-combustion mitigation - limitations in efficiency, stability or lifetime are associated with the role of key solid-fluid interfaces in the systems, and their evolution in the operating environments. By developing a better understanding of interfaces, researchers will be better able to design new materials, devices, and optimised processes that have reduced energy demand or longer productive lifetimes.

This five-year EPSRC funded Prosperity Partnership between Imperial College London, Diamond and Shell, known as InFUSE, will examine how technologies like batteries, lubricants, chemical production, and carbon capture and storage (CCS) can be improved by understanding interfaces in these systems, enhancing sustainability and enabling a transition to a green economy. The partnership aims to increase our fundamental understanding of interface behaviours through a cross-cutting approach studying morphology, structure and chemistry from the atomic to the macroscale, and their dynamic evolution under a range of extreme operational parameters.

InFUSE will prioritise engaging with diverse groups of the next generation of thinkers who will pave the way for a greener, more sustainable world. The programme will fund more than 20 new PhD studentships creating interdisciplinary cohorts working together towards the energy transition. At Diamond, three PDRA positions will help bridge the activities of this cohort with Diamond and drive exciting developments in sample environments correlative workflows and data analysis methods across the Spectroscopy, Imaging and Structures and Surfaces groups.

Machine Operation and Development

Richard Walker, Technical Director

2021/22 was our 15th year of operation, and like the previous year, continued to be influenced by the ongoing pandemic. The first Run of the period continued the restricted schedule of the previous year, with User Mode running from 09:00 Tuesday to 09:00 Saturday, with start-up/Machine Development on Mondays. However in mid-June, we resumed standard 6-day running, from 09:00 Wednesday to 09:00 Tuesday interspersed with Machine Development days.

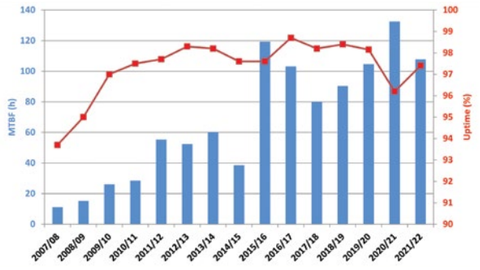

Figure 1. Mean Time Between Failures (MTBF) and Uptime by operating year.

A total of 189 days (4532 hours) were scheduled for User Mode operation, including 5 beamline start-up days. All operation was in standard multibunch mode (900 bunch train) with total current of 300 mA, there was no "hybrid" or "low-alpha" operation.

The annual operating statistics are shown in Figure 1. The overall MTBF continued to be good at almost 108 hrs, and each of the five operating Runs achieved a MTBF in excess of 72 hrs, which is the target minimum. However, the 97.4% uptime was disappointingly below the target of 98%. We suffered from a few extended downtimes, two events associated with the cryo-plant accounted for 42% of the total downtime, while three further issues in other parts of the RF system contributed 23%, and a couple of power distribution events contributed 8%. Three-quarters of all beam trips were recovered in under 2 hrs, but with the above longer outages the overall Mean Time To Repair (MTTR) was 2.5 hours.

Radiofrequency Developments

Significant progress has been made with the RF upgrade programme which is aimed at increasing the resilience of machine operation. A 60 kW solid state amplifier has been installed and commissioned and will be used to power the already installed second booster RF cavity. The third normal conducting HOM-damped cavity was installed in the storage ring in March 2022. This will be powered by a new 120 kW solid state amplifier. Owing to travel restrictions, the Factory Acceptance Test of the amplifier which took place in December 2021 was witnessed via video link (Figure 2, left). As shown, full power operation was demonstrated even with 18 power transistors disconnected. The amplifier has now been installed at Diamond (Figure 2, right) and awaits the Site Acceptance Test.

Insertion Device Developments

Cryogenic permanent magnet undulators (CPMUs) provide an increase in photon flux for beamlines, especially in the hard X-ray region, by providing more magnetic field for a given operating gap using the enhanced performance of new permanent magnet materials at temperatures down to 77K (-196°C). Since the first Diamond designed and built device, CPMU-1, was installed for beamline I24 (ID24) in March 2020, three further CPMUs have been completed, and a fifth is under construction. CPMU-2 was installed as ID03 (see Figure 3), while CPMU-3 has replaced CPMU-1 as ID24, due to some unexpected problems with that device. CPMU-4 will shortly be installed as ID04 and CPMU-1, following repair, will be re-deployed as ID11 later this year.

Figure 4 shows the improved X-ray flux from CPMU-2 compared to the previous insertion device for beamline I03, especially at higher photon energies.

Diamond-II Update

Significant progress has been made with the design of the Diamond-II machine upgrade in the last year during the TDR (Technical Design Report) phase, which is now nearing completion. The TDR was successfully reviewed at the beginning of March 2022 by the Diamond-II Machine Advisory Committee and is currently undergoing final editing.

Several key decisions have been made in the last year:

- the injection scheme will be a conventional 4-kicker + "thick/thin" septum for commissioning, refilling the machine and as a backup, while single bunch aperture sharing will be used during user operation for improved transparency of injection.

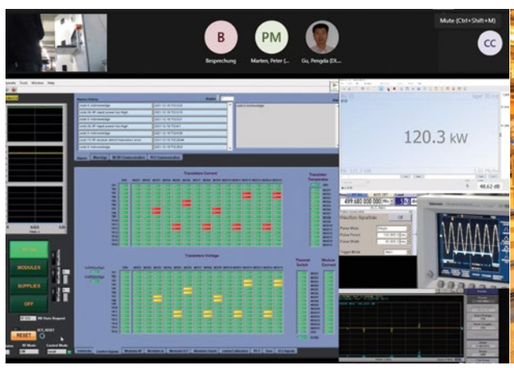

Figure 2. left - 120 kW solid state amplifier Site Acceptance Test witnessed via video link, right – amplifier installed at Diamond.

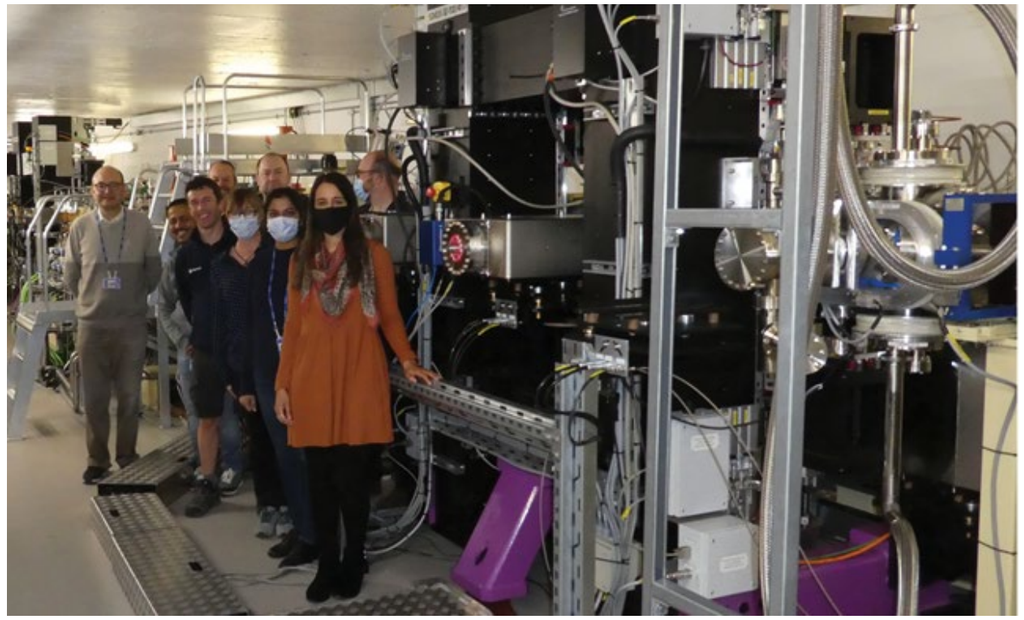

Figure 3. Insertion Device Group and CPMU-2 installed as ID03.

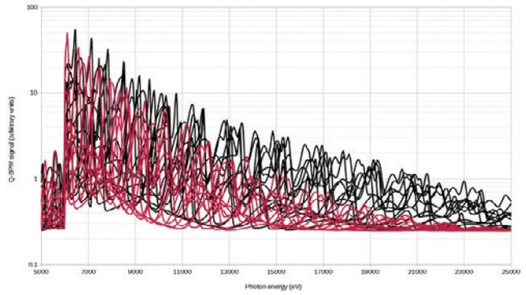

Figure 4 . Photon intensity measured on the I03 beamline with CPMU-2 (black curves) and with the previous insertion device (red lines).

- the standard fill pattern will consist of 5 bunch trains with 5 gaps of 7 buckets.
- the 3rd harmonic cavity will be a passive superconducting "Super3HC"-type cavity.
- the girders will be motorised under local control.
- the linac energy will be increased from 100 MeV to 150 MeV, using 3 new shorter accelerating sections, tuned to the new storage ring and booster RF frequency.

Prototyping of some of the key components for Diamond-II is underway. A prototype gradient dipole magnet has been built and is undergoing magnetic measurements (Figure 5). A full-scale prototype girder has been delivered and vacuum vessels for a complete girder vessel string have been ordered.

Figure 5. Prototype gradient bending magnet undergoing magnetic measurement using a stretched wire bench.

X-ray Technologies at Diamond

It is self-evident that in order for our instruments to produce world-leading science, we need to have world-class optics, detectors and computing technologies at our fingertips; technological advances never stop but are continually evolving. This section describes the support and advances in the Optics and Metrology Group, Detector Group and Scientific Software Controls and Computation department at Diamond Light Source. Advances which are supporting and enhancing our capabilities today are described, but also developments that will keep us competitive over the next few years. These groups are very active in calculations and specifications for beamlines and instruments being put forward and planned for Diamond-II, an integrated upgrade of the synchrotron, beamlines and computational facilities. The pandemic may have slowed some developments and made it harder to work physically alongside our colleagues, but it has also opened opportunities for remote operation for staff, users and collaborators. These advances continue to keep us competitive worldwide, and Diamond is proud to be at the forefront of many of these technologies.

Optics and Metrology Group

Kawal Sawhney, Optics and Metrology Group Leader

The Optics & Metrology (O&M) group continues to provide expert operational support to all beamlines of Diamond Light Source and is actively involved in designing upgraded and new flagship beamlines for Diamond-II. An extensive research and development programme within the O&M group is underway to investigate the optical challenges posed by Diamond-II. This now includes establishing in-house X-ray optic fabrication facilities. The Optics Fabrication Building (OFB) is under construction and will house Diamond's Multilayer Fabrication Facility, the only one in the UK. Development of metrology hardware is also progressing to enable measurement of the enhanced-quality X-ray mirrors needed for Diamond-II. The new technique of laser Speckle Angular Measurement (SAM), developed by our group, enables slope errors of X-ray mirrors to be characterised in two dimensions with nanoradian resolution. Laser interferometry in collaboration with the National Physical Laboratory (NPL) has measured 0.5 nrad angular steps of Diamond's Nano-Angle Generator. The synergy of fabrication and state-of-the-art metrology will stimulate optical developments at Diamond which cannot be made elsewhere in the UK.

Over the next few years, Diamond will join other synchrotrons around the world in upgrading its storage ring. The Diamond-II project will yield brighter X-ray beams but will also require substantial changes to the layout of many beamlines. The Optics & Metrology Group continues to provide optical designs and calculate power loads for current beamlines and the three new flagship beamlines: SWIFT (spectroscopy), K04 (XChem fragment screening project), and CSXID (Coherent Soft X-ray Imaging and Diffraction). The Optical Metrology Laboratory (OML) will be moved to a new site to accommodate CSXID at straight 17. Theoretical modelling tools have been developed to predict the temperature distribution and surface distortion under X-ray beam of cryo-cooled monochromator crystals. Other theoretical developments include: a new type of Ptychography that can determine the aberrations of an optical component using a partially coherent X-ray beam[1]; and demonstration of a new imaging technique that records phase variation in all directions simultaneously[2].

Multilayer optics fabrication facility

Diamond has until now depended on commercial vendors to provide X-ray optics. However, many types of optics are manufactured by only a few suppliers, in some cases only a single vendor, making Diamond vulnerable to supply disruptions and limiting the flexibility to order bespoke optics for highly specialised applications. In-house manufacturing capabilities will help Diamond to meet these challenges, and to manufacture niche optics that are not commercially available. This will become increasingly important as Diamond-II progresses. Finally, the fabrication facilities will enable a new generation of young scientists and engineers to be trained in the UK. In October 2021, construction began on the new Optics Fabrication Building (OFB) outside Zone 4 (Fig. 1). It will house Diamond's new Multilayer Fabrication Facility, the first of its kind in the UK. This new facility will deposit highly uniform multilayers on substrates up to 1000 mm long. Multilayer optics have already proven their worth at several Diamond beamlines by acting as monochromators capable of providing two orders of magnitude more flux than traditional double-crystal monochromators, whilst maintaining energy resolution of ~ 1%. They have enabled focusing of X-rays up to 76 keV at I15-1, where standard mirrors struggle to reflect X-ray efficiently above 25 keV. Further applications of multilayer optics are expected in macromolecular crystallography, nano-tomography and fluorescence microscopy. Completion of the OFB is scheduled for August 2022, after which the Multilayer Fabrication Facility will be installed, commissioned and optimised by summer 2024.

Figure 1: Artist's conception of Diamond's Optics Fabrication Building.

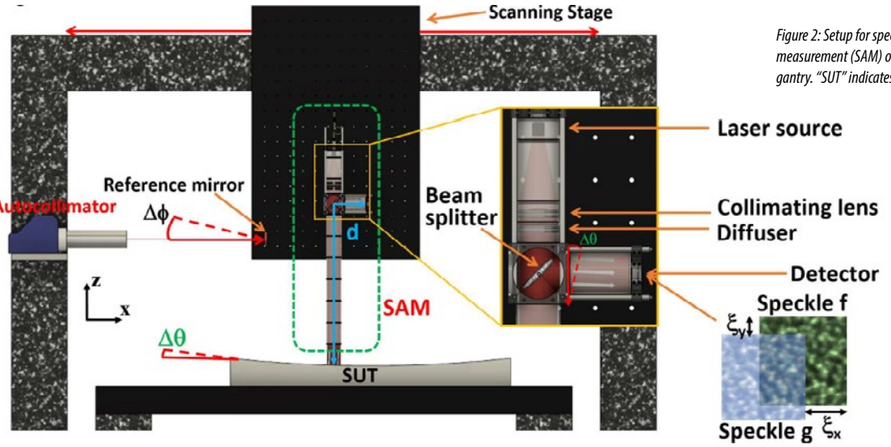

Figure 2: Setup for speckle angular measurement (SAM) on the Diamond-NOM gantry. "SUT" indicates the surface under test.

Nano-precision mirror metrology

Upcoming diffraction-limited storage rings like Diamond-II are already creating demand for X-ray mirrors shaped to an even higher accuracy than achieved by today's most advanced manufacturing techniques. Meeting this demand will require metrology instruments of increased speed and precision, which ideally are cost effective and do not compete with user experiments for X-ray access to beamlines. In the OML, a novel Speckle Angular Measurement (SAM) instrument for measuring a mirror's figure has been installed on the Diamond-NOM gantry (Fig. 2)[3]. A laser beam collimated by a lens is scattered by a diffuser, which introduces a two-dimensional speckle pattern. Variations of the sagittal and tangential slope, at each position on the mirror illuminated by the laser, will shift the speckle pattern as recorded by the camera. Precise tracking of the speckle displacements as the laser is scanned along the mirror's surface yields a two-dimensional map of the mirror's slope. An advanced sub-pixel algorithm enables slope measurements on the nanoradian level. The SAM technique thus adds two-dimensional capabilities to a one-dimensional slope profiler at low cost and in little space. Results are in good agreement with the OML's Fizeau interferometer. The SAM instrument can also measure strongly curved surfaces (radius < 0.5 m) beyond the curvature range of the Diamond-NOM. Not only synchrotrons and XFELs, but also astronomical telescopes, can benefit from this technique.

Partnering with NPL to inspect nano-positioning motion stages

Accurate nano-positioning of samples and X-ray optics will become increasingly important for Diamond's beamlines. Yet without careful calibration and correction, many commercial nano-positioning devices do not meet beamlines requirements. Common problems include vibrations, parasitic motions, temperature drifts, control issues and misalignment between the components of composite stacks of motion stages. Successful commissioning of nano-positioning systems requires a calibrating stage that makes accurate, reproducible motions on the nanoradian level, and instruments capable of measuring these extremely small motions. Thanks to a collaboration with the National Physical Laboratory (NPL), both components are now in operation in Diamond's Precision Metrology Laboratory (PML), which characterises motion stages for Diamond's beamlines. Diamond previously developed the Nano-Angle Generator (NANGO), a flexure-based, piezo-actuated stage capable of precise angular motions from milliradians down to nanoradians. NANGO is used to calibrate metrology instruments by rotating a reference optic through known angles. NPL contributed a dual-beam laser interferometer with a 200 kHz acquisition rate. This is far above the 25 Hz acquisition rate of a digital autocollimator and makes dynamic behaviour observable. The interferometer is composed of a rotatable part, which is mounted on the NANGO rotary stage, and a fixed part. The NPL interferometer has demonstrated that NANGO can make distinct steps of 500 picoradians, sinusoidal oscillations at 0.4 Hz with an amplitude down to 125 picoradians, or 1 nanoradian oscillations at 40 Hz. Plans are being made to construct a three- or four-beam version of the NPL interferometer for simultaneous measurement of orthogonal angles and translations. The combination of Diamond's NANGO and the NPL's interferometer has produced a state-of-the-art system at the forefront of nanometrology for the synchrotron and XFEL community.

References:

1. Moxham, T. E. J. *et al.* Aberration characterization of x-ray optics using multi-modal Ptychography and a partially coherent source. *Appl. Phys. Lett.* **118,** 104104 (2021). DOI: 10.1063/5.0041341
2. Wang, H. *et al.* Hard X-ray omnidirectional differential phase and dark-field imaging. *PNAS* **118**, e2022319118 (2021). DOI: 10.1073/pnas.2022319118
3. Wang, H. *et al.* Nano-precision metrology of X-ray mirrors with laser speckle angular measurement. *Light: Science & Applications* **10,** 195 (2021). DOI: 10.1038/s41377-021-00632-4

Advanced X-ray directional imaging with sandpaper

Related publication: Wang, H., & Sawhney, K. Hard X-ray omnidirectional differential phase and dark-field imaging. *Proceedings of the National Academy of Sciences* **118,** (2021). DOI: 10.1073/pnas.2022319118

Publication keywords: X-ray phase contrast; Dark-field; Material science; X-ray speckle

X-ray Differential Phase Contrast Imaging, which measures the gradient of a sample's phase shift, can reveal more detail in a weakly absorbing sample than conventional absorption contrast. However, normally only the gradient's component in two mutually orthogonal directions for existing methods is measurable.

Diamond Light Source's scientists have developed a simple method to produce omnidirectional differential phase images, which record the gradient of phase shifts in all directions of the imaging plane. Importantly, the omnidirectional dark-field images can be simultaneously extracted to study strongly ordered scattering structures. Existing methods require special optics, such as advanced phase gratings or absorption masks, along with a stringent experimental setup.

Over the last decade, the speckle method has been extensively developed for advanced imaging and high precision metrology at the Test Beamline (B16). B16 offers the flexibility of bespoke and novel setups, which was ideal for the R&D work.

The technique allows the omnidirectional differential phase and dark-field images to be simultaneously extracted from a single data set with the use of a simple modulator. The omnidirectional differential phase and dark-field images resolve the directional dependence of complex microstructures, which is inaccessible to conventional X-ray imaging techniques.

Potentially, the proposed technique could be transferred to laboratory X-ray micro-focus sources for wider application. Using a highly efficient flat panel detector would further reduce the radiation dose. The proposed omni-directional method paves the way for X-ray scattering tensor tomography for the inspection of both biomedical and material science samples.

Over the last two decades, various X-ray directional differential phase contrast and dark-field imaging techniques have been developed for unlocking the hidden secrets of our world and enriching our understanding of it. X-ray Differential Phase Contrast Imaging, which measures the gradient of a sample's phase shift, can reveal more details in a weakly absorbing sample than conventional absorption contrast. In addition, X-ray dark-field images describe the scattering power due to the structural variation and density fluctuation. Therefore, these two techniques can provide complementary information to each other. However, normally only the differential phase contrast and dark field images in two mutually orthogonal directions are measurable[1-3]. As a result, the risk of overlooking structures with strong but varying orientation within the sample is high. Therefore, it will be desirable to generate the omni-directional phase shift changes or dark-field signals to pick up detailed information along all directions[4].

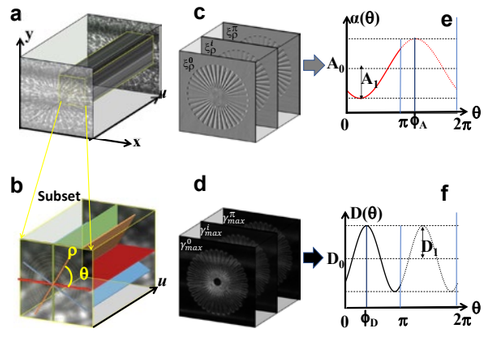

Figure 1: A schematic illustration of the extraction of the directional differential phase and dark-field images of a sample star pattern. (a) the collected stack of speckle images in Cartesian coordinates, (b) the select subset from (a) is transformed into polar coordinates. (c) and (d) the extracted speckle displacement along the polar directions and the maximum of the cross-correlation coefficient images. (e) and (f) the differential phase and dark-field signal modulation as the polar angle changes from 0 to 2π.

In this study, the researchers describe a new algorithm to extract both the omnidirectional differential phase and dark-field signals with a randomly structured wavefront modulator, such as a sandpaper. To achieve the omnidirectional information and minimise the necessary radiation dose, the modulator is scanned along a spiral trajectory. Fourier analysis is then performed to obtain the phase changes and scattering signal of the sample in all directions of the imaging plane. In addition, the proposed method shows great potential to decouple the isotropic and anisotropic scattering signals by analysing the omnidirectional dark-field images.

The experiment was carried out at Diamond Light Source's B16 Test Beamline. As a demonstration of the capabilities of the proposed technique, a phantom with 36 actinomorphic star patterns was purposefully chosen because its features are distributed along all the directions in the imaging plane. In addition, a woodlouse sample was also tested because it has complex biological structures containing both isotropic and anisotropic scattering properties.

The principle of the proposed technique is illustrated in Fig. 1. One stack of reference speckle images was first collected without sample in the beam, and then the same scan was repeated to generate the sample speckle image stack when the sample was moved into the beam. As illustrated in Fig. 1a, for each pixel in the speckle image plane a surrounding subset was selected. The corresponding transformed virtual speckle stack in polar coordinate is shown in Fig. 1b. The correlation coefficient maps were calculated by cross-correlating the two virtual speckle images. As shown in Fig. 1c and 1d, both the differential phase and the dark-field images can be obtained from the same dataset by applying the pixel-wise cross-correlation algorithm by following the above procedure. As demonstrated in Fig.1e and 1f, the Fourier and the phase term can then be extracted by using the Fast Fourier Transform (FFT) analysis for differential phase and dark-field image stacks.

Figure 2 shows the retrieved differential phase amplitude and dark-field amplitude; and the corresponding main orientation. Both the amplitude and the main orientation for the differential phase image shows better contrast

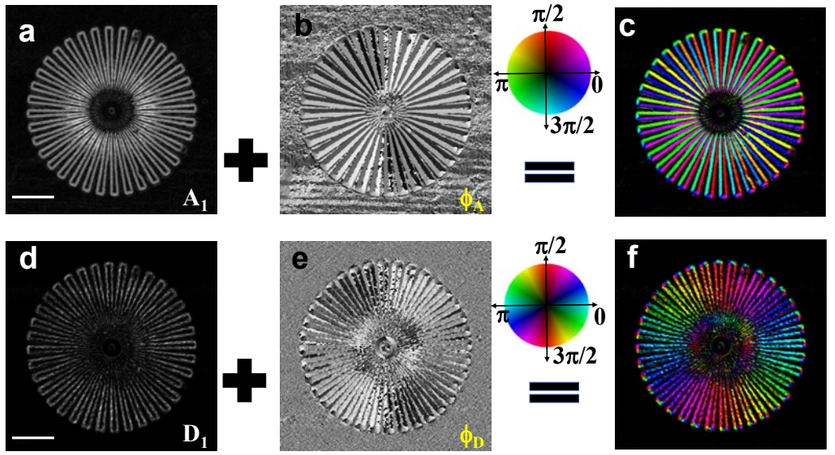

Figure 2: The omnidirectional differential phase and dark-field images for a phantom with 36 actinomorphic star patterns (a) and (b) The retrieved amplitude and main orientation differential phase. (c) The constructed omni-directional differential phase, as rendered in an HSV colour scheme. (d) and (e) The corresponding retrieved amplitude and main orientation of dark-field. (f) The constructed omni-directional dark-field, as rendered in an HSV colour scheme.

than the ones for the dark-field image. In order to show the directional information, the hue-saturation-value (HSV) colour scheme is used with the Hue given by the orientation and the Value equal to the corresponding amplitude. Fig. 2c and Fig. 2f are the directional differential phase and dark-field rendered in a HSV colour scheme. Here, only the edge of the star patterns can be observed from the directional dark-field image, whereas the directional differential phase image also shows the direction of the phase gradient on each bar.

The differential phase and phase images of woodlouse sample are presented in Fig. 3. As shown in Fig. 3a and 3b. the higher scattering signals for the edge of the lateral plate are shown in both the average and amplitude of the directional dark-field images for the woodlouse. On the other hand, the lung and part of the thorax (marked with arrows in Fig. 3a) show strong average scattering but only very weak directional scattering. This indicates that the lung tissue and the retained food (containing rotting plants) in the thorax show isotropic scattering signals. The average scattering map shows both isotropic and anisotropic scattering signals, while the directional scattering map shows only the anisotropic scattering signals. In the HSV colourmap of the directional scattering signal in Fig. 3c, the directional scattering of the lateral plane can be clearly identified along different orientations. The corresponding differential phase images from Fig. 3d to Fig. 3e show complementary information to the dark-field images. Consequently, the main orientation angle image for differential phase can provide enhanced contrast to the weak phase signal, and it can be used to study multiple features of complex samples.

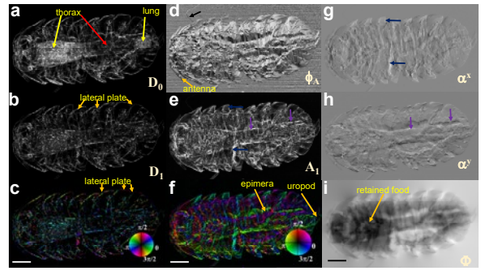

Figure 3: The omnidirectional differential phase and dark-field images for a woodlouse sample(a) and (b) The retrieved average and amplitude of dark-field signal of a woodlouse sample. (c) The constructed omni-directional dark-field, as rendered in an HSV colour scheme. (d) and (e) The main orientation and normalized amplitude of differential phase. (f) The constructed omni-directional differential phase, as rendered in an HSV colour scheme. (g) and (h), The calculated horizontal and vertical differential phase.

In summary, the researchers have demonstrated that the omnidirectional differential phase and dark-field images can be simultaneously extracted from a single data set with the use of a simple modulator. They have shown that the retrieved multi-modal images from the proposed approach can reveal a wide variety of internal structures within one sample. The directional differential phase images reveal the directional dependence of the weakly absorbed features, complementing the directional dark-field images. In addition, the retrieved main orientation image of the directional differential phase can further improve the contrast for thin samples, while the amplitude image of the directional differential phase shows the phase changes along all directions in the imaging plane at once. Moreover, high-quality horizontal and vertical differential phase images and phase shifts can be automatically calculated from the above amplitude and main orientation images[5]. The omnidirectional differential phase and dark-field images resolve the directional dependence of complex microstructures, which is inaccessible to conventional X-ray imaging techniques.

References:

1. Pfeiffer, F. *et al.* Phase retrieval and differential phase-contrast imaging with low-brilliance X-ray sources. *Nature Physics* **2**, 258–261 (2006). DOI: 10.1038/nphys265
2. Wang, H. *et al.* Hard-X-ray directional dark-field imaging using the speckle scanning technique. *Physical Review Letters* **114**, 103901 (2015). DOI: 10.1103/PhysRevLett.114.103901
3. Kagias, M. *et al.* 2D-omnidirectional hard-X-ray scattering sensitivity in a single shot. *Physical Review Letters* **116**, 093902 (2016). DOI: 10.1103/PhysRevLett.116.093902
4. Kagias, M. *et al.* Diffractive small angle X-ray scattering imaging for anisotropic structures. *Nature Communications* **10**, 5130 (2019). DOI: 10.1038/s41467-019-12635-2
5. Wang, H. *et al.* Reply to Kagias and Stampanoni: High-sensitivity hard X-ray directional differential phase imaging. *Proceedings of the National Academy of Sciences* **118,** (2021). DOI: 10.1073/pnas.2116067118

Funding acknowledgement:
This work was carried out with the support of Diamond Light Source Ltd.

Corresponding author:
Dr. Hongchang Wang, Diamond Light Source Ltd, hongchang.wang@diamond.ac.uk

Detector Group

Nicola Tartoni, Detector Group Leader

Last year's focus for the Detector Group was on the development of the Arc Detector for Diamond's X-ray Pair Distribution Function (XPDF) beamline (I15-1). The Tristan10M detector delivered to the Small-Molecule Single-Crystal Diffraction Beamline (I19) was further characterised and is ready to be used routinely for time resolved experiments on I19 in 2022. Finally, the Detector Group worked with the French synchrotron (SOLEIL) on new Ge detectors that may be useful for a number of beamlines.

The Arc Detector

The ARC detector project for I15-1 is the major development project which has been the main commitment of the Detector Group in the past 12 months. The ARC detector is devoted to the X-ray pair distribution function technique of beamline I15-1 and the detector system consists of an array of 24 sensors arranged in an arc geometry with a radius of 25 cm. In order to guarantee an acceptable detection efficiency at the photon energies of I15-1 (40.05 keV, 65.40 keV, and 76.69 keV) the sensors are in CdTe. The sensors are pixelated with pixel pitch of 55 microns and each sensor is bonded to 3 Medipix3RX read-out chips. The sensors are mounted in a module, which include the electronics. Four modules are mounted in a supermodule which plugs into the mechanical structure of the detector system. The project is close to delivery and the detector head has been assembled and populated with 24 modules, which is the number of modules that had been planned when the project was launched. Figure 1 shows the detector head fully populated with six supermodules at the end of the assembly procedure. Figure 2 shows the detector head mounted at beamline I15-1. One peculiar aspect of this project is that the Schottky contact technology was chosen for the sensors instead of the most common ohmic one. Although Schottky sensors polarise more quickly than ohmic ones when they are exposed to radiation, they recover much faster when the bias voltage is removed and then applied again. A few seconds of voltage removal is enough to restore the sensors to the pristine condition which delivers a better duty cycle for this particular application. A comparison between Schottky and ohmic sensors, which was done a few years ago with a realistic test at I15-1, showed that the Schottky ones enabled a larger overall exposure time with respect to ohmic sensors. The additional advantage of Schottky sensors is that they can be biased with a voltage which is higher than the ohmic ones. This enables a faster charge collection and thus limits the charge diffusion and improves the spatial resolution.

TheTristan10M Detector

The Detector Group continued working on various aspects of the Tristan detectors. The Tristan10M, delivered to I19, was fully characterised and the results have been published to a conference[1]. Tristan10M has been scheduled to be used at I19 for several time resolved user experiments in 2022. It is worth reminding that Tristan time stamps events with a notional time accuracy of 1.56 ns (notional time resolution of the Timepix3 ASIC) and that it can acquire data continuously for a long time (up to 81 days) thanks to the extensions in the firmware developed by the Detector Group. The continuous acquisition with high accuracy time stamp enables to run experiments much more efficiently than running the same experiments by using gated detectors such as conventional photon counting detector systems. These characteristics were highly appreciated by a group who work on XPCS technique at MAX IV (Sweden). The Detector Group loaned a Tristan10M to MAX IV in May 2021 so that they could test the novel concept of data driven detector in an actual experiment. A research group from the University of Stockholm carried out an experiment in June 2021 at the beamline NanoMAX at MAX IV. The experiment ran very smoothly and several datasets with a time resolution of 1 microsecond were obtained. Figure 3 shows a plot of a dataset taken at MAX IV.

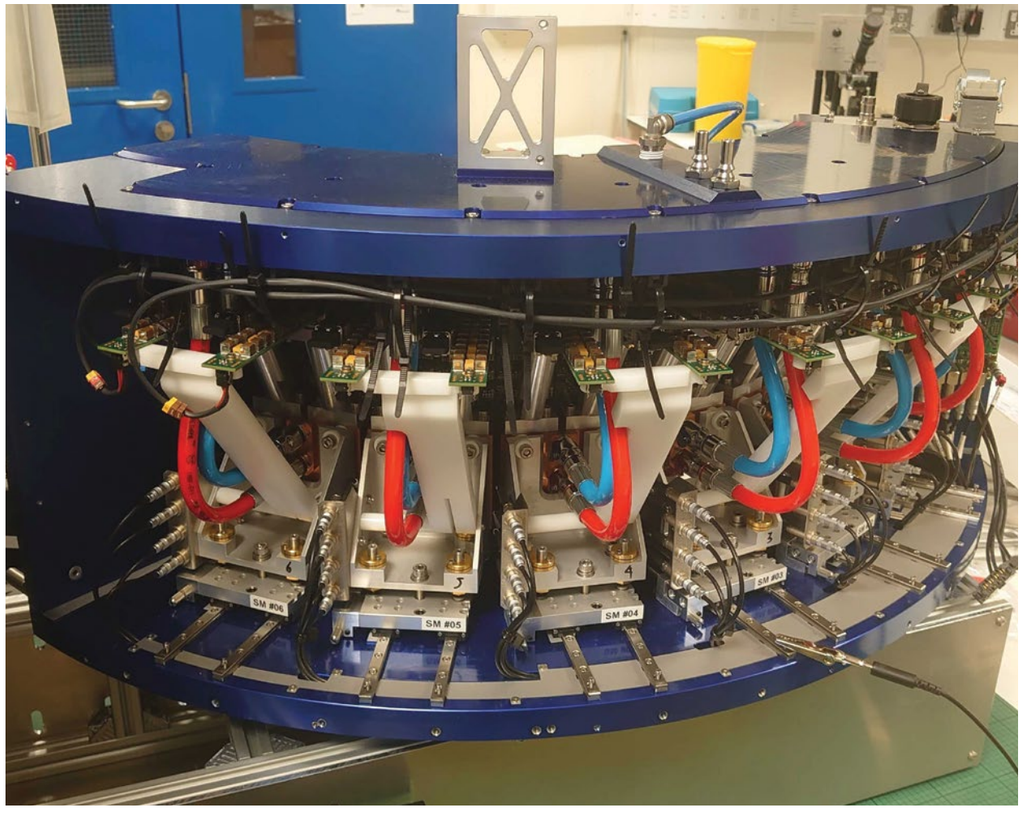

Figure 1: The detector head of the arc-detector on the mounting table. The detector is fully populated and the back side of the 6 supermodules can be noticed in the picture.

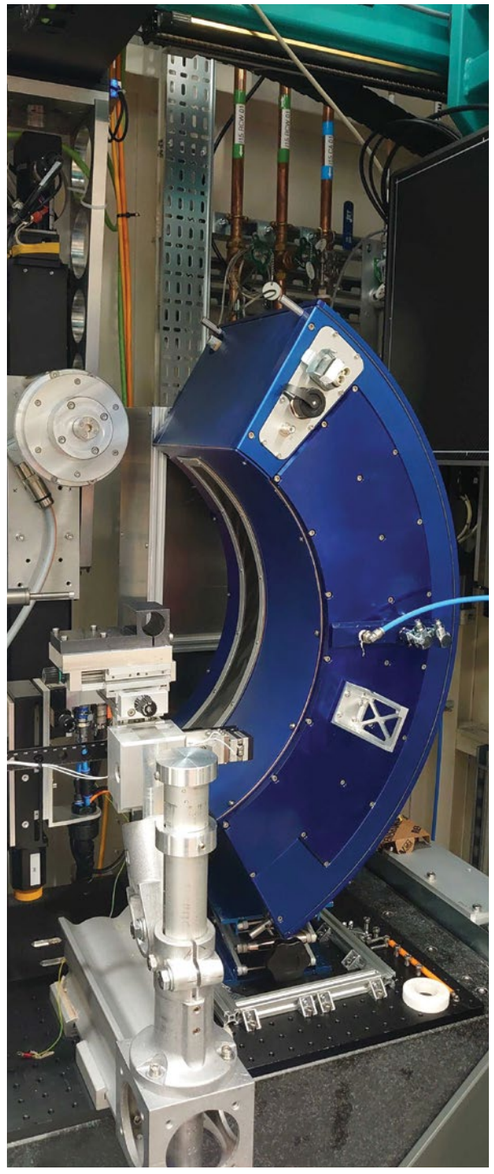

Figure 2: The detector head closed and mounted on the beam line I15-1.

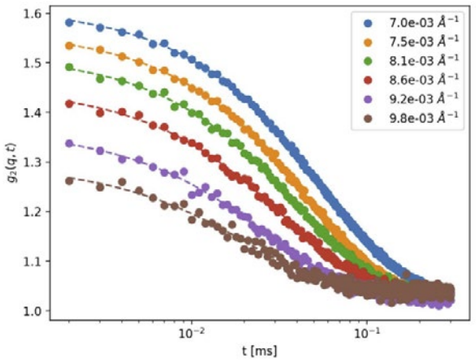

Figure 3: XPCS data set of 100nm Si particles in water taken at the beam line NanoMAX at MAXIV with the Tristan1M detector (plot courtesy of Clemens Weninger (MaxIV)).

Collaboration for new Ge detectors

In addition to the two projects mentioned above, the Detector Group at Diamond is leading two activities to develop Ge detectors. Both activities aim to improve the throughput and compactness of monolithic multi-element Ge detectors. The first activity is a collaboration with Synchrotron SOLEIL and it is in fact a continuation of the pioneering work already autonomously undertaken by the Detector Group to improve the segmentation and the speed of Ge detectors[2,3]. The ultimate goal of the collaboration with SOLEIL is to develop a detector with a large number of small elements to enhance the throughput. This system should make use of the Xspress4 pulse processor to reject the charge shared events electronically without the use of a collimator, like in the current versions of commercial detectors. The collaboration with SOLEIL is currently completing the phase 0 (the first of three phases) this year which is supposed to evaluate the detector technology from a particular vendor.

Diamond and SOLEIL are also co-leader of work package 2 of the European project LEAPS-INNOV. This work package develops more compact Ge detectors for XAFS and XRF applications. Whilst the prototype currently being developed by LEAPS-INNOV is limited in the number of channels and therefore in its throughput, the innovative solutions adopted may be re-used for systems with larger number of channels as those envisaged by the collaboration between Diamond and SOLEIL. It is thought that detector systems with very high throughput will be indispensable for Diamond-II and therefore it could be a wise investment to progress to the other two phases (phase 1 and 2) of the collaboration with SOLEIL.

References:

1. Z. Chen *et al.* Tristan10M detector: characterization of a large area detector for time resolved experiments based on Timepix3 chip. *JINST*, (pre-pub), 2022.
2. N. Tartoni *et al*. Hexagonal pad multichannel Ge X-Ray spectroscopy detector demonstrator: comprehensive characterization. *IEEE Transactions on Nuclear Science* **67,** 1952-1961 (2020). DOI: 10.1109/TNS.2020.3004923.
3. N. Tartoni *et al.* Monolithic multi-element HPGe detector equipped with CMOS preamplifiers: construction and characterization of a demonstrator. *IEEE Transactions on Nuclear Science* **62,** 387-394 (2015) DOI: 10.1109/TNS.2014.2381492.

Scientific Software, Controls and Computation

Mark Heron, Head of Scientific Software, Controls, and Computation

The Scientific Software, Controls and Computation (SSCC) department manages all software, computing and control systems to facilitate and support the science programme of Diamond. Over the last year there has been an increasing emphasis on planning for Diamond-II. The department functions as eight groups: Scientific Computing, Data Analysis, Data Acquisition, Beamline Controls, Accelerator Controls, Electronic Systems, Scientific Information Management Systems and Cyber Security. The overall structure and function of these areas recognises the importance of, and is optimised to provide, the best possible delivery and support for software, computing and control systems.

There have been a number of changes in SSCC over the last year. A Scientific Information Management Systems (SIMS) group was formed, and an interim group leader appointed; a new Head for Data Analysis was appointed; and a new role as Head of the Integrated Software Programme for Diamond-II was created and an appointment made. Throughout most of the last year the majority of SSCC staff worked remotely, whilst always ensuring adequate on-site cover. Maintaining effective and timely communication was seen as imperative to be able to support operations effectively.

The last year has seen an increasing emphasis on planning and making preparations for Diamond-II. A series of work packages for software, computing and controls have been developed and estimates have been made of the resources required to deliver the plan. Further details of Diamond-II work relating to the following areas are reported below: Development of the New Software Architecture; Diamond-II Software and Computing; Design of New Electron Beam Position Monitor.

In the previous Annual Review, it was reported that a Strategy for Scientific Software, Controls and Computation had been published; this presented a vision for how the department will meet forthcoming challenges in software, controls and computing, and a set of SSCC goals was specified. The goals are listed below, together with a progress report:

SSCC Goal	Report on Progress
Deliver high quality software, computing and controls provision and support in order to enable Diamond's science programme: from experiment approval to publication.	• As reported, examples of related work:- • Development of a new software architecture; • Design for a new data centre; • Design of new electron beam position monitor; • Automation of Electron Microscopy Single Particle Analysis Data Processing.
Establish strong partnerships, internally and externally with the Science and Technology Facilities Council (STFC), other facilities, universities, etc; to deliver best in class software and computing in a collaborative, effective and sustainable way.	• Development with Birmingham University of services to run on the Baskerville Tier 2 HPC system. • Support for STFC in the development of an Outline Business Case for the campus Research Computing Centre. • A strong and long-running collaboration on the Odin Data Acquisition and Controls software framework with the STFC Detector Systems Software Group. • Well-established collaborations with SOLEIL, and more recently MAX-IV, on the PanDaBox for low-latency experiment triggering and synchronisation. • Collaborations with NSLS-II and other EPICS sites to adopt and progress BlueSky developments.
Deliver a step change in experiment capabilities and efficiencies, across the science programme, through: intuitive useable applications; automated analysis of data; remote access capabilities; automation of instrument and sample management; high speed readout of detectors; and near real-time data process for visualisation feedback.	• Preparations for a step-change in experimental capabilities and efficiencies as part of the D-II planning.
Widen experimental data exploitation through delivering: FAIR and Open Data, and through new capabilities in data science (Machine Learning (ML) and Artificial Intelligence (AI)), modelling and analysis.	• Significant developments in delivering FAIR and Open Data, with changes proposed to the Diamond Data Policy, existing data embargoes extended, and a comprehensive user consultation planned for 2022.
Realise a hybrid computing model, which delivers on-site computing services to those applications for which low latency and high bandwidth are essential, with all other services delivered through cloud computing.	• Development in containerisation to facilitate greater use of external computing resources. • Substantial increase in external computing resource, largely through the use of the IRIS compute cluster provided by STFC. • Close work with STFC to support the planning for the Research Computing Centre.

Selected highlights from exciting SSCC developments across a broad range of activities during the past year are presented:

A New Data Centre

Diamond currently operates two data centres with combined capacity of 500 kW. These house the required IT resource of approximately 18,000 compute cores and 20 PB of high-performance storage needed today for first level data capture and processing of data from the photon beamlines and electron microscopes. In addition, subsequent processing utilises shared cloud-based resource primarily operated by STFC as the IRIS service to the science community. Today the first data centre is 100 % full and having been constructed in 2011 the cooling infrastructure is nearing its end-of-life, and the second data centre is 60 % full. As a result, there is limited capacity for future IT resource to support the anticipated growth in data volumes and processing needs.

Racks in the current data centres support IT loads of up to 10 kW per rack, while modern IT equipment can achieve IT loads up to 80 kW per rack and higher. This combination of need for greater capacity and changing technology has led to the specification for a new data centre.

During the past year, the technical design for the new data centre has been developed in conjunction with a company that specialises in the design and construction of data centres. The resulting design provides for an operating power envelope of up to 1 MW of IT load. The design provides for 40 racks to house the IT equipment. These are specified as: 20 off low power racks at 25 kW per rack, 15 off high power racks at 60 kW per rack and 5 off network racks at 5 kW per rack. The low power racks will use rear door cooling and the high power a combination of rear door cooling and water to chip cooling.

The design affords a high-level of resilience and to be fault tolerant to minimise the downtime of the IT services. This is achieved through two separate electrical supplies, with one fed through uninterruptable power supplies to protect against short mains outages. The cooling systems also includes redundancy and extract the heat load through a mixture of chilled water to rear door coolers for the low power racks and a combination of rear door coolers and direct water to chip from dry air coolers for the high-power racks. This combined cooling approach provides: flexibility to accommodate the mixed IT load required; support for the move to new IT technologies with higher power densities; and gives a good operational efficiency in terms of data centre cooling.

As of spring 2022, the technical design for the data centre has now been reviewed, with a model of it shown in Fig. 1. By the summer of 2022, the detailed design work should be finished and the construction project commencing with timescales for completion and handover of summer 2024.

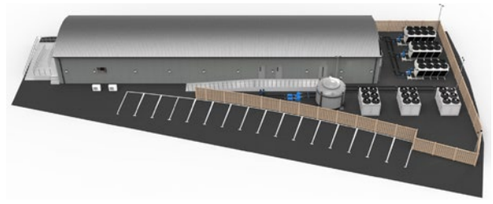

Figure 1: Model of Diamond's New Data Centre (Courtesy Oper8 Global Ltd).

Planning for Diamond-II Software and Computing

Diamond-II will deliver photon beams with substantially increased spectral brightness. This major enhancement will enable significant new science. Experiments will become more complex and will be conducted with higher spatial and temporal resolutions. To facilitate these there must be greater automation of experiments, faster detectors, rapid data processing and reduction, and the introduction and development of new data processing techniques. The latter will exploit recent developments in Artificial Intelligence and Machine Learning toolkits, automating data reduction and analysis. Science will benefit too from a more open software environment; an open environment will facilitate a greater level of collaboration between software and scientist, profiting also from a lowered threshold of entry for conducting experiments. All these changes will be made possible by the significant enhancement of Diamond's software and computing capabilities delivered as part of the Diamond-II upgrade. These developments will enable the major increase in data, transforming data into scientific knowledge.

During the Summer of 2021, key core software, controls and computational development areas were identified through a series of internal workshops. These identified areas are:

- Science Specific Data Analysis Software Developments
- Detector Readout
- Data Archiving
- Post-visit Data Analysis Services
- High Performance Sample Stages
- User Administration and Information Management
- Modernisation of Data Acquisition Software Framework

Science Specific Data Analysis Software Developments

Developing data analysis software will be key to enabling new science. Developments will address limitations in the software for delivering computationally intensive science. Accelerating these applications will benefit the Ptychography, Tomography and MX science domains. Speedier and more robust algorithms will benefit Ptychography experiments. The Tomography domain will also welcome speed alongside improvements to usability and the introduction of packaged services. Macromolecular crystallography will see the necessary step change in performance realised via a migration to in-memory architecture and the use of GPU/FPGA accelerations. Real-time analysis will be important to all, with automatic processing of data through all the analysis pipelines.

Detector Readout

Detector data rates are being seen to double every seven and a half months. Diamond currently has data rates of up to 4 GB/s from a single detector. Data is transferred from all the detectors to central storage, and the existing 50-80 GB/s high performance file systems can handle the demands from multiple beamlines. Integrating detectors with high-speed file systems reliably is however becoming increasingly challenging. As the data rates continue to increase, this will only be more so. Developments in this area will address the need to stream data to data-consumers and for detectors to write directly to memory data processors, without the file system.

Data Archiving

Diamond's current data archiving solution hosts over 20 PBs of data, but it will not scale effectively to cope with the order of magnitude change to data volumes expected with Diamond-II. For Diamond-II, the total volume of data will increase significantly in to the 100s PBs. To support the larger more complex data the usability of the archive will be enhanced, to provide greater functionality in terms of how data is selected and how it is moved out of the archive and processed. This will be a key enabler of better data processing services and open data.

Post-visit Data Analysis Services

Transferring data from Diamond to users' home institutions for processing presents Diamond's existing users with significant challenges due to the size of the data and network limitations (See Fig. 2). When the users get the data back to their home institute, the computing resources and software to process it may not be readily available. Furthermore, new users expect to see results and not the raw data alone. Whilst Diamond provides some post visit data analysis services today, for the computationally intensive science domains, MX and

Tomography, they are increasingly in demand. Post-visit data analysis services will enable users to fully remotely process and evaluate the data collected on Diamond-II.

High Performance Sample Stages

Some beamlines will experience greater than a hundred times increase in brightness of the photon beams. This will enable detectors to operate much faster with frame rates as high as 10 kHz. To make best use of the fast acquisition the sample will need to move faster as part of being scanned. This will need faster servo loops in the motion controller, and so a new generation of motor controllers will play a key role in delivering these fast applications.

User Administration and Information Management

Automated remote sessions will increasingly become the norm with Diamond-II. The metadata from the proposal process will need to be integrated with session allocation, sample registration and logistics, processing pipelines and the resulting visualisation and analysis of experimental results. Users will then be able to perform data mining, data analysis and gain access to enhanced search capabilities to fully exploit the value stored within metadata repositories. These changes will in part be realised by greater integration of the Laboratory Information Management System and User Administration into the Data Catalogue.

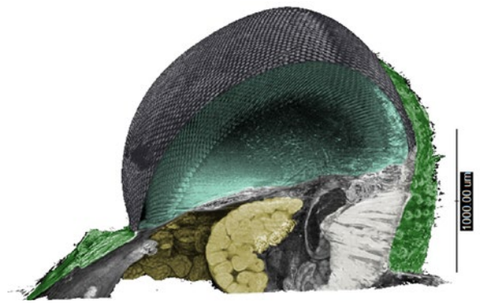

Figure 2: A coloured reconstruction of a bee's compound eye, produced from studies on I13 is an example of the type of large dataset that will become increasingly common on Diamond-II. Courtesy of Gavin Taylor, Emily Baird, Andrew J Bodey & Andreas Enstrom (University of Lund).

Modernisation of Data Acquisition Software Framework

The beamline software architecture supports the full life-cycle of a science experiment at Diamond – from requesting beamtime and shipping samples, to planning and running experiments, to analysing and archiving results. The existing software has evolved over the last twenty years to successfully facilitate world-leading science across Diamond's many beamlines, balancing the competing demands for flexibility and high-throughput, automated experiments. Diamond-II provides an opportunity to build on this, addressing issues that have arisen over time and enhancing functionality to allow the new regimes offered by the upgrade to be fully exploited.

For the last year, work has been undertaken by the Data Acquisition, Data Analysis, Controls and SIMS groups to document the new architecture and to plan for the transition from the existing architecture. Input has been sought from the beamline scientists and the support engineers, to ensure that requirements are elicited and validated early on and that all sides are involved in this process. From the science perspective, there is a desire to improve the delivery and robustness of the software, providing timely releases for features with minimal beamline disruption. Opportunities for automation and performance, as well as better monitoring and diagnosis of issues, are also sought. From the support perspective, similar concerns are also identified. In addition, there is a need to improve maintainability and extensibility – problems increasingly of concern as the current software stack ages and technologies reach end-of-life.

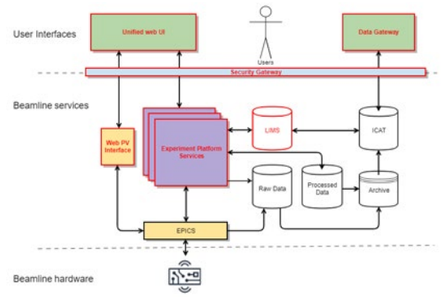

Figure 3: Functional View of the Target Beamline Software Architecture.

A multi-year programme of work has been identified to manage the architecture upgrade. This consists of many work packages, scheduled in a way to reduce risk – with uncertainties being mitigated through the use of early prototypes. Significant items of work include:

- Decomposition of the existing Generic Data Acquisition (GDA) monolithic application, into a set of well-defined, stand-alone services. Figure 3 shows Services being deployed as and when needed.
- Replacement of Jython scripting (now end-of-life) with a move to Python 3.
- Migration to a new experiment control library – called Bluesky – to simplify scan definition, device configuration and enable the move away from Jython.
- Consolidation of the multiple different user interfaces, with the long-term goal of providing a unified web platform for the scientific and technical user interfaces.
- Enhance security, through the use of Role Based Access Control.
- Use of operating system level virtualisation to deliver software in packages called Containers to simplify and improve management of deployments.
- Improve support for modern highly automated (Fig. 4) and adaptive experiments.

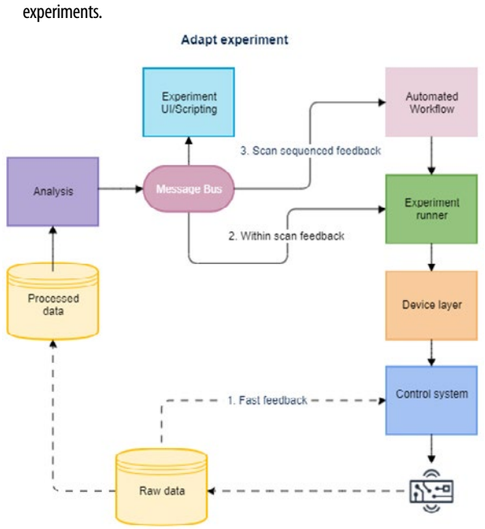

Figure 4: New workflow for automated adaptive experiments.

The architecture documentation is nearing completion and an external review is due in the first half of 2022. Initial prototyping work has begun as part of evaluating software technologies and a development roadmap defined. This work will form the basis of software developments for the new flagship beamlines for Diamond-II and upgrades to the existing beamlines.

Design of New Electron Beam Position Monitor

An example of an early development undertaken for Diamond-II is the design of a New Electron Beam Position Monitor. This is a joint development by the Accelerator Controls Group in SSCC, and the Diagnostics Group in Technical Division.

Positional stability of the electron beam in the Diamond-II storage ring determines the stability of the photon beam delivered to the experiment samples. With very small photon beams – as small as 30 µm × 4 µm - and long lever arm due to the length of the photon beam path then the electron beam for Diamond-II will have to be very stable – 0.9 µm × 0.12 µm - in both horizontal and vertical planes. This, combined with faster X-ray detectors, places increasing demands on measuring the electron beam position and its stabilisation. This requires increased performance from both the Electron Beam Position Monitors (EBPMs), used to measure the beam position, and the Fast Orbit Feedback (FOFB) system used to correct any measured disturbances (Fig. 5).

The feedback update rate for Diamond-II will be increased from 10 kHz to 100 kHz, or one position update every 10 µs, and the processing delay (from beam disturbance to correction of beam) will be reduced from 700 µs to 100 µs. Achieving this requires a complete redesign of the EBPM and FOFB systems.

The electron beam position is computed by measuring the signal from four RF pickups mounted in the vacuum vessel in what is called the EBPM button block. For an accurate and stable EBPM measurement it is necessary to measure this signal with exceptionally high stability, and it is therefore necessary to take into account the environmentally driven drifting of measurements between adjacent channels. Classically, this compensation is done via some form of chopper circuitry, which involves switching the received signal among the four processing channels. Unfortunately, this introduces significant switching noise which will interfere with the higher feedback rates. Therefore, a different technique is used: a pilot tone is introduced at a frequency near the button RF signal and this tone is used as a compensation mechanism.

The signal processing occurs in a series of stages: the signal is processed electronically in the Diamond-II Analogue Front End (D2AFE) where the pilot tone is injected, the signal is filtered to reject frequencies more than 15 MHz away from the button RF signal, and the signal level is adjusted. The signal is then digitised at a carefully chosen frequency, close to 215 MSamples/s, before being down converted to the 100 kHz fast feedback rate. The raw button and pilot signal levels at this stage are then converted to X & Y positions before transmission to the FOFB node for feedback processing.

This updated position is then transmitted over dedicated Gigabit Ethernet links to a central controller node, where a complex multidimensional controller based on an Internal Model Controller (IMC) using Generalised Singular Value Decomposition is used to compute corrector updates. Corrector magnets distributed around the ring are grouped into "fast" and "slow" correctors, with fast correctors acting at between 50 Hz and 10 kHz and slow correctors acting below 100 Hz. The central controller computes an update to each fast corrector every 10 µs, and to each slow corrector every 300 µs, and transmits these updates over Gigabit Ethernet to each corrector.

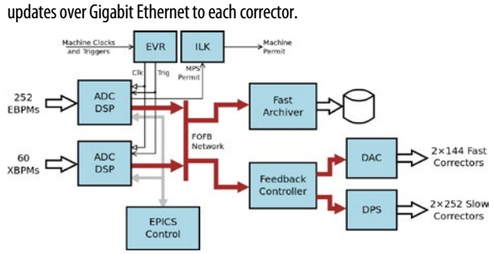

Figure 5: Overview of how the electron beam position (EBPM) measurement system, x-ray beam position (XBPM) and corrector magnets are connected through signal processing and Fast Orbit Feedback controller. The system is synchronised by a global clock decoded in an Event Received (EVR) and provides a permit to the global machine protection system as an interlock (ILK).

Automation of Electron Microscopy Single Particle Analysis Data Processing

The Cryogenic Electron Microscopy (cryo-EM) Single Particle Analysis (SPA) pipeline line has undergone considerable work over the last year to provide users with an automated pipeline that is web based. Historically, users had to log into Diamond's systems and interact with the datasets in a way that was non-optimal. The goal is to provide a fully automated high throughput cryo-EM service akin to the well-established pipelines available on photon beamlines for the analysis of macromolecular crystallography data. This transition is a vital step in achieving the longer-term strategic objectives of improving throughput and the ease of use.

The automated service deployed was particularly important over the COVID pandemic as all user sessions had to be run remotely. Using a web interface – called Synchweb – users can start processing their data almost immediately after collection on the microscopes, with the addition of a few parameters. Once initialised the pipeline will run unsupervised, displaying several key processing results (see Fig. 6), including motion correction, distortion correction, particle picking, ice thickness estimation and 2D classification, for the users to assess. The results are updated regularly and give the users the confidence that their data is of the quality required for high resolution structure determination. The data model is implemented in collaboration with other European facilities such that metadata collected and processed is available for wider collaboration across the community. This capability allows our users to work towards adopting FAIR (Findable, Accessible, Interoperable, and Reusable) data policies over time. A unique part of the pipeline is the ice thickness estimation, that is performed by bespoke in-house software, which is an important parameter in the determination of high resolutions structures.

https://doi.org/10.1016/j.str.2022.01.005.

In the coming months, additional functionality will be added to the SPA pipeline to increase the information content available to the users and identify performance bottlenecks in the analyse pipelines to improve the processing times to solution. The next development will be a second processing pipeline for cryo-tomography data collections. An agreement is already in place for an updated data model so that appropriate pipelines can be developed and optimised to provide our users with a new capability.

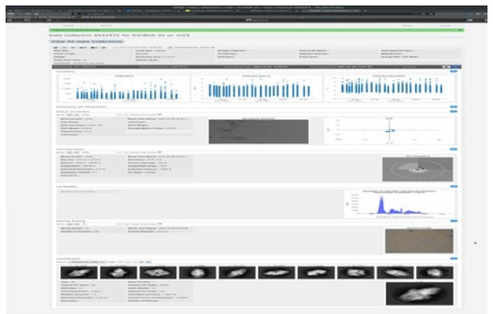

Fig 6: A web-based user interface of the data processing pipeline giving a summary of the results and status of the motion correction stage of data processing.

Industrial Liaison

Industrial Liaison Office

Another extraordinary year has passed and life at Diamond Light Source is gradually returning to normal. It has been a great pleasure to see our valued clients returning in person for experiments and although there have been fewer in person meetings and events this year, the Industrial Liaison team are looking forward to getting out and about and meeting in person over the coming year.

The industrial programme at Diamond is thriving and we have had our busiest year to date. Diamond is now working with 200+ clients in 22 countries. The many years of preparation and work in establishing efficient and reliable workflows for remote and mail-in experiments have shown their worth over the last couple of years, enabling the team to respond quickly and provide seamless support for our clients as the world around us pivoted to remote working. Our data collection services across the techniques available at Diamond continue to be extremely popular and have gained widespread adoption with our clients who value the flexible approach and trust us to collect precious data with the same professionalism and care that they would apply themselves.

The physical science industrial programme is now fully operational and as restrictions on the complexity of experiments and numbers of people participating in experiments are eased, we are excited to take part in complex *in situ* team experiments once again and continue to build our successful programme for diffraction, spectroscopy, scattering and imaging experiments. The life sciences industrial programme was only very briefly paused in early 2020 and since then has continued to develop and grow at a great pace. Demand remains high for our macromolecular crystallography, cryo-Electron Microscopy (cryo-EM), fragment screening and small angle scattering services and a new crystallisation service has been launched to help support clients at the early stages of drug discovery giving access to Diamond's facilities and expertise.

The eBIC for Industry team (L-R): Jason van Rooyen, Hazel Aitkenhead and Mani Karuppasamy.

This year we have welcomed two new members of the ILO team, both providing technical expertise, professional efficiency and a welcoming smile to our cryo-EM clients. Dr Hazel Aitkenhead joins us from the University of Oxford and is experienced in protein production and high throughput discovery science. Dr Manikandan (Mani) Karuppasamy joins us from the Tata Institute for Genetics and Society in Bangalore, India and brings a wealth of experience of cryo-EM studies on a range of industrially relevant systems.

Although our primary focus remains our client projects, the ILO team continues with our own research and this year ILO PhD student Paul Edwards, Elizabeth Shotton, Anna Kroner and the University of Leeds team, led by Prof. Sven Schroeder, were the first users of the Versatile Soft X-ray (VerSoX) beamline (B07-B). The team used B07-B to measure the C, N and O K-edge spectra of a range of solid, organic crystal systems using Near Edge X-Ray Absorption Fine Structure (NEXAFS). The results were used to test the hypothesis that NEXAFS can be used as a quick diagnostic tool to characterise pharmaceutical materials where crystallographic methods may not give a definitive answer and provide an alternative route for characterisation of these complex materials. Undertaking complex experiments on a brand-new facility while working under tight COVID restrictions is a significant challenge and we thank all the teams at Diamond and Leeds whose hard work ensured a successful outcome.

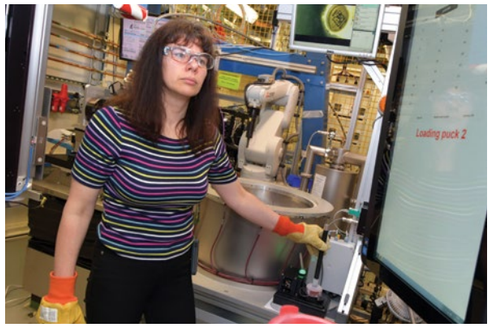

Jitka Waterman loading pucks for MX experiments.

Alex Dias and Ailsa Powell preparing pucks for XChem experiments.

Elizabeth Shotton, Anna Kroner and Paul Edwards, along with the B07-B team and the Leeds team led by Sven Schroeder, were first users on B07-B.

A study of the hydration behaviour of fluconazole, an antifungal drug, known to crystallise in at least five polymorphs was undertaken by Leigh Connor in collaboration with scientists from Pfizer and the University of Manchester[1]. The team used high resolution powder diffraction studies on the High Resolution Powder Diffraction beamline (I11) to show that both age and polymorphic form impact the drug's kinetic stability to hydration. In particular, an initially undetectable monohydrate form of the drug was shown to have a seeding effect which impacted the hydration kinetics.

Collaborating with Activirosomes Ltd, Claire Pizzey and the B24 beamline team published the results of a large project aimed at characterising a novel vaccine platform using a 3D correlative microscopy approach. Active virosomes (AVs) are essentially novel vaccine formulations that present on their surface selected viral proteins as antigens, acting to provoke an "anti-viral" immune response. AVs are internalised by host cells and deliver a viral payload of genes used to express viral antigens intracellularly. These can then be transported to the host cell surface resulting in a second wave of antigen exposure and a more potent immuno-stimulation. The target virus antigens selected for this work were category B priority pathogens, Chikungunya and Zika viruses. To date, there is no drug treatment nor vaccine available for immunisation against these pathogens; therefore, the development and optimisation of appropriate vaccines remains an urgent requirement for world health. A 3D correlative microscopy approach, combining cryo Structured Illumination Microscopy (cryoSIM) and cryo-soft X-ray tomography, allowed visualisation of the 3D ultrastructure and antigen loading of AV populations (with and without viral payload) and assessment of morphological variations across batches[2]. Preliminary results also verified antigen expression on the surface of host cells, demonstrating the effectiveness and robustness of the technique for characterising novel vaccine formulations such as AVs. Financial support for the Activirosomes Ltd project was provided by the Bridging for Innovators (B4I) scheme through STFC. An ongoing collaboration with Activirosomes Ltd will continue to increase productivity by optimising protocols for commercial vaccine analysis.

Diamond continues to support our industrial clients across a wide range of techniques and facilities with experiments ranging from routine analysis to complex bespoke solutions. Please do not hesitate to contact us on industry@diamond.ac.uk to discuss your analytical needs, we are happy to help.

References:

1. Basford, P. A. *et al.* Does the age of pharmaceuticals matter? Undetectable hydrate seeds impact hydration behavior. *Crystal Growth & Design*, **21** 1912–1916 (2021). DOI: 10.1021/acs.cgd.1c00100

2. Okolo, C. A. *et al.* Correlative imaging using super-resolution fluorescence microscopy and soft X-ray tomography at cryogenic temperatures provides a new way to assess virosome solutions for vaccine development. *Journal of Microscopy*, **284** 214–232 (2021). DOI: 10.1111/jmi.13054

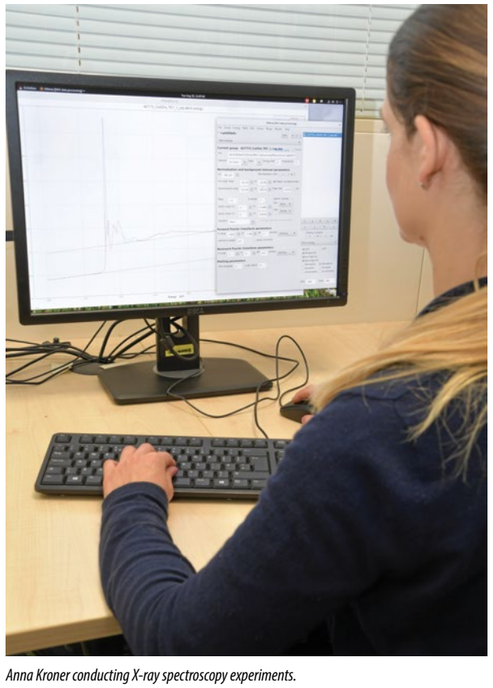

Anna Kroner conducting X-ray spectroscopy experiments.

Engaging with Diamond Light Source

Communications and Engagement Team

Over the past year the COVID pandemic has continued to impact on Diamond Light Source's engagement activities and has required us to maintain our focus on developing and delivering remote activities. This has led to new partnerships and audiences, which we are continuing and using to improve our existing programmes as we take the first steps back to in-person events.

Using the methodologies developed to integrate virtual activities into visitor numbers, Diamond has had approximately 7,323 significant interactions[1] with 'virtual' visitors. These include 2,949 for scientific and technical events, 267 undergraduate and postgraduate interactions, 3,828 school students and members of the public, and 279 VIPs and stakeholders. The majority of these (6,987) have been virtual, but we have started to welcome some visitors back on site (336) and also engage at offsite events (336).

[1]Significant Interaction is defined as a talk/tour/meeting of 30+ minutes, typically longer.

"The Diamond Tour is always the highlight of the week when we have residential training."

"An amazing opportunity and experience, the tour guide was very informative."

A coordinator and student from a PhD student visit.

This year we have worked hard to adapt to the changing needs of audiences as the pandemic has evolved. With students no longer home schooling we now offer bespoke schools visits to fit around timetables and have developed partnerships to reach out to new audiences. These include existing relationships such as those with STFC, at RAL and Daresbury, but also new ones; we have been working with Salters' Institute, Canterbury Christ Church University and University of Oxford to develop new videos, workshops and 'zines' to engage with school students.

Working within careful guidelines we have delivered limited on-site activities and in July were delighted to welcome 36 schools work experience students to Diamond, undertaking 18 different projects ranging from Beamline Controls to Crystallisation. We have also started to welcome a small number of group visits such as PhD students back to site and look forward to hosting many more events soon.

Throughout 2021 Diamond undertook an assessment process run by the National Co-ordinating Centre for Public Engagement (NCCPE) and in October we were delighted to be presented with the Bronze Engage Watermark award. This recognises the commitment of Diamond to Public Engagement and gives us a development plan, which we have already started to implement, with activities such as engagement awards for staff and developments in strategy.

"To achieve a Bronze Award is a significant landmark, signalling your commitment to public engagement."

"There is an exemplary public engagement team, who had really led effective engagement."

Feedback from the NCCPE on the award of a Bronze Watermark Award.

Diamond has continued its commitment to widening participation, working with groups such as the Amos Bursary and participating in the IF Oxford Science Festival, delivering live outreach activities in areas of lower science engagement.

We have also seen the fruition of our Diamond Board Game project and in the autumn hundreds of the games, designed to inspire and inform students about careers in science research, were distributed to schools across the country.

David Price and Amy Griffin with the Bronze Engage Watermark Award.

Amy Griffin presenting a thermal camera to children at the IF Oxford Science festival.

"We are now in receipt of the class set of games. They look wonderful! My homework for the weekend is to try one out, ready to begin using them in school."

Teacher using the Diamond Board games in school

Higher Education Engagement

Our undergraduate and postgraduate programmes play vital roles in Diamond's wider mission to be a world-leading centre for synchrotron science and to keep the UK at the forefront of scientific research. Our student-dedicated programmes aim to welcome and harness the talent, curiosity and development of students both at undergraduate and postgraduate level and provide them with exciting opportunities to encourage and nurture a career in STEM, ultimately contributing to the wider skills agenda in the UK.

Despite a delayed and virtual start to their placements, our 2020 Year in Industry cohort successfully delivered their final project presentation in August 2021 via Zoom and gave staff the opportunity to gain insight into their research, any challenges and results. We were also able to organise an in-person yet socially distanced poster session for the students in the Diamond House atrium which was attended by staff on-site over lunchtime.

We were pleased to welcome 12 new Year in Industry students as part of the 2021 cohort intake in September and more importantly, were able to induct them in-person, on-site at Diamond with social distancing and safety measures in place. Our 2021 cohort have since been working on-site progressing their projects, as well as completing various training including Scientific Communications, Peer Reviewing and Presentation Skills.

In June 2021, we welcomed our 15 Summer Placement students, three of whom had been transferred from the 2020 cohort due to COVID and cancellation of last year's programme. As restrictions were still prominent over summer at Diamond, our cohort worked in a hybrid fashion, progressing their projects both on-site and from home, covering life and physical sciences, engineering and software computing. After a summer of work experience, training and networking, the students presented their results to staff via end of project presentations streamed online.

"My experience at Diamond has trained me both professionally and personally, training which I don't think I would have received elsewhere. I'll fondly remember the experience for many years to come."

Harry Rostron, 2021 Summer Placement Student

Our 2020 Year in Industry students at their end of project Poster Session in the Diamond Atrium, with one student presenting remotely!

Our 2021 Year in Industry Cohort after completing their two-day Presentation Skills Workshop, held at Cosener's House in Abingdon, March 2022.

Our 2021 Year in Industry students (right to left: Parnavi, Ishika, Zaeem and Alex) in discussion during our Peer Review Training session.

> *"It was my best summer so far. I met great people, explored Oxfordshire, built a software package I can show to future employers, and got paid to do it."*
>
> *Aurys Silinga, 2021 Summer Placement Student*

Our 2021 PhD Cohort made up of 24 students co-funded by Diamond and 15 universities and world leading facilities, have begun their studentships and we have been able to induct the majority of them on an individual basis here at Diamond. This brings the total number of active Diamond PhD Studentships to 109. We received 54 submissions to our 2022 Diamond Doctoral Studentship call for proposals, which were linked with 33 different universities and institutions. Following the internal review process, we will be welcoming 21 students in October 2022. The PhD student annual progress meetings with Diamond and the student engagement team continue to be valuable for both us and the students, providing a formal opportunity to check in with each student in year 2 and above individually. These enable us to understand how students are progressing with their projects and is a chance for them to flag any achievements or concerns they may have. Diamond has supported 19 PhD students to date with extensions to their studentships due to impact from COVID-19 and we have worked closely with our partners at universities to finalise these.

Student visits were impacted quite heavily due to the pandemic, being affected both by access to site and a change in teaching arrangements at universities. However, Diamond managed to support eight virtual and 11 in-person visits from undergraduate and postgraduate groups, offering a range of talks and training.

Scientific Workshops and Conferences

As a world-leading centre for synchrotron science, Diamond drives and supports science at UK universities and research institutes. Organising and planning events and workshops helps us to engage with our user community and potential users and provide opportunities to learn more about our instruments as well as shape future developments.

It has been a busy year of online workshops and webinars. Due to the pandemic, several of our regular events adapted to virtual mode including the Synchrotron Radiation School, HyperSpy and the X-ray Absorption Spectroscopy workshop. A number of new events were also introduced to the virtual events calendar such as the B24 Correlative Cryo-Imaging workshop and the DIAD User workshop. The Early Career Scientist Symposium worked particularly well online – allowing a much larger audience – seeing a record number of 270+ delegates. We have continued to engage our user community in preparations for the new beamlines for Diamond-II with several User Working Group meetings over the last few months.

Planning has begun for a move back toward in-person events for spring/summer 2022. August will see Diamond hosting IXS2022, our first international conference since the pandemic. We are excited to welcome the Inelastic X-ray Scattering community to Oxford to share new scientific discoveries and the latest developments in the instrumentation, experimental approaches and theories.

Date	Event	Number of attendees
19-23 April 2021	Hyperspy Workshop	100
20-21 April 2021	Vacuum Training Course	50
10-12 May 2021	Serial MX User Workshop	22
13-14 May 2021	bioSAXS Workshop	45
21 May 2021	GCRF START Collaboration Webinar	36
1-4 June 2021	Advanced SAS Training School	16
07 June 2021	GCRF START Closing Event	97
09-11 June 2021	XAS Workshop	38
23-25 June 2021	B24 Workshop	53
1-3 September 2021	S4SAS Conference	145
07-08 September 2021	DIAD Users Workshop	105
22 September 2021	I08 Webinar	134
01 October 2021	SWIFT Beamline User Working Group	15
05-07 October 2021	SR School (Part 1)	50
13-14 October 2021	SR School (Part 2)	50
27 October 2021	CSXID Beamline User Working Group	15
28 October 2021	SWIFT Beamline User Working Group	15
08-12 November 2021	Early Career Scientists Symposium	790
12 November 2021	SWIFT Beamline User Working Group	15
22-25 November 2021	eBIC cryo-ET Workshop	400
29 Nov - 10 Dec 2021	DLS-CCP4 Workshop	20
18 January 2022	Apprenticeship Open evening 1	17
26 January 2022	Apprenticeship Open evening 2	12
17 February 2022	Apprenticeship Open evening 3	3
21-24 February 2022	eBIC workshop Becoming an 'independent' single particle data collector	20
01 March 2022	Active Material Laboratory Introduction	96
11 March 2022	I06 laser-PEEM facility - User Working Group	11
17-18 March 2022	ePSIC/Birmingham Remote Demo Sessions	96

Addressing Global Health and Energy Challenges with START

In June 2021, we celebrated the achievements of the Synchrotron Techniques for African Research and Technology (START) programme[1]. Funded by a £3.7 M Global Challenges Research Fund (GCRF) grant provided by the UK's Science and Technology Facilities Council (STFC), the GCRF START programme equipped labs, supported research posts, and trained early-career scientists in the UK and Africa from 2018 to the close of the grant in 2021[2]. Diamond Light Source played a pivotal role providing scientists with crucial access to world class synchrotron techniques, beamtime, training and mentoring.

Research focused on structural biology and energy materials to address key United Nations' Sustainable Development Goals for health (SDG 3), energy (SDG 7), climate (SDG 13), and life-long learning (SDG 4). To improve energy efficiency and storage, scientists explored novel materials for solar cells, batteries, and fuel cells, as well as active and selective catalysts for fuels and chemical production. Diseases were studied for drug targets and vaccines, and 'green' biotechnology investigated for food security, industrial processing, and tackling toxic waste.

START's unique impact

More than 66 papers were published, many in leading journals. Dozens of protein structures were deposited in the global Protein Data Bank and over 264 Diamond synchrotron shifts were carried out through more than 61 beamtime sessions. Careers were enhanced and diversity improved. 41 PDRAs (post-doctoral research associates) and technicians were funded for three years (31 African; 10 UK). START's 25 leading Principal Investigators (PIs) and Co-Investigators (Co-Is)—seven from the UK and 18 from Africa—trained and mentored more than 92 postgraduates. Over 50% of 23 structural biology positions funded by GCRF START were held by female scientists.

Workshops and conferences hosted hundreds of international participants online and in person, including three African Neutron and Synchrotron Data Analysis Competency (ANSDAC) workshops with participants from over 10 African countries. GCRF START's Sci-ART project collaborated with the Keiskamma Trust, a South African community-led NGO[3].

Structural biology highlights

The structural biology landscape in South Africa was transformed resulting in further understanding of potential treatments for SARS-CoV-2 (COVID-19), snakebite envenomation, HIV, tuberculosis, malaria, bilharzia, human papilloma virus, cardiovascular disease, human metabolic disorders, African Horse Sickness virus, and industrial enzymes for the manufacture of medicines and commodity chemicals.

Nine START Co-Is built infrastructure at seven institutions, which now include six fully capable protein crystallography laboratories that can access synchrotrons world-wide, four labs own X-ray diffractometers and, uniquely

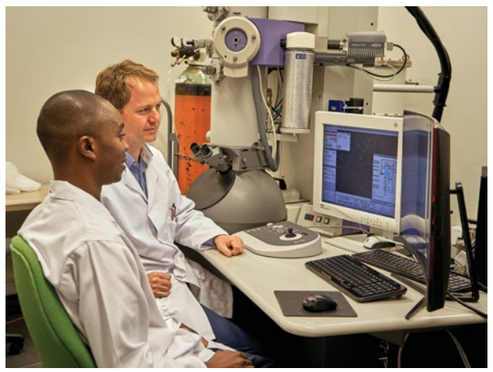

Dr Andani Mulelu (L) and Dr Jeremy Woodward next to the cryo-electron microscope at the University of Cape Town, South Africa. Photo Credit: Rebekka Stredwick.

GCRF START Energy Materials Workshop delegates in Cape Town. Photo credit: Rebekka Stredwick.

in Africa, the University of Cape Town's (UCT's) Aaron Klug Centre for Imaging and Analysis now houses a cryo-electron microscope equipped with a direct electron detector. Groups at eight institutions regularly collected X-ray diffraction data at Diamond and cryogenic Electron Microscopy (cryo-EM) data at the UK's national electron Bio-Imaging Centre (eBIC).

Access to fragment-based drug discovery resources on the XChem beamline (I04-1) at Diamond enhanced research prospects for early career scientists like START PDRA's Dr Blake Balcomb and Dr Anton Hamann from the University of Stellenbosch's Strauss Laboratory in their work to design medicines for tuberculosis, malaria, and *S. aureus* infections. Likewise, Dr Carmien Tolmie's studies on enzymes to develop drug targets for fungal infectious diseases are benefitting from exposure to X-ray crystallographic fragment screening for structure-based drug design. Dr Tolmie was promoted to academic staff at the University of the Free State following her role as a START-funded PDRA.

Notable examples include the determination of a broadly neutralising HIV antibody structure by START Co-Is Professors Lynn Morris and Penny Moore and START-funded PDRA Dr Thandeka Gwete-Moyo from South Africa's National Institute of Communicable Diseases (NICD). After using beamlines I04, I04-1 and I03 at Diamond, Thandeka reported: *"START has given me opportunities I could have never imagined".* The NICD now has structural biology projects to understand how antibodies recognise and stop SARS-CoV-2 variants of concern.

Another highlight is the determination of structures of substrates bound to hyperthermophilic amidases by UCT's START Co-I Professor Trevor Sewell and START PDRA Dr Stanley Makumire. The highlight of the research was the visualisation of a plant nitrilase by START PDRAs Dr Andani Mulelu, Angela Kirykowicz, and START Co-I Dr Jeremy Woodward using Diamond. The scientists were able to explain and modify the substrate specificity of these enzymes.

Dr Mohamed Fadlalla, Research Officer at the University of Cape Town's Centre for Catalysis. Photo credit: Rebekka Stredwick.

Energy materials highlights

To meet global energy demand, affordable, clean, and sustainable energy solutions are urgently required. The challenge is stability under environmental conditions and scaling up of fabrication, especially in remote areas. To address these challenges, scientists from as far as Zimbabwe, South Africa, UK, and Egypt collaborated with START.

Groups from South Africa's University of the Witwatersrand (Wits) and the UK's University of Oxford used cutting-edge evaporation and synchrotron techniques for the development of photoactive layers for cost-effective solar cell prototypes. Exposure to new skills led to new opportunities, including the award of British Council Newton Travel Grant to Kenyan researcher Dr Francis Otieno for research visits to Diamond and University of Oxford. Through investing his skills teaching postgraduates in Kenya, Francis continues START's legacy.

Energy Materials PhD student Gugulethu Nkala, on a workshop tour of Diamond Light Source. Photo credit: Gugulethu Nkala.

PhD students Michelle Nyoni, Michelle Thiebaut and Gugulethu Nkala are some of the increasing numbers of female energy research students at Wits. Nyoni and Thiebaut study lithium-iron phosphate and lithium-vanadium phosphate respectively, examining them as cathode materials to improve lithium-ion battery performance, safety, affordability, and environmental footprint. Nkala explores renewable energy storage systems and aims to fabricate a solid-state electrolyte for an all-solid-state battery. START provided valuable X-ray Absorption Spectroscopy (XAS) data analysis skills which the students not only applied to their data collected at Diamond, but also to research at Brookhaven National Laboratory.

In 2019, START PDRA Dr Mohamed Fadlalla and MSc student Chris Mullins identified parameters of iron-based bimetallic catalysts, which led to enhanced CO_2 hydrogenation performance. A key area of investigation was the effect of alloying in these materials on performance using *in situ* studies at Diamond focusing on XAS. This involved new collaborations with UCT's Centre for Catalysis and c*Change, the UK's Catalysis Hub, and the Universities of London (UCL), Cardiff, and Southampton. START Co-I Professor Peter Wells (Southampton/Diamond) and Egyptian Dr Khaled Mohammed (Southampton) provided specific XAS expertise; computational modelling was supported by START PDRA Dr Michael Higham (UK Catalysis Hub/Cardiff/UCL) following his successful secondment to UCT's Centre of Catalysis in 2019/2020. Subsequently, Dr Fadlalla was promoted to Research Officer and awarded prestigious university and national grants for his research going forward. New projects in the pipeline involve fuel cell storage to power vehicles and other devices.

Building on START's legacy

"START has been an exciting journey, which has reaped fantastic results in a remarkably short space of time," says Professor Chris Nicklin, Diamond Science Group Leader and GCRF START Principal Investigator. *"African researchers are keen to apply synchrotron techniques to their research problems and find African and joint solutions to global challenges. There is a huge appetite for a 'START 2,' especially if the ambition of an African Light Source is to be realised."*

Options to continue START's momentum include:

- an Africa Block Allocation Group (BAG) at Diamond
- funding for infrastructure in African laboratories and open hardware
- skills transfer through visits/exchanges
- training using existing networks such as c*Change and ANSDAC
- continuing international support networks to grow and retain early-career scientists

References:

1. https://start-project.org/
2. Nicklin, C. *et al.* Synchrotron Techniques for African Research and Technology: A Step-Change in Structural Biology and Energy Materials. *Synchrotron Radiation News*, 1–6 (2022).DOI: 10.1080/08940886.2022.2043684
3. https://start-project.org/keiskamma-sciart-collaboration/

Dr Carmien Tolmie using an X-Ray diffractometer at the University of the Free State, South Africa. Photo Credit: R. Machado.

Governance and Management

Diamond Light Source Ltd was established in 2002 as a joint venture limited company funded by the UK Government via the Science and Technology Facilities Council (STFC), now under UK Research & Innovation (UKRI), and by the Wellcome Trust, owning 86% and 14% of the shares respectively. Diamond now employs 786 scientists, engineers, technicians and support staff from 44 countries worldwide. The Chief Executive and Directors are advised by committees representing key stakeholder groups, including the Science Advisory Committee (SAC), Diamond Industrial Science Committe (DISCo) and Diamond User Committee (DUC).

Diamond is free at the point of access for researchers accessing Diamond via peer review, and provided the results are published in the public domain for everyone's benefit. Allocation of beamtime is via a peer review process to select proposals on the basis of scientific merit and technical feasibility. Twelve peer review panels meet twice a year to assess the proposals submitted for each six-month allocation period. Diamond also welcomes industrial researchers through a range of access modes including proprietary research.

Board of Directors

Prof. Sir Adrian Smith (Chairman)
Prof. Andrew Harrison OBE
Marshall Davies
Prof. Michael Fitzpatrick
Dr Morag Foreman
Prof. Mark Thomson
Andrea Ward
Prof. Keith Wilson

Company Secretary
Dr Linda Gregory

As at April 2022

Executive

Prof. Andrew Harrison OBE took the helm as CEO of Diamond Light Source in January 2014. He was previously Director General of the Institut Laue-Langevin neutron source in Grenoble, France, where he had worked since 2006. With a background as an inorganic chemist and Professor of Solid State Chemistry at the University of Edinburgh, Andrew brings a wealth of experience of scientific leadership to the organisation. Andrew was awarded an OBE in the Queen's Birthday Honours Lists 2020 for services to science during the COVID-19 response.

Prof. Laurent Chapon joined Diamond as Director of Physical Sciences in 2016 from the Institut Laue-Langevin in Grenoble, France. Whilst there, Laurent was Senior Fellow and Leader of the Diffraction Group for over five years. He is an expert in materials science as well as X-ray and neutron diffraction techniques. He was the first Diamond-II Programme Director and left Diamond in the beginning of 2022.

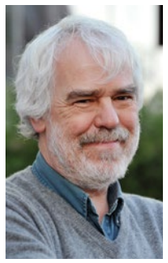

Prof. Sir David Stuart is MRC Professor of Structural Biology at the University of Oxford, and Joint Head of the Division of Structural Biology at the Department of Clinical Medicine. He was appointed Director of Life Sciences at Diamond in 2008. His principal research interests include the structure of viruses and viral proteins as well as cellular proteins, especially those that interact with viruses. Dave was knighted in the New Year Honours list 2021 for services to medical research and the scientific community.

Prof. Richard Walker joined Diamond Light Source as Technical Director in January 2002. He was previously Director of the Light Sources Division at Sincrotrone Trieste in Italy, and prior to that he was a key member of the Daresbury Laboratory SRS team. Richard is a visiting Professor of Physics at the University of Oxford.

Andrea Ward joined Diamond as Director of Finance and Corporate Services in 2019, with 15 years' experience as a Senior Finance professional. During a 12-year tenure at Vertex Pharmaceuticals, she worked with the Board to lead finance and procurement functions in Europe, later moving to Canada with the business to assist with acquisition and commercialisation opportunities. Andrea has also worked at ResMed and the Ontario Lottery and Gaming Corporation.

Staffing and Financial Information

Outline Organisational Chart

Chief Executive's Office
Communications, Engagement & Impact
Industrial Liaison
Safety, Health & Environment

Science Division

Science Groups:
Biological Cryo-Imaging
Crystallography
Imaging and Microscopy
Macromolecular Crystallography
Magnetic Materials
Soft Condensed Matter
Spectroscopy
Structures and Surfaces

Scientific Software, Controls & Computation Groups:
Accelerator Control Systems
Beamline Control Systems
Data Acquisition
Scientific Computing
Scientific Software

Detector Group
Experimental Hall Labs Services
Optics & Metrology
Planning & Projects Office
User Office

Technical Division
Accelerator Physics
Diagnostics
Engineering
Insertion Devices
Installation & Facility Management
Operations
Power Supplies
Radiofrequency Systems
Vacuum

Finance and Corporate Services
Corporate IT
Commercial Management, Governance & Legal
Finance
Human Resources
Procurement & Goods Handling
Soft Facilities

Summary of Financial Data

	2010/11	2011/12	2012/13	2013/14	2014/15	2015/16	2016/17	2017/18	2018/19	2019/20	2020/21	2021/22
Operating Costs £m	33.5	36.5	39.9	42.5	44.5	54.6	56.9	62.8	64.5	65.7	69.2	68.7
Total Staff (Year End)	419	438	481	507	534	582	609	639	680	742	775	786
Capital Expenditure – Operations £m	8.6	5.1	8.0	7.5	6.2	8.0	10.5	12.8	17.4	17.8	24.1	21.2
Phase II £m	16.2	9.9	2.8	0.8	0.2	0.0	0.0	0.0	0.0	0.0	0.0	0.0
Phase III £m	3.0	10.3	14.2	17.2	23.7	20.6	11.5	3.7	1.0	0.0	0.0	0.0
Other capital projects £m					4.8	5.6	7.3	4.3	5.3	1	2.1	2

Figures up to and including 2014/15 exclude VAT, thereafter figures include VAT.

Committee Membership

The Scientific Advisory Committee (SAC) advises the CEO and the Science Directors on the scientific and technical questions impacting the specification, design, commissioning and operation of the facility; experimental and user support facilities, and opportunities for scientific exploitation.

Dr Tom Hase (Chair)
University of Warwick (UK)

Dr Paul Adams
Lawrence Berkeley National Laboratory (USA)

Dr John Barker, Evotec
(DISCo Representative)

Dr Bridget Carragher
New York Center for Structural Biology (USA)

Prof. John SO Evans
University of Durham (UK)

Prof. Chris Hardacre
University of Manchester (UK)

Prof. Phil King
University of St Andrew (UK)

Dr Adrian Mancuso
European XFEL

Dr Lisa Miller
Brookhaven National Lab/NSLS-II (USA)

Dr Jörg Raabe
PSI (Switzerland)

Prof. Matt Rosseinsky
University of Liverpool (UK)

Prof. Andrea Russell
University of Southampton (UK) - (Chair of the DUC)

Prof. Mary Ryan
Imperial College (UK)

Prof. Christian Schroer
DESY (Germany)

Prof. Sam Shaw
University of Manchester (UK)

Prof. Titia Sixma
Netherlands Cancer Institute (Netherlands)

Prof. Elizabeth Wright
University of Wisconsin-Madison (USA)

The Diamond Industrial Science Committee (DISCo) advises the CEO and Directors on opportunities for industry to be engaged in research at Diamond, industrial research priorities that will help shape operational strategy, including the best way to exploit the current suite of beamlines and to develop the case for investment in future beamlines, and to develop best practice for industrial engagement.

Dr Malcolm Skingle
GlaxoSmithKline (Chair)

Dr John Barker
Evotec

Dr Andrew Barrow
Rolls-Royce

Prof. Dave Brown
Institut de Recherches Servier

Dr Paul Collier
Johnson Matthey

Dr Rob Cooke
Sosei Heptares

Dr Cheryl Doherty
GlaxoSmithKline

Prof. Peter Dowding
Infineum

Prof. Jonathan Hyde
NNL

Dr Andrew Johnson
IQE

Dr Olga Kazakova
NPL

Prof. Ken Lewtas
Lewtas Science & Technologies

Dr Ellen Norman
RSSL

Dr John Pollard
Vertex Pharmaceuticals (Europe) Ltd

Dr Richard Storey
AstraZeneca

Dr Pamela Williams
Astex Pharmaceuticals

The Diamond User Committee (DUC) has been set as a platform for discussion between Diamond and the user community of matters relating to the operation and strategy of Diamond.

Dr Imad Ahmed
University of Oxford

Dr Arnaud Basle
University of Newcastle

Dr Gavin Bell
University of Warwick

Dr Jamie Blaza
The University of York

Dr David Briggs
The Francis Crick Institute

Dr Ann Chippindale
University of Reading

Dr Sean Connell
CIC bioGUNE

Dr Kevin Edmonds
The University of Nottingham

Dr Enrique Jimenez-Melero
The University of Manchester

Dr Tim Knowles
University of Birmingham

Dr Marcus Newton
University of Southampton

Dr Robin Perry
University College London

Prof. Andrea Russell
University of Southampton (Chair)

Dr Neil Telling
Keele University

Dr Andrew Thomas
The University of Manchester

Dr Arwen Tyler
University of Leeds

Membership as at April 2022

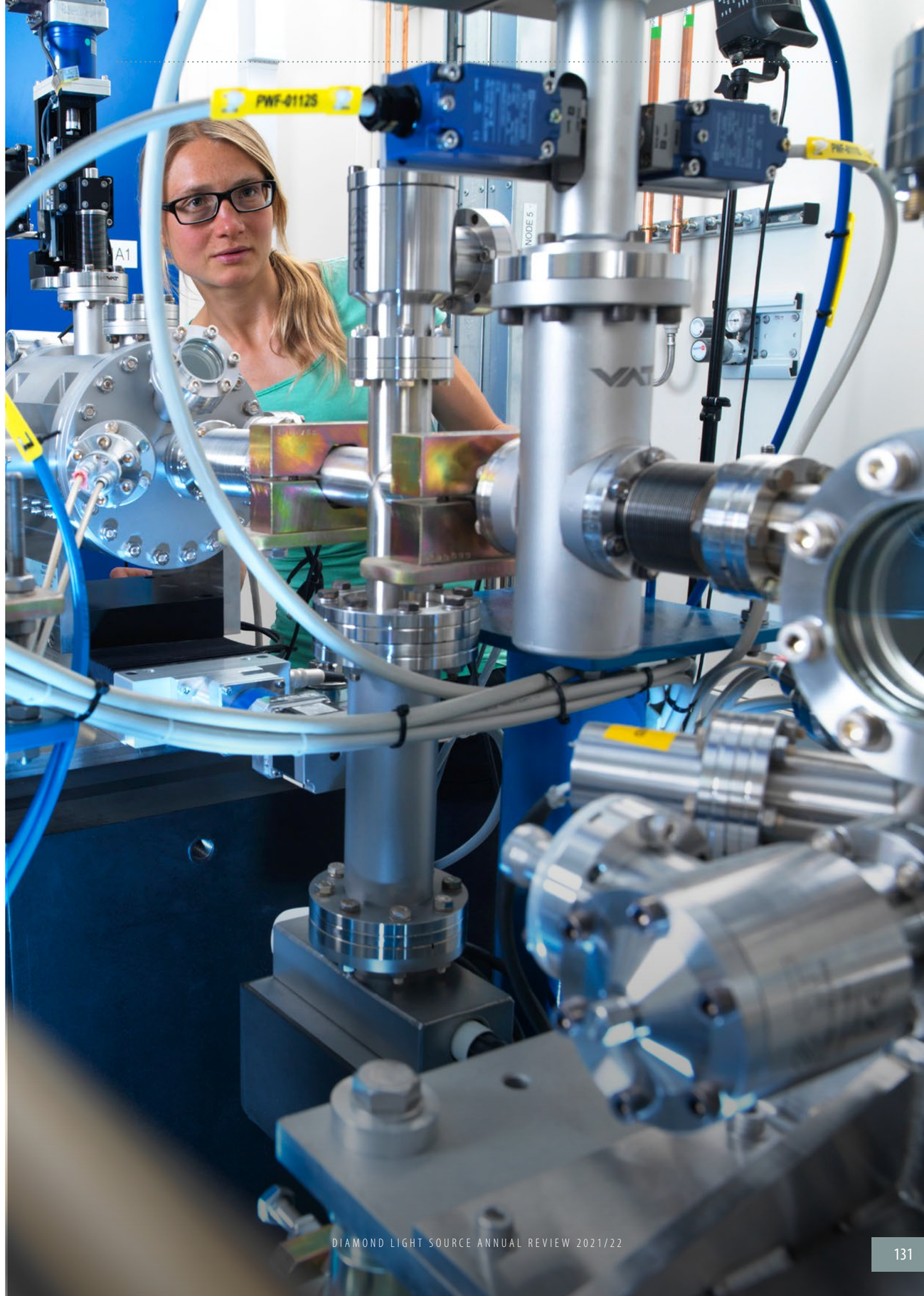

Diamond Light Source Ltd
Harwell Science & Innovation Campus
Didcot, Oxfordshire OX11 0DE
Tel: +44 (0)1235 778 639
Fax: +44 (0)1235 778 499
www.diamond.ac.uk

Acknowledgement:
We would like to thank the authors and all colleagues who contributed to this publication.

Published June 2022

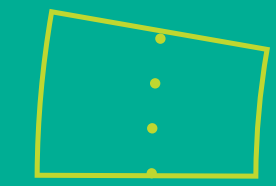

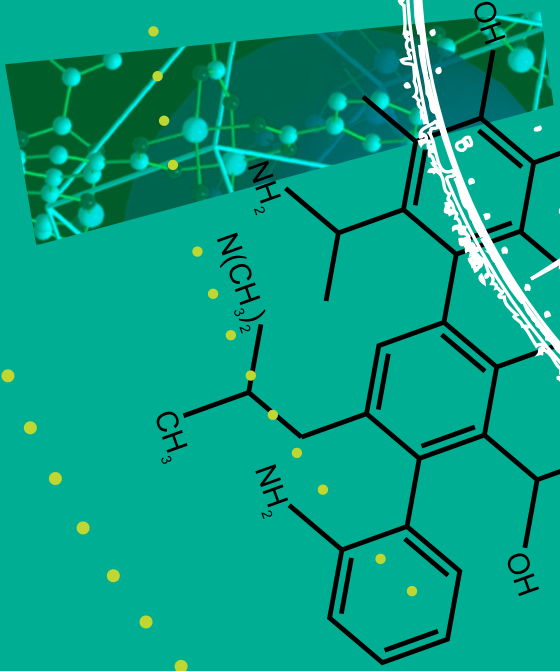

2022

Celebrating Diamond's 20th anniversary and 15 years of research and innovation